EDS.
MARCOS MATEUS · RAMIRO NEVES

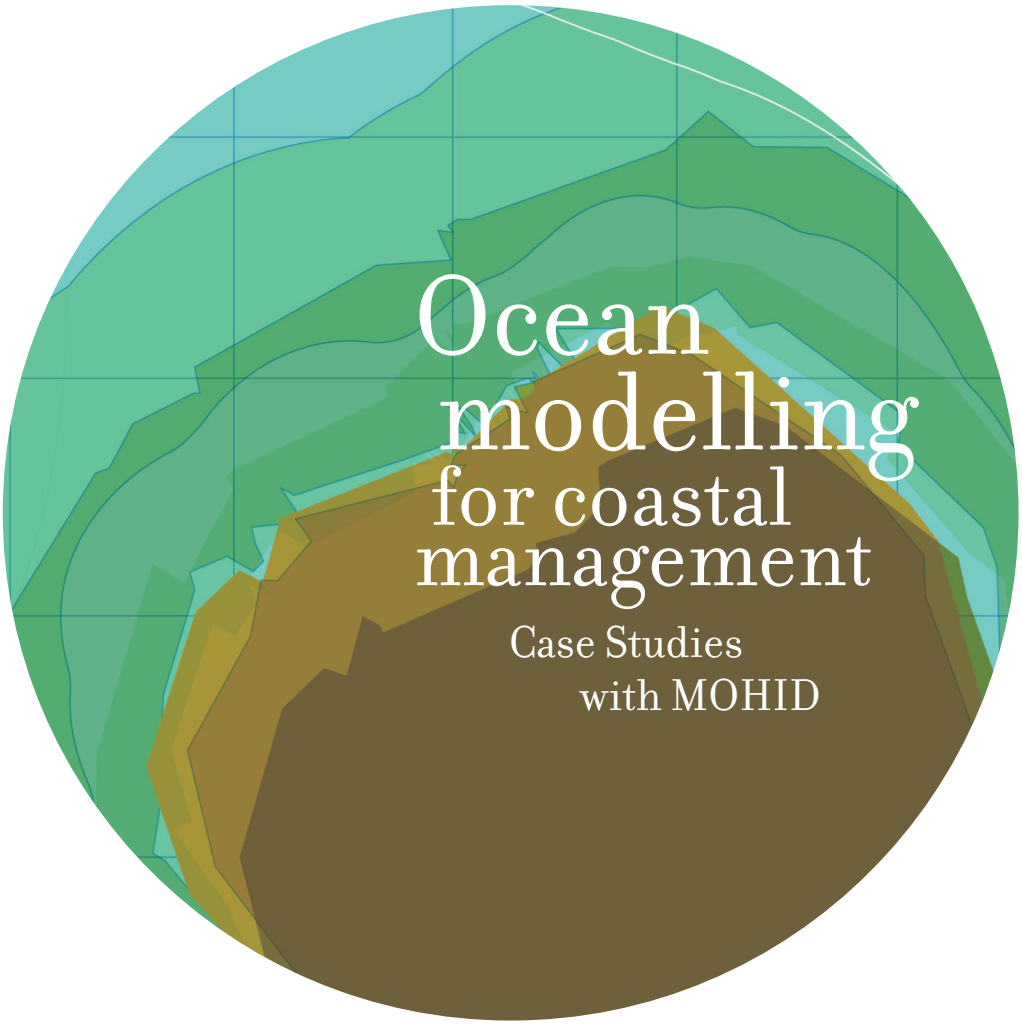

Ocean modelling for coastal management

Case Studies with MOHID

PRESS

TITLE

Ocean modelling for coastal management
– Case studies with MOHID

EDITORS
Marcos Mateus, Ramiro Neves

GRAPHIC ART PRODUCTION
Manuela Morais

DESIGN
Golpe de Estado- Produções Criativas, Lda.

PAGINATION
BSK Consulting Lda.

PRINTED AND BOUND BY
Tipografia Lousanense, Lda.

ISBN
978-989-8481-24-5

LEGAL REGISTRATION
352204/12

PUBLISHED AND DISTRIBUTED BY:
IST Press

IST PRESS

Director
Pedro Lourtie

Instituto Superior Técnico
Av. Rovisco Pais
1049-001 Lisboa
Portugal
www.istpress.ist.utl.pt

Color version book
www.mohid.com/books/2013OceanModellingMOHID.pdf

CONTENTS

CONTRIBUTORS

* Leading authors

Aliaga, Valentín
TAXON Estudios Ambientales S.L.
Polígono Industrial Oeste - C/ Urugay, s/n
Parcela 8/27. Nave 31
30820 Alcantarilla (Murcia)
Spain

Ascione, Isabella
MARETEC
Instituto Superior Técnico
Universidade Técnica de Lisboa
Av. Rovisco Pais
1049-001 Lisboa
Portugal

Belmonte, Antonio
TAXON Estudios Ambientales S.L.
Polígono Industrial Oeste - C/ Urugay, s/n
Parcela 8/27. Nave 31
30820 Alcantarilla (Murcia)
Spain

Campuzano, Francisco J.*
MARETEC
Instituto Superior Técnico
Universidade Técnica de Lisboa
Av. Rovisco Pais
1049-001 Lisboa
Portugal

Chambel-Leitão, Paulo*
HIDROMOD
Rua Rui Teles Palhinha, nº4 - 1º, Leião
2740-278 Porto Salvo
Portugal
Email: paulo.chambel@hidromod.com

Chícharo, Luís
CIMAR/CCMAR – Centro de Ciências do Mar
Faculdade de Ciências e Tecnologia
Campus de Gambelas, Universidade do Algarve
Faro
Portugal

Chícharo, Maria Alexandra
CIMAR/CCMAR – Centro de Ciências do Mar
Faculdade de Ciências e Tecnologia
Campus de Gambelas, Universidade do Algarve
Faro
Portugal

Cho, Kyoung-Ho
Coastal Disaster Research Center
Korea Institute of Ocean Science and Technology
Ansan
Korea
Email: kcho@kiost.ac

Choi, Jin-Yong
Coastal Disaster Research Center
Korea Institute of Ocean Science and Technology
Ansan
Korea

Coelho, Henrique
Universidade Lusófona de Humanidades e
Tecnologias
Faculdade de Engenharia e Ciências Naturais
Campo Grande, 376
1749 - 024 Lisboa
Portugal

de Pablo, Hilda*
MARETEC
Instituto Superior Técnico
Universidade Técnica de Lisboa
Av. Rovisco Pais
1049-001 Lisboa
Portugal
Email: hildadepablo@ist.utl.pt

Dias, João Miguel
CESAM
Physics Department, University of Aveiro
Campus de Santiago
3810-193 Aveiro
Portugal

Ezzatti, Pablo
Instituto de Computación
Facultad de Ingeniería
Universidad de la República
Uruguay

Fernández, Mariana
Instituto de Mecánica de los Fluidos e Ingeniería
Ambiental
Facultad de Ingeniería
Universidad de la República
Uruguay

Fossati, Mónica*
Instituto de Mecánica de los Fluidos e Ingeniería Ambiental
Facultad de Ingeniería
Universidad de la República
Uruguay
Email: mfossati@fing.edu.uy

Franz, Guilherme
MARETEC
Instituto Superior Técnico
Universidade Técnica de Lisboa
Av. Rovisco Pais
1049-001 Lisboa
Portugal

García, Pablo E.
Computational Hydraulic Program
Hydraulic Laboratory
National Institute for Water (INA)
Autopista Ezeiza-Cañuelas
Tramo Jorge Newbery, Km 1,620
Casilla de Correo Nº46, 1802, Ezeiza
Buenos Aires
Argentina

Gutiérrez, Jose M.
TAXON Estudios Ambientales S.L.
Polígono Industrial Oeste - C/ Urugay, s/n
Parcela 8/27. Nave 31
30820 Alcantarilla (Murcia)
Spain

Hyun, Sang-Kwon*
ARA Consulting & Technology
Bucheon, Gyeonggi
Korea

Junior, Jader Lugon
Instituto Federal de Educação
Ciência e Tecnologia Fluminense
Macaé, Rio de Janeiro
Brasil

Lecertúa, Emilio
Computational Hydraulic Program
Hydraulic Laboratory
National Institute for Water (INA)
Autopista Ezeiza-Cañuelas
Tramo Jorge Newbery, Km 1,620
Casilla de Correo Nº46, 1802, Ezeiza
Buenos Aires
Argentina

Lee, Dong-Young
Coastal Disaster Research Center
Korea Institute of Ocean Science and Technology
Ansan
Korea

Leitão, José Chambel
HIDROMOD
Rua Rui Teles Palhinha, nº4 - 1º, Leião
2740-278 Porto Salvo
Portugal

Lima, Edgar Barbosa*
Departamento de Modelagem Computacional
Universidade do Estado do Rio de Janeiro
Nova Friburgo, Rio de Janeiro
Brasil

Lopes, João
Escola Superior de Tecnologia
Campus da Penha, Universidade do Algarve
Faro
Portugal

Malhadas, Madalena S.
HIDROMOD
Rua Rui Teles Palhinha, nº4 - 1º, Leião
2740-278 Porto Salvo
Portugal

Martins, Flávio
Escola Superior de Tecnologia
Campus da Penha, Universidade do Algarve
Faro
Portugal

Mateus, Marcos*
MARETEC
Instituto Superior Técnico
Universidade Técnica de Lisboa
Av. Rovisco Pais
1049-001 Lisboa
Portugal
Email: mmateus.maretec@ist.utl.pt

Menéndez, Ángel N.
Computational Hydraulic Program
Hydraulic Laboratory
National Institute for Water (INA)
Autopista Ezeiza-Cañuelas
Tramo Jorge Newbery, Km 1,620
Casilla de Correo Nº46, 1802, Ezeiza
Buenos Aires
Argentina

Mesa, Mirtha Irizar
Centro de Investigáciones Hidraulicas
Instituto Superior Politécnico Jose Antonio Echeverria
Havana
Cuba

Moita, Maria Teresa
IPMA, I.P. – Instituto Português do Mar e da Atmosfera
Av. Brasilia, s/n
1449-006 Lisboa
Portugal

Morais, Pedro*
International Center for Coastal Ecohydrology
Solar do Capitão-Mor, Horta das Figuras
Faro
Portugal
Email: pmorais@ualg.pt

Neto, Antônio José da Silva
Departamento de Modelagem Computacional
Universidade do Estado do Rio de Janeiro
Nova Friburgo, Rio de Janeiro
Brasil

Neves, Ramiro*
MARETEC
Instituto Superior Técnico
Universidade Técnica de Lisboa
Av. Rovisco Pais
1049-001 Lisboa
Portugal
Email: ramiro.neves@ist.utl.pt

Nogueira, João*
Universidade Lusófona de Humanidades e Tecnologias
Campo Grande, 376
1749-024 Lisboa
Portugal
Email: joaorobertn@gmail.com

Oliveira, Ana Paula
IPMA, I.P. – Instituto Português do Mar e da Atmosfera
Av. Brasilia, s/n
1449-006 Lisboa
Portugal

Otero, Luis
Grupo de Física Aplicada
Departamento de Física, Universidad del Norte
Km 5 vía a Puerto Colombia, Barranquilla
Colombia

Perán, Alberto I.*
TAXON Estudios Ambientales S.L.
Polígono Industrial Oeste - C/ Urugay, s/n
Parcela 8/27. Nave 31
30820 Alcantarilla (Murcia)
Spain
Email: alberto@taxon.es

Piedra-Cueva, Ismael
Instituto de Mecánica de los Fluidos e Ingeniería Ambiental
Facultad de Ingeniería
Universidad de la República
Uruguay

Pierini, Jorge
Comisión de Investigaciones Científicas (CIC)
IADO-UNS-CCT BB
CC 804
Bahía Blanca
Argentina

Pina, Pedro
Water and Utilities Account Manager
Bentley Systems (South Europe)
Rua Teresa de Jesus Pereira nº 36 3 Esq
2560 Torres Vedras
Portugal

Pinto, Lígia*
MARETEC
Instituto Superior Técnico
Universidade Técnica de Lisboa
Av. Rovisco Pais
1049-001 Lisboa
Portugal
Email: ligia.pinto@ist.utl.pt

Quental, Teresa
IPMA, I.P. – Instituto Português do Mar e da Atmosfera
Av. Brasilia, s/n
1449-006 Lisboa
Portugal

Re, Mariano*
Computational Hydraulic Program
Hydraulic Laboratory
National Institute for Water (INA)
Autopista Ezeiza-Cañuelas
Tramo Jorge Newbery, Km 1,620
Casilla de Correo Nº46, 1802, Ezeiza
Buenos Aires
Argentina
Email: mre@fi.uba.ar

Ribeiro, João
HIDROMOD
Rua Rui Teles Palhinha, nº4 - 1º, Leião
2740-278 Porto Salvo
Portugal

Rodrigues, Pedro Paulo Gomes Watts
Departamento de Modelagem Computacional
Universidade do Estado do Rio de Janeiro
Nova Friburgo, Rio de Janeiro
Brasil
Email: pwatts@iprj.uerj.br

Santoro, Mariano
Instituto de Mecánica de los Fluidos e Ingeniería Ambiental
Facultad de Ingeniería
Universidad de la República
Uruguay

Senabre, Tomás
TAXON Estudios Ambientales S.L.
Polígono Industrial Oeste - C/ Urugay, s/n
Parcela 8/27. Nave 31
30820 Alcantarilla (Murcia)
Spain

Silva, Alexandra
IPMA, I.P. – Instituto Português do Mar e da Atmosfera
Av. Brasilia, s/n
1449-006 Lisboa
Portugal

Sobrinho, João L.*
MARETEC
Instituto Superior Técnico
Universidade Técnica de Lisboa
Av. Rovisco Pais
1049-001 Lisboa
Portugal
Email: joao.sobrinho@ist.utl.pt

Vaz, Nuno*
CESAM
Physics Department, University of Aveiro
Campus de Santiago
3810-193 Aveiro
Portugal
Email: nuno.vaz@ua.pt

ACKNOWLEDGEMENTS

M. Mateus • R. Neves

The editors would like to thank the authors who contributed to this book for their enthusiasm and willingness to share their own work and experience as MOHID users. The MOHID model is the result of a collaborative effort and cumulative development of more than 20 years of work, and, while it is impossible to acknowledge here all those involved, we dedicate the book to this vast team of technology experts and scientists.

The MOHID modelling system is an open source code with hundreds of active users worldwide, and we would like to express our gratitude to this wide community of users for their contribution to the continuous advance and improvement of the model. Finally, our thanks go to the IST Press team for the professional advice and assistance throughout the editing process.

THE MOHID CONCEPT

R. Neves

CHAPTER SYNOPSIS

Mathematical models transform conservation principles into quantification tools. They must satisfy the Gauss theorem when applied to a physical space delimited by open surfaces and must guarantee conservation when dealing with transformation processes that in environmental systems are mostly due to biological activity, involving energy fluxes in the form of mass transfer between consumers and producers.

MOHID is an environment modelling system dealing with transport and with biogeochemical transformation processes in complex geometries. It was developed to be used by researchers and by professionals and to be applicable to a large range of scales and physical conditions. Researchers require tools able to test hypotheses and compare options. Professionals require efficiency for quick results production. A wide range of scales requires the consideration of the corresponding transport processes and of interactions between scales.

This chapter describes the MOHID architecture and engineering developed to satisfy the requirements derived from the range of user profiles, physical scales and biogeochemical processes to be considered. The architecture designed permitted the integration of several models in the modelling system and the engineering adopted simplified the development of the information tools necessary to manage field data and model results in complex systems.

1 INTRODUCTION

The actual MOHID architecture was designed in the late nineties based on previous team experience and on the information technologies becoming available to the FORTRAN modelling community resulting from the publication of the new FORTRAN 90 language, but also from the development of standard data formats as HDF[1] and of more performing personal computers. Together with the HDF format personal computers permitted the use of small pieces of software not available in former mainframes that have strongly improved modellers productivity.

Scientific developments carried up to the nineties in the framework of a set of Ph.D theses concerned with hydrodynamics [1-4] and with eulerian ecological modelling [5] and M.Sc. theses mostly concerned with lagrangian transport [6] and ecological modelling [7,8] supported the design of the MOHID architecture. These developments included 2D and 3D developments, mesoscale and Boussinesq wave modelling and eulerian and lagrangian models. These developments generated different models of difficult maintenance in a quick scientific and technological evolving context. The need to combine them generating a modular system where differences were handled in specific parts of the code was high.

The new MOHID model should be able to deal with 2D and 3D simulations, to deal with Eulerian, Cartesian or Lagrangian vertical coordinates, to deal Eulerian or Lagrangian transport references and to use the same biogeochemical formulations independently of the number of spatial dimensions or space reference and should allow alternative formulations for every process in order to be flexible in terms of scientific developments.

[1] HDF was developed by the National Center for Supercomputing Applications and is now supported by The HDF Group: http://www.hdfgroup.org/)

The finite-volume method already used by Martins [4] was adopted to make the spatial description independent of the vertical coordinate and of the number of vertical dimensions and all the transformations processes occurring inside the volume were programed using a 0D formulation in order to make them independent of the spatial reference, being the code sharable by the eulerian and the lagrangian formulations.

A fractional time step was used in order to split the resolution of processes using the most adequate temporal discretization or calculation sequence in each of them. This approach was necessary to decouple the resolution of the transport and transformation processes, but also to decouple the resolution of biogeochemical processes creating the independence need to aggregate developments carried out by different people.

The resolution of evolution equations in their integral form simplified the design of the desired architecture. This form requires the explicit consideration of fluxes across the surfaces surrounding the integration volumes easing conservation during transport which is often violated in mathematical models when flux divergence is computed.

After accomplishment of the requirements described above a modular system to simulate free surface flows was achieved in the early years of 2000 decade. The Leitão [9] thesis was the first accomplished using this new concept that was described in [10]. The flexibility of the system simplified the subsequent development of a MOHID version to simulate catchments and all together these developments created a user's community that justified heavy investments on Information Technologies. *MohidStudio*[2] was developed to simplify the implementation of the model, assessment and processing of input data and the management of simulations, ncluding results visualizing and archiving. *AquaSafe*[3] was designed to automate procedures including the production of web services to integrate results of different models and field data in order to adequate the products to corporate user needs.

2 THE CONSERVATION EQUATION

MOHID is formulated using the integral approach stated in Equation 1, which describes the conservation principle – "The rate of accumulation inside a control volume balances the input and output fluxes plus sources minus sinks":

$$\frac{\partial}{\partial t}\left(\iiint_{CV}\beta dV\right) = -\iint_{surface}\left[\left(\beta\vec{u}.\vec{n}\right)+\left(-\vartheta\vec{\nabla}c.\vec{n}\right)\right]dA+\iiint_{CV}(S_0-S_i)dV \tag{1}$$

where CV is the Control Volume, u is the fluid velocity relative to the volume surface ϑ is the diffusivity and (S_0–S_i) are the property β rate of production per unit of volume. Using the Gauss theorem, Equation 1 is transformed into the differential conservation equation:

$$\frac{\partial\beta}{\partial t} = -\frac{\partial}{\partial x_j}\left(u_j\beta-\vartheta\frac{\partial\beta}{\partial x_j}\right)+(S_o-S_i) \tag{2}$$

[2] *MohidStudio* is a trademark of Action Modulers (http://www.actionmodulers.com) and software aims to simplify the implementation of MOHID and facilitate the interaction between modelling and field data.

[3] *Aquasafe* is a trademark of Hidromod (http://www.hidromod.com). It was designed to automate procedures including the production of web services to integrate results of different models and data.

Equation 2 states that the rate of change of a property in a point balances the divergence of the advection plus diffusion fluxes at that point plus the production minus the consumption rate per unit of volume. Manipulating Equation 2 one can write the conservation equation in a lagrangian reference where the time derivative states that the rate of change in an elementary volume of fluid balances diffusion across its boundaries plus sources minus sinks:

$$\frac{d\beta}{dt} = \frac{\partial}{\partial x_j}\left(\vartheta\frac{\partial\beta}{\partial x_j}\right) + (S_o - S_i) \tag{3}$$

If the surface of the control volume used into Equation 1 is moving at the fluid velocity Equation 3 is obtained. In this case the surface could be deformed, but the total volume inside the surface would remain constant. If instead the surface of the controle volume could also move in order to build an envelope of the molecules initially inside the volume[4] the space occupied by the control volume would increase in time, but the total flux of β across the surface would be zero. The volume increase is a result of the entrainment of surrounding fluid and consequently the concentration β inside the control volume will change according to the difference between the concentration inside the volume and the concentration of the entrained fluid. The MOHID lagrangian module computes dilution through a volume increasing rate.

3 MOHID ASSESSMENT OF ENVIRONMENTAL SYSTEMS

Equation 1 requires volume integration to compute rates of accumulation and rates of transformation and surface integration to compute rates of exchange due to advection and to diffusion. The calculation of these fluxes requires the knowledge of the velocity and diffusivity along the Control-Volume (CV) surface, which value depends on the scales resolved by the model.

3.1 Aquatic environments

Figure 1 shows the MOHID vertical layout for aquatic systems. On the top of the water column is separated from the atmosphere by the air-water interface and the benthic layer separates the water column from the sediment at the bottom. MOHID includes modules for the processes in the water column, in the sediments and in the interfaces and uses atmospheric information provided by meteorological models or data from meteorological stations to describe the atmosphere.

Air-water fluxes are the only variables owned by the air-water interface. They can be specified by the meteorological model or computed using air temperature, moisture, wind speed, cloud cover and solar radiation and coefficients provided by the user. Precipitation has to be specified by the user. On the contrary the benthic interface layer lying between the water column and the sediment computes fluxes but is also owner of state variables having negligible mobility (filter feeders, microphytobenthos, decomposers, etc.).

Properties in the water column exchange material among them using the water as a transport agent. The planktonic properties move at the water speed, but particulate material can

[4] Random velocity associated to the Brownian movement (generating molecular diffusion) or to turbulent movement mix the initial fluid with surrounding fluid the surface has to have additional movement to surround the initial molecules, i.e., the volume increases as a result of diffusion.

have their own velocity too. It is the case of sediments that have its own settling velocity or oil that moves vertically in the water column to reach its stability depth (usually the surface) or fish larvae and dinoflagellates that can have alternated upward and downward movements in the water column. Macroalgae and suspended filter feeders are also water column properties – although they do not move with the water – because they can exchange material with several layers in the water column (macroalgae length can be long compared with water column height and thus with model vertical layer thickness).

The module Water-Properties manages the simulation in the water column. It uses the geometry, velocity, water fluxes, and diffusivity whose computation is managed by the Hydrodynamic module and invokes modules in charge of solving the equation terms associated to the property's activity (e.g., sources/sinks, settling, swimming, adsorption/desorption). The module water properties also manages the calculation of state variables derived from others, as is the case of water density or light intensity.

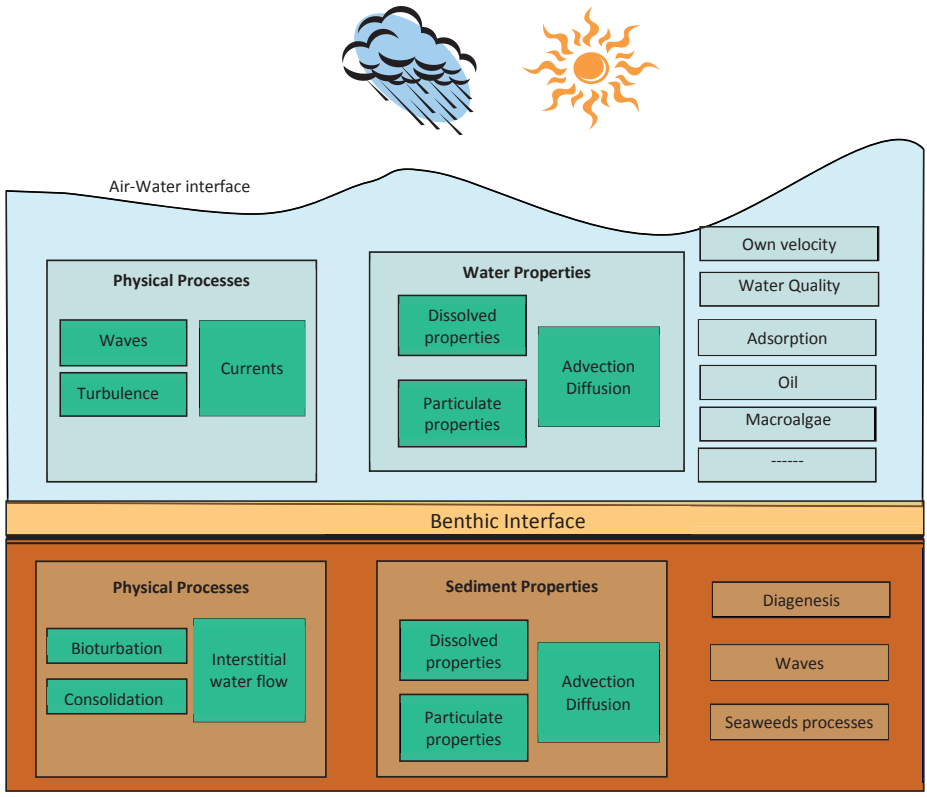

Figure 1. *Layout of MOHID vertical description of the aquatic environment. The water column is separated from the atmosphere by the Air-Water interface and from the consolidated sediment by the Benthic interface.*

Processes in the sediment have the same origin and structure as the processes occurring in the water column, but are much slower due to lower mobility of the dissolved material. There is advection due to interstitial water movement generated by sediment consolidation and/or by groundwater exfiltration. Diffusion is molecular in the lower layers and is induced by animals' activity – bioturbation – in the upper 10 cm layer. Like in the water column properties can be dissolved and unlike in the water column most material is particulate. Because of the low water content and mobility exchanges between deposited sediment and water column are slow and sediment is mostly anoxic.

In shallow zones with low sediments deposition rate seaweeds can develop injecting organic matter inside the sediment through roots' growth and extracting mineral nutrients regenerated by organic matter mineralisation. In regions with high settling rate accretion of sediments is usually the main mechanism to maintain organic matter content in the sediment. The Sediment-Properties module manages the transport of properties inside the sediments computing advection using the water movement associated to the consolidation process (in absence of groundwater exfiltration) and diffusion using bioturbation diffusivity and invokes modules in charge of computing reactions and exchange between dissolved and particulate phases. Fluxes at the interface sediment-water are managed by the benthic layer which can accumulate particulate matter "fluff layer" and computes fluxes of dissolved properties.

Particulate material deposited in the fluff layer maintains its ordinary critical shear stress for erosion and is transferred into sediment at a low rate (or the order of mm/month). Material transferred into the sediment acquires its critical stress for erosion and generates a flux of properties as a function of the concentration in the benthic layer. Fluxes of dissolved material are computed using the concentration difference between water and sediment and an exchange coefficient function of the flow next to the bottom (in the first layer).

Salt marshes and tidal flats are a limit case of the representation shown in Figure 1. In these areas the sickness of the water column is zero at low water periods, allowing these zones to exchange directly with the atmosphere.

3.2 Land environments

Vertical structure of land environments is identical to vertical structure of aquatic environments, although the relative importance of the compartments is very much different. In fact, on land a water column is an exception, although it can occur during flood events or in ponds and in the sediment (i.e., in the soil) water flow is usually much more intense than in the aquatic sediment, being soil usually not saturated with water. As a consequence, in normal conditions, on land surface runoff occurs only in rivers and generalised surface runoff occurring only during storm events.

Figure 2 represents schematically the elements composing a catchment. The soil is the sediment equivalent in the aquatic environment. The river network (or ponds) is the water column equivalent in aquatic environment and soil surface is similar to salt marches, the major difference being the inundation frequency and the fact that the sediment below land surface is usually unsaturated.

The correspondence between compartments in land and aquatic environments permits the use of the same data structure to describe them and consequently both models can share the software architecture.

4 MOHID GEOMETRY

Evolution processes in a three dimensional environment are described by conservation Equations 1 to 3, which can describe balances to finite volumes or at one point. Mathematical models have to describe nature using discrete values computed in a grid. The consideration of the grid as a finite number of adjacent volumes to which the conservation Equation 1 is applied simplifies the respect of the mass conservation principle and permits the use of irregular grids as that shown in Figure 3.

MOHID has adopted the integral form of the equations, fluxes being computed over the faces of the finite volumes (cells). Inside the volumes source and sink terms are computed based on the local values. Diffusive fluxes are computed at each cell face using concentration values on each side of the face and advection is computed using the water discharge across the cell face and a concentration estimated using a spatial interpolation in order to generate upstream, central differences, QUICK or TVD methods.

Diffusivity and water fluxes are computed by the hydrodynamic module over the face using a staggered grid approach where velocities are computed on the faces of the cells described on Figure 3. In the hydrodynamic module (as in the hydrological module) a conservative approach is also considered for advection and diffusion, meaning that velocities are also computed using finite volumes obtained by interpolation of the control volumes used for scalars.

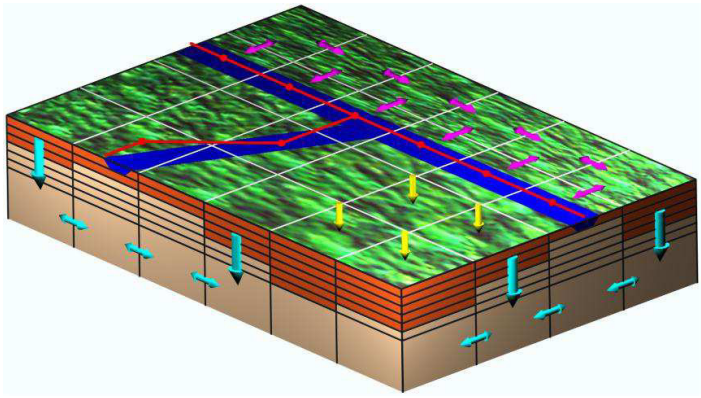

Figure 2. *Vertical description of a catchment. The surface gets rain and at surface we can have a river network in normal conditions and generalised surface runoff during rain events. It is also at surface that vegetation grows and in the soil one can have a non-saturated zone (vadose zone) on the top of a saturated zone. All these compartments can exchange water in two senses.*

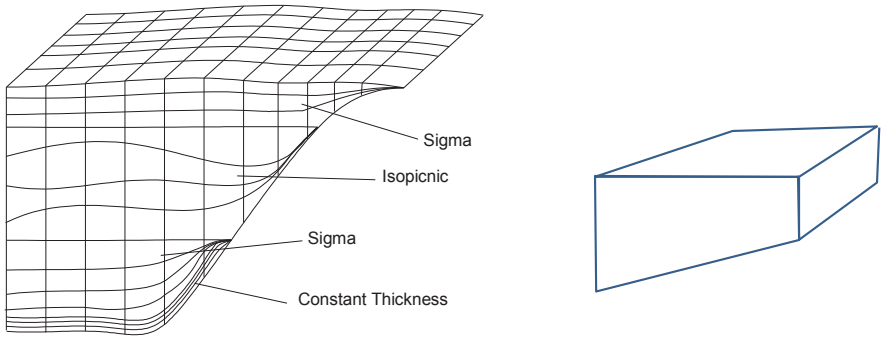

Figure 3. *Example of spatial descretization combining domains with different types of coordinates (left) and an example of a finite-volume (right).*

Most MOHID applications use parallelepiped control volumes with orthogonal horizontal axes simplifying the calculation of the internal products necessary to compute fluxes. However MOHID can also use curvilinear grids as that shown on Figure 4. The curvilinear grid is adequate to compute flows in horizontal anisotropic systems (e.g., rivers). It saves memory and increases the transversal resolution, but it requires simplifications for momentum fluxes calculation, to be computationally efficient.

On vertical direction the internal product involved on the calculation of fluxes is simple because the area of cell surfaces projected on a horizontal plane is constant and uniform for every vertical column. Vertical water fluxes are computed considering the rate of change of the cell volume and incompressibility.

5 VERTICAL COORDINATE

The integral form of the conservation equation adopted by MOHID permits a very versatile definition of vertical coordinates. The most suitable coordinate is the one that minimises advective fluxes between adjacent cells. In fact advective fluxes in presence of Courant numbers very much different from unit are a major source of numerical diffusion. Vertical velocities are usually much smaller than horizontal velocities and consequently the corresponding Courant number can be much smaller than one. The consideration of a lagrangian grid where cell boundaries have some vertical movement minimises the vertical diffusion.

Rigid rectangular coordinates are the simplest because, apart from the surface layer, they do not move in time. They are adequate to simulate horizontal flows where topography plays a minor role. This is the case of the deep oceans. On the contrary the sigma coordinate varies between zero at the bottom and 1 at the surface and consequently the layer thickness varies according to water column depth which depends on the bathymetry and on the movement of the free surface. Sigma coordinates are the most adequate to simulate the flow in coastal shallow areas. Both coordinates can be combined with the lagrangian coordinate option to minimize numerical diffusion associated to high frequency waves.

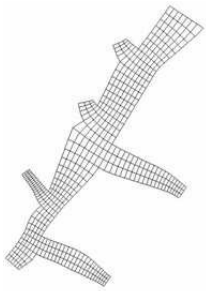

Figure 4. *Example of a curvilinear grid used in MOHID.*

Different coordinates can be combined in a simulation using the concept of a vertical dominium as shown on Figure 3. The simulation of ocean flows (or flows in deep artificial reservoirs) is dominated by baroclinic effects in the deeper zones and by topography in the shelf zone. The use of a Cartesian coordinate between the bottom and the shelf break and a sigma coordinate between the shelf break and the free surface is usually the most convenient combination. A 2D vertically integrated simulation is a particular case of a 3D sigma model. It is a 3D sigma model with just one layer.

MOHID includes procedures to combine Cartesian and sigma coordinates (lagrangian or not) using simple data specification. The user must specify the number of vertical domains to be used, the type of coordinate to use in each of them and the spatial step.

6 TEMPORAL DISCRETIZATION

Stability and accuracy but also computational software structure are determined by temporal discretization options. Explicit models generate the simplest codes but have to verify the CFL condition. The Crank-Nicolson (semi-implicit) codes have computation complexity identical to implicit codes and have better accuracy.

MOHID uses semi-implicit algorithms to compute the processes with higher stability restrictions and explicit algorithms for others. Gravity waves, vertical advection and diffusion and particulate matter settling are among the most restrictive processes and are computed using implicit algorithms.

Numerical instabilities are usually generated by excessive transport or consumption. Advection and diffusion generate instabilities when the material removed from one cell in a time step exceeds the existing material at the beginning of the time step and the sink terms generate instabilities when the consumption calculated by the model in one time step exceeds the existing material. The sequential calculation of processes in explicit algorithms minimises the probability of introducing instabilities and can simplify the algorithm itself (e.g., computing sequentially the transport in different directions) of computing sequentially the biogeochemical processes (e.g., respiration, natural mortality, predation, etc.). Equation 4 describes the procedure using the addition associative property:

$$\frac{\partial \beta}{\partial t} \approx \frac{\beta^{t+\Delta t} - \beta^{t}}{\Delta t} = \frac{\beta^{t+\Delta t} - \beta^{*}}{\Delta t} + \frac{\beta^{*} - \beta^{**}}{\Delta t} + ... + \frac{\beta^{***} - \beta^{t}}{\Delta t} \tag{4}$$

Applying this approach to Equation 5 one gets a set of algebraic equations as described in Equation 6.

$$\frac{\partial \beta}{\partial t} + u_j \frac{\partial \beta}{\partial x_j} = \frac{\partial}{\partial x_j}\left(\vartheta \frac{\partial \beta}{\partial x_j}\right) + f_1 + f_2 \tag{5}$$

$$\begin{aligned}
\frac{\beta^{***} - \beta^{t}}{\Delta t} &= \left(-u_1 \frac{\partial \beta}{\partial x_1}\right)^{t} + \left(-u_2 \frac{\partial \beta}{\partial x_2}\right)^{t} + \frac{\partial}{\partial x_1}\left(\vartheta \frac{\partial \beta}{\partial x_1}\right)^{t} + \frac{\partial}{\partial x_2}\left(\vartheta \frac{\partial \beta}{\partial x_2}\right)^{t} \\
\frac{\beta^{**} - \beta^{***}}{\Delta t} &= \left(-u_3 \frac{\partial \beta}{\partial x_3}\right)^{**} + \frac{\partial}{\partial x_3}\left(\vartheta \frac{\partial \beta}{\partial x_3}\right)^{**} \\
\frac{\beta^{*} - \beta^{**}}{\Delta t} &= (f_1)^{**} \\
\frac{\beta^{t+\Delta t} - \beta^{*}}{\Delta t} &= (f_2)^{*}
\end{aligned} \tag{6}$$

In the algorithms described in (6) the second step would be implicit and the others would be explicit. This procedure permits the optimization of the numerical algorithm and the subdivision of the model into modules that modify the state variables independently. The procedure is useful within a research group, but is especially useful to combine developments by several research groups. This is the case of biochemical models where sometimes higher trophic levels are computed using Energy Budget concepts instead of mass budgets as is the case for planktonic primary producers.

7 MODULAR STRUCTURE

A modular structure combined with object oriented programing is essential to develop complex models dealing with very much different processes and groups of state variables. This is essential for managing memory and especially to restrict the effects of software bugs to a single module. The temporal discretisation described above simplifies the implementation of the modular approach.

MOHID modules are combined in terms of geometrical requirements and in terms of groups of state variables. There is a central module (Module Model) in charge controlling the whole system and key modules as WaterProperties, Hydrodynamics, Geometry, AdvectionDiffusion, Atmosphere and Benthos that are always used to simulate free surface flows and the modules PorousMedia and SurfaceRunOff that are used in MOHID Land instead of the module Hydrodynamics.

The module WaterProperties defines the variables that will be simulated in each run. In this module are specified the modules and the state variables necessary to simulate a particular state variable. The Atmosphere Module specifies how the interaction with the atmosphere will be done. If fluxes are available (e.g., generated by an atmospheric model) MOHID will use those fluxes. Otherwise the module InterfaceAirWater will compute the fluxes using atmospheric state variables specified as boundary conditions.

8 SOFTWARE ENGINEERING

MOHID evolved from a sequential FORTRAN 77 model to an object oriented model programed in FORTRAN 95 and its subsequent evolutions. The whole structure of the system is divided into FORTRAN modules, each of them having the functionality of an object class. The design of MOHID uses several object oriented features like encapsulation, polymorphism, function overloading and inheritance. Objects have four standard methods: (i) constructor, (ii) selector, (iii) modifier and (iv) destructor.

The EnterData is a critical MOHID module. It parses ASCII data files written in format similar to XML and extracts information required by each module using a ”direct access” approach. This module permits a variable form of input data files, allowing input data files with unread data. This structure allows a user to develop alternative process formulations requiring different data sets without interfering with users requiring different inputs.

A detailed description of the software engineering approach is described in [11]. Each of the more than 50 classes that form the MOHID Framework is designed to fill out standard requirements, regarding programming rules and definition concepts, in order to establish a straightforward connection of the whole code. This standardization is reflected in memory organization, public methods systematization, possible object states, client/server relationship and errors management. Each class is responsible for managing a specific kind of information. The design of a class, in FORTRAN 95, can be accomplished by the MODULE statement allowing encapsulation (using the PRIVATE statement) assuring that all the information associated to an object is only changed by the object itself, reducing errors due to careless information handling in other classes.

A MOHID class is defined as a derived type, which has, in addition to its specific information, two required variables InstanceID and Next. InstanceID relates to the identification number of the class instance, that is the object's ID, which is attributed when the object is created. Each time a new object is created, it is added to a collection of objects, stored in a linked list. Next relates to the object stored after the current in the list. Global class variables are designed to be one-way and can only be scanned in one direction.

Each class has only two global variables, defined as derived type pointers. They are the first object in the linked list (FirstObject), which works as an anchor or starting point to scan the list of instances of the module, and a pointer to the current active object (Me). The procedure to access an object is to, starting on the first object, scan the list and find the corresponding one through its ID number.

9 CONCLUDING REMARKS

An integrated modelling system must build on a wide scientific experience, on an integrator concept and must be supported by performing information technologies. MOHID development evolved along those lines. After a set of individual developments experience necessary to support an integrating concept was acquired. The integral form of the evolution equation showed to be the umbrella required for the numerical assessment of environmental systems. The integral approach associated to a flexible morphological and temporal description of the

modelling object created the conditions to develop an integrated modelling architecture. The association of the modelling architecture to an adequate software engineering permitted the development of the MOHID system which is satisfying the needs of consultancy bodies and of researchers, being used in tenths of applied and research projects.

The MOHID code is open permitting the continuous inclusion of new developments. On aquatic ecosystems new developments are being carried on the benthic system, including on processes in the sediments and on terrestrial systems the interaction between the vadose and saturated zones and between these and surface water and their implications on vegetation development and soil pollution processes are being object of several projects.

REFERENCES

1. Neves, R., 1985. Etude Expérimentale et Modélisation des Circulations Transitoire et Résiduelle dans l'Estuaire du Sado. Ph.D. Thesis, University de Liège.
2. Silva, A., 1991. Modelação Matemática Não Linear de Ondas de Superfície e de Correntes Litorais. Ph.D. Thesis, Technical University of Lisbon.
3. Santos, A. J., 1995. Modelo Hidrodinâmico Tridimensional de Circulação Oceânica e Estuarina. Ph.D. Thesis, Technical University of Lisbon.
4. Martins, F., 1999. Modelação Matemática Tridimensional de Escoamentos Costeiros e Estuarinos usando uma Abordagem de Coordenada Vertical Genérica. Ph.D. Thesis, Technical University of Lisbon.
5. Portela, L., 1996. Modelação matemática de processos hidrodinâmicos e de qualidade da água no estuário do Tejo. Ph.D. Thesis, Technical University of Lisbon.
6. Leitão, P. C., 1996. Modelo de Dispersão Lagrangeano Tridimensional. M.Sc. Thesis, Technical University of Lisbon.
7. Rodrigues, V.R., 1997. Ecological and water quality modelling in coastal areas using the lagrangian approach. M.Sc. Thesis, Technical University of Lisbon.
8. Miranda, R., 1999. Nitrogen Biogeochemical Cycle Modelling in the North Atlantic Ocean. M.Sc. Thesis, Technical University of Lisbon.
9. Leitão, P. C., 2003. Integração de Escalas e Processos na Modelação do Ambiente Marinho. Ph. D. Thesis, Technical University of Lisbon.
10. Miranda, R., Braunschweig, F., Leitão, P.C., Neves, R., Martins, F. and A. Santos, 2000. MOHID 2000, A Coastal integrated object oriented model. Hydraulic Engineering Software VIII, WIT Press.
11. Braunschweig, F., F. Martins, P. Chambel and R. Neves, 2003. A methodology to estimate renewal time scales in estuaries: the Tagus Estuary case. Ocean Dynamics 53(3): 137-145.

HYDRAULIC IMPACT STUDIES ON THE COASTAL ZONE OF BUENOS AIRES CITY

M. Re • P. E. García • E. Lecertúa • Á. N. Menéndez

CHAPTER SYNOPSIS

Background
The city of Buenos Aires is built on the coastal zone of the Inner Rio de la Plata. Buenos Aires has been continually reclaiming land from the Río de la Plata River since the 19th century, through the use of soil produced by the urbanization process. The morphological changes produced by this activity, has impacted on the hydraulic behavior of the coastal zone.
In relation to a new reclamation land project by the Government of the city of Buenos Aires, a numerical modelling study has been undertaken to assess the hydraulic impact. The main issues to be tackled, regarding the hydraulic impact of the project, are the following: changes in water currents in the navigation channels; variations in the sedimentation pattern, especially in the navigation channels; behavior of the heat plumes produced by the discharge from the cooling system of *Central Costanera* power plant; changes in the pollutant transport pattern along the coast.

Results
Impact criteria, based on four impact indicators were built, comparing the model results for the infill scenario with the ones for the present situation. Modeling results were translated into practical and meaningful outputs for decision makers.
The coastal infill produces an impact on velocities zone of approximately 1700 m on the longitudinal extent and 600 m on the lateral extension (from the current coastline). The construction of the island in any of their variants, usually more than doubles the longitudinal and lateral extent of the impact zone.
The presence of infill does not significantly change the longitudinal extension of the thermal plume in either directions, but produces an offshore displacement. The highest sedimentation rates occur in the coastal zone, in the inlets (artificial) and the navigation channel. The introduction of infill generates an offshore displacement of the area of maximum rate of sedimentation.

Conclusions
The study shows that the methodology developed, including the definition of indicators, is suitable to quantify the impact of hydraulic works involving coastal morphological changes. The proposed hydraulic impact criteria, applied to the results of the numerical model, provide impact maps from which the degree of perturbation caused by coastal works can be readily quantified. These impact maps are then ready to be used by decision-makers. The use of MOHID system allowed running nested models with a high efficiency.

1 IMPACT OF A COASTAL INFILL

1.1 Introduction

The city of Buenos Aires (Figure 1) is built on the coastal zone of the Inner Río de la Plata. It has been continually reclaiming land from the Río de la Plata, through the use of soil produced by the urbanization process. Since the 19th century to the current configuration of the coast, the artificially filled surface is about 2,054 ha, with progradation ranging from 400 to 1,000 m, depending on the coastal sector [8].The new land has been incorporated to urban use (city harbor, city airport, parks, university campus, real estate, etc.). The morpho-

logical changes produced by this activity, has impacted the hydraulic behavior of the coastal zone. These impacts have induced limitations on other coastal activities, such as navigation, recreation, water pumping, and wastewater disposal.

Presently, reclamation land projects needs for approval an environmental impact study, in which the hydraulic impact assessment is one of the main components. The hydraulic impact can be quantified through adequate mathematical modelling of the system. The results of the model must then be translated into practical and meaningful outputs, to fill the gap that usually exists between the practitioner engineer and the decision maker.

In this work, criteria are defined in order to characterize the hydraulic impact, leading to *impact maps*, ready to be interpreted by decision makers. These criteria are applied to a reclamation land project by the Government of the city of Buenos Aires.

1.2 Problem characterization

The Inner Río de la Plata has freshwater due to the large fluvial discharge (with a mean value of about 22,000 $m^3\ s^{-1}$) from the main tributaries, the Paraná and Uruguay rivers; but, at the same time, the water currents are tidally dominated as a consequence of its large width (of the order of 50 km). Moreover, due precisely to its large width, wind waves are internally generated, which creates a hydrodynamic climate akin to a coastal zone.

The Inner Río de la Plata transports a relatively high load of fine texture suspended sediment, mainly originated in the Paraná River basin. Though the bottom morphology in the coastal zone adjacent to the city of Buenos Aires is relatively stable, siltation occurs in the nearly stagnant sites generated by coastal works.

Figure 1. *Location of study zone. Coastal zone of the southern part of Buenos Aires City.*

The main human activities in the coastal zone of the city of Buenos Aires are the following: water extraction for consumption, disposition of wastewater, commercial and sport navigation, and recreation. In particular, the reclamation project is adjacent to a cooling system discharge from a thermal power plant (*Central Costanera*). The impact indices to be built must provide indications on how these activities could be affected.

In the first phase of the project, the infill area is around 11 ha adjacent to the coast, in order to dispose soil to be extracted for the construction of a diversion tunnel for an urban stream (scenario CR). For the second phase, a 30 ha island is proposed. Different scenarios considering both phases were studied, Figure 2 (scenarios IE and IS: island with and without bridge abutments; and scenario IR: with a different design for the island). The case without infill is scenario SR.

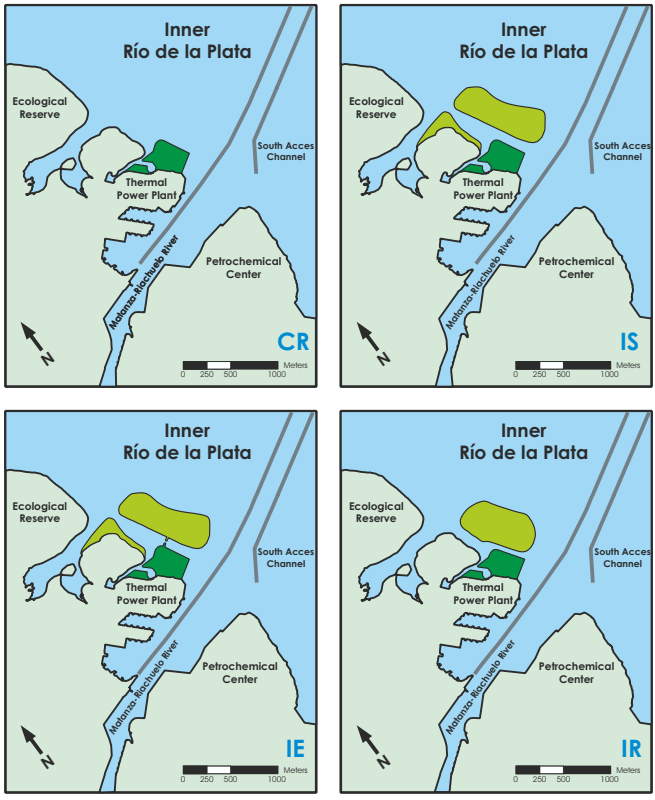

Figure 2. *Reclamation project scenarios. Scenario CR: a coastal infill area of 11 ha. Scenario IS: the coastal infill and a 30 ha island. Scenario IE: the coastal infill and a 30 ha island, considering the bridge abutments. Scenario IR: the coastal infill and a 30 ha island, considering a different design.*

2 MODEL SETUP

2.1 Model implementation

Modeling system MOHID, developed by MARETEC (Marine and Environmental Technology Research Center) at the Instituto Superior Técnico (IST) of the Universidad Técnica de Lisboa, was used for the present study. It allows 3D modelling of hydrodynamic problems, using the Navier-Stokes equations with the hydrostatic and Boussinesq approximations, and including sediment and pollutant transport. It is specially suited for coastal and estuarine problems [1, 2, 3, 9, 10, 13, 14].

The model has been implemented in three nested domains (Figure 3). Domain #1 (Río de la Plata), the largest and with the lowest resolution, provides boundary conditions to Domain #2 (intermediate resolution), which in turns feeds with boundary conditions to Domain #3, the submodel where the problem-zone is represented with the highest resolution. Thermal stratification effects are solved only to the scale of Domain #3; hence, 2D modelling is used for domains #1 and #2. Each domain was delimited based on the criteria to avoid effects of the infill on the boundary conditions. The Digital Elevation Model (DEM) for the river bottom was built based on point-elevation data provided by the Navy Hydrographic Service (SHN). Domain #3 includes the representation of the navigation channels to access the coastal ports (Buenos Aires and Dock Sud).

Two of the driving forces of the system are imposed as boundary conditions for Domain #1: the tidal wave at the ocean-side open boundary, and the discharge from the main tributaries (Paraná and Uruguay rivers) at the river head. The wind field is considered as a source term for domains #1 and #2, and as a surface boundary condition for Domain #3. Additionally, in Domain #3 the coastal discharge of the Matanza-Riachuelo River is explicitly considered, together with the inflow and outflow of the cooling system of the thermal power plant (Figure 4). The ocean tidal wave was specified at the mouth of the Rio de la Plata, from results obtained with the regional model RPP2D [11, 12]. The surface wind field was generated with NCEP/NCAR reanalysis data [6].

Energy dissipation, due to horizontal axis eddies generated at the bottom, is parameterized with an effective roughness height, equivalent to a Manning factor of 0.015 [5], and a constant value eddy coefficient (0.001 $m^2\ s^{-1}$), as recommended for estuaries. The vertical axis eddy dissipation is considered through Samgorinsky's model [15]. The temporal step is chosen so as the Courant Number does not exceed 4, the recommended limit for MOHID.

2.2 Model validation

Three hydrodynamic scenarios were defined: i) Mean scenario: a period with a moderate wind situation (representative of a mean hydrodynamic scenario), ii) Survey scenario: the period when an ad-hoc survey was performed at the problem-zone and, iii) Extremes scenario, storm surges situations (*Bajante* and *Sudestada*).

2.2.1 Mean scenario

Current velocity measurements for the period 10 March to 20 April 2004, obtained by the water supply company (AySA) at two different locations, were used to validate the hydrody-

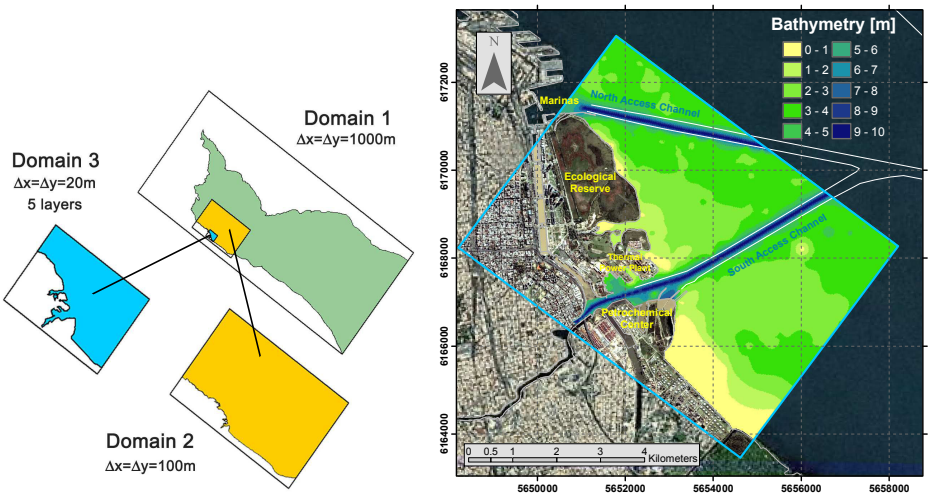

Figure 3. *Domains and bathymetry (Domain 3).*

namic model out of the thermally stratified flow region. The comparison between data and results from the submodel of Domain #2 is considered as satisfactory (Palermo and Bernal), as illustrated in Figure 5 for a six days time window.

2.2.2 Survey scenario

An ad-hoc survey was performed on 21 January 2009, in order to obtain vertical profiles of flow velocity and temperature in the neighborhood of the power plant cooling water discharge. Measurements were taken at 11 stations, with three points per station (at 0.2, 0.6, and 0.8 of the local depth). Figure 6 shows the comparison between simulation and instantaneous measurements of velocity for one of the stations, showing a good agreement.

2.2.3 Extremes scenarios

Water level measurements in Buenos Aires provided by SHN, were used to validate the model during two significant extreme events: *Bajante* at November 2002 (negative storm surge) and *Sudestada* at May 2000 (positive storm surge). Figure 7 shows a very good agreement between observed and simulated levels.

3 HYDRAULIC IMPACT ASSESSMENT

3.1 Impact criteria

Four impact indicators were built, based on the comparison of the model results for the infill scenario with the ones for the present situation, considered as a reference:

#1: Absolute value of the flow velocity difference vector, for the instants of maximum ebb and flood velocities, i.e., the instants for which the impacts are highest; this is an indicator of the change both in intensity and direction of the velocity vector, significant to establish impacts on navigation;

Figure 4. *Discharges and intakes at* Central Costanera.

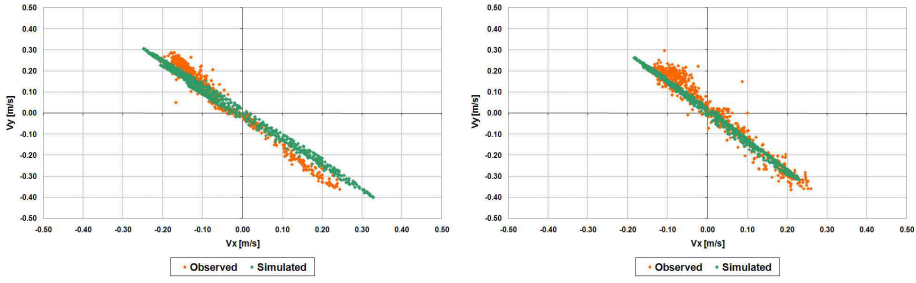

Figure 5. *Current velocities rose. a) Palermo. b) Bernal. Domain 2 results.*

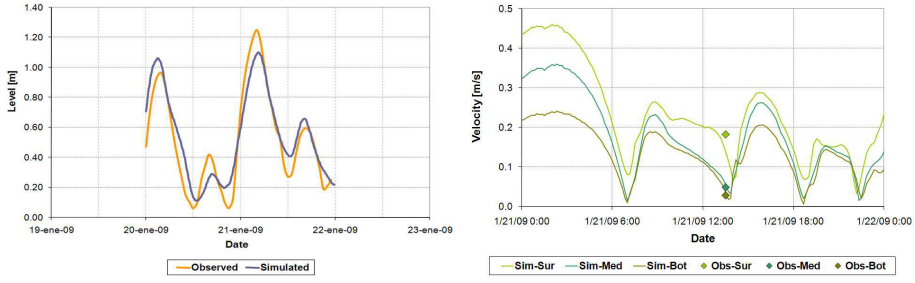

Figure 6. *Levels at Palermo during the survey and velocities at problem zone (three depths at the same point: 0.2 h, 0.6 h and 0.8 h).*

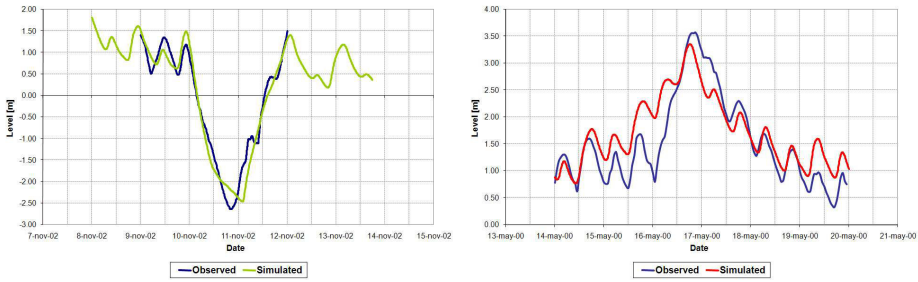

Figure 7. *Levels at Palermo (Buenos Aires). a)* Bajante *Novermber 2002. b)* Sudestada *May 2000.*

#2: Difference between the absolute values of the flow velocity, for the instants of maximum ebb and flood velocities; this is an indicator of the change in the intensity of the velocity vector, also significant for navigation;

#3: Temperature difference, for the instants of maximum ebb and flood velocities; this is an indicator for the impact of the thermal plume issued by the thermal power plant;

#4: Difference between the mean values of Krone factor (T_r) for a tidal cycle; this is an indicator of the change in the siltation rate, especially significant for dredging activities along the navigation channels.

Krone factor is calculated as [7]:

$$T_r = \begin{cases} 1 - \frac{u_*}{u_{*d}} & if \;\; u_* < u_{*d} \\ 0 & if \;\; u_* \geq u_{*d} \end{cases} \tag{1}$$

here u_* is the instantaneous shear velocity, and u_{*d} its critical value for deposition, which has been estimated from previous studies [4] and was adopted as u*d = 8 mm s^{-1}. Krone factor ($0 \leq T_r \leq 1$) affects the maximum potential siltation rate, which is the product between the silt concentration and the fall velocity corresponding to its mean diameter.

3.2 Thermal stratification

Thermal stratification effects were not found to be significant. Besides, 2D modelling provided thermal plumes somewhat more extended than the 3D model, i.e., the results of the former are conservative. These effects are illustrated in Figure 8, which shows the plumes for a particular instant during ebb flow. Hence, the limits of the impact zones were determined based on the 2D model, which is much more efficient from the computational point of view.

3.3 Impact on velocities

3.3.1 Mean Scenario

Taking a velocity of 2 cm s^{-1} as a detection threshold of change, coastal infill (scenario CR) produces an impact zone of approximately 1,700 m on the longitudinal extent and 600 m on the lateral extension (from the current coastline). The construction of the island in any of their variants, usually more than doubles the longitudinal and lateral extent of the impact zone at the maximum of the flood period. At the maximum of the ebb period, there is a doubling of the longitudinal length and a lower increase (about 50%) of the lateral extent, except for the

scenario IS. The inclusion of the bridge abutments (scenario IE versus scenario IS) implies an increase of about 15% in the longitudinal extent and 30-80% in the lateral extent of the impact area (Figure 9).

For all scenarios, there is an impact on velocities on a stretch of the South Channel, but not in the case of the North Channel. In the flood flow, the impact on the South Channel is a decrease in the intensity of the current, which is a positive impact on commercial navigation. In the ebb flow, there is an increase and a decrease, although this increase of intensity (negative impact) only exceeds 5 cm s^{-1} for the scenario IR.

3.3.2 Extremes Scenario

The areas of impact on current velocities, adopting the same detection threshold, are generally larger during extreme events (negatives and positives storm surges).

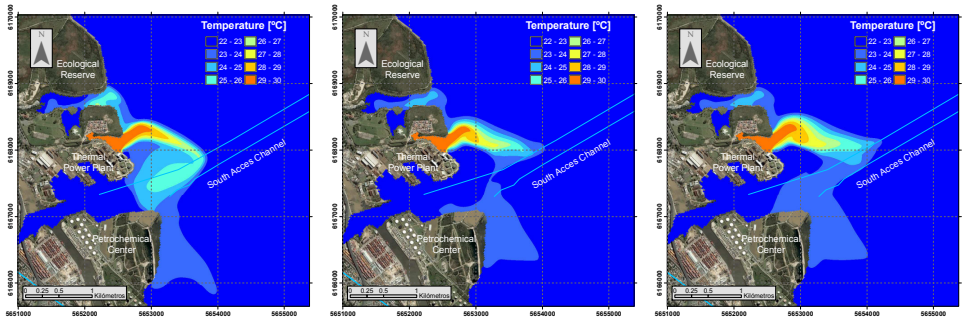

Figure 8. *Comparison of plumes according to 3D and 2D models. a) 2D. b) 3D, bottom layer. c) 3D, surface layer.*

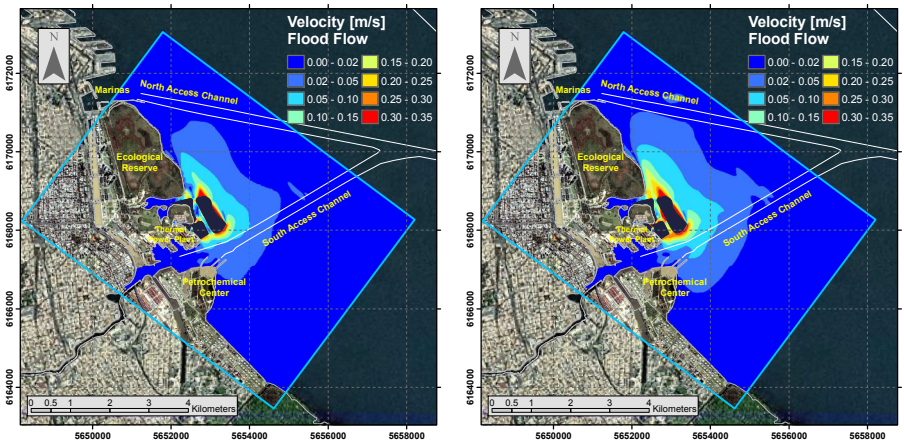

Figure 9. *Absolute value of the velocity difference. a) Scenario IS. b) Scenario IE.*

Tables 1 and 2 show ratios between longitudinal and lateral extents of the impact zone, related to mean conditions extents. Unless the longitudinal extent (which decreases), in the case of the rising period during the negative storm surge, the extensions have an increase ranging from 0 to 150%, with extremes exceeding 400% for the lateral extension during the ebb flow for both events.

For the scenario CR, impact on South Channel is only observed on the falling period of the negative storm surge and on the rising period of the positive storm surge (Figure 10a), but not during periods of mean levels recovery. There is no impact on the North Channel. As for the IS scenario, there is impact on the South Channel for all circumstances, affecting the North Channel during the rising period of the positive storm surge (Figure 10b).

Table 1. *Impact zone extents related to mean conditions. Maximum ebb velocity.*

Scenarios	Negative storm surge (***Bajante***)		Positive storm surge (***Sudestada***)	
	Longitudinal extent [m]	Lateral extent [m]	Longitudinal extent [m]	Lateral extent [m]
CR	1.75	2.14	1.25	1.00
IS	1.76	5.83	1.49	5.00

Table 2. *Impact zone extents related to mean conditions. Maximum flood velocity.*

Scenarios	Negative storm surge (***Bajante***)		Positive storm surge (***Sudestada***)	
	Longitudinal extent [m]	Lateral extent [m]	Longitudinal extent [m]	Lateral extent [m]
CR	0.59	1.17	1.76	2.50
IS	0.75	1.13	1.38	1.88

3.4 Impact on the thermal plume

3.4.1 Mean Scenario

The presence of an infill does not significantly change the longitudinal extension of the thermal plume (resulting from the discharge of the thermal power plant), but produces an offshore displacement, which not exceed 300 m (Figure 11).

Taking a temperature difference of 3 ^{o}C as a threshold of thermal plume significant impact, scenarios CR and IS only produce impact at the ebb flow, with increases in temperature not exceeding 4 ^{o}C (negative impact), and decreases that can reach 5 ^{o}C (positive impact). For the two remaining scenarios increases to 5 ^{o}C at the flood flow are generated, and increases and decreases of up to 5 ^{o}C during the ebb flow.

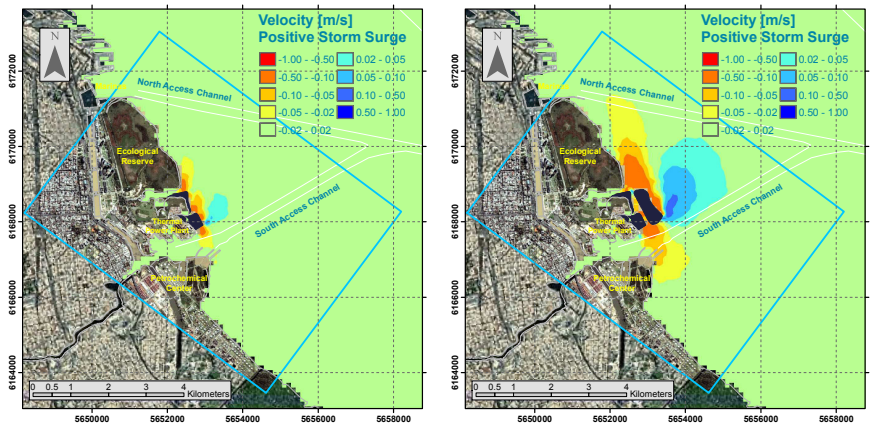

Figure 10. *Difference between absolute values of the velocity vector for the instant of maximum velocity (rising period, positive storm surge). a) Difference CR-SR. b) Difference IS-SR.*

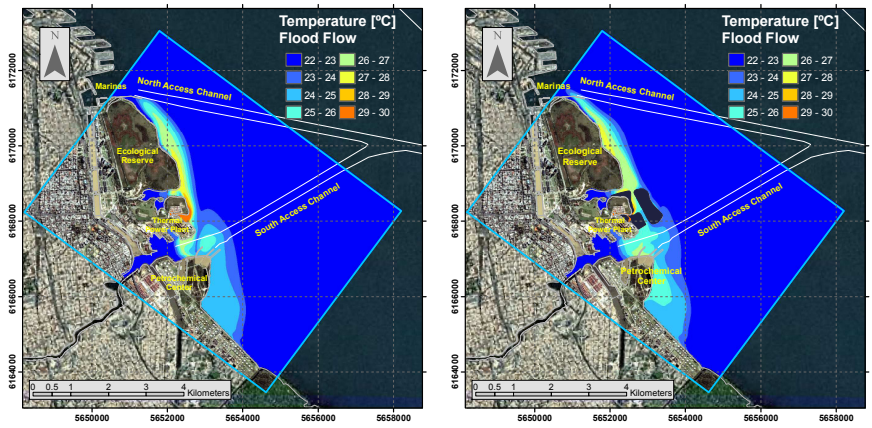

Figure 11. *Thermal plumes for the instant of maximum flood velocity. a) Scenario SR. b) Scenario IS.*

It is particularly remarkable the effect of the presence of bridge abutments (scenario IE), because the increase of flow resistance that they generate increases the temperature at the NW of the island (Figure 12). For the same reason, and associated with narrowing of the channel between coastal infill and island, scenario IR also produces greater increases in temperature. For scenarios CR and IS there is no negative impact over temperature along the existing shoreline.

3.4.2 Extreme Scenario

For all the infill scenarios, changes in the thermal plume extension related to the case without infill, are not considered too significant for both extreme events. If a temperature difference of 3 ^{o}C is taking as a threshold of significant impact of the thermal plume, it is observed that the impact is related to the channel between the coastal infill and the island.

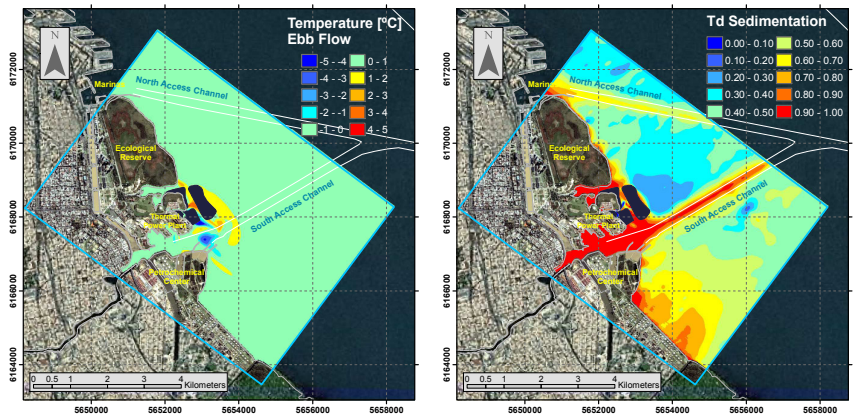

Figure 12. *Temperature difference for the maximum ebb velocity. a) Scenario IS. b) Scenario IE.*

3.5 Impact on sedimentation

3.5.1 Mean Scenario

The highest sedimentation rates occur in the coastal zone, in the inlets (artificial) and the navigation channel (Figure 13). The introduction of infills generates an offshore displacement of the area of maximum rate of sedimentation. Considering 0.1 as a significant change in the value of the sedimentation indicator (10%), infills produces rings of increased sedimentation around them (Figure 14), with greater elongation toward the NO. There is no reduction of sedimentation in the lateral of the infill (direction NE) and in the channel between the island and the coast (except in the case of the IE and IR scenarios, because their relatively high hydraulic resistance).

No significant impact on sedimentation was observed in the North and South Channels. This situation indicates that it is not expected a significant variation in maintenance dredging.

3.5.2 Extreme Scenario

As in mean conditions, the greatest impact on sedimentation occurs in the coastal zone, in the inlets (artificial) and the navigation channel. The introduction of infills does not cause significant changes in the sedimentation indicator (Figure 15). Scenario CR indicates no relevant difference. Regarding the scenario IS, during the negative storm surge there are rings of significant decrease in sedimentation around the infill whit an increased in sedimentation on the laterals of the infill. An inverse behavior occurs during the positive storm surge.

4 CONCLUSIONS

The proposed hydraulic impact criteria, applied to the results of the numerical model, provide impact maps from which the degree of perturbation caused by coastal works can be readily quantified. These impact maps are then ready to be used by decision-makers.

In particular, the application of this methodology to the problem of a coastal infill for the city of Buenos Aires, has lead to the following significant conclusions: (i) a zone of around 2 km in

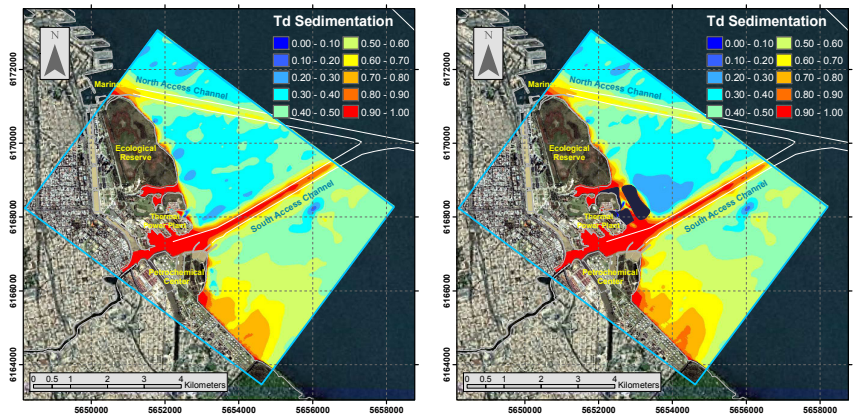

Figure 13. *Distribution of the sedimentation indicator (mean conditions): a) Scenario SR, b) Scenario IE.*

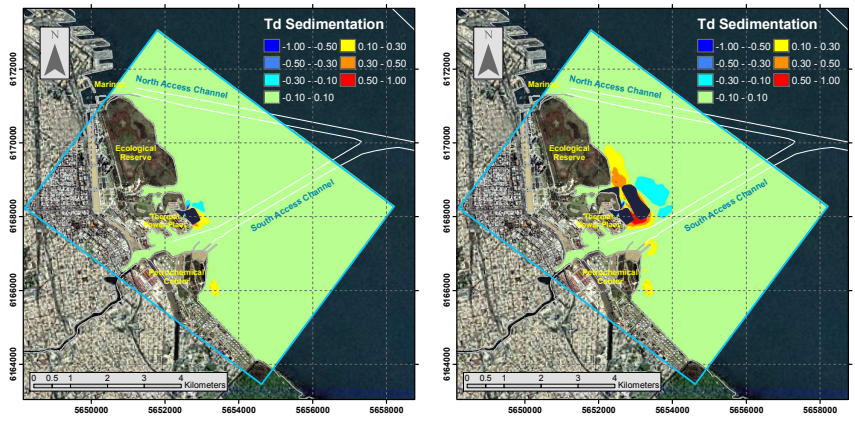

Figure 14. *Difference between sedimentation indicators (mean conditions): a) CR-SR, b) IE-SR.*

length and 700 m in width will suffer from a significant change in the flow velocity; this could only affect negatively sport navigation; on the contrary, commercial navigation is impacted positively due to the decrease of cross velocities relative to the navigation channel axis; (ii) the thermal plume of Central Costanera will only affect the infill border, but not the existing coastline; (iii) a relatively thin (from about 100 to 200 m wide) ring of increased siltation will be produced around the infill, but no impact will occur on sedimentation along the navigation channels.

The use of MOHID system allowed running nested models with a high efficiency. The excellent father-son communication between nested models, made it possible to study the problem-zone in great detail and with an acceptable computational cost.

ACKNOWLEDGEMENTS

This paper presents part of the work performed for the Government of the City of Buenos Aires, whose support is acknowledged.

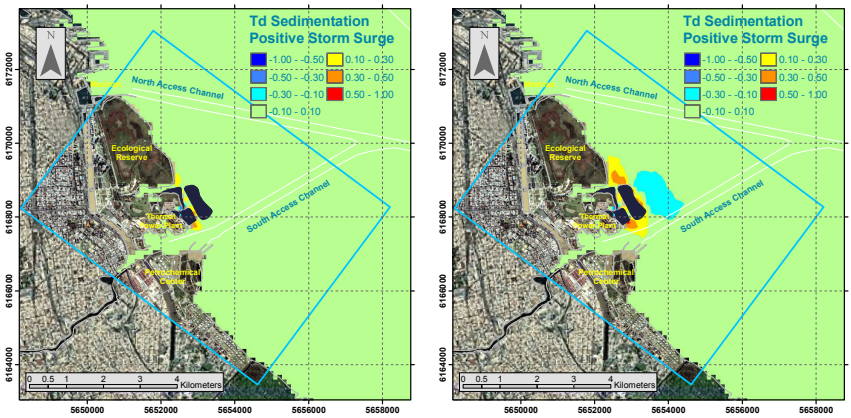

Figure 15. *Difference between sedimentation indicators (extreme conditions): a) CR-SR, b) IE-SR.*

REFERENCES

1. Cancino, L., Neves, R. (1999). "Hydrodynamic and sediment suspension modelling in estuarine systems, Part I: Description of the numerical models'', Journal of Marine Systems, 22, 105-116.
2. Coelho, H., Neves, R., White, M., P. C. Leitão, Santos, A. (2002). "A Model for Ocean Circulation on the Iberian Coast'', Journal of Marine Systems, 32 (1-3), 153-179.
3. Fossati, M., Fernández, M., Piedra-Cueva, I. (2008). "Modelación hidrodinámica tridimensional del Río de la Plata utilizando modelos encajados'', XXIII Congreso Latinoamericano de Hidráulica, Cartagena, Colombia.
4. Harrison, A.J.M., Owen, M.W., 1971, Siltation of fine sediments in estuaries. IAHR XIV Congress.
5. Jaime, P.R., Menéndez, A.N. (1999). "Modelo hidrodinámico Río de la Plata 2000'', Informe INA-LHA 183-01-99, INA, Argentina.
6. Kalnay et al. (1996). "The NCEP/NCAR 40-year reanalysis project'', Bulletin of the American Meteorological Society 77 (3): 437-471.
7. Krone, R. B., 1962, Flume studies of the transport of sediment in estuarial shoaling process final report. Hydraulic Engineering and Salinity Engineering Research Laboratory, University of California, Berkley, USA, 110 pp.
8. Marcomini, S.C., López, R.A., 2004, Generación de nuevos ecosistemas litorales por albardones de relleno en la costa de la ciudad de Buenos Aires, Revista de la Asociación Geológica Argentina, 59 (2): 261-272.
9. Martins, F., P. C. Leitão, A. Silva, R. Neves (2001). "3D modelling of the Sado Estuary using a new generic vertical discretization approach'', Oceanologica Acta, 24 (1), 51-62.
10. Neves, R., 1985, Étude Expérimentale et Modélisation des Circulations Transitoire et Résiduelle dans l'Estuaire du Sado. Ph. D. Thesis, Univ. Liège
11. Re, M., Menéndez, A.N. (2003). "Modelo Hidrodinámico del Río de la Plata y su Frente Marítimo'', Informe INA-LHA 03-216-03, INA, Argentina.
12. Re, M., Menéndez, A.N. (2007). "Impacto del Cambio Climático en las Costas del Río de la Plata'', Revista Internacional de Desastres Naturales, Accidentes e Infraestructura Civil, 7 (1).
13. Trancoso, A., Saraiva, S., Fernandes, L., Pina, P., Leitão, P., Neves, R. (2005). Modelling macroalgae using a 3D hydrodynamic-ecological model in a shallow, temperate estuary. Ecological Modelling, 187: 232–246.
14. Saraiva, S., Pina, P., Martins, F., Santos, M., Braunschweig, F., Neves, R. (2007) "Modelling the influence of nutrient loads on Portuguese estuaries'', Hydrobiologia, 587:5–18.
15. Smagorinky, J.S (1963). "General turbulence model of the atmosphere'', Monthly Weather Review: 91, 99-164.

DEVELOPMENT OF A RÍO DE LA PLATA WATER LEVEL HEIGHT FORECASTING SYSTEM BASED ON THE MOHID WATER MODELLING TOOL

M. Fossati • P. Santoro • M. Fernández • P. Ezzatti • I. Piedra-Cueva

CHAPTER SYNOPSIS

Background
In recent years the forecasting models strategy has been developed applying the MOHID water system model in the South Atlantic Ocean and the Río de la Plata. After the initial development of the forecasting system several changes were made in order to improve it. Also, several circulation analyses were performed using the PDT system to improve the understanding of the tidal hydrodynamic in the area.

Results
Several high performance computing tools were applied in order to reduce the computational time using the hardware platform available. Also, several aspects of the South Atlantic hydrodynamic model were evaluated and improved: the study domain, the bathymetry data, the open boundary condition for astronomical tide, and the bottom friction coefficient. Higher changes in the simulated astronomical tide were produced by the improvement in the local bathymetry of Río de la Plata. Moreover, for the coastal control stations located outer the Río de la Plata the most influential parameter was the open boundary condition through the relaxation time.

Conclusions
Using the MOHID hydrodynamic model coupled with the WRF atmospheric model, a forecast water level height system was performed. The system is capable of doing real-time simulations and predicting water levels generated by astronomic and meteorological effects in the Río de la Plata region. This system constitutes a very powerful tool for the management of fluvial-maritime transport.

1 INTRODUCTION

Operational oceanography involves the retrieval, dissemination, and interpretation of measurements obtained in the seas and oceans with the purpose of making a forecast of future conditions [1]. Operational modelling includes simulations of current as well as future conditions. Pre-operational modelling involves similar simulations in terms of initial and boundary conditions, and the specification of forcings, but these are done in hindcast mode. The results presented in this chapter report the progress made in pre-operational modelling for the Río de la Plata fluvial-estuarine system.

Even though the Río de la Plata is very important for Argentina and Uruguay from an economic and environmental point of view, a global management system based on an operational model has not been developed yet. Several problems related with the management of this complex system arose, showing a need to develop an operational system capable of monitoring and predicting hydraulic and environmental variables of interest (water levels, wave climate, currents, salinity, and sediments). In 2008, a research project was carried out in order to develop a pre-operational numerical tool, based on the application of last-generation hydrodynamic and atmospheric numerical models, to support the management of the Río de la Plata – Uruguay River complex system.

The forecasting models strategy has been developed applying the MOHID water system model in the south Atlantic Ocean and the Río de la Plata [2]. The developed system, called PDT system, is capable of predicting sea level variations in the Río de la Plata, and therefore constitutes a numerical tool of great value for the fluvial-maritime navigation and regional environmental management. In order to represent the propagation and generation of astronomic and meteorological waves in the South Atlantic, the model was implemented in a mother domain covering most of the South Atlantic Ocean (hereafter South Atlantic model). Subsequently, a subdomain focused on the Río de la Plata was configured using a nested grid (hereafter Río de la Plata submodel). The results obtained include astronomic and meteorological sea level variations in the Río de la Plata. Comparisons of modelled water levels with data have shown very good qualitative and quantitative agreement [2].

The MOHID modelling system presents an integrated modelling philosophy, not only of processes (physical and biogeochemical), but also of different scales (allowing the use of nested models), and systems (estuaries and watersheds). The MOHID model is considered to be one of the most elaborated models of this type, designed with a reliable and robust framework, and various vertical coordinates.

After the initial development of the forecasting system several changes were made recently in order to improve it. Also, several circulation analyses were performed using the PDT system to improve the understanding of the tidal hydrodynamic in the area. This chapter aims to describe the basics of the PDT system, the improvements made on it, and the analyses performed with the developed tool. At this time the tool is under development and the first stages have been extremely successful. The MOHID water modelling system has several advantages when used in this kind of research projects: the continuous development and improvement, the facility in the exchange of data, and the simplicity of the structured code that allows making modifications with ease.

2 STUDY AREA

Uruguay is located in the east coast of South America between Argentina and Brazil (Figure 1). It has an area of 176,215 km^2 and a population of 3.46 million. To the Southwest, in the border with Argentina, lies the estuary of Río de la Plata. The Río de la Plata is a complex body of water with fluvial-estuarine characteristics located between 34°00' – 36°10' S latitude and 55°00' – 58°10' W longitude. The Río de la Plata basin has the second largest catchment area (3,170,000 km^2) of South America behind the Amazons basin. The Río de la Plata discharges into the South Atlantic Ocean.

The flow dynamics in the Río de la Plata and the ocean front are very complex due to the topographic variation of the river (Figure 1) and the influence of continental flows, astronomical, and meteorological tides coming from the Atlantic Ocean. The Río de la Plata behaves as a micro-tidal estuary, i.e. the river level variations produced by astronomical tides are much lower than those generated by the wind action and oceanic waves. The Paraná and Uruguay rivers provide more than 97% of the continental water inlet with an annual mean flow of 22,000 $m^3\ s^{-1}$. Two main regions can be identified based on the morphology and dynamics of the

Río de la Plata. A shallow area located along the Punta Piedras–Montevideo line separates the inner from the outer region. The inner region has a fluvial regime with bidimensional flow. In the outer region the increase in river width generates complex flow patterns. This outer region is formed by brackish waters of variable salinity according to the tides, winds, and fresh water contributions of the river basin, extending approximately up to Punta Rasa in Argentina and Punta del Este in Uruguay. A more detailed description of the area and data analysis is presented in related studies [3, 4, 5].

3 THE PDT PRE-OPERATIONAL FORECASTING SYSTEM

To describe the circulation of the Río de la Plata, the group of models should consider the atmospheric processes acting over the continental platform and over the adjacent oceanic region. Moreover, the hydrodynamic model should have different spatial resolutions and consider different types of water bodies: on the one hand, the South Atlantic Ocean and its interaction with the atmospheric processes; and on the other hand, the Río de la Plata and lower Uruguay River. This leads to the use of nested domains to describe the system. Therefore, the hydrodynamic model was first implemented on a regional scale domain, over the South Atlantic Ocean, to reproduce the generation and propagation of tidal and meteorological waves. Subsequently, a hydrodynamic submodel with higher resolution was implemented focused on the Río de la Plata and its ocean front. This submodel was nested in the regional scale model. The implemented system was calibrated and validated. Comparisons of modelled water levels with data have shown very good qualitative and quantitative agreement [2]. In this section the main characteristics of the system are briefly presented.

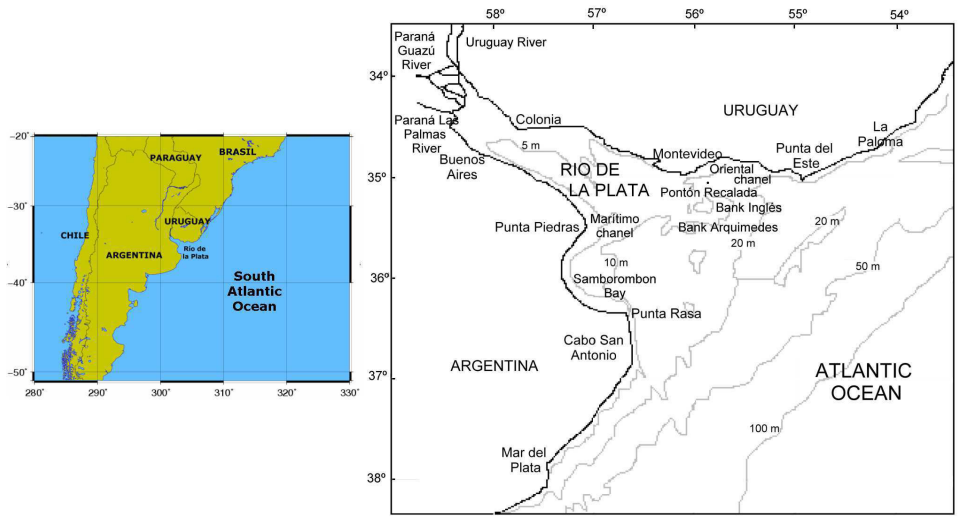

Figure 1. *South Atlantic Ocean and Río de la Plata location.*

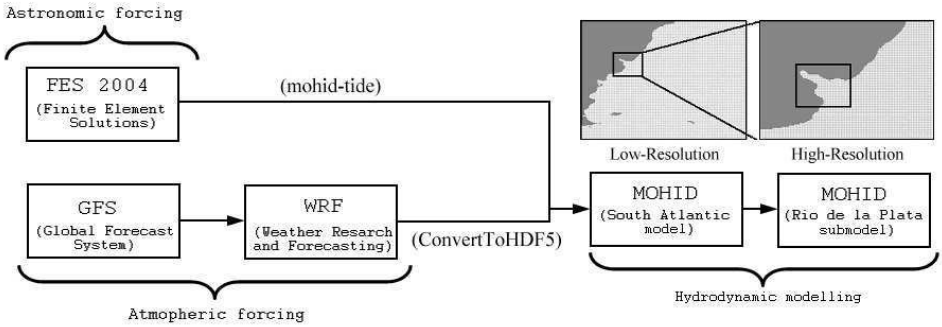

Figure 2. *PDT pre-operational forecasting system scheme.*

3.1 Implementation of the system

The numerical model MOHID was used in this study. The hydrodynamic model makes use of FES2004 (global tidal atlas) solution for tidal forcing and WRF meso-scale model for atmospheric forcing. The WRF model receives the initial and boundary conditions from a global atmospheric model (GFS). Figure 2 presents a scheme of the system of models described above.

The domain of the South Atlantic model is bounded within the interval 22^o – 60^o S and 20^o – 70^o W. It includes most of the continental platform and its adjacent oceanic area in order to represent the meteorological effects once forced with the atmospheric model. The horizontal grid of this model was implemented using the latitude-longitude coordinates system, it has 150,131 active nodes and a spatial resolution of 0.1^o (11.1 km). Data from the General Bathymetric Chart of the Ocean (GEBCO) with a spatial resolution of 0.06^o were used to represent the bathymetry of the area of interest (Figure 3, left panel). The Río de la Plata submodel, unidirectional nested in the South Atlantic model, was implemented using the latitude-longitude coordinates system. Its domain is bounded within the interval 33.76^o – 38.09^o S and 59.00^o – 54.10^o W. The horizontal grid has 9,600 active cells and a spatial resolution of 0.033^o (3.7 km), one third of the spatial spacing used in the mother model grid. The bathymetry of the Río de la Plata domain and its coastal line was generated using the same information used for the South Atlantic model (Figure 3, right panel).

In the case of the South Atlantic domain tidal forcing is imposed in the open boundary condition. Meteorological forcings (winds and atmospheric pressure from WRF model) are imposed in the surface boundary condition. The Weather Research and Forecasting (WRF) system [6] is designed to be a flexible portable code that is efficient in a massively parallel computing environment. It is suitable for a broad spectrum of applications across scales ranging from meters to thousands of kilometers. The WRF System consists of the following major components: WRF Software Framework (WSF), Advanced Research WRF (ARW) dynamic solver, Standard Initialization package (SI), WRF Variational Data Assimilation (WRF-Var), numerous physics packages contributed by WRF partners and the research community, and several graphics programs and conversion programs for other graphics tools [7].

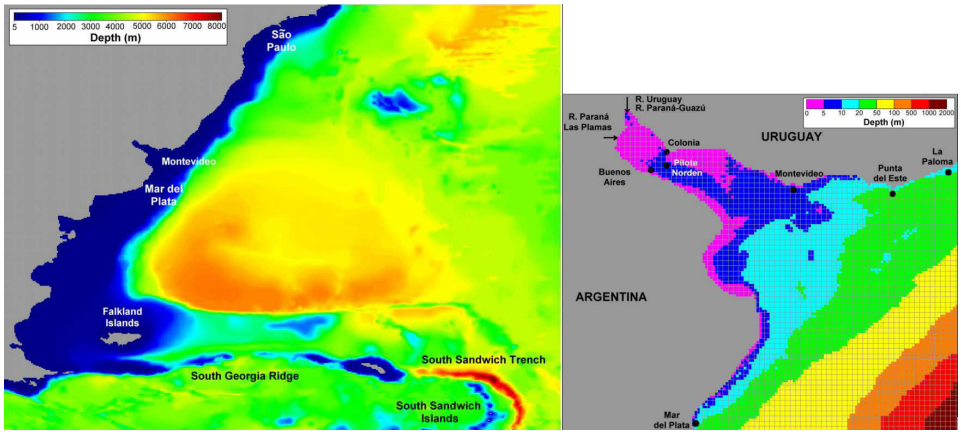

Figure 3. *Bathymetry of the South Atlantic domain (left panel) and bathymetry of the Río de la Plata domain (right panel)*

The WRF was implemented in a domain that ranges approximately from 61.5^o W, 76^o S to 19^o W, 14^o S with a spatial resolution of 60 Km. This domain was defined to match the South Atlantic hydrodynamic model domain. The initial and boundary conditions are obtained with the Global Forecast System (GFS) model. Four daily GFS forecasts (produced at 00, 06, 12, and 18 UTC) for up to 180 hours are available at the NCEP website with a temporal resolution of 3 hours and a spatial resolution of 1^o. Every WRF atmospheric simulation starts at 00 UTC and results are saved every 3 hours for up to 96 hours. The sea level pressure field and the horizontal components of wind speed at 10m of the sea surface obtained with the atmospheric forecasts are used to force the hydrodynamic model. A conversion files format was applied to the WRF output in order to forcing the MOHID model using the ConvertToHDF5 tool included in the MOHID software package.

3.2 Pre-operational system

The coupling of the hydrodynamic model with the atmospheric forecast model allows the prediction of water levels in the entire Río de la Plata and its ocean front region. At present, the system is still working in a preliminary way. Nevertheless, in order to build a pre-operational system the execution of the models and their interaction were automated. The system runs in Linux due to the better performance of the implemented models in this operating system and because it simplifies the automation process. All the procedure was automated using the shell scripting technique.

The pre-operational system follows the steps described below:

1. Download and store the results of the global atmospheric model GFS;
2. Execution of the atmospheric model WRF using the results of the GFS as initial and boundary conditions;

3. Extraction of the forecast of the atmospheric variables of interest (wind velocity at 10 m and sea level pressure) from the WRF output file;
4. Format conversion and grid interpolation of the atmospheric data into an HDF5 format file;
5. Execution of the MOHID using the forecast obtained with the WRF as the atmospheric forcings;
6. Post-processing of the results.

The pre-operational system was implemented in a computer with LINUX operating system that has two Intel(R) Pentium(R) 4 CPU 2.80 GHz processors, 1024 KB of cache memory and 1 GB of RAM memory. The 4.9 Mohid serial version was used. As an example, a 96 hours forecast was done in approximately 18 hours; 11 hours spent in downloading and storing the GFS data (approx. 890 MB), 2.5 hours spent in the WRF simulations, and 4.5 hours running MOHID. Downloading the atmospheric data from the GFS model is the longest step and could be speeded up by improving the connection.

4 IMPROVEMENTS OF THE SYSTEM

4.1 South Atlantic Hydrodynamic Model

The aim of this analysis was to improve the representation of astronomical tidal sea-surface height variations obtained with the South Atlantic hydrodynamic model described before. To achieve this, the main implementation characteristics of the hydrodynamic model, such as model domain, bathymetry, bottom friction, and open boundary condition, were reviewed. Sensitivity tests to these characteristics allowed us to investigate their individual impact on the results of the model and to obtain an optimal solution as determined by comparisons with several coastal tide gauges. When comparing the results of the model with the sea level series measured at coastal stations, particular attention was given to the most energetic tidal component, the principal lunar semidiurnal M2. A significant improvement in the model tidal representation at the coastal stations of the Río de la Plata was achieved by complementing the GEBCO bathymetric database with local data. Noticeable improvements in tidal representation for most of the coastal stations within the model domain were obtained by tuning the relaxation time (Blumberg and Kantha boundary condition) and the bottom friction coefficient.

For these analyses several simulations of 3 months were performed modifying only one parameter each time. In order to compare the solutions obtained in the simulation, the main tidal harmonics from the water level series were computed in several coastal control stations (Figure 4). The main tidal harmonic in the area, the semidiurnal M2 component, was specially controlled. Measured water level series are available at the Río de la Plata coastal control stations (Figure 4, right panel) and theoretical tidal amplitude and phase of the main harmonic M2 are available in the Argentinean continental platform (Figure 4, left panel).

The RMSE (root mean square) normalized by the observed amplitude was used to compare the M2 measured amplitude and phase with the M2 modelled amplitude and phase for each control station:

$$RMSE = \frac{\sqrt{\frac{1}{2}\left(H_M^2 - 2H_M H_T \cos\left(G_M - G_T\right) + H_T^2\right)}}{H_T} \quad (1)$$

Where H_M and G_M are the amplitude and phase of the M2 harmonic calculated from the model, and H_T and G_T are the amplitude and phase of the theoretical M2 harmonic calculated from the measurements. Moreover, in order to compare the results in the rest of the domain, the isophase and isoamplitude maps were computed for each simulation. For doing this, a harmonic analysis was performed to the hourly water level series computed by the model in each cell of the domain. The amplitude and phase for each tidal component was obtained in each cell and finally, using the contour function in MATLAB Software, the maps were obtained. The harmonic constants were calculated from the simulated series using the t_tide tool [8].

4.1.1 Model domain revision

The South Atlantic domain used in the PDT system was revised. A sensitivity test using the original domain and other two different domains was performed (Figure 5). For the sensitivity test, a simulation of 1 year with astronomical forcing was made using each domain. To compare the results obtained with the domains a control point net was defined in the intersection zone of the three domains. The hourly water level series at each point of this net was used in the comparison. Firstly, the Principal Component (EOF) Analysis was applied to the water level series. Secondly, parameters such as the RMSE value were used to compare the results. The sensitivity test showed that the main aspects of the tidal propagation in the Río de la Plata are well represented by the domain number 2 (Figure 5). This domain is smaller than the original domain, the number 1 in Figure 5, so the consequence is a reduction in the computational cost.

4.1.2 Bathymetry improvement

In this stage the bathymetry generation procedure was revised and corrected (Figure 6). The GEBCO data used for the original bathymetry was merged with better local data for the Río de la Plata zone. The GEBCO data of less than 50 m at the area between 33.5^o S and 38.5^o S were eliminated. In this way the GEBCO data with more incertitude were replaced by better quality bathymetry data from the Río de la Plata zone. The transition zone between the two types of data was controlled in order to avoid discontinuities. Moreover, a filter using the MOHID tool FilterBathymetry was applied. The filter applies an averaging over the cells depth smoothing the differences in depth between the adjacent cells. The new bathymetry was finally constructed with a combination of a filtered version and a non filtered version; in the outer Río de la Plata zone the filtered version with a radius (number of adjacent cell) equal to 5 was used, and in the inner Río de la Plata zone the data by the non filtered version was used. In the Figure 6 the original and the new bathymetry of the Río de la Plata zone are compared. With the new bathymetry the simulated astronomical tide was improved; the normalized RMSE obtained with all control stations decreases from 37.8% to 21.7% while the normalized RMSE obtained only with the Río de la Plata control stations decreases from 39.2% to 16.4%.

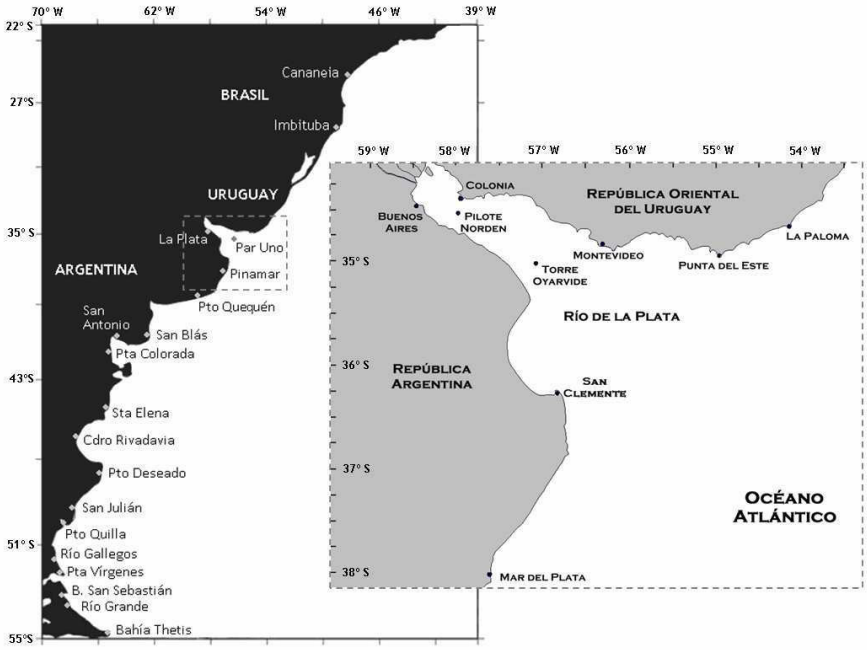

Figure 4. *Location of the coastal control stations used for amplitude and phase comparison of the M2 main harmonic.*

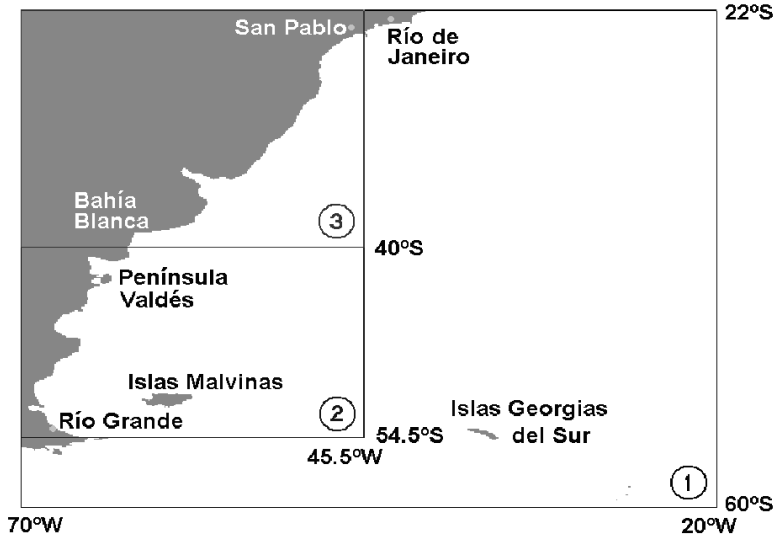

Figure 5. *South Atlantic domains used in the analysis.*

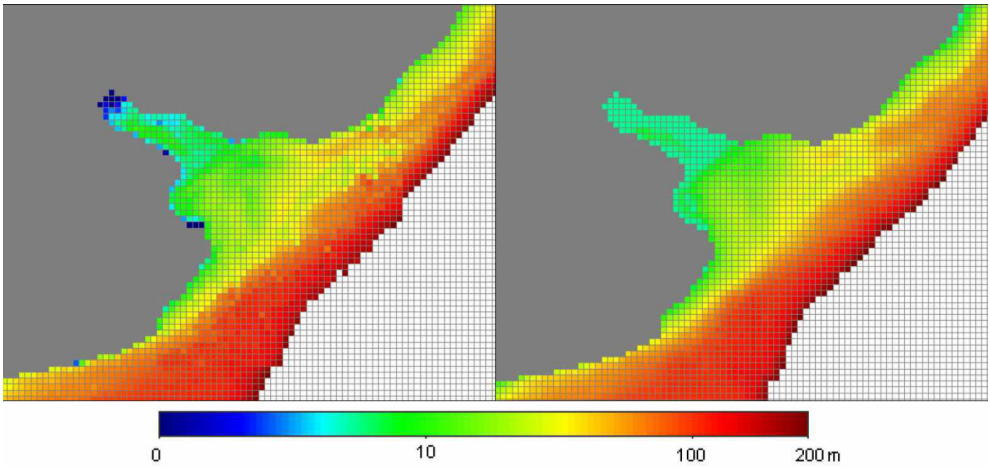

Figure 6. *Original bathymetry (left panel) and the improved bathymetry (right panel) for the Río de la Plata zone.*

4.1.3 Open boundary condition revision

The open boundary condition in the Atlantic South domain was reviewed. In the astronomical tidal forcing simulations the open boundary condition is used to impose the tidal waves. The tidal waves are calculated from the amplitudes and phases to the 13 harmonic components: M2, N2, S2, K2, 2N2, O1, Q1, K1, P1, Mf, Mm, Mtm, MSqm. This information is extracted from the FES2004 global atlas by the mohid-tide tool, for every other cell throughout the entire open boundary of the domain. Also the MOHID model allows the imposition of a radiation condition in the open boundary. In this stage of the improvement of the original condition a radiation boundary condition was established. Some authors claim that the best radiation open boundary condition for the water level elevation is the Flather condition [9]. Nevertheless, the Flather proposed radiation condition needs a reference solution for the water level elevation and the barotropic velocity at the boundary. In this case only the water level elevation is known, so the Blumberg and Kantha [10] radiation condition is a good alternative, for which we must define the relaxation time.

Following the recommendations for the relaxation time, 3 different configurations were evaluated (a, b, and c). For the boundary cells with major depths (greater than 3000 m) the relaxation time was 100 s (a), 200 s (b), and 300 s (c); whereas for the boundary cells with minor depths (lower than 200 m) the relaxation time was about 1000 s (a), 1500 s (b), and 2000 s (c); following the relationship between them 1:10. For the boundary cells with depths between 200 m and 3000 m a transition relaxation time was defined linearly proportional to the relaxation time of the shallow and deep cells defined above.

The obtained results show that the boundary relaxation time has an influence over the tidal propagation in the Argentinean coastal stations but not in the Río de la Plata zone. The RMSE calculated for the Río de la Plata zone did not change along the three configurations

analyzed. The best solution (with the minor normalized RMSE value) was obtained with the configuration of relaxation times 100 s and 1000 s. Moreover the obtained amplitude and phase maps for each simulation were very similar.

4.1.4 Adjustment of the bottom roughness coefficient

The bottom roughness coefficient for the Atlantic Ocean domain was adjusted using the bottom friction formulation presented in Equation [2]; where n is the Manning number, g is the gravity acceleration, and h is the depth. Three different configurations were defined differing in the Manning number: 0.005, 0.010, and 0.015. Three different simulations were performed with the three defined Manning numbers imposed to the entire domain. The best results were obtained with the lower Manning number, equal to 0.005. Moreover, it was observed that the isoamplitude and isophases maps were not so sensible to the bottom roughness coefficient.

$$C_f = \frac{2gn^2}{h^{1/3}} \tag{2}$$

5 APPLYING THE HIGH PERFORMANCE TOOLS STRATEGY

The hardware platform employed to carry out the experiments is a multicore machine with eight cores. In order to evaluate the developed tool, the MOHID model and its related tools were installed on a Linux operated system.

Firstly, we compiled the source code using the Intel Fortran compiler and fine tuned the binary generated using the optimization flags. Additionally, two different parallel programming tools available on MOHID were studied, OpenMP and MPI. The MPI standard was used to improve the performance of the resolution of the hydrodynamic model following a nested domain strategy, each nested domain was computed by one MPI process using the pipeline paradigm. On the other hand, the OpenMP API was used to reduce the runtime needed to compute each domain following the shared memory paradigm.

Thus, both HPC techniques allowed us to compute large domains with high precision grids on a reasonable runtime, and this improvement enabled the use of the simulation tool in an operational mode.

6 SYSTEM APPLICATIONS

6.1 Study of the main astronomical waves

The improved South Atlantic hydrodynamic model was used to study the tidal astronomical waves in the zone. In Figure 7 the amplitude and phase maps for the semidiurnal M2 tidal component for the entire domain (left panel) and for the Río de la Plata (right panel) are presented. The improved model shows the main characteristic of the M2 tidal component in the zone. The RMSE is 24% when considering all coastal control station, and it decreases to 19.1% when considering only the coastal control stations located at Río de la Plata.

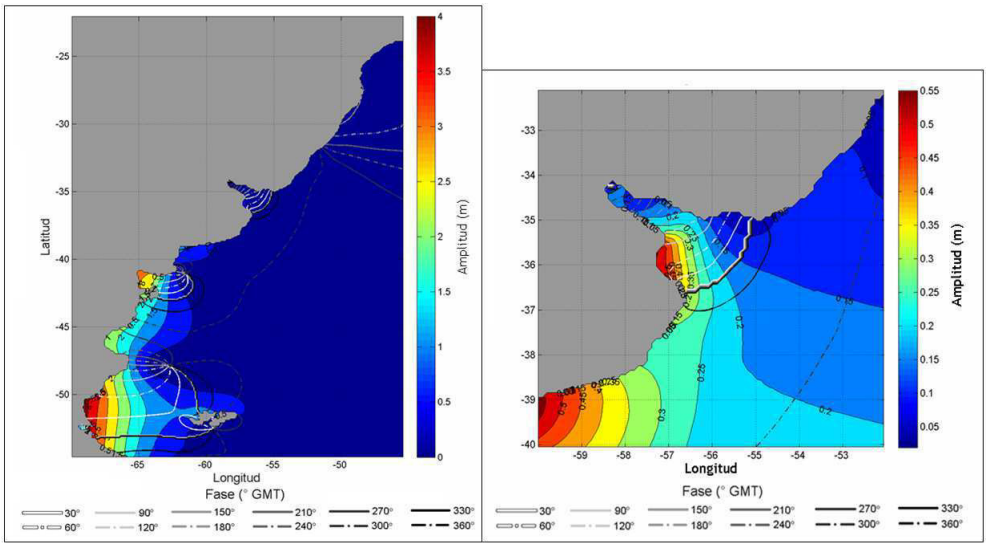

Figure 7. *Amplitude and phase maps for the M2 constituent obtained with the improved model for the entire domain (left panel) and a detail of the Río de la Plata zone (right panel).*

6.2 Determination of the meteorological tide generation

The meteorological tide generation and propagation characteristics of the Río de la Plata are examined in this section using the original South Atlantic Río de la Plata modelling system described before. Also, the evaluation of the relative importance of the remote and the local forcings was performed based on numerical experiments with some simplification.

First, a simulation without meteorological forcing was made to obtain a pure astronomical solution, and then this solution was subtracted to the solutions including meteorological forcings to remove the astronomical variability. Two simulations were made to observe the generation zones of the meteorological tide events observed in Río de la Plata using wind and sea level pressure (SLP) as forcings. The first one includes wind and SLP forcings in both the regional domain and Río de la Plata sub domain (called Rwp_Swp), and it aims to evaluate the generation of meteorological tide events in the father domain which are associated to the remote forcing. The second one includes wind as SLP forcing only in the Río de la Plata domain (called R_Swp), so it aims to evaluate the generation of meteorological tide events only by the action of the meteorological forcings in a local spatial scale. The simulated period was June – July, 2007.

The water level series obtained from the complete simulation Rwp_Swp were compared with the water level series measured at several points in the Río de la Plata, checking the accuracy of the model reproducing the meteorological events. Nevertheless, the meteorological water level series obtained with the simulation R_Swp, only with atmospheric forcing in the local model, did not reproduce the whole meteorological measured signal thus showing the relevance of the remote forcing.

To determined where the meteorological tide events are generated, correlation maps between the water level series at one location inside the Río de la Plata (at Pilote Norden, see location in Figure 1 right panel), and the water level series for each cell of the domain were calculated. This procedure was repeated for different temporal lags, allowing us to see where was the signal observed at Pilote Norden at previous instants. The time series extracted from the domain cells were processed with the Matlab software. Figure 8 shows the correlations maps for various temporal lags, correlations greater than 0.8 have been highlighted by filling the contour map. It should be noted that maximum correlations take place approximately at Mar del Plata for lag 17 hours. For greater lags the region of maximum correlation is located at higher latitudes, showing that 40 hours before the observation of the meteorological tide events at Pilote Norden the signal was situated approximately at 45^o S.

These results show where the events were generated. A similar analysis calculating correlation maps was made between the observed sea level heights and the Reanalysis wind fields to identify the forcing conditions that generate the events. As a result, maximum correlations were obtained between the filtered sea level height series at Pilote Norden and the southwest component of the wind.

7 CONCLUSIONS

Using the MOHID hydrodynamic model coupled with the WRF atmospheric model, a forecast water level height system was performed. The system is capable of doing real-time simulations and predicting water levels generated by astronomic and meteorological effects in the Río de la Plata region. This system constitutes a very powerful tool for the management of fluvial-maritime transport. Nevertheless, the relevance of the system for the management of the area requires continuous development and improvement of the system.

The modelling system consists of a group of integrated models. Although the area of interest is the Río de la Plata region, the system of models needs to be implemented in a bigger domain that includes a large area of the South Atlantic Ocean and then, using the nesting approach, the model can focus on the Río de la Plata region. The atmospheric forcings introduced in the hydrodynamic model are obtained with the WRF model while the astronomic forcings are obtained from the FES2004 global tidal atlas. The WRF is initialized with the GFS global model forecasts.

The original system is now going through an improvement stage. Several high performance computing tools were applied in order to reduce the computational time using the hardware platform available. Also, several aspects of the South Atlantic hydrodynamic model were evaluated and improved: the study domain, the bathymetry data, the open boundary condition for astronomical tide, and the bottom friction coefficient. The improvement in the local bathymetry in the Río de la Plata produced the bigger changes in the simulated astronomical tide. Moreover, for the coastal control stations located outer the Río de la Plata the most influential parameter was the open boundary condition through the relaxation time. The least influential parameter over the simulated M2 tidal component characteristic was the Manning number evolved in the bottom roughness coefficient formulation.

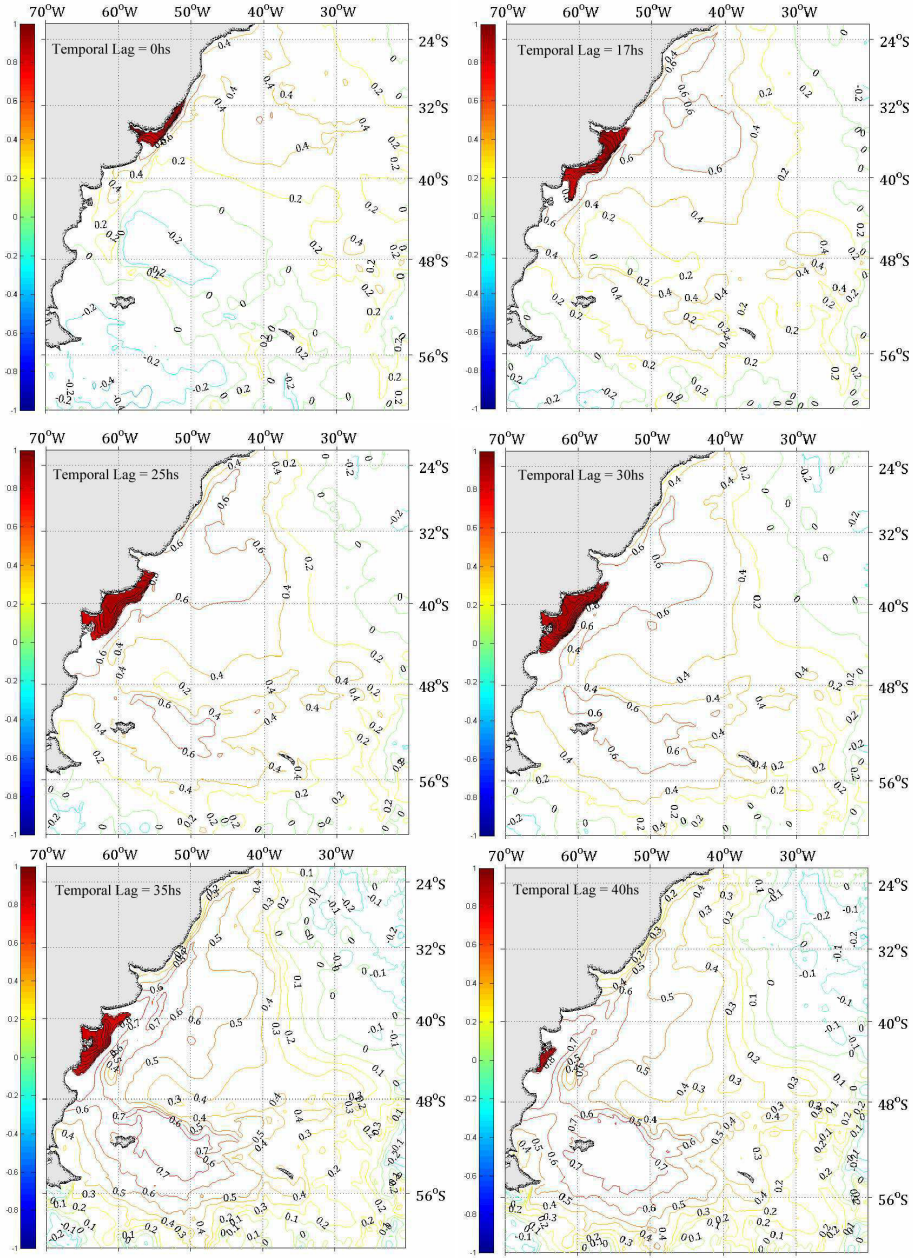

Figure 8. *Correlation maps among the modelled meteorological tide at Pilote Norden and the rest of the domain for different temporal lags.*

REFERENCES

1. Prandle, D., Operational Oceanography - A view ahead, Coastal Eng. 41 (2000) 253-259.
2. Santoro, P.; Fernández, M.; Fossati, M.; Cazes, G.; Terra, R.; Piedra-Cueva, I. Pre-operational forecasting of sea level height for the Río de la Plata. Applied Mathematical Modelling 35 (2011) 2462-2478
3. Piedra Cueva, I. Fossati, M., Residual currents and corridor of flow in the Río de la Plata, Applied Mathematical Modelling 31 – 3 (2007) 564-577.
4. Fossati, M., Piedra-Cueva, I., Numerical modelling of residual flow and salinity in the Río de la Plata, Appl. Math. Modell. 32 (2008) 1066–1086.
5. Fossati, M.; Bellón, D; Lorenzo, E.; Piedra-Cueva, I. Currents measurements in the coast of Montevideo, Uruguay. RCEM 2009 Proceedings. River, Coastal and Estuarine Morphodynamics. Santa Fe, Argentina, september 2009.
6. Michalakes, J., J. Dudhia, D. Gill, T. Henderson, J. Klemp, W. Skamarock, W. Wang, The Weather Research and Forecast Model: Software Architecture and Performance, Proceedings of the Eleventh ECMWF Workshop on the Use of High Performance Computing in Meteorology. Eds. Walter Zwieflhofer and George Mozdzynski. World Scientific (2005) 156 – 168.
7. Wang, W., Barker , D., Bruyère , C., Dudhia, J., Gill. D., Michalakes, J., Advanced Research WRF (ARW) Version 2.1 modelling system User's Guide (2005).
8. Pawlowicz, R.; Beardsley, B.; Lentz, S. Classical tidal harmonic analysis including error estimates in MATLAB using T TIDE. Computers & Geosciences 28, 2002, pp. 929–937.
9. Flather, A. (1976). A tidal model of the northwest European continental shelf. Mem. Soc. R. Sci. Liege, 10 (6), pp. 141–164.
10. Blumberg, A. & Kantha, F. (1985). Open boundary condition for circulation models. Journal of Hydraulic Engineering, ASCE, Vol. 111, pp. 237-255.

PHYSICAL ANALYSIS OF A TIDAL CHANNEL (ESPINHEIRO CHANNEL, PORTUGAL): A MODELLING STUDY

N. Vaz • J. M. Dias

CHAPTER SYNOPSIS

Background
The implementation of a 3D marine model to Ria de Aveiro lagoon is described in this study. The main goal of this implementation is to develop a numerical tool to research the stratification/mixing balance in one of the four main channels of the Ria de Aveiro: the Espinheiro Channel. Some of the major findings are then summarized. The simulations were performed for distinct periods where markedly tides and river discharge occurred. Tidal currents and salinity data were analyzed at the channel's mouth during several tidal cycles.

Results
A flood-ebb asymmetry was found in stratification with higher values on peak flood than on peak ebb. The cross-section structure of the channel's inlet was found homogeneous in terms of salinity, but lateral differences in current velocity were found with ebb predominance near the south margin and flood predominance near the north margin, producing a exportation (importation) of salt from the channel to the ocean near the south (north) margin.

Conclusions
All the results are consistent with observations, revealing that if adequately applied the 3D models are a suitable tool for the study and management of complex marine systems like the Espinheiro Channel.

1 INTRODUCTION

Estuarine systems are interface regions where salt water from the ocean is measurably diluted by the freshwater from land drainage [1]. These systems are highly variable and rich, supporting important economic and social activities.

Nowadays, a major motivation to implement and improve hydrodynamic models is the importance of three-dimensional (3D) localized processes in the scope of the hydrodynamic influence on water quality of estuarine areas. Observational programs often do not cover the entire study areas, therefore 3D estuarine hydrodynamic models may be used to complement observations. The set-up and development of models that describe the dynamical behavior of estuaries and coastal systems occupy much of the literature. In fact, [2] and [3] have presented a predictive model (based on ROMS) for the Chesapeake Bay and the Hudson River estuary, respectively, describing the set-up of the model for these two estuaries. GETM was applied to study transport pathways and residence time in a macrotidal estuary (Willapa Bay, Washington) [4], and to study the temporal and spatial dynamics of the North Sea using a numerical system [5] and MOHID was applied to study the dynamics of a tidal channel, located inside Ria de Aveiro lagoon (Portugal) [6]. These few examples demonstrate the importance of the set-up and application of numerical models to research estuarine and coastal dynamics.

Recent observations in estuarine regions have revealed an asymmetry in stratification and turbulent mixing over the tidal cycle. At the Columbia River estuary, a flood-ebb asymmetry

was found with enhanced shear and stratification during ebb and stronger mixing and weaker stratification during flood tides [7]. It was suggested that this asymmetry is induced by a strain-induced buoyancy flux that stabilizes on ebb and destabilizes during the flood tide [8]. At Chesapeake Bay, a three-dimensional numerical model was used to investigate this issue [9] showing that the asymmetric tidal mixing causes significant variation in salinity distributions over the flood-ebb cycle. However, until recently was not performed any research about the tidal variability effects in the stratification/mixing balance along the Espinheiro channel (Ria de Aveiro).

The Espinheiro Channel is a mesotidal and shallow branch of Ria de Aveiro, a coastal lagoon located in the Northwest Portuguese coast. This channel has a great importance in the local dynamics once it connects the major source of freshwater of the lagoon (Vouga river) to the Atlantic Ocean. The channel is approximately 11 km long, has an average width of about 200 m and a mean depth along its longitudinal axis of about 10 m (Figure 1). The tides at the channel propagate from the nearby ocean and are mixed semi-diurnal, with M_2 being the most important constituent, representing more than 90% of the tidal energy [10]. The channel's dynamics is mainly controlled by the interaction of tides and incoming river flow [6, 11]. The channel's vertical structure is strongly dependent on the tidal strength and river inflow, turning from well-mixed to partially stratified [11, 12]. The channel's behavior adjusts dynamically to changes in the main forcing [13]. In the lower channel (near the mouth), tidal currents present values between 0.6 (flood) and $\sim$1.0 m s^{-1} (ebb) during neap tides. Tidal currents are higher during spring tides, ranging from 1.5 (flood) to 1.6 m s^{-1} (ebb). The Espinheiro channel presents characteristics of an ebb-dominated channel [6]. A full description of the channel can be found at [6] and [12].

A 3D baroclinic numerical model (MOHID, [14]) was used to perform hindcast simulations of the Espinheiro Channel. The simulations covered short periods of time in order to assess the channel's vertical structure under different tidal and river inflow conditions. In this work, the effect of tidal variability on stratification is described at the lower channel (located near the channel's mouth). Moreover, the cross-sectional characteristics of this zone are also studied in terms of its hydrography and velocity patterns. The effect of river inflow in the hydrography and residual circulation patterns at the channel's mouth is also investigated.

To perform the study of the mixing processes in the Espinheiro Channel, a 3-dimensional baroclinic model was used. The model has the ability to simulate flooding and drying of tidal flats. The model was first implemented for the entire lagoon, in a two-dimensional mode (depth-integrated), with a closer look to the central area (where Espinheiro Channel is located), in order to study the dependence of the thermohaline horizontal structure with the tidal regime and freshwater inflow.

Although this kind of applications reveals some of the main features of the horizontal thermohaline structure, mixing processes within the lagoon are driven not only by freshwater discharge and the barotropic component of the pressure gradient due to tides, but also by its baroclinic component due to salinity gradients (horizontal and vertical). Due to the shallowness and complex geomorphology of the lagoon, as well as to the existence of large intertidal areas

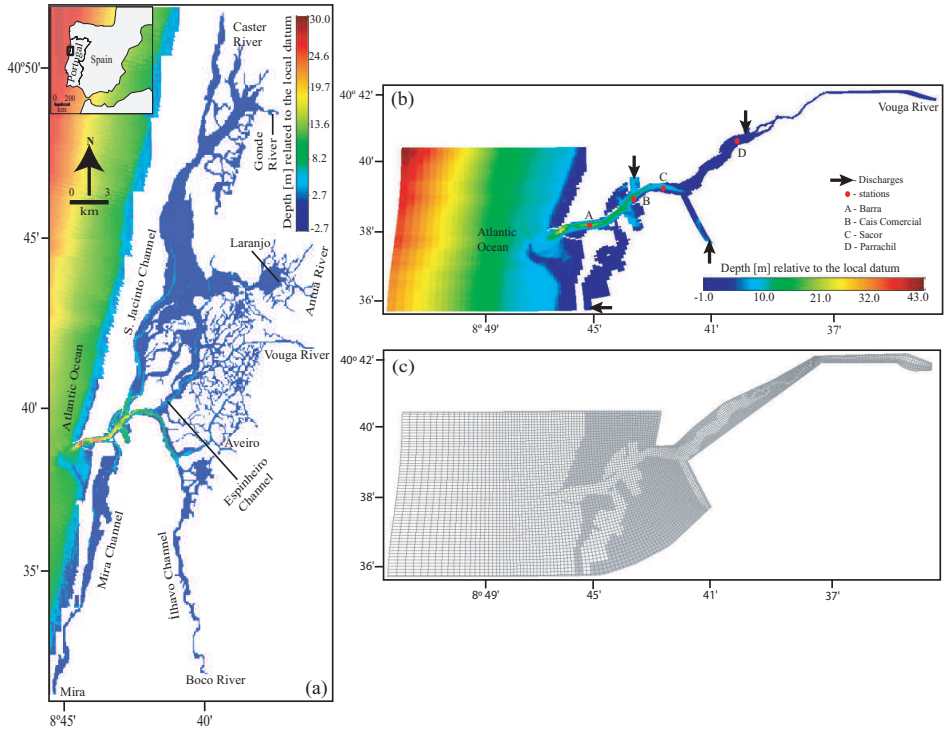

Figure 1. *(a) Bathymetry of the Ria de Aveiro lagoon and adjacent coastal area. Major tributaries are marked; (b) Bathymetry of the Espinheiro Channel with the discharge points (marked with arrows) and its major freshwater tributary. The location of the stations used in the hydrodynamic calibration procedure is marked. Depths are in meters (over the local datum); (c) Horizontal curvilinear coordinate system [6].*

it is not advisable the study of the entire system in a three-dimensional mode. In order to overleap this difficulty, a high resolution three dimensional application was developed for the Espinheiro Channel.

Ria de Aveiro has four main channels, and due to their unique characteristics each one of them may be considered as an independent estuary connected to a common inlet. The hydrology of each channel is determined by different tidal prisms and freshwater inputs.

2 THE STUDY AREA

Ria de Aveiro is a shallow mesotidal lagoon located in the Northwest coast of Portugal (40°38' N, 8°44' W). It has a very irregular geometry (see Figure 1) being characterized by narrow channels and by the existence of intertidal areas, namely mud flats and salt marshes. The lagoon has a maximum width and length of 10 and 45 km, respectively. In spring tide covers an area of 83 km^2 at high tide reducing to 66 km^2 at low tide [15]. The averaged depth of the lagoon is 1 m, except in its navigation channels where dredging operations are often carried out. One single inlet at the western boundary allows the water exchange between the Atlantic Ocean and the lagoon. This inlet has about 20 m deep, 1.3 km long and 350 m wide.

Ria de Aveiro has four main channels, and due to their unique characteristics each one of them may be considered as an independent estuary connected to a common inlet. The hydrology of each channel is determined by different tidal prisms and freshwater inputs. The Ria receives freshwater mainly from two rivers, the Antuã (5 $m^3\ s^{-1}$ average flow) and the Vouga (50 $m^3\ s^{-1}$ average flow) [10, 16]. Vouga River is responsible by approximately 2/3 of the freshwater input into the lagoon [10]. The other rivers have negligible flow, except the freshwater source in the south end of the Mira Channel, which consists of a small system of ponds and rivers with a poorly known flow.

The estimated tidal prism for the lagoon's mouth at extreme spring and extreme neap is 136.7×10^6 and 34.9×10^6 m^3, respectively [15]. Near station C ($\sim$4 km upstream) it is about 40×10^6 at extreme spring and 15×10^6 m^3 at extreme neap tide [15]. The total estimated freshwater input for the lagoon is very small (about 1.8×10^6 m^3 during a complete tidal cycle [16]) when compared to the tidal prism at the mouth. The small ratio between the freshwater input and the tidal prisms indicate that the circulation is mainly induced by tides. However, the combination of these two factors (tidal regime and freshwater inflow) highly influences the thermohaline horizontal patterns [17]. A prior hydrological characterization led to the conclusion that Ria de Aveiro can be considered vertical homogeneous during dry seasons. However, after important rainfall the stratification becomes important near the freshwater inflow locations [10, 17].

The Espinheiro Channel has a low ratio between tidal amplitude and depth, revealing an ebb-dominated channel [15]. The channel is very dynamic, presenting current velocity maximums higher than 2 $m\ s^{-1}$ [15]. The longitudinal salinity differences lie between 20 and over than 30 psu, depending on the freshwater input [17]. The channel can be divided into three distinct regions: (a) a marine or lower estuary dominated by ocean waters, (b) a middle estuary where the mixing between the fresh and salt water occurs and (c) an upper or fluvial estuary characterized by freshwater, but subject to a daily tidal action [12]. This delimitation is dynamic and can change seasonally (or in lower time scales) due to tides, winds or freshwater inflow. Residence times lower than 2 days were computed for the whole study area [18], revealing a good water renewal. A full description of the channel can be found at [6] and [12].

3 NUMERICAL MODEL

The Espinheiro Channel's predictive model presented in this study is an implementation of MOHID ([14], www.mohid.com). The model is a baroclinic finite volume model, designed for coastal and estuarine shallow water applications, like Ria de Aveiro, where flow over complex topography, flooding and drying of intertidal areas, changing stratification or mixing conditions are all important. MOHID allows an integrated modelling approach of physical and biogeochemical processes. A complete description of the model's physics can be found in several works [14, 19].

A complex application of MOHID has been configured to study the Espinheiro Channel dynamics, consisting in a local 3D application supported by a general 2D model of the entire Ria de Aveiro. Bathymetry in the channel was extracted from topohidrographic data obtained

from a general survey performed by the Hydrographic Institute of the Portuguese Navy in 1987/1988. To define Ria de Aveiro bathymetry this topohidrographic data was complemented with more recent data resulting from dredging operations in several channels (1998) as well as with results from surveys performed by the local harbor administration close to the lagoon's mouth (2002) (Figure 1).

An orthogonal curvilinear coordinate system was designed to follow the general orientation of the channel including its major tributaries and the near coastal ocean. The grid spacing is less than 100 m in the longitudinal and about 50 m in the cross channel direction. High resolution is used in order to properly resolve the physical features of the channel. The total number of grid points is 200×200 and in the vertical direction the model uses 10 sigma layers. The domain was designed to resolve the channel's dynamic and not the dynamics of the near coastal ocean.

At the bottom, the 3D model uses shear friction stress imposed assuming a velocity logarithmic profile. The vertical eddy viscosity and diffusivity are computed using a turbulence model (GOTM, [20]). Coefficients of horizontal viscosity and diffusivity are set to 2 $m^2\ s^{-1}$. Initial conditions for the hydrodynamic model are null free surface gradients and null velocity in all grid points. Initial conditions for the 3D transport model are constant values of salinity and water temperature (typical values for each run). At the ocean open boundary the model is forced by the tide determined from 38 tidal constituents obtained after harmonic analysis [21] of data measured at a tidal gauge located close to the lagoon's mouth in 2002.

Freshwater inflow was imposed at the landward boundary and at the arrow marked boundaries water inflow/outflow, salinity and temperature fluxes were also prescribed. The solutions imposed at the arrow marked boundaries were computed using a 2D model application for the entire Ria de Aveiro lagoon. This 2D model computes sea surface height, current velocity, salinity and water temperature which are then imposed to the 3D model. Details about this 2D application can be found in previous works [11, 17]. On the offshore open boundary and at the river boundary constant values of salinity and water temperature were prescribed (S_{Sea} = 36 psu and S_{River} = 0) psu, water temperature varies from run to run, accordingly to the local climatology).

A set of simulations, covering spring and neap tide periods of 2003 and 2004 was performed. Two of the simulations include two spring tide periods with low and high river inflow (26/09/2003 and 25/11/2003) and two neaps also with high and low river inflow conditions (29/01/2004 and 25/07/2004). The river inflow imposed at the landward boundary was 2.06 (September 2003) and 72.74 $m^3\ s^{-1}$ (November 2003), and for the neap simulations was 2.0 (July 2004) and 143.16 $m^3\ s^{-1}$ (January 2004). Another period was simulated – June 2004 – when the river inflow ranges from medium-to-low, with maximum and minimum freshwater discharges of the order of 20 $m^3\ s^{-1}$ and 2 $m^3\ s^{-1}$, respectively. Details about these simulations can be found in a previous work [6]. The hydrodynamic was spun up from rest over 2 days ($\sim$4 tidal cycles), which is considered a fair adjustment period. The spin-up period is not included in the results and therefore the initial state of a run refers to the end of the spin-up period.

4 RESULTS

4.1 Flood-ebb asymmetry

To study the effects of tidal flow and river discharge on stratification/mixing processes along the Espinheiro Channel, the model should accurately predict tidal heights and tidal currents in the channel. This evaluation was previously performed [6], showing that the skill coefficient between data and model outputs is of the order of 0.9 in the four stations marked in Figure 1. Consequently the results show that the model accurately predicts tidal heights in the channel.

Then, the model was applied to research the flood-ebb asymmetry for a neap and a spring tide during June 2004. It was selected a station in the lower portion of the channel (Station A, see Figure 1 for location) and were chosen two instants during the tidal cycle: one representing the peak flood and the other representing the peak ebb. As shown in Figure 2a and 2b, the depth-averaged current oscillates at the semi-diurnal frequency. The barotropic current presents ebb intensities about 30% (10%) higher than the flood values at neap (spring) tide. The vertical profiles of salinity and current velocity between the peak flood and ebb tides are compared in Figure 2c and 2f, respectively.

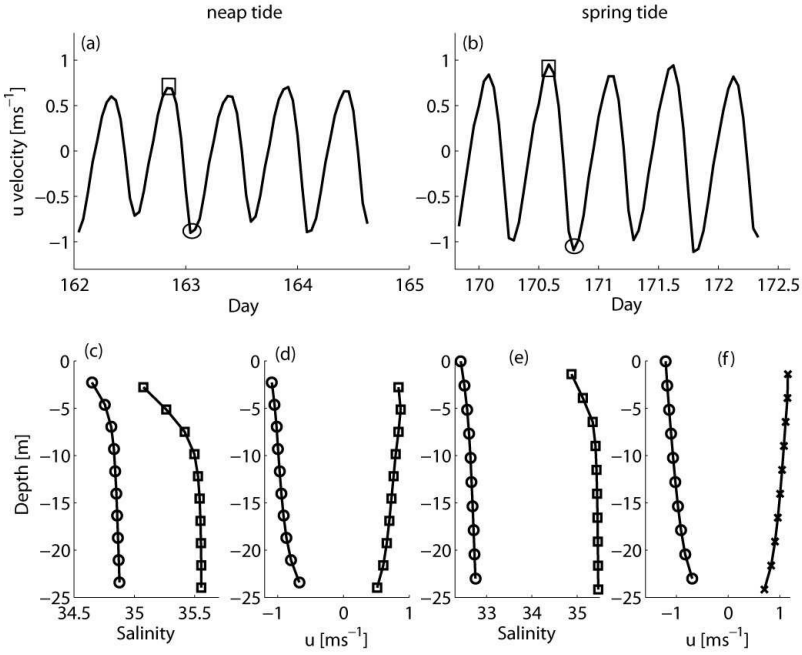

Figure 2. *Time series of along-channel depth-averaged velocity (u component) at station A at neap and spring tide for June 2004; (c, d). Vertical profiles of salinity and current velocity at the peak flood (squares) and peak ebb (circles) at neap tide and (e, f) spring tide. (From [22])*

Both at neap and spring tide, the salinity profiles (Figures 2c and 2e) show higher stratification on peak flood than on peak ebb. This feature may be induced by the higher ebb tidal velocities that increase turbulent mixing, inducing a decrease on stratification. At neap tide, the peak flood velocity profile shows a subsurface maximum ($\sim$5 m depth) and a quasi-linear distribution on ebb tide (Figure 2d). On the flood, this slight drop of the water velocity may be caused by the non-tidal pressure gradient that reinforces the tidal pressure gradient at the deepest layers, but opposes it near the surface. On ebb, the non-tidal pressure gradient reinforces the tidal pressure gradient near the surface, but opposes it at the bottom layers, resulting in a nearly linear depth distribution of the depth-average velocity. At spring tide, the depth variation of the barotropic current is nearly linear at peak flood and peak ebb.

4.2 Residual circulation

Superimposed on the back-and-forth tidal water flow there is an averaged steady water motion, known as residual circulation. This circulation has a time scale similar to the tidal cycle time scale, and amplitude which is typically one or two orders of magnitude lower than that of the tidal currents. In spite of its small amplitude, the residual circulation can determine the long-term transport which is very important for the ecological systems dynamics.

In this study the residual circulation was determined from model results at two different levels: on the surface (Figure 3a) and near the bottom (Figure 3b). The results revealed here represent the residual flow driven by tides and freshwater inflow during the spring tides of November 25th (river flow of 72.74 $m^3\ s^{-1}$). The residual values were calculated by tidally averaging the transient solution computed by the model and are about one order of magnitude lower than the tidal currents within Espinheiro Channel. The hydrodynamic and salinity simulations cover a period of 4 days (plus spin-up). The model results were averaged for four and eight tidal cycles, however the results did not change revealing its independency from the average time.

Without freshwater inflow, the tide induced residual currents are seaward on the surface and bottom, revealing an ebb-dominated channel (not shown), in accordance with results from a previous study [16]. In that study the authors applied a depth-integrated numerical model to capture the barotropic residual circulation in Ria de Aveiro, induced by tides, river inflow and winds. The results presented in the present study are consistent with an ebb dominated channel, where the surface and near bottom currents are always directed seaward. Nevertheless, currents show some spatial variability. The surface currents are more intense, flowing out the estuary (Figure 3a). This jet-like current spreads over the full channel width for almost all the channel area. However, it intensifies near the south margin of the inlet. The bottom current is also seaward but less intense. The results presented in this section have shown that the model can qualitatively capture some of the characteristics of the tidally averaged estuarine circulation revealed in a prior study [15].

4.3 Cross-sectional tidally averaged velocity and advective salt tranport

In the frame of this investigation the model was also used to provide insight on the transport of water and salt through the channel's inlet (near station A). Simulations for January and

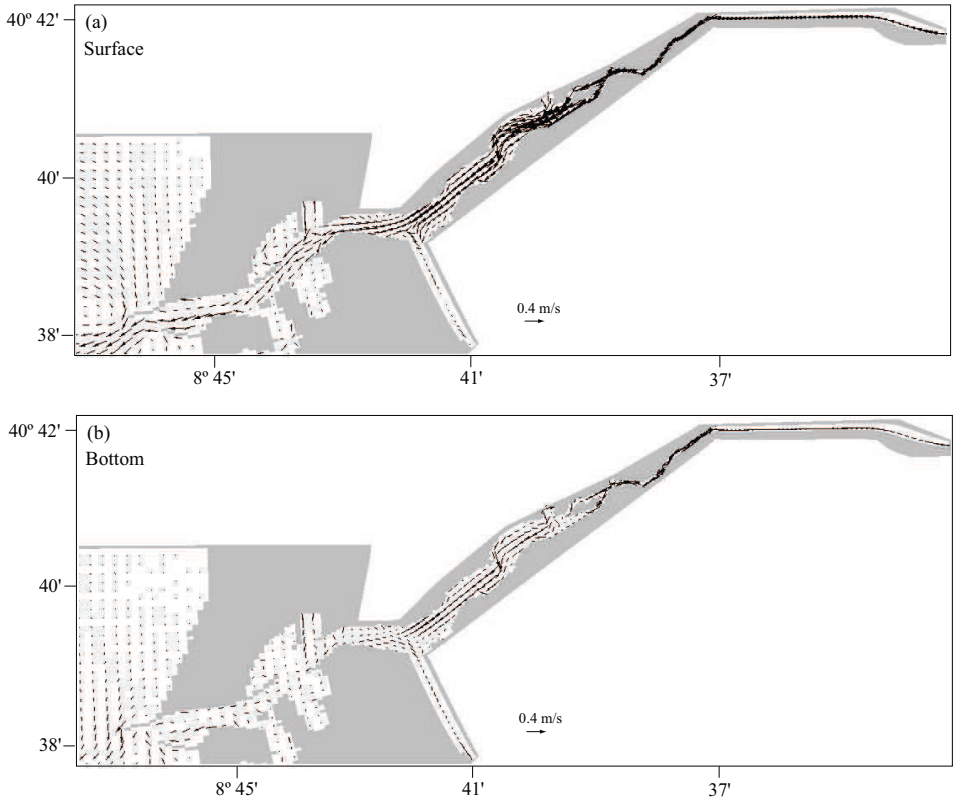

Figure 3. *Averaged residual flow: (a) surface layer and (b) bottom layer. Simulation period: 24/11/2003 to 27/11/2003. River inflow of 73* $m^3\ s^{-1}$.

July were performed and the results obtained are presented here. The cross-channel section has a triangular shape (smooth slope from the center to the margin) with a deeper zone close to the center, and may be considered representative of the lower region of the channel. At this location, the channel width is about 350 m and the maximum depth is $\sim$25 m. The longitudinal velocity and salinity were averaged over four complete tidal cycles to remove the tidal periodicities and reveal the characteristic features of the estuarine circulation [23, 24].

In Figure 4, the lateral and vertical structure of the tidally averaged (or residual) salinity and longitudinal velocity component is shown. Positive values are referred as landward velocities and negative values as seaward values. At the channel mouth, during low river flow periods (July simulation, river flow of $\sim$2 $m^3\ s^{-1}$), the salinity structure is nearly homogeneous, revealing a well mixed section (see Figure 4b). However, the residual velocity pattern is different, with higher ebb currents near the south margin decreasing toward the middle of the section while flood currents are found close to the north margin. During medium (not shown) and high river inflow events (January simulation, Figure 4a), the salinity structure presents a stratified water column but the channel may be considered as laterally homogeneous in terms

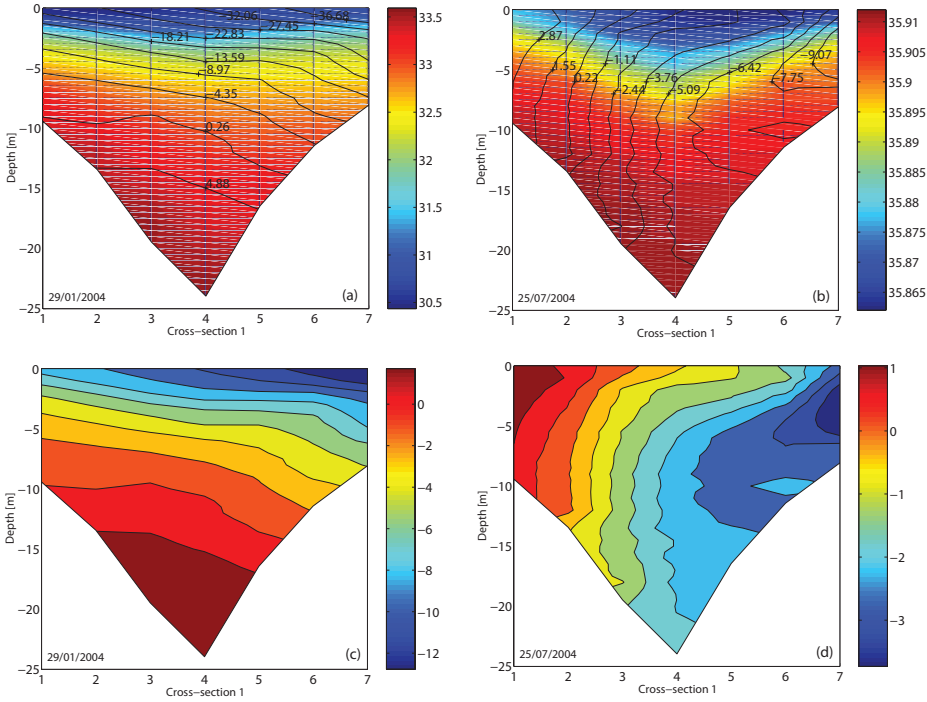

Figure 4. *(a, b) Cross-sections of tidally averaged salinity (shading) and longitudinal velocity component (contour,* cm s^{-1}*); (c, d) predicted tidally averaged salt transport (*cm s^{-1}*) for cross-section 1, near the mouth of the lagoon. (a, c) are for neap tide and river flow of 143* m^3 s^{-1} *and (b, d) are for a neap tide and river flow of 2* m^3 s^{-1}*. (From [6])*

of salinity. During the January simulation, when the river inflow is high (143.16 m^3 s^{-1}), the residual velocity pattern, at cross-section 1 reveal flood currents near the bottom and ebb currents at mid-column and on the surface, revealing a stratified water column and nearly flat isotachs through the cross-section.

Near the mouth of the channel, the predicted tidally averaged salt transport presents a pattern similar of that observed for velocity, with a net up-channel flux (positive) in the proximity of the north margin of the section decreasing toward the center of the channel, and a net down-channel flux (negative) from the middle toward the south margin of the channel. This feature is visible in all simulations, except for the January simulation (Figure 4c), where following the same pattern of the residual velocity, the cross-section presents a net up-channel flux near the bottom and a down-channel flux on the upper layers. During this period the gravitational circulation becomes an important mechanism for transport of salt at cross-section 1. Another feature found during the analysis is that, in general, the salinity values are higher during the flood than during the ebb, leading to a landward transport. This is the tidal cycle correlation term of the salt transport and can be important in branching and curved estuaries [4, 25]. The

September and July simulations were carried out under similar river inflow (about 2 $m^3\ s^{-1}$), showing a higher down-channel salt transport during spring tide (not shown) than during neap tide (July simulation, Figure 4d). This result is expected since the residual currents present higher values at spring tide.

4.4 Estuarine stratification

To evaluate the estuarine stratification at the mouth of the Espinheiro Channel under different conditions of tidal ranges and river inflow, the Estuarine Richardson number, R_{iE}, [1, 25] was calculated. This number expresses the ratio of the potential energy gain due to freshwater discharge to the mixing power of tidal currents, and it is defined as:

$$Ri_E = g\left(\frac{\Delta\rho}{\rho}\right)\left(\frac{Q_f}{bU^3_{RMS}}\right) \tag{1}$$

where Q_f is the river inflow, b is the width of the section where the data were collected, Δ_ρ is the density difference between sea and freshwater, ρ is the mean density and U_{rms} is the root-mean-square tidal velocity. If R_{iE} is greater than 0.8 the estuary is considered highly stratified, if it is smaller than 0.08 the estuary is considered well mixed and finally, if $0.08 < R_{iE} < 0.8$ the estuary is considered partially mixed [25]. Moreover, the water column stability was analyzed using the buoyancy frequency (N) [26], calculated at the two locations previously referred. N is defined as:

$$N = \left(\frac{g}{\rho}\frac{\Delta\sigma_t}{\Delta z}\right)^{\frac{1}{2}} \tag{2}$$

where ρ is the density, σ_t is the density at atmospheric pressure (1000 $kg\ m^{-3}$) and z is the depth measured from the surface.

In July and September, when the river inflow is $\sim$2 $m^3\ s^{-1}$, and independently of the tidal regime, the region in the vicinity of the Espinheiro Channel mouth reveals a well mixed water column, presenting a Richardson number of 0.001 (September) and 0.01 (July), respectively. This area of the channel becomes highly stratified when the river inflow is higher than 100 $m^3\ s^{-1}$ (January), presenting a Richardson number of 0.95. Under spring tide regime and river inflow of $\sim$70 $m^3\ s^{-1}$ (November), this area presents well mixed characteristics (Richardson number of 0.05) due to the high tidal currents which increase turbulence, and hence vertical mixing.

The characteristic of the whole flow has been analyzed using R_{iE}. This information can be complemented by means of the Buoyancy frequency (N). In Figure 5 the N values are depicted as a function of the layer's depth for the four simulations performed. The figure shows higher values of N on the surface layers and low values near the channel's bed (for all simulation periods), indicating a more stratified water column on the surface and more homogeneous close to the bed. The higher values of N are visible during the November and January simulations when the river flow is high. The Espinheiro Channel is a small system where the river inflow has a major role in determining the stratification patterns. Buoyancy inflow from river tends to maintain stratification in the channel. On the other hand, the friction induced by the tidal flow causes mixing.

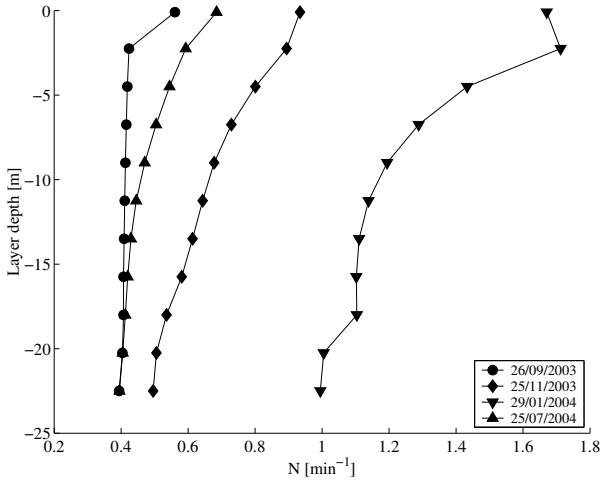

Figure 5. *Buoyancy frequency, N (min^{-1}), as a function of layer depth (m). (From [6])*

Due to the small length of the channel, even close to the channel's mouth, which is the deepest area of the channel, the river inflow is confined to the surface and tends to maintain stratified a small portion of the water column (3.0 – 5.0 m, depending on the river inflow). At this location, the tidal velocities are high, and tend to activate turbulent mixing, producing the well mixed portion of the water column. In general, these model results do not illustrate the existence of a visible pycnocline. Instead, a monotonic decrease of *N* toward the channel's bed is visible. This fact may indicate an overestimated mixing of the water column. This feature was also observed in the study of Ria de Ferrol (NW Spain) [27], where under low river inflow is not visible the pycnocline. In the Espinheiro Channel, only under high river runoff (January simulation) is visible a pycnocline at a depth of $\sim$2.5 m. In this case, the maximum buoyancy frequency is 1.71 min^{-1}.

5 CONCLUSION

A 3D baroclinic numerical model (MOHID) was used to perform hindcast simulations of the Espinheiro Channel covering short periods of time in order to assess the channel's vertical and cross sectional structure under different tidal and river inflow conditions. The flood-ebb asymmetry was examined at a station located near the channel's mouth. At this location, the barotropic velocity oscillate at the semi-diurnal frequency, and the water column show higher stratification on peak flood than on peak ebb, which is consistent with results found for the Columbia River estuary [7].

The residual currents were also examined. The general characteristics within the domain are those of an ebb dominated channel, revealing a more intense current near the surface due to the freshwater inflow. This feature is common to other estuaries like the Galician Rias or Chesapeake Bay where surface residual currents enhanced by the river inflow are visible. Another feature revealed from the analysis of the residual circulation at the entrance channel

of Ria de Aveiro, is that in the vicinity of the north margin of the inlet channel's the residual currents present positive (inward) values, and close to the south margin the residual currents present negative (outward) values. This may suggest that, at the entrance channel of the lagoon, the water flow during the flood period has a preferential path near the north margin and during ebb the preferential path is near the south margin of the channel's entrance. These preferential water flow paths may be related to the existence of two long jetties which induces, during the flood period, a water movement close to the north margin of the channel's inlet. The preferential path during the ebb period may be related to the channel's curvature which induces a flow path close to the south margin of the lagoon's inlet.

The tidally averaged cross-sectional and vertical structure of the channel were examined. Under low-to-medium river runoff the channel is laterally homogeneous in terms of salinity. However, the residual velocity structure is different, presenting landward velocities near the north margin of the channel and seaward velocities at the south margin. When the river inflow is high (higher than 100 $m^3\ s^{-1}$), the channel presents a typical estuarine behavior, with landward residual currents near the bottom and seaward currents at the top layers.

The tidally averaged salt transport follows the same patterns found for the residual currents, presenting landward salt transport at the north margin and seaward salt transport at the south margin under low-to-medium river runoff. When the river flow is high, the landward salt transport was found near the channel's bed, being seaward at the top layers.

It is well known that the river flow, which causes an inflow of buoyancy, tends to maintain stratification, and that the tidal flow induces mixing due to the turbulence generated by friction effects. At the channel's mouth, tidal currents are higher activating turbulent mixing, and generating well mixed conditions, except during high river runoff events when this area is partially stratified. In general, at the channel's mouth, the stratification found in the model results tends to extend throughout the water column, revealing no distinctive pycnocline. This pattern was also observed in a ROMS application for the Hudson River estuary [3]. At the Espinheiro Channel, a visible pycnocline is found when the freshwater runoff is higher than 100 $m^3\ s^{-1}$, revealing a more stratified surface layer. In this channel, the higher tidal currents are frequently able to homogenize the water column. Near the channel's mouth, the water exchange is mainly due to the tide, except under high river flow events when the freshwater extends its influence from the channel's head to its mouth.

In summary, the Espinheiro Channel is a very dynamic estuarine region. The lack of a consistent and permanent monitoring program for this zone turns necessary the use of numerical models to study in detail its dynamics. The results obtained with this study points to the inevitability of future application of pre-operational methods to successfully monitor this channel.

ACKNOWLEDGEMENTS

This paper was partially supported by the Portuguese Science Foundation through the research projects DyEPlume (PTDC/MAR/107939/2008) and BioChangeR (PTDC/AAC-AMB/121191/2010), co-funded by COMPETE/QREN/UE. The first author of this work is supported by the Portuguese Science Foundation program Ciência2008.

REFERENCES

1. Dyer, K.R., 1997. Estuaries. A Physical Introduction, second ed. Wiley, New York, 195pp.
2. Li, M., Zhong, L., Boicourt, W.C., 2005. Simulations of Chesapeake Bay estuary: sensitivity to turbulence mixing parameterizations and comparison with observations. Journal of Geophysical Research 110 (C12004).
3. Warner, J.C., Geyer, W.R., Lerczak, J.A., 2005. Numerical modelling of an estuary: a comprehensive skill assessment. Journal of Geophysical Research 110 (C05001).
4. Banas, N.S., Hickey, B.M., 2005. Mapping exchange and residence time in a model of Willapa Bay, Washington, a branching, macrotidal estuary. Journal of Geophysical Research 110 (C11011).
5. Stips, A., Bolding, K., Pohlmann, T., Burchard, H., 2004. Simulating the temporal and spatial dynamics of the North Sea using the new model GETM (general estuarine transport model). Ocean Dynamics 54: 266–283.
6. Vaz, N., Dias, J.M., Leitão, P.C., 2009. Three-dimensional modelling of a tidal channel: The Espinheiro Channel (Portugal). Continental Shelf Research 29: 29-41.
7. Jay, D.A., Smith, J.D., 1990. Residual circulation in shallow estuaries. II. Weakly stratified and partially mixed, narrow estuaries, Journal of Geophysical Research, 95: 733-748.
8. Stacey, M.T., Ralston, D.K., 2005. The scaling and structure of the estuarine bottom boundary layer, Journal of Physical Oceanography, 35: 55-71.
9. Li, M. and Zhong, L., 2007. Flood-ebb and spring-neap variations of mixing, stratification and circulation in Chesapeake Bay, Continental Shelf Research, 29(1): 4-14
10. Dias, J. M., Lopes, J. F., Dekeyser, I., 1999. Hydrological characterization of Ria de Aveiro, in early summer, Oceanologica Acta, 22 (5): 473-485.
11. Vaz N., Dias J.M., Leitão P.C., Nolasco R., 2007. “Application of the Mohid-2D model to a mesotidal temperate coastal lagoon”. Computers & Geosciences 33: 1204-1209.
12. Vaz, N., Dias, J.M., 2008. Hydrographic characterization of an estuarine tidal channel. Journal of Marine Systems 70 (1–2): 168–181.
13. MacCready, P., 1999. Estuarine adjustment to changes in river flow and tidal mixing. Journal of Physical Oceanography 29: 708-726.
14. Martins, F., Leitão, P., Silva, A., Neves, R., 2001, 3D modelling in the Sado estuary using a new generic vertical discretization approach, Oceanologica Acta, 24 (1): S51-S62, suppl. S.
15. Dias, J.M., 2001. Contribution to the study of the Ria de Aveiro hydrodynamics. Ph.D. Thesis, University of Aveiro, Portugal, University of Aveiro, 288pp.
16. Moreira, M.H., Queiroga, H., Machado, M.M., Cunha, M.R., 1993. Environmental gradients in a southern estuarine system: Ria de Aveiro, Portugal, implication for soft bottom macrofauna colonization. Netherlands Journal of Aquatic Ecology 27 (2–4): 465–482.
17. Vaz, N., Dias, J.M., Leitão, P., Martins, I., 2005. Horizontal patterns of water temperature and salinity in an estuarine tidal channel: Ria de Aveiro. Ocean Dynamics 55: 416–429.
18. Dias, J.M., Lopes, J.F., Dekeyser, I., 2003. A numerical system to study the transport properties in the Ria de Aveiro lagoon. Ocean Dynamics 53: 220–231.
19. Leitão, P., Coelho, H., Santos, A. and Neves, R., 2005. Modelling the main features of the Algarve coastal circulation during July 2004: A downscaling approach. Journal of Atmospheric & Ocean Science, 10:4: 421-462.
20. Burchard, H., Bolding, K., Villarreal, M. R., 1999. GOTM, a general ocean turbulence model: Scientific documentation, technical report, Eur. Comm., Ispra, Italy
21. Pawlowicz, R., Beardsley, B., Lentz, S., 2002. Classical tidal harmonic analysis including error estimates in MATLAB using T_TIDE. Computers and Geosciences 28: 929–937.
22. Vaz N., Dias J.M., 2011. Cross-sectional and stratification patterns induced by tidal and river discharge changes in a tidal channel: a modelling study. Journal of Coastal Research. SI64: 1614-1618.

23. Pritchard, D., 1952. Salinity distribution and circulation in the Chesapeake Bay estuarine system. Journal of Marine Research 15: 33–42.

24. Hansen, D.V., Rattray, M., 1965. Gravitational circulation in straits and estuaries. Journal of Marine Research 23: 104–122.

25. Fischer, H.B., List, J.E., Koh, R.C.Y., Imberger, J., Brooks, N.H., 1979. Mixing in Inland and Coastal Waters. Academic Press, New York.

26. Pond, S., Pickard, G.L., 1983. Introductory Dynamical Oceanography, second ed. Pergamon Press, Oxford, 329pp.

27. deCastro, M., Gomez-Gesteira, M., Prego, R., Alvarez, I., 2004. Riaocean exchange driven by tides in the Ria of Ferrol (NW spain). Estuarine, Coastal and Shelf Science 61: 15–24.

ALTERNATIVE METHOD TO INITIALIZE REGIONAL OCEAN MODELS USING GEOSTROPGIC VELOCITIES: APPLICATION TO THE BAY OF BISCAY

J. Nogueira • H. Coelho • M. Juliano • P. C. Leitão

CHAPTER SYNOPSIS

Background
An alternative initialization method to [1] was developed to reduce the spin up time on regional Ocean Model simulations. The method was applied to the regional model of the circulation in the Bay of Biscay. Two initialization schemes were tested and compared using *in situ* data (Argo floats and microwave SST); a *slow start* initialization where the model starts at rest and forces were slowly switched [1]; a direct initialization where the model starts with initial velocity, sea level fields and forces switched on.

Results
Both gives a final circulation pattern compatible with the literature but the results shown that the direct initialization with a geostrophic velocity field computed from sea level and density fields of the global model leads to an improved thermohaline structure in the deep layers of the ocean.

Conclusions
The low computational cost and the quality of the results justify the application this method in operational schemes.

1 INTRODUCTION

Numerical Ocean models are based on the resolution of Navier-Stokes equations for a specific physical situation. Like all differential equations, they admit an infinite number of solutions and just one represents our physical problem. The determination of this solution is made by the choice of the boundary conditions and further, the choice of the initial condition. Even with a good choice of boundary conditions, an unbalanced initial condition can leads the numerical model to unrealistic motions during the initialization transient process (mostly inertial-gravity waves) with the consequence of an irreversible state far from the true one. Transient processes generated with a crude initialization have important consequences on the long-term model trajectory [2]. The rigid-lid approximation on large-scale ocean models can filter out those quickly propagating inertia-gravity waves [3]. For free-surface models this is not true and a careful spin up must be done to avoid undesirable consequences like the destruction of the initial state or divergence of the model [4]. Several techniques based on a nudging method were tested to filter out this noise [5-6]. The price paid by these techniques is a loss of physical realism during the spin up period.

In coastal models, Open Boundary Conditions (OBC) can also be important to prevent undesirable consequences caused by the inertial-gravity waves generated during the initialization process. In fact Radiation Boundary conditions can prevent reflections of such waves. A set of Boundary Conditions [7] can be constructed, in which a Flow Relaxation Scheme (FRS) applied to temperature (T), salinity (S) and velocities (U, V) [8] is combined with a radiation scheme [9] for the barotropic mode. This boundary condition scheme was used in MOHID by [10]. However, initial state is still a problem that must be carefully treated and as previously shown, a full set of initial and boundary conditions must be estimated [11].

Different approaches were developed to define an optimal state that makes the initial field (observations) physically consistent with a model. A complete review of those methods was made by [12]. [4] developed a strong methodology to construct a consistent initial state based on optimal interpolation applied to an inverse method. This method ensures that the initial state satisfies the fundamental mass balance, avoiding the generation of mass fluxes associated with a crude interpolation/extrapolation scheme. An application of this method to the Gulf of Lion where a compromise between computational cost and equilibrium of initial state was considered reproduced the main hydrological and circulation patterns [13].

When a combined scheme of open boundary conditions with radiation and flow relaxation is used on a regional ocean model, a reference solution must be given. Usually this reference solution is obtained with climatological fields, from a set of data, or from a global ocean model with lower resolution. For downscaling methodology, where the reference solution is given by a global ocean model, the initialization and forcing of the embedded model can be done with a variational initialization and forcing platform (VIFOP) where the variational strategy ensure that the forcing fields satisfy the fundamental mass balance [14]. This methodology was applied in the framework of the international project MFSTEP [15].

The problem of the regional model initialization in a downscaling approach can also be done with a scheme where the global solution is interpolated/extrapolated to the regional model grid and the forcing terms are slowly switched [1]. This methodology can prevent large gradients that may result from inconsistencies between forcing mechanisms (wind and tide) and the initial density field. This methodology reduces the spin up period and gives a solution able to reproduce the main features of a regional model (see [1] for a detailed description of the methodology). For operational applications, this initialization has at least two problems: the spin up time is yet too large and smooths the density gradients.

In this paper our objective is to construct an initial state for a regional ocean model consistent with the reference solution for OBC. This state must have a low computational cost and further, it should be a good approximation to the dynamic state for the ocean given by the initial reference solution. The methodology used is very simple and consists on the construction of an initial model state based on the reference solution. An interpolation/extrapolation of the mass field (density and water level) from the reference solution into the model grid is processed. With the field obtained the correspondent geostrophic velocities are computed. This state, near the dynamic equilibrium and consistent with the global model, allows to switch directly the forcing terms. Since the global model does not have tidal forcing, the correspondent terms are slowly switched at the open boundaries. In a downscaling methodology, this method was successfully applied to a 3 level nesting model of the estuarine Tagus plume [16].

A two level one-way nesting model is implemented for which the level 1 is a 2D barotropic tidal-driven model with a variable horizontal resolution (0.03^o-0.04^o) covering all the Bay of Biscay. The level 2 is a 3D baroclinic model with the same horizontal resolution. Two runs of 1 year with different initialization methods are compared. For the comparative analysis the reference solution and a set of available data (Argo floats and Microwave SST images) have been used.

2 METHODOLOGY

2.1 The model

The MOHID system uses a finite volume approach [17-18] to discretize the primitive equations. In this approach, the discrete form of the governing equations is applied macroscopically to a control volume. This makes the actual way of solving the equations independent of cell geometry and permits the use of a generic vertical coordinate that allows minimizing the errors of some of the classical vertical coordinates [18]. The equations are discretized horizontally in an Arakawa-C manner staggered grid. The temporal discretization is carried out by means of a semi-implicit (ADI) algorithm with two time levels per iteration.

The domain is defined between (-10.58; -0.734) E and (43.3; 49.9) N. The bathymetry used for the intercomparison is from SHOM (Service Hydrographique et Oceanographique de la Marine) and presents an initial resolution of 1'. No measure was undertaken in the Spanish territorial waters, thus, the bathymetry there is taken from ETOPO.

A variable horizontal resolution (0.03^o-0.04^o) is used and the vertical discretization is the same used by Mercator (43 layers, with the following thicknesses from the surface to the bottom: 6.26; 7.01; 7.49; 8.65; 9.46; 11.02; 12.31; 14.43; 16.37; 19.27; 22.13; 26.09; 30.17; 35.52; 41.17; 48.26; 55.81; 64.93; 74.61; 85.88; 97.64; 110.86; 124.32; 138.89; 153.27; 168.26; 182.54; 196.9; 210.08; 222.94; 234.31; 245.15; 254.39; 263.09; 270.24; 276.96; 282.26; 287.3; 291.11; 294.83; 297.49; 300.21; 302.01).

2.2 OBC and Initialization

The solution from the Mercator-Océan PSY2V1 system for the 2004 period was interpolated for the new grid with triangulation in the horizontal and with linear interpolation in the vertical. For the extrapolation procedure, the nearest neighbour approach was used (straightforward method of assuming null horizontal gradient). The atmospheric fields (momentum and heat fluxes at the surface boundary) used to force the model are provided by the Météo-France of a high resolution (spatial 0.1^o and 3 hour time step) forecast system - Aladin. For this study, only the three main French rivers were considered: Loire, Gironde and Adour. The Loire and the Gironde flows are greater than the Adour flow, by at least a ten-fold factor.

One of the main conclusions that come out from [7] is that to impose a consistent open boundary condition it is necessary to have a good reference solution (in this case the Mercator solution). In this work, to define the open boundary condition, a similar methodology to the one presented [10].

For the spin-up procedure two methodologies were tested. The first implemented is based on a slow connection of the forces - Slow Start [1]. This methodology consists in defining an initial condition where salinity and temperature initial fields are interpolated/extrapolated from the Mercator solution and null velocity field and sea level gradient are assumed. A coefficient that varies linearly between 0 and 1 along the "connection" period of 5 days is multiplied by the baroclinic force and wind stress. This method was applied for the Algarve coastal circulation [1] reproducing many of the features described in the literature.

In the second methodology used all forces (except tidal force) are switched on at the first iteration - direct initialization. The velocity and sea surface height initial fields have non zero values consistent with the salinity and temperature initial fields, trough the geostrophic equilibrium (Figure 1). Tidal force is switch progressively in a linear way along of the first 12 hours.

2.3 Data

To compare and validate the results of the two initialization methods and of the Mercator solution, *in situ data* from Argo float[1] profiles and satellite sea surface temperature (SST) measurements from Advanced Microwave Scanning Radiometer[2] are used.

The Argo float [19] descends to a pre-programmed parking depth (typically 1000 to 2000 m) and drifts freely. Every 10 days it ascends from its parking depth to the sea surface. As it rises, temperature and salinity are measured continuously and transmitted to satellite when arrived at the surface. After the transmission, the float descends again and starts a new cycle. The global Argo profiles and trajectories are managed by the Global Ocean Data Assimilation Experiment and available from http://www.usgodae.org. We get all profiles fondly in the region during the period January 2004 to December 2004 and this where compared with the model's data results (resulting from the linear interpolation of the model data to the same location and time period of the Argo float profile). Only profiles with a quality flag indicating 'good data' and 'probably good data', have been used. The two resulting profiles (each model run and Argo floats) where then statistical compared and analyzed. Vertical profiles of temperature, salinity and density and T-S diagrams with model and Argo data, where also elaborated to analyse the thermohaline structure.

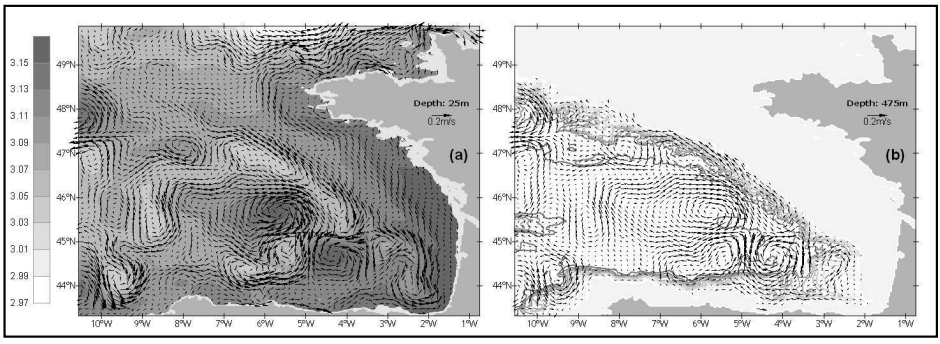

Figure 1. *(a) Initial field of Sea Surface Height (grey scale) and Surface geostrophic velocities at 25 m deep. (b) Bathymetry (contour interval is 500 m) and Surface geostrophic velocities at 475 m deep.*

[1] These data were collected and made freely available by the International Argo Project and the national programmes that contribute to it. (http://www.argo.ucsd.edu, http://argo.jcommops.org). Argo is a pilot programme of the Global Ocean Observing System.

[2] Microwave OI SST data are produced by Remote Sensing Systems and sponsored by National Oceanographic Partnership Program (NOPP), the NASA Earth Science Physical Oceanography Program, and the NASA REASoN DISCOVER Project. Data are available at www.remss.com.

For the SST measurements we get a multi-sensor improved SST product derived from optimally Interpolated sea surface temperature (MISST) colleted by Microwave Radiometer SSTs (AMSR-E, TMI). The data are available from http://www.remss.com. We have used daily MISST images, on a 0.25^o longitude by 0.25^o latitude grid, covering the Biscay Bay. They are different SST products resulting from a combination of satellite measurements and *in situ* observations (e.g., [20]). However, infrared measurements are strongly influenced by water vapour and cloud contamination [21], which can cause biases in regions where cloud cover is nearly constant. This means that studies using infrared SST data in those regions must often use composite images at weekly or monthly time intervals. In contrast to infrared radiation, microwave radiation is capable of penetrating through cloud. Also, the daily images actually distributed by the data servers, can be used in real time to validate the forecasting systems models, despite the lower horizontal resolution (when compared with high resolution infrared images). The daily MISST images have been statistical compared with the daily sea surface temperature from MOHID model data. For this purpose, the SST model data where daily averaged to the MISST resolution grid. An annual evolution of the resulting statistical parameters was also performed for both initializations methods and for the Mercator solution.

3 RESULTS AND DISCUSSION

3.1 Energy Analysis

Figure 2 shows the kinetic energy and enstrophy behaviour of the model for the first month. Both initializations lead model to a stable solution in the first 7 days, but with the geostrophic velocities initialization the system goes faster to a state near to equilibrium. Further, Slow start initialization loses some kinetic energy as a result of the initial deviation from equilibrium.

The proximity from equilibrium state can also be seen on the enstrophy representation (Figure 2) where it can be seen that the system reaches in the first day a value of the same order of magnitude as in the day 31. An energy gap between the two initialization methods keeps up until the end of the simulation (31 December). The energy loss on the Slow Start initialization is due possibly to the density gradient diffusion during the adjustment of the velocity field to the mass field.

Looking for the time series of the kinetic energy during the run period (1 year simulation), represented on Figure 3, we can observe an annual cycle that probably is related with the annual cycle of the wind field (also in Figure 3, for the same period). In both energy and wind speed results we have filtered out the tide cycle (making a lunar period average), keeping only the low- frequency part of those quantities. [22] have compared the mean wind stress with the eddy kinetic energy climatology obtained from twelve years of sea level anomaly from altimetry data, and the two data sets shows a strong correlation. The kinetic energy obtained with the simulation that was the geostrophic initialization is very similar to those described in [22]. A lag of 2-3 months observed on the energy variability (relatively to the results of those authors) could be explained by the same difference between our wind speed variability and the mean win stress variability given in [22].

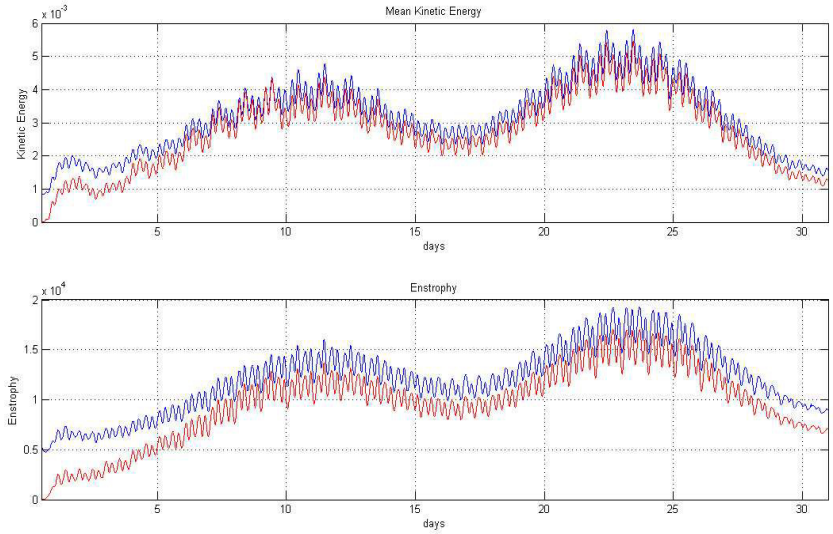

Figure 2. *Mean relative kinetic energy (*$m^2\ s^{-2}$*) (top) and Enstrophy (*$m^2\ s^{-2}$*) variation along time (days) for the first month (bottom): Geostrophic initialization (blue line) and Slow Start initialization (red line).*

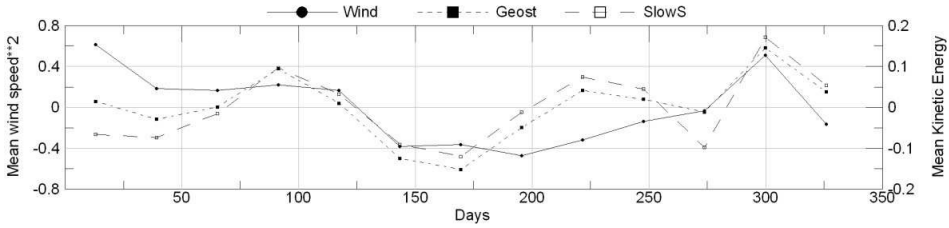

Figure 3. *Mean relative kinetic energy and mean wind speed variation along time (days), from the filtered time series (variables are dimensionless and they represent a mean relative deviation).*

The relation between those two quantities (kinetic energy and wind speed) in the Bay of Biscay is not clear on the literature. In a resume of the main aspects of the circulation on this region, [23] have estimated the current strength associated with each process. As [24] pointed out, the most energetic motion in the Bay of Biscay is connected with the high-frequency tides and internal waves. However, our time series do not consider this high-frequency kinetic energy. [24] for the Armorican shelf, in autumn, found a link between the fluctuations observed in the velocity field and wind events.

Using the filtered series of the kinetic energy and the square value of the wind speed (the wind stress is proportional to the square value of the wind speed) we have computed the Pearson correlation coefficient between those two quantities. The results are very different for each initialization scheme: 0.62 for the geostrophic initialization and 0.29 for the slow start. Taking the square of those values, we can say that: in the simulation with geostrophic velocities

initialization, 39% of the kinetic energy variability is explain by the wind speed variability; in the simulation with Slow Start initialization we have just 9% of the kinetic energy variability explained by wind speed variability.

[26] did an exhaustive study of the wind driven response: they point out the determinant role of the wind stress on the general circulation in the Bay of Biscay. Those results leads us to conclude that the model with geostrophic velocities initialization have a better wind driven response than the model with a slow start initialization. In fact, the geostrophic velocities computed with the initial density and sea level fields derived from Mercator solution give us a good approximation to a state that is dynamically in balance with the wind forcing on the entire water column. Thus, the model initialized with geostrophic velocities to have a better response to wind driven forcing than when he is initialized from the rest. To reinforce this idea we have computed for both simulations, the skewness of the difference between kinetic energy and wind speed (for both series we use the mean deviation normalized of the filtered time series). The skewness standard error is 0.62 for both distributions indicating a good symmetry relatively to the wind speed in both simulations. The results of the skewness (-0.13) to geostrophic initialization and -0.29 to slow start) shows a better fit between the kinetic energy and the wind speed for the simulation with geostrophic velocities initialization.

3.2 Residual Circulation

One of the main goals of the initialization with geostrophic velocities is the circulation pattern after 1 day run (Figure 4). In fact, if we compare the residual velocity field obtained after 1 day, with the results show on Figure 1, it is clear that the first one is very close to the initial solution. Particularly, the current at the Armorican slope has a very clear signature in the first 500 m with current intensities ranging between 5-10 cm s^{-1} consistent with the literature.

[27] point out that those slope currents are persistent (with a seasonal variability) and its signature extends from the surface until 3-4 km depth (2-10 cm s^{-1}). An analysis of the slope current system in the Bay of Biscay show that complete flow reversals can occur if the effect of the large-scale density structure drives a weak slope current and at the same time wind blows with a strong opposite alongshore component [28-29]. Even with some undesirable transient processes over the slope during the initialization process, the solution after one month keeps the structure of the slope current. The general pattern at the first day is close to the general circulation described by [23]. The persistence of the main currents is due to the proximity of the initial state to the dynamic state of the reference solution. The balance between the mass (density and sea level) and the velocity fields gives an important stability to the model.

3.3 Hydrology

To analyse the Sea Surface Temperature (SST) and the vertical thermohaline structure, Microwave SST (see section 2.3 for the details) and the Argo floats profile (section 2.3) were used. Quantitative model skill metrics such as the correlation coefficient (R), the bias, the root mean square error (rmse) and the skewness of the difference between the model results and the *in situ* data was calculated. This statistics were applied to both initializations methods for one year.

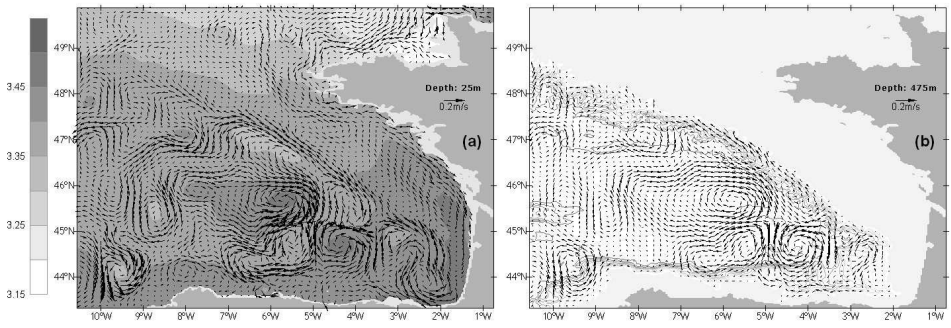

Figure 4. *: (a) Mean Sea Surface level and residual velocities at 25 m deep after 1 days of run (2 January); (b) Bathymetry (contour interval is 500 m) and residual velocities at 475 m deep for the same period.*

The results for the SST analyses (Figure 5 and Figure 6) show that both simulations have a good agreement with the data. There are not significantly differences between the initializations. Analysing the images between May and July some discrepancies can be observed at southwest boundary. Differences are due to the over-heating obtained in Mercator solution for this period, reflected in a large bias (Figure 5). Simulation with slow start initialization is more sensible to this over-heating. Initial dynamic coherence of the simulation with geostrophic velocities initialization gives to the model the ability to resist to an artificial density gradient imposed at the boundary by the reference solution.

Good ‘‘behavior” at the surface temperature leads to conclude that both simulations reach a stable solution during the initialization despite some initial inconsistencies due to crude interpolation/extrapolation of the reference solution. Figure 6 give an example of the agreement between model (with geostrophic velocities initialization) and microwave SST satellite data. The good fit between both values is clear, and statistical parameters show a small deviation between them.

Vertical thermohaline structure was analyzed with the available *in situ* data give from Argo floats. Temperature and salinity profiles and also (T,S) diagrams was compared with the data. Global results for BIAS, RMSE, Pearson correlation coefficient and skewness (Table 1) have values very close and a global analysis shows that no significant differences between the two methodologies arises (skewness was computed for the series obtained with the difference between model results and data). However, the values of skewness parameter reflect that the simulation with geostrophic velocities is more consistent with data.

Notice that the lack of Mediterranean water in Mercator solution (Figure 7) avoids a good analysis of salinity results. The best statistical results were obtained for (T,S) diagrams (density results) showing that the simulation with geostrophic velocities initialization provides a better fit with data than the slow start initialization (the skewness is improved on 3%). In both simulations the correlation coefficient and the skewness results are very satisfactory. The skewness standard error is 0.28 for both distributions.

Figure 5. *One year comparison between Microwave SST and the results of the two simulations (also for Mercator solution): (a) Pearson correlation coefficient; (b) Bias; (c) Root mean square error.*

Better skewness results obtained with geostrophic initialization can be explained with the good fit on deep waters (below the Mediterranean water) that can be observed in almost (T,S) diagrams (Figure 7). The agreement of the solution with geostrophic initialization stresses the good approach of geostrophic velocities on deep waters region. Argo floats do not have the Labrador Sea Water (LSW) core but they represent quit well the transient region between Mediterranean waters and LSW. In the Bay of Biscay, the depth associated with those waters is located between 1500 m and 2000 m 88 [30]. Those water masses were detected in this area on 1993 with a core centered at 1700 dbar [31].

In order to get a relevant statistical analysis, results on different layers of 500 meters were compared. The salinity correlation coefficient for Mercator solution above 1500 meters takes values of the order of 0.5, showing that statistical conclusions cannot be achieved on those depths. Results for density in depths ranging between 1500-2000 meters (Table 2) shows that the simulation initialized with geostrophic velocities provide a better description of the vertical thermohaline structure relatively to the simulation with the slow start initialization.

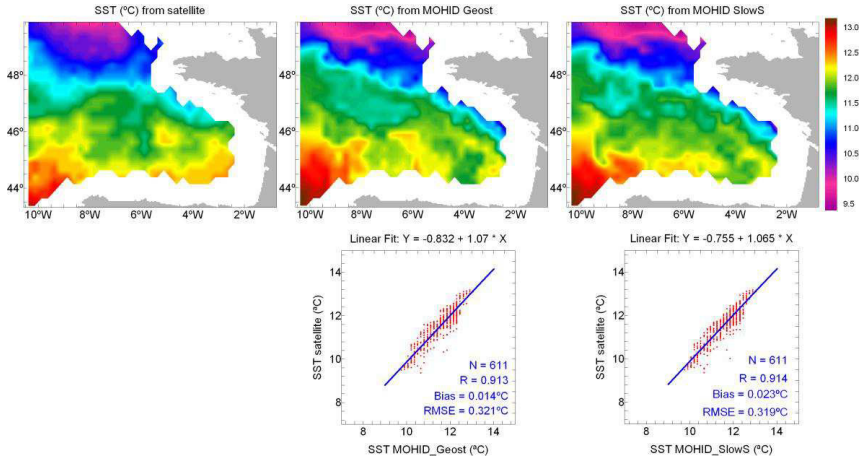

Figure 6. *Sea Surface temperature for the day 2004-03-15 from satellite, from model initialized with geostrophic velocities and slow start methodology.*

Table 1. *Annual statistical parameters computed for simulations and Mercator solution on Argo buoys.*

	Pearson correlation	Bias	RMSE	Skewness
Salinity				
Mercator solution	0.81	-0.078	0.15	-1.29
Geostrophic initialization	0.84	-0.077	0.14	-1.11
Slow start initialization	0.85	-0.076	0.14	-1.18
Temperature				
Mercator solution	0.98	-0.49	0.89	-0.31
Geostrophic initialization	0.98	-0.36	0.81	-0.66
Slow start initialization	0.98	-0.34	0.78	-0.75
Density				
Mercator solution	0.99	0.016	0.084	-0.85
Geostrophic initialization	0.99	-0.001	0.069	-0.38
Slow start initialization	0.99	-0.004	0.065	-0.39

Table 2. *Annual statistical parameters computed for simulations and Mercator solution on Argo buoys (results for density in a depth ranging between 1500-2000 meters).*

	Pearson correlation	Bias	RMSE
Mercator solution	0.839	0.027	0.028
Geostrophic initialization	0.847	0.001	0.016
Slow start initialization	0.826	0.000	0.019

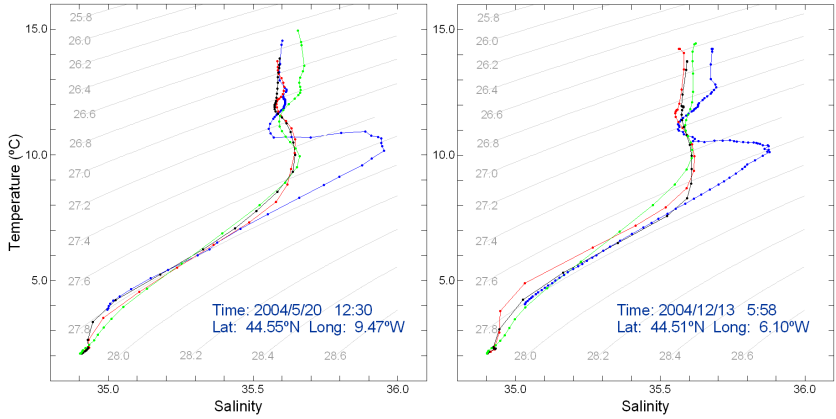

Figure 7. *(T,S) diagrams from: Argo floats (blue line); Mercator solution (green line); simulation with geostrophic initialization (black line); simulation with slow start initialization (red line). Sigma density isolines are represented (grey lines).*

4 CONCLUSIONS

In a downscaling methodology, the initialization with geostrophic velocities computed from the reference solution lead the model to a stable behaviour during the spin up period. The model starts from a dynamic state allowing an instantaneous switch on of all the forcing terms associated with the reference solution. The comparison between model results and *in situ* data is very satisfactory suggesting that unrealistic transient processes associated with a crude interpolation/extrapolation do not have irreversible consequences on the model behaviour.

Comparing this alternative methodology with slow start initialization described in this paper, results show that the initialization with the geostrophic velocities avoids a decrease of kinetic energy and enstrophy during the spin up period. This difference is maintained during 1 year of simulation suggesting that the initial state of the model obtain with this method is nearest the true state.

Using the geostrophic velocities initialization, a significant correlation between total low-frequency kinetic energy and the wind speed was observed for the Bay of Biscay. This correlation seems to be compatible with the literature, and seem to be an advantage relatively to the initialization with slow start method.

This methodology is particularly important in deep zones leading to a good thermo-haline description of the deep waters. Results show that, on deep zones geostrophic velocity initialization improves the solution obtained with slow start methodology. The (T,S) diagrams indicates an hydrologic structure compatible with literature.

This affordable initialization approach has a very low computational cost relatively to variational methods, and leads the model to a near true initial state. Relatively to the slow start initialization, the spin up time is drastically reduced. Those arguments could be an advantage to use this methodology on operational Oceanography.

ACKNOWLEDGEMENTS

This work was carried out in the frame of INSEA program. The authors wish to thank Ramiro Neves, Guilhaume Rifflet, Rodrigo Fernandes and Nuno Vaz for their contributions during this work. A special thanks to Ricardo Lemos for helping us with statistical analysis.

REFERENCES

1. Leitão P., H. Coelho, A. Santos, R. Neves 2005. Modelling the main features of the algarve coastal circulation during july 2004: A downscaling approach. Journal of Atmospheric & Ocean Science. 10 (4): 421-462.
2. Auclair F., P. Marsaleix and C. Estournel, 2001. The penetration of the Northern Current over the Gulf of Lions (Mediterranean) as a downscaling problem. Oceanologica Acta. 24: 529–544.
3. Malanotte-Rizzoli P., R. E. Young, and D. B. Haidvogel, 1989: Initialization and data assimilation experiments with a primitive equation model. Dynamics of Atmospheres and Oceans. 13, 349–378.
4. Auclair F., S. Casitas and P. Marsaleix 2000. Application of an Inverse Method to Coastal Modeling. Journal of atmospheric and oceanic technology. 17: 1368-1391.
5. Woodgate R. A., and P. D. Killworth, 1997: The effects of assimilation on the physics of an ocean model. Part I: Theoretical model and barotropic results. Journal of atmospheric and oceanic technology. 14: 897–909.
6. Woodgate R. A., 1997: The effects of assimilation on the physics of an ocean model. Part II: Baroclinic identical-twin experiments. Journal of atmospheric and oceanic technology. 14: 910–924.
7. Marchesiello P., J. C. McWilliams and A. Shchepetkin 2001. Open boundary conditions for long-term integration of regional oceanic models. Ocean Modelling 3, 1-20.
8. Martinsen E.A., and H. Engedahl. 1987. Implementation and testing of a lateral boundary scheme as an open boundary condition in a barotropic ocean model. Coastal Engineering. 11, 603-627.
9. Flather R.A. 1976. A tidal model of the northwest European continental shelf. Memoires Societe Royale des Science de Liege. 6 (10), 141-164.
10. Coelho H., R. Neves, M. White, P. Leitão and A. Santos 2002. A model for ocean circulation on the Iberian coast. Journal of Marine Systems. 33: 153-179.
11. Gunson J. R. and P. Malanotte-Rizolli 1996. Assimilation studies of open-ocean flows .1. Estimation of initial and boundary conditions. Journal of Geophysical Research. 101, C12, 28457-28472.
12. De Mey, P., 1997: Data assimilation at the oceanic mesoscale: A review. Journal of the Meteorological Society of Japan. 75: 415–427.
13. Estournel C., X. Durrieu de Madron, P. Marsaleix, F. Auclair, C. Julliand and R. Vehil 2003. Observation and modeling of the winter coastal oceanic circulation in the gulf of Lion under wind influenced by the continental orography (FETCH experiment). Journal of Geophysical Research. 108, C3, 8059, doi:10.1029/2001JC000825.
14. Auclair F., C. Estournel, P. Marsaleix and I. Pairaud 2006. On Coastal ocean embedded modelling. Geophysical Research Letters. 33, L14602, poi:10.1029/2006GL026099.
15. Estournel C., F. Auclair, M. Lux, C. Nguyen and P. Marsaleix 2007. “Scale oriented” embedded modeling of the North-Western Mediterranean in the frame of MFSTEP. Ocean Science Discussions. 4: 145-187.
16. Vaz N., L. Fernandes, P.C. Leitão, J.M. Dias, R.Neves (this issue). The Tagus estuarine plume forced by freshwater inflow and wind.
17. Chippada S., C. Dawson, M. Wheeler, 1998. A Godonov-type finite volume method for the system of shallow water equations. Computer Methods in Applied Mechanics and Engineering. 151(01): 105-130.
18. Martins F., R. Neves, P.C. Leitão, and A. Silva (2001) 3D modeling in the Sado estuary using a new generic coordinate approach. Oceanologica Acta. 24, S51-S62.
19. Gould, J., and the Argo steering team, 2004: Argo profiling floats bring new era of in situ ocean observations. Eos Trans. AGU, 85(19), 185, doi:10.1029/2004EO190002.

20. Reynolds, R. W., N. A. Rayner, T. M. Smith, D. C. Strokes, and W. Wang, 2002: An improved in situ and satellite SST analysis for climate. Journal of Climate. 15, 1609-1625.
21. Vazquez-Cuervo, J., E. M. Armstrong, and A. Harris, 2004: The effect of aerosols and clouds on the retrieval of infrared sea surface temperature. Journal of Climate. 17: 3921-3933.
22. Caballero A., A. Pascual, G. Dibarboure an M. Espino 2008. Sea level and Eddy Kinetic Energy variability in the Bay of Biscay, inferred from satellite altimeter data. Journal of Marine Systems. 72: 116-134.
23. Koutsikopoulos, C. and B. Le Cann 1996. Physical processes and hydrological structures related to the Bay of Biscay anchovy. Scientia Marina. 60 (Supl. 2): 9-19.
24. Van Aken H. M. 2002. Surface currents in the Bay of Biscay as observed with drifters between 1995 and 1999. Deep-Sea Research I. 49: 1071–1086.
25. Lazure P., F. Dumas and C. Vrignaud 2008. Circulation on the Armorican shelf (Bay of Biscay) in autumn. Journal of Marine Systems. 72: 218-237.
26. Pingree R. D. and B. Le Cann 1989. Celtic and Armorican slope and shelf residual currents. Prog. Oceanog. 23: 303-338.
27. Pingree R. D. and B. Le Cann 1990. Structure strength and seasonality of the slope currents in the Bay of Biscay region. J. Mar biol. Ass. U.K. 70:857-855.
28. Friocourt, Y., B. Levier, S. S. Drijfhour and B. Blanke 2008. On the Dynamics of the Slope Current System along the West European Margin. Part I: Analytical Calculations and Numerical Simulations with Steady-State Forcing. Journal of Physical Oceanography. 38: 2597-2618.
29. Friocourt, Y., B. Levier, S. S. Drijfhour and B. Blanke 2008. On the Dynamics of the Slope Current System along the West European Margin. Part II: Analytical Calculations and Numerical Simulations with Seasonal Forcing. Journal of Physical Oceanography. 38: 2619-2638.
30. Friocourt, Y., B. Levier, S. Speich, B. Blanke and S. S. Drijfhour 2007. A regional numerical ocean model of the circulation in the Bay of Biscay. Journal of Geophysical Research. 112, C09008, doi:10.1029/2006JCC003935.
31. Fiuza A. F. G., M. Hamann, I. Âmbar, G. Diaz del Rio, N. Gonsález and J. M. Cabanas 1998. Water Masses and their circulation off western Ibéria during May 1993. Deep-Sea Research I. 45: 1127-1160.

DETERMINATION OF A SUBMARINE OUTFALL DISCHARGE LOCATION BASED ON A 3D HYDRODYNAMIC-LAGRANGIAN HIGH RESOLUTION MODEL IMPLEMENTED FOR THE RÍO DE LA PLATA IN SOUTH AMERICA

M. Fossati • M. Fernández • I. Piedra-Cueva

CHAPTER SYNOPSIS

Background
Waste water treatment and the disposal of its residuals is one of the most important aspects of coastal management. The usage of preliminary waste-water treatment plants and subsequent ocean disposal via submarine outfalls for domestic sewage is one option that needs to be carefully studied. In this chapter, the evaluation of different alternatives of sewage disposal through submarine outfalls for the city of Montevideo is presented. Different outfall locations, lengths, and geometries were modelled using two models; a 3D-hydrodynamic-baroclinic model and a lagrangian tracer transport model that simulates the movement of the submarine discharge plume.

Results
The hydrodynamic model was implemented using a nested domain approach with four 3D grids of increasing horizontal resolution. The particles evolution was simulated in a high resolution grid. A net of control boxes was defined to evaluate the evolution of the plume in the coastal areas of interest, specially the beaches. Two submarine outfall locations for the projected discharge were evaluated. The numerical results were processed statistically in order to compare them with the standards of the local legislation for water quality.

Conclusions
The final result of the process is a submarine outfall design that verifies the economic and environmental requirements by minimizing the environmental impact.

1 INTRODUCTION

Uruguay's capital city, Montevideo, has one million and a half inhabitants. Along Montevideo's coast there are several beaches that are visited by the city's residents and tourists during the summer. Over the last few years an improvement plan for the sewage systems of Montevideo has been under study. Since the 1990's a first submarine outfall exists in the area covering the main part of the city (the *Punta Carretas* outfall). Nevertheless the city's growth has required the planning and design of a second submarine outfall.

Montevideo's municipality requested the Institute of Fluid Mechanics and Environmental Engineering (IMFIA) to undertake an evaluation of different discharge alternatives based on the use of numerical models. In this chapter, the methodology and main results of these studies are presented. Different outfall locations, lengths, and geometries were modelled using two models; a 3D-hydrodynamic-baroclinic model and a lagrangian tracer transport model. These models were applied in the coastal zone of Montevideo obtaining the temporal variation of currents, water levels, salinity, and concentration of the discharged substance at every point of the analyzed domain. The numerical results were processed statistically and compared with the standards of the local water quality regulation. Following this methodology, a submarine outfall design that verifies the economic and environmental requirements by minimizing environmental impacts, was obtained.

The numerical model used in this study was the MOHID, a three-dimensional water modelling system developed by MARETEC - IST (Marine and Environmental Technology Research Center - Instituto Superior Técnico), from the Technical University of Lisbon. During the last few years several modelling studies in the Río de la Plata River and the Atlantic Ocean have been done using the MOHID [1, 2].

In this book chapter we present the main characteristics of the modelling study developed in order to solve the management issue of sewage disposal in the sea water. The characterization of the study area, the main tasks for the implementation of the model, the overall and site specific methodology applied, and finally the results are showed. In addition to the long history of MOHID's successful applications to oceanic, coastal, lagoons, and estuarine waters and previous applications in Río de la Plata [1, 2], this model was selected mainly for its capacity to integrate the near and the far field solutions for a submarine jet discharge. Also, due to the big area and high resolution requirements the nested domain approach included in the MOHID system was a determining factor in order to capture the dynamics of the submarine outfall discharge plume in an affordable CPU time.

The design of Montevideo's outfall discharge is presented here. The study was made during the 2008 year. The same methodology and base tools were used for the design of the other submarine discharge in Uruguay (Punta del Este city). Nowadays the outfall discharge for Punta del Este is in construction and in the next year the construction of the new submarine outfall for Montevideo will start. Both designs were developed considering the environmental results obtained in this modelling study.

2 THE STUDY AREA

Uruguay is located in the east coast of South America between Argentina and Brazil. It has an area of 176,215 km^2 and a population of 3.46 million. To the southwest, in the border with Argentina, lies the estuary of Río de la Plata. This water body is located between 34°00' - 36°10' South latitude and 55°00' - 58°10' West longitude, and has the second largest basin of South America (3,170,000 km^2) after the Amazonic (Figure 1, left panel).

The flow dynamic in the Río de la Plata and adjacent Atlantic Ocean is very complex due to the topographic variation of the river (Figure 1, right panel) and the influence of continental flows, astronomical and meteorological tides coming from the ocean, and the local winds. The Río de la Plata behaves as a micro-tidal estuary in the central zone, i.e. the river level variations produced by astronomical tides are much lower than those generated by the wind action and oceanic waves. The Paraná and Uruguay rivers provide more than 97% of the continental water inlet with an annual mean flow of 22,000 $m^3\ s^{-1}$ [3]. The fresh water mixes with the oceanic water creating a zone of brackish waters. Montevideo is located at the central estuarine zone of the Río de la Plata river where the salinity shows significant seasonal fluctuations [4].

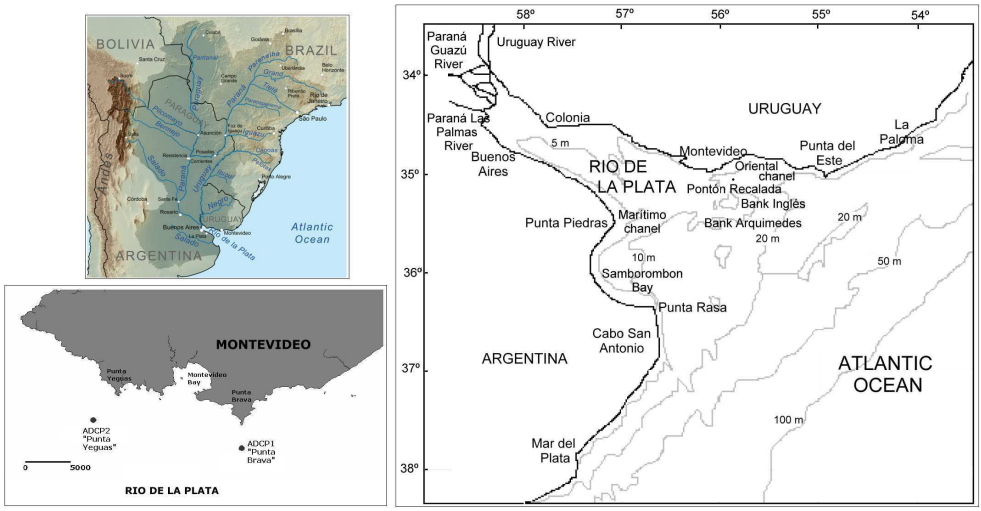

Figure 1. *Río de la Plata and Montevideo city location and morphology.*

3 NUMERICAL MODELS

3.1 Hydrodynamic model implementation

In order to capture the dynamics of the submarine outfall discharge plume in an affordable CPU time, the hydrodynamic model was implemented using a nested domain approach. A system of four rotated 3D grids of increasing horizontal resolution was defined to describe the system. We used Cartesian coordinates in the horizontal direction with the x direction, following the axis of the river (almost southeast). Sigma coordinates with 10 layers equally spaced were used in all nested levels in order to obtain an adequate representation of turbulence in vertical.

The computational domain is shown in Figure 2, left panel. The larger domain has been extended in the oceanic limit in order to avoid boundary effects inside the Río de la Plata area. The study area is approximately of 250,000 km^2, bounded by the city of Mar del Plata to the South, the coast of Brazil to the North, the continental shelf to the East, and Uruguay and Paraná rivers to the West. The open boundary extends into the continental shelf to approximately the 2,000 m isobath and approximately 350 km from the coastal points. The alignment of the South and North oceanic boundaries is perpendicular to the coast and follows the continental shelf slope. This alignment simplifies numerically the income of the astronomical and meteorological wave tides which travel northward along the coast of Argentina entering the estuary from the South. On the other hand, the offshore boundary is almost parallel to the continental shelf avoiding strong bathymetry gradients along the model limit.

The first level of nested grid corresponds to the largest domain with a regular grid of 5,941 active cells. The resolution in both x and y directions is 5 km in the fluvial and estuary zone and 9 km in the oceanic zone (Figure 2, right panel). The second level focuses on the estuarine

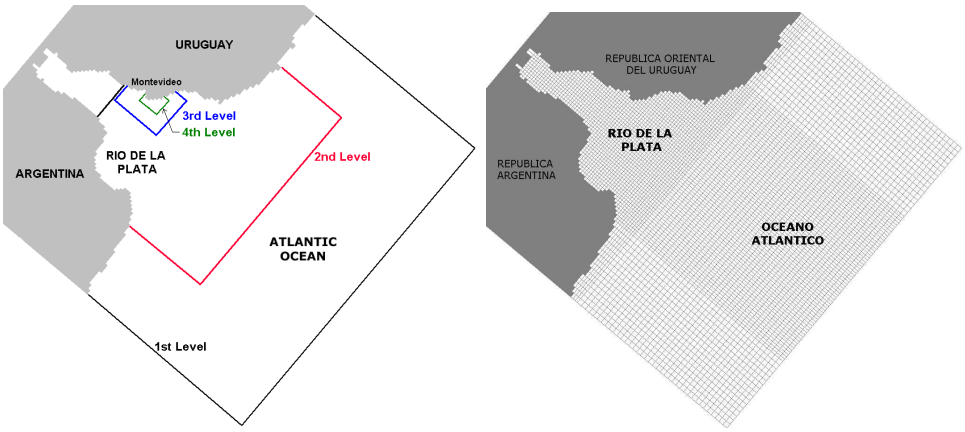

Figure 2. *Domains of the 4 resolution levels (left panel) and grid of the first level (right panel).*

zone of the Río de la Plata in an area of approximately 92,000 km^2. The South boundary has an extension of 163 km and the North boundary has an extension of 137 km from the coastal points. The horizontal grid is uniform with a grid cell of 2 km generating a total of 22,978 active cells. The third and fourth levels defined in this exercise are focused in Montevideo's coastal zone, covering an area of 5,100 km^2 and 900 km^2 approximately, respectively. Both are uniform grids with 1 km and 100 m grid size in both directions. The total number of active cells is 5,166 and 90,000 respectively.

The bathymetry was generated using mapping information from nautical charts for the Río de la Plata and the continental shelf. Figure 3 shows bathymetry in the first and four levels. The coastal zone of Montevideo includes approximately 13 km with several sandy beaches and a big bay (Montevideo's Bay) covering an area of 12 km^2 and navigation channels. Navigation channels are about 11 m deep, the rest of the area is 8 m deep with a slow slope shoreward. The hydrodynamic model was calibrated and validated considering the main forces: fresh water flow, astronomical and meteorological tides in the oceanic boundary, and wind acting on the ocean surface.

The boundary conditions are specified for the open ocean, the place of discharge of the major tributaries, and the free surface. The water surface elevation was specified for the ocean open boundary condition. The surface elevation results from the addition of astronomical oscillations and non-astronomical oscillations due to meteorological effects. The astronomical oscillations at the open boundary were obtained from the FES2000 astronomical tide atlas and correspond to the overlap of the main harmonic components M2, O1, Q1, N2, and S2 for the selected time period. The non-astronomical oscillations were calculated as the difference between measured and astronomical hourly levels at two coastal stations, Mar del Plata and La Paloma (Figure 3). To extend the water level series information to the entire ocean boundary, an interpolating strategy was used and validated. Density in the area is controlled by salinity [5] so only salinity variations are considered in the density equation of state. The free

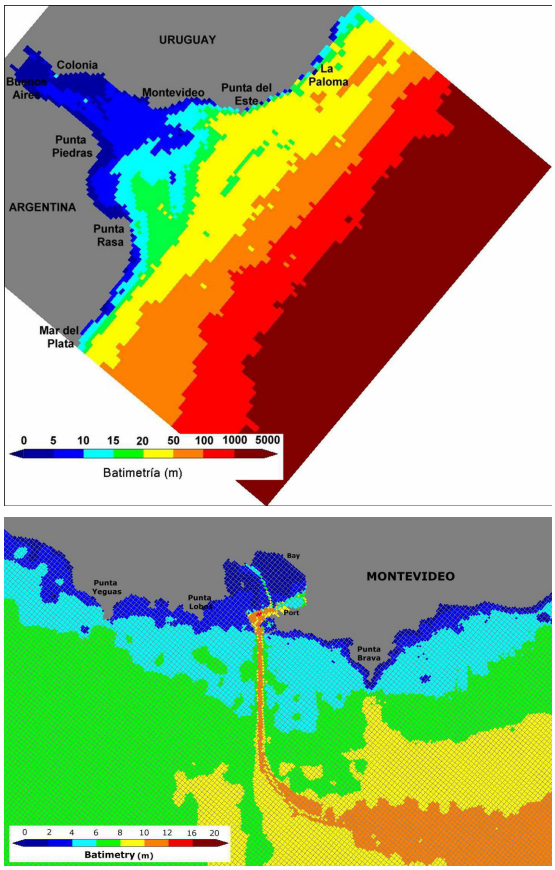

Figure 3. *Bathymetry of the first (left panel) and four (right panel) level.*

surface wind effect was included using measurements from the area (Montevideo). In this way the wind effect was considered time varying but uniform in space. A constant salinity value of 38 ppt was imposed in the ocean boundary. The characteristics of the hydrodynamic model implementation are presented in Table 1.

The initial condition in the first nested model is a hot start solution obtained by spinning up the model through six months run forced by freshwater river runoff and astronomical tide with a constant salinity value at its open ocean boundary. During this simulation the salinity field is generated. The lateral boundary condition at coastal boundaries is a free slip condition, imposed by specifying a zero normal component of mass and momentum diffusive fluxes at cell faces in contact with land. No fluxes at the surface and bottom were considered. The initial conditions in the second, third, and fourth nested models were interpolated from the previous level. The flow and salinity boundary conditions are interpolations of the calculation obtained in the previous level. The wind is also added in each level as an external forcing on the free surface.

Table 1. *Characteristics of the hydrodynamic nested models.*

Resolution Level	Domain Area (km^2)	Spatial Resolution (m)	Time step (s)	Boundary Conditions
1^{st} level	250,000	3000 to 9000	40	Continental, Freshwater discharge Open boundary, Astronomical and Meteorological tide Free surfasse, Uniform wind
2^{nd} level	92,000	2000	20	Open boundary, U, V and S from 1^{st} level solution Free surfasse, Uniform wind
3^{rd} level	5100	1000	10	Open boundary, U, V and S from 2^{nd} level solution Free surfasse, Uniform wind
4^{th} level	900	100	5	Open boundary, U, V and S from 2^{nd} level solution Free surfasse, Uniform wind

This study was performed with the 4.9 MOHID parallel version using a computer with 4 processors and a 4GB memory ram. The parallelized code allows running the 4 nested models simultaneously, each one in one processor with a restriction in the time interval relations. Since the time interval for any nested model has to be a submultiple of the previous grid level, the time intervals for the final configuration were 40 sec, 20 sec, 10 sec, and 5 sec for the first, second, third, and four nested grid respectively.

3.2 Calibration and Validation

In previous studies [1] the hydrodynamic model MOHID was implemented to solve the main dynamic at the Río de la Plata and the adjacent Atlantic Ocean using only one grid for the entire domain (the first level described before). Thus the main calibration parameters (bed roughness, wind stress, horizontal and vertical turbulence schemes) were determined. During this calibration-validation process the same parameters were defined as start parameters in all nested levels and the model results were controlled in comparison with data mainly from the coastal zone of Montevideo. January and March of 2004 were used as periods of calibration and validation respectively.

In Figure 4, upper panel, the comparison between the measured water level elevation in Montevideo's costal station and the modelled water level elevation obtained in the 3rd nested grid for January 2004 is presented. The model correctly follows the main variability of water level reproducing the low waters (as in day 20) and the high waters (day 15).

The currents in the model were controlled using currents measurements with two 1200 kHz ADCPs of the Teledyne RD Instruments Company (called Punta Brava and Punta Yeguas) located approximately 3,500 m away from Montevideo's coast (Figure 1, lower panel). The equipment was installed specially for these submarine outfall study and the data was analyzed to improve the coastal zone circulation knowledge [6]. The Punta Brava ADCP was programmed to collect current intensity and direction with a vertical resolution of 0.35 m and the Punta Yeguas with 0.5 m. Both ADCPs collected data every 30 minutes. Figure 5, upper panel, shows the measured and modelled currents in bottom, mid depth, and surface at Punta Brava station during the first eight days of January 2004. The model correctly reproduced the main direction and intensity of the measured currents in PB.

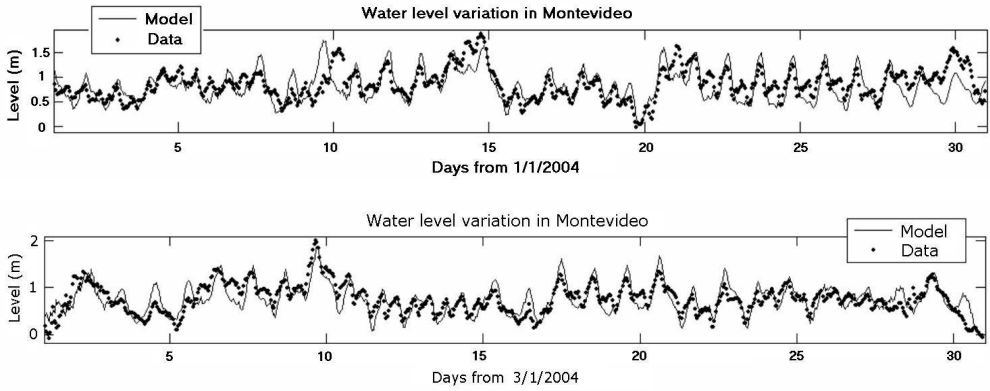

Figure 4. *Water level modelled and measured in Montevideo station. January 2004 (upper panel) and March 2004 (lower panel).*

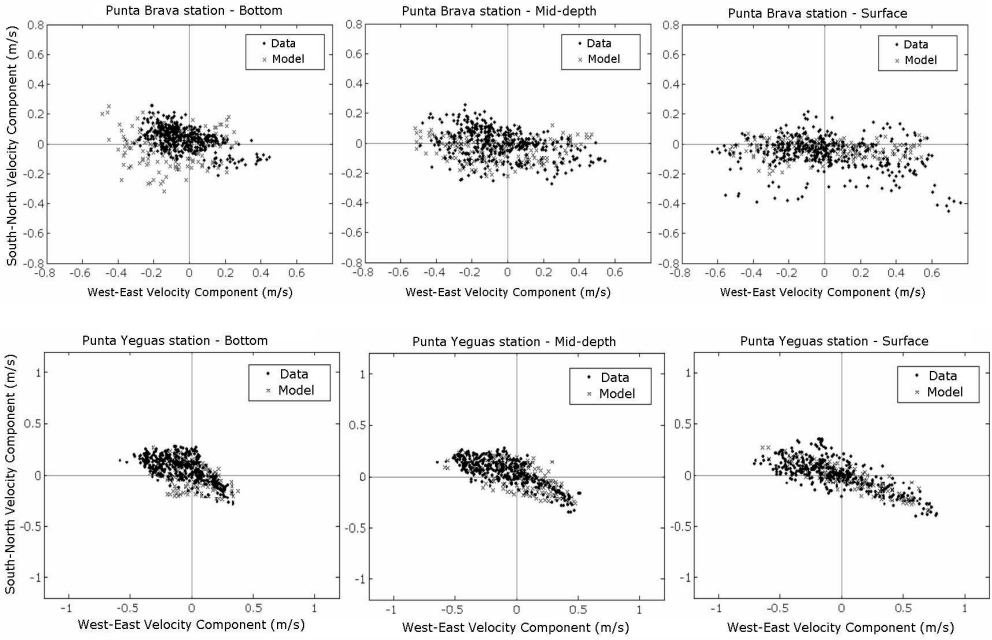

Figure 5. *Comparison of measured and modelled currents at bottom, mid-depth, and surface. Period from 1/1/2004 to 1/8/2004 at Punta Brava station (upper panel) and period from 3/11/2004 to 3/18/2004 at Punta Yeguas station.*

The obtained results for the validation period March 2004 are presented in Figures 4 and 5, lower panels. The water level series reproduced by the model in Montevideo show the same fluctuations (in amplitude and phase) as the measured water level elevation. The comparison between the measured and modelled currents in bottom, mid depth, and surface at Punta Yeguas station show that the model represents the main measured currents behavior.

The hydrodynamic simulation of a relevant period of time, representative of the average conditions of flow, was made in order to be used on the submarine outfall studied. A period of 53 days during the summer of 2004 (27 December 2003 to 17 February 2004) was simulated using the four nested levels in order to represent the conditions of use of the beaches. These are the most restrictive conditions due to water temperature and the duration of the sunlight.

3.3 The lagrangian model

In order to analyze the disposal alternatives and evaluate their potential impacts, the water quality module of MOHID was used. Lagrangian transport models are very useful to simulate localized processes with sharp gradients, as it is the case of submarine outfalls. The lagrangian transport module of the MOHID simulates the movement of the plume generated by a permanent discharge of polluted particles using the currents fields calculated with the hydrodynamic module. The near field model (MOHIDJET) was used to simulate the dynamic of the plume close to the discharge.

In this implementation the discharged particles are modelled as passive substances and therefore they do not affect the currents field or the density of the receiving water body. The discharged substance is faecal coliform and the processes included in the far field evolution are advection, diffusion, and bacterial natural decay. The particles evolution was simulated in the grid detail level (high resolution grid centered in the zone of the discharge). The limits of the high resolution grid are defined reasonably far from the point of discharge in order to guarantee mass conservation of the discharged pollutant. The currents, water levels and salinity field were used in the calculation of the pollutant evolution.

In addition to Montevideo's future submarine discharge, the existing coastal submarine outfall must be included in the simulations. In this way two points of discharge were defined in each simulation and the particles coming from each outfall were followed to identify the source of contamination for each beach.

One of the most relevant processes involved in the evolution of a pollutant discharged in a water body is the bacterial decay rate with is represented by the T90 (time for a 90% decay in concentration). A formulation that integrates salinity, temperature, and solar radiation is used to calculate the T90 [6]. This formulation was calibrated by adjusting the minimum daily (20 hours) and the maximum daily (72 hours) value of T90 for Montevideo's coastal zone. Instead of the bacterial decay rate, the advection and diffusion of the discharged substance controlled the evolution of the plume. The advection process is related with the main flow (calculate in the hydrodynamic model). The diffusion process is related to the turbulent movement in two different scales: eddies larger than the particles and eddies smaller than the particles. In the simplification used in the model the turbulent flow component is represented proportional to the mean flow with a coefficient. In this way the proportional coefficient represents the

turbulence intensity of the flow. Because there are no measurements of pollutants dispersion for Montevideo's coastal zone, a value of 20% was supposed for the turbulence intensity. In order to guaranty the quality of the final solution at the end of the study, a sensibility analysis to these parameters was made.

4 SUBMARINE OUTFALL LOCATION STUDY

4.1 Methodology

Firstly, the simulation of two alternatives for disposal was carried out (Figure 6) using the lagrangian transport model that reads the current fields obtained with the hydrodynamic model. Both alternatives have a length of 2,000 m with different alignments, North - South for the first alternative (called PY2000 alternative), and 41° to westward from the North-South alignment for the second alternative (called PY2000W alternative). The average water depth is 7 m for both locations. The existing outfall discharge of Montevideo, called Punta Carretas, was included in the simulation in order to represent the combined effect in the city beaches (Figure 6). However, the model can determine the source of the contaminant at each beach for the processing and analysis.

A preliminary diffuser design (Figure 7) was defined to simulate the submarine discharge: 200 m of diffuser with 40 horizontal (α=0 in Figure 7) 0.2 m diameter ports aligned with the main pipe (β=0 in Figure 7) and discharging in single ports at 1.5 m of the bottom. The effluent characteristics defined for the year 2050, for the projected submarine outfall, are 2.89 m s^{-1} of flow rate and 10^7 UFC/100ml of faecal coliform concentration. The flow rate value for the existing Punta Carretas submarine outfall implemented in the model is 3.29 m s^{-1} with the same faecal coliform concentration. In order to analyze the results of the plume dispersion model, a net of monitoring boxes was defined in the bathing beaches (Figure 6). These boxes include several grid cells in the horizontal plane and 10 layers in the vertical direction. Every instant, the model computes the concentration of faecal coliforms in each box. Using this information, the concentration of pollutant frequency curve was calculated for every beach.

The model results should be compared with the water quality standard for recreational proposes. There is wide range of criterion when it comes to water quality standards [7]. The local legislation on water quality of beaches uses a classification based on the geometric average of 5 samples of faecal coliform concentration (MG5) extracted daily from the beach.

The legislation defines the following categories: excellent (MG5 $<$ 250 UFC/100ml), very good (250 UFC/100ml $<$ MG5 $<$ 500 UFC/100ml), barely acceptable (500 UFC/100ml $<$ MG5 $<$ 1000 UFC/100ml), and not acceptable water quality for recreational purposes (MG5 $>$ 1000 UFC/100ml). Considering this normative, the requirement for the chosen alternative will be to, at least, fall in the very good quality category for all the beaches. From the modelled results, the beach water quality category was defined using the following methodology. First, a daily coliform concentration for each beach is calculated by finding the average of model results between the hours when the beach is in use, from 8am until 8pm. Second, the MG5 for the entire period is calculated, obtaining a number of 48 MG5 values for each beach, for the 53 days of the simulation. Finally, the value corresponding to the 95% limit, taken from the frequency curve, is the final value which is compared with the normative.

Figure 6. *Monitoring boxes representing the beaches and location of the outfalls discharges.*

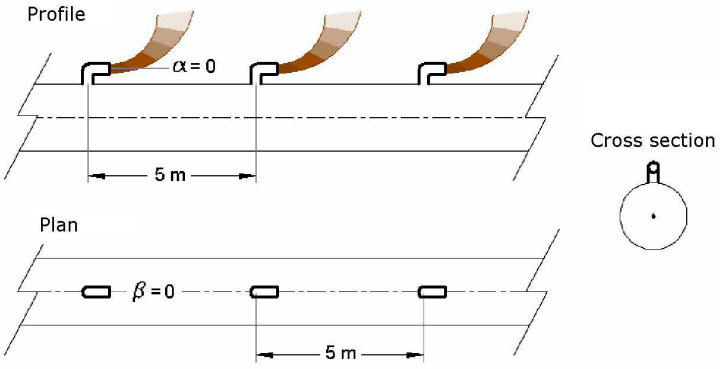

Figure 7. *Plan view, profile and cross section of the preliminary diffuser design.*

5 RESULTS AND DISCUSSION

The main results after the simulation of the two alternatives for the new outfall discharge was that both alternatives, PY2000 and PY2000W, meet the quality criteria imposed on the new outfall. This means that the 10 controlled beaches would be classified as very good quality beaches for bathing if the outfall is built. Nevertheless, the interaction of the new outfall plume with the plume of the existing outfall of Punta Carretas is lower for the PY2000W alternative. Also, the mean initial dilution obtained for the PY2000W alternative (60) is greater than the obtained for the PY2000 alternative (40), due to more intense currents in the PY2000W discharge location.

Figures 8, 9, and 10 show examples of the results obtained from the outfall location analysis. Figure 10 presents the outfalls plumes obtained with the lagrangian transport model for one particular instant (PY2000W alternative). It is possible to see that the location of the

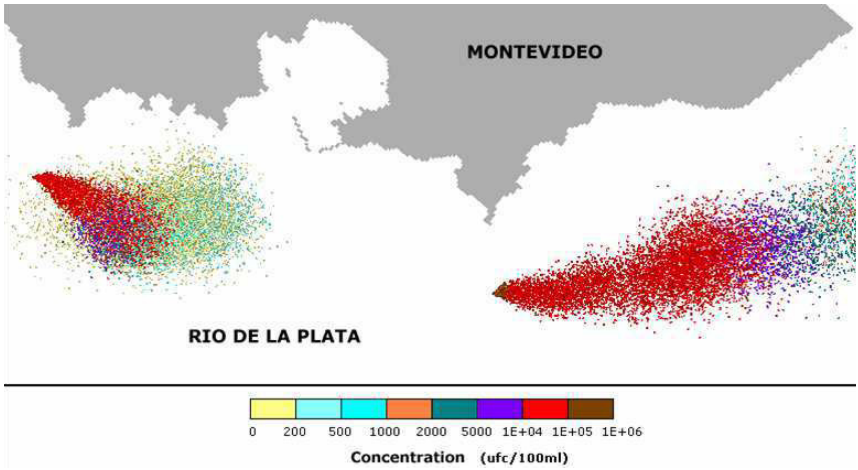

Figure 8. *Example of the result obtained with the lagrangian transport model for one instant. PW2000W alternative discharge.*

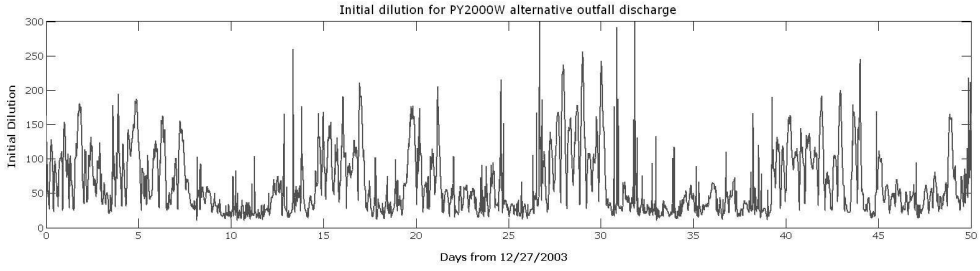

Figure 9. *Initial dilution time series for the PY2000W alternative.*

discharged particles for both outfalls follow a seaward current flow. Figure 11 shows the initial dilution time series obtained with the MOHIDJET model for the PY2000W alternative. Finally, Figure 10 shows the coliform concentration time series obtained for the Santa Catalina beach generated by both alternatives PY2000W and PY2000. The fluctuation between non zero concentration values with high concentration values responds directly to the main flow direction variation in Montevideo's coastal zone, from East to West and from West to East.

The presented comparison shows different levels of contamination in this beach with more affectation with the PY2000 alternative than the PY2000W alternative located farther to the beach than the previous one. For the same cause the PY2000W alternative generates more affectation in Pajas Blancas beach than the PY2000 alternative. In Punta Espinillo and La Colorada beaches both alternatives plumes arrive occasionally. In relation to the eastern beaches, neither PY2000 nor PY2000W discharges arrive to Pocitos, Malvin, Verde, and Carrasco beaches. Also, the PY2000W alternative discharge arrives occasionally at Cerro and Ramirez beach while PY2000 plume reaches these beaches several times.

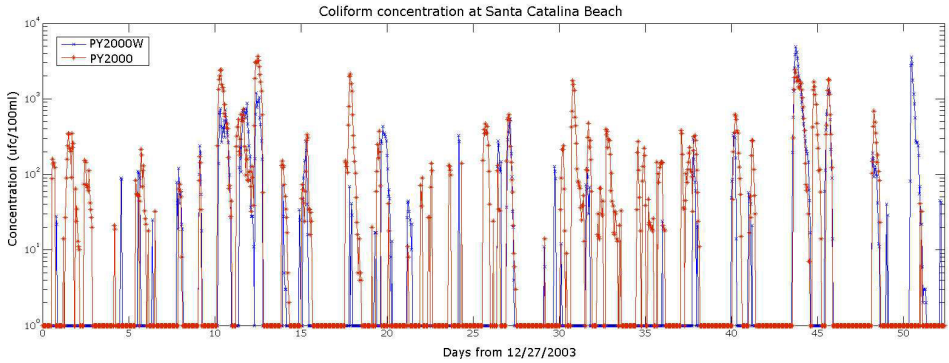

Figure 10. *Coliform concentration time series at Santa Catalina for the PY2000 and PY2000W alternatives discharges.*

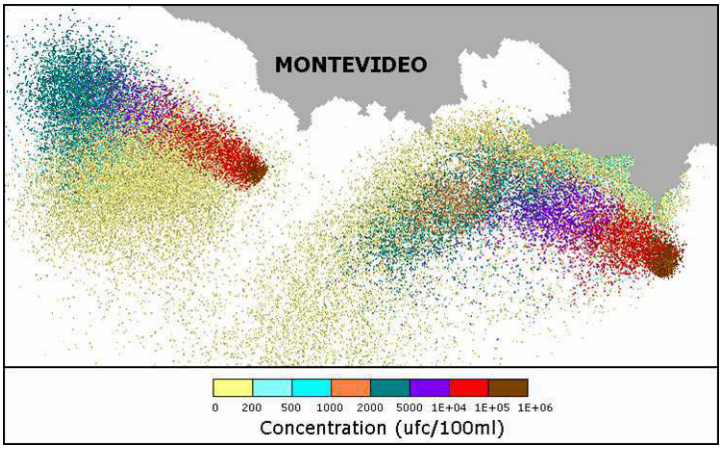

Figure 11. *Example of the result obtained with the lagrangian transport model for one instant at the sensitivity analysis. PW2500W alternative discharge.*

A sensitivity analysis of the model results to the assumed lagrangian model parameters was made. It is a recommended practice when we based the results in assumed parameters. Both alternative options, PY2000 and PY2000W, were analyzed with a turbulence intensity of 40% representing more substance diffusion than the original study and consequently a more exigent condition for the design. The results show higher particle dispersion everywhere when compared to the normal dispersion conditions presented before.

The obtained results show that the PY2000W, in extreme conditions, will affect more the coast than the PY2000 alternative. Finally, the possibility of a larger length, 2500 meters, was evaluated in both alignments (PY2500W and PY2500) using only the extreme dispersion conditions (Figure 11). The beaches quality classification obtained for both alternatives are

equal to the corresponding discharge in a 2000 m. This means that the elevation of the cost resulting in an increase in the length of discharge is not worth from an environmental point of view.

6 CONCLUSIONS

The final disposal of wastewater in coastal zones is a solution frequently implemented by developing countries. To design this type of solutions several aspects need to be considered. One of these aspects is the water body assimilative capacity for receiving the discharge without affecting other uses of the water body on the area. In this work a lagrangian tracer transport model has been used based on the current fields previously calculated with a 3D hydrodynamic model and the near field calculated with a jet plume model. The numerical results were processed statistically in order to evaluate different sewage disposal alternatives considering the standards of the local water quality regulation.

The progress made on computer resources and numerical tools as the MOHID model makes it possible to analyze different solutions for this problem in an integrated way. Moreover, this approach provides elements that are important when making decisions, minimizing the environmental impact. The good results obtained in these studies validate the used methodology and show us the value and great utility of these numerical tools for use in similar projects.

ACKNOWLEDGEMENTS

The authors wish to acknowledge the support of the entire MOHID engineering team, the economic support provided by the Uruguayan Government especially by the Montevideo's Municipality and the data provided by the Argentinean and Uruguayan Oceanographic Services (SHN and SOHMA)

REFERENCES

1. M. Fossati and I. Piedra-Cueva, "Modelacion tridimensional de la circulacion en el rio de la plata," in *XXII Congreso Latinoamericano de Hidraulica*, 2006.

2. P. Santoro, M. Fernandez, M. Fossati, G. Cazes, R. Terra, and I. Piedra-Cueva, "Pre-operational forecasting of sea level height for the rio de la plata," *Applied Mathematical Modelling*, vol. 35, no. 5, pp. 2462–2478, 2011.

3. I. Piedra-Cueva and M. Fossati, "Residual currents and corridor of flow in the rio de la plata," *Applied Mathematical Modelling*, vol. 31, pp. 564–577, 2007.

4. M. Fossati and I. Piedra-Cueva, "Numerical modelling of residual flow and salinity in the rio de la plata," *Applied Mathematical Modelling*, vol. 32, no. 6, pp. 1066–1086, 2008.

5. R. Guerrero, M. Acha, M. Framinan, and C. Lasta, "Physical oceanography of the rio de la plata estuary," *Continental Shelf Research*, vol. 17, no. 7, pp. 727–742, 1997.

6. M. Fossati, D. Bellon, E. Lorenzo, and I. Piedra-Cueva, "Currents measurements in the coast of montevideo, uruguay," in *RCEM 2009 Proceedings. River, Coastal and Estuarine Morphodynamics*, 2009.

7. H. Salas, "History and application of microbiological water quality standards in the marine environment," *Water Science and Technology*, vol. 18, no. 11, pp. 47–57, 1986.

FAECAL POLLUTION MODELLING AS A MANAGEMENT TOOL IN COASTAL AREAS: A CASE STUDY IN ESTORIL, PORTUGAL

M. Mateus • P. Pina • H. Coelho • R. Neves • P. C. Leitão

CHAPTER SYNOPSIS

Background
Over the last decade a considerable investment has been made in the major bathing area of the Estoril coast (Portugal) to mitigate feacal pollution and to achieve compliance with the mandatory standards of the EC Bathing Water Directive. This chapter reports a study made in 2004 combining hydrodynamic, numerical drogues dispersion and *Escherichia coli* (E. coli) decay modelling techniques. Validated with field data this work aimed at identifying a potential source of pollution of the bathing water of Torre beach, where high counts of faecal indicators have occasionally been reported.

Results
Results show that hydrodynamic processes govern the distribution of contaminants in the receiving area and that its abundance is also strongly influenced by light. The modelling approach was able to provide evidences of the impact of a punctual source of contamination on the surrounding bathing areas.

Conclusions
The study reported here has lead to the eradication of the pollution source and subsequent improvement of local water quality, leading to the classification of St. Amaro Beach (Oeiras Bay) as a bathing area.

1 SEWAGE DISPOSAL IN COASTAL AREAS

The discharge of untreated or partially treated sewage effluents into coastal areas has been a common practice in many developing countries for some decades now. In European countries, especially those facing inner sea or limited water supplies, the pollution of water systems is a steadily growing challenge because it poses a threat to human health and has major socio-economic impacts. Concern about the effects on the quality of such water bodies have, therefore, become a major issue is coastal management.

The ability to quantitatively relate waste loads with temporal and spatial changes in the receiving water body is a requirement for reliable decisions to achieve specific water quality objectives. And these relationships are quite sensitive to natural environment conditions. As for the persistence of faecal indicator bacteria, studies have revealed a number of environmental parameters, especially solar radiation, salinity, and temperature, that cause their declining [1–4].

The use of numerical models to assess pollution effects caused by sewage discharge has become widespread [5–10]. The residence time of faecal contaminating agents is very low when compared to other pollutants, usually ranging from less than an hour to some dozens of it, and occasionally up to some days [1]. The short life span of these organisms outside their hosts imposes limitations to their spread in the water, even under intense hydrodynamic regime. Nevertheless, their potential to compromise water quality standards in bathing areas must be assess, with numerical models playing a significant role in this process.

This chapter reports on a case study that goes back to 2003, where the application of such a model was required. The study was prompted to evaluate the hypothesis of a brook (Ribeira da Lage) being a possible cause of water contamination in one particular beach (Torre beach, Fig. 1), characterized by an irregular water quality record in routine analysis.

Achieving this goal has required the integration of experimental work (to test the adequateness of feacal decay models), field work (several campaigns and monitoring programs) and modelling studies. The experimental work lead to the choice of an algorithm for E. coli decay in the water available in the literature. This algorithm, in turn, was programmed into MOHID allowing coupling of hydrodynamic models with a dynamic T90 decay model for E. coli.

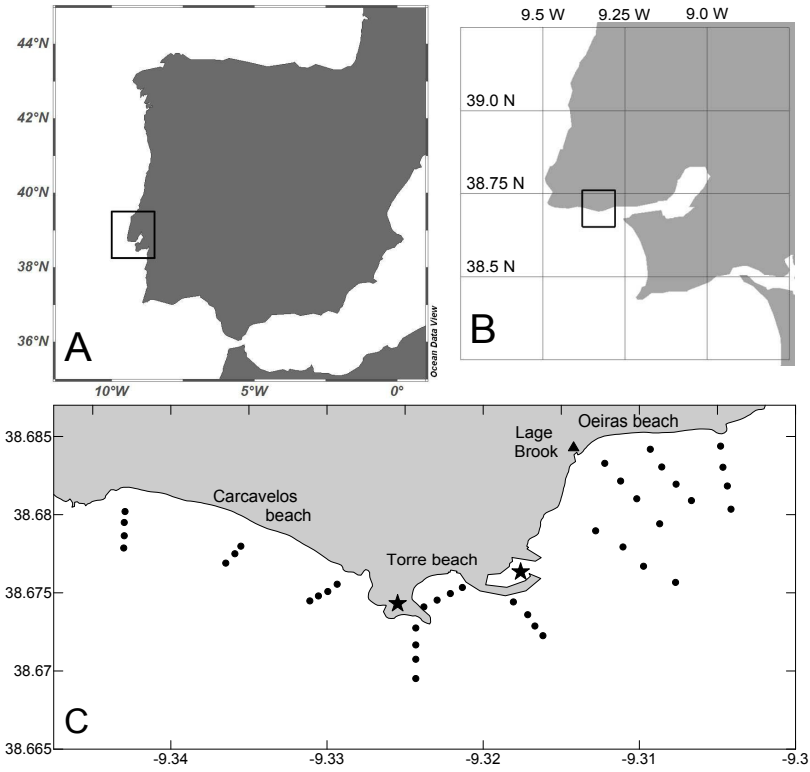

Figure 1. *Location of the study area and stations (dots) monitored during the campaigns undertaken in May (2004). The system is located near the Tagus estuary, one of the biggest estuaries in Iberia (A), on the western side of the estuary mouth (B). Estoril cost extends for another 20 km northwest ward. Two structures set the limit to the Torre beach (C), namely, an old fort on the left and a marina on the right side (marked with stars).*

2 THE STUDY AREA

The study site is located in the Estoril coast near Tagus estuary in Lisbon, Portugal (Fig. 1). Since this is a popular vacation site during summer months, improvements in water quality have been a major concern in order to minimize public health risks. The goal has been to ensure that contamination levels achieve compliance with Directive (76/160/EEC) Imperative standards for bathing water quality in all the beaches along the Estoril coast. The Estoril coast has suffered significant intervention since mid-1990, mostly related to the identification and eradication of point sources. By the time this study was made there were no treated effluents of wastewater treatment plants in the area or any other identified source of feacal pollution.

The Estoril coast line has a complex morphology, characterized by several piers, bays, rocky and sandy beaches. Water circulation patterns are largely determined by the coast orientation and its irregular pattern, where sandy bays are interrupted by rocky geological structures. The Torre beach (Fig. 1) is located near the mouth of Tagus River, in an area where flow velocities usually reach higher values. The hydrodynamic regime is very complex with tidal meandering currents and eddies in the near coastal section. Previous field studies using current meters and Acoustic Doppler Current Profiler equipment revealed that off the coast of Carcavelos beach (west of Torre beach) starts an eddy formation in mid ebb that grows to the size of almost all Estoril coast in low tide. To the east of Torre beach, in Oeiras beach, several eddies form both during ebb and flood. A schematic representation with the general circulation pattern of the studied area is shown in Figure 2.

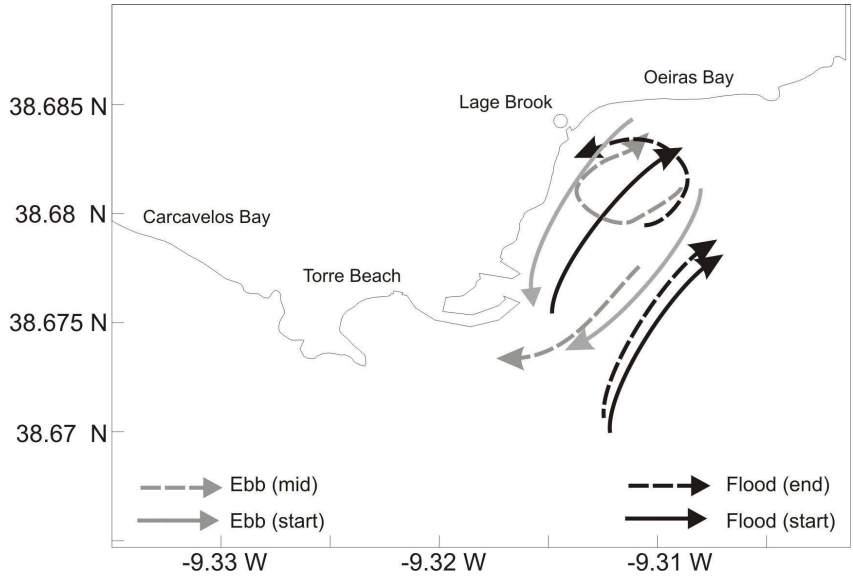

Figure 2. *Major circulation patterns in the study area. Arrows are used to illustrate the general circulation pattern and do not quantify the intensity of currents. Dashed arrows show the direction of eddies formed during ebb and flood start.*

The Lage brook, located at the west end of Oeiras beach (marked as a triangle in Fig. 1), was a known source of faecal contamination based on earlier water quality analysis. It drains from a relatively large watershed, where clandestine domestic sewage discharge were known to occur, but the flow regime during spring and summer is low ($\sim$0.04 $m^3 s^{-1}$). The dynamic dispersion of its plume is mostly controlled by the eddy rotation. Torre beach is a small bay between two man-made structures: a marina pier and the surrounding walls of a fort (marked as stars in Fig. 1). The local circulation in this small area consists, basically, of a continuous recirculation, with significant tidal differences. These were induced by a small eddy resulting from the interaction of currents along the coast and the water mass located inside the small bay. The recirculation pattern inside the bay tends to prevent outside water to reach the beach, thus lessening the water renovation in it.

EXPERIMENTAL AND FIELD WORK

2.1 Experimental faecal decay test

A review of the literature available at the time was performed to evaluate faecal decay algorithms derived in situ and laboratory studies of mortality rates of E. coli. Among the models that were found we have selected two based on their adequacy to the nature of our study. For simplicity the algorithms are referred to by the name of their authors, namely Canteras et al [11] and Chapra [12]. Both models considered the decay of E. coli as a function of water temperature, salinity and light radiation.

Laboratory experiments were realized to evaluate the response of both algorithms, according to the methodology proposed by other authors in similar studies [13,14]. Starting with known concentrations of E. coli and salinity, several water samples were exposed to different levels of light radiation and temperature. The results obtained in the laboratory essays were then compared with each algorithm prediction to determine which reproduced the observations more accurately. The outcome of these experiments led to the choice of the Canteras et al algorithm for our study.

2.2 Water sampling strategy

The monitoring program to assess the water quality in Torre beach had the duration of 10 weeks (13 May to 15 July 2003), with sampling being carried out in the morning twice a week, usually between 7-9 a.m. Samples were transported and stored at 4^o C. Water analyses were performed in less than 24h after sampling with E. coli enumeration made by the membrane filtration method following the recommendations of the American Public Health Association (APHA) [15].

To identify possible faecal contamination sources in the surrounding area, a parallel sampling program was established. Four sampling campaigns were made (8, 14, 21 and 28 May 2003) to determine the contamination field for the area. For simplicity, campaigns are numbered from C1 to C4, and this terminology will be used henceforth. These campaigns considered 32 sampling stations between Carcavelos and Oeiras beach (dots in Fig. 1). Samples were taken by boat twice a day, one in early morning and the other in the beginning

of the afternoon, so that both tidal periods could be considered. The sampling period was never greater than 30 minutes in both morning and afternoon campaign. The same procedure described earlier for storage and enumeration faecal bacteria was followed.

3 MODELLING APPROACH

3.1 Hydrodynamic model

The MOHID hydrodynamic model was used to achieve an accurate characterization of the flow regime of the study area. MOHID is a 3D finite volumes model [16] using an Arakawa-C grid [17] to perform the computations. A discrete form of the governing equations is applied macroscopically to the cell control volume. The grid is defined explicitly and the equations are solved using the same procedures, irrespectively of the cell geometry.

The hydrodynamic governing equations are the momentum and the continuity equations. The hydrodynamic model solves the primitive equations in Cartesian coordinates for incompressible flows. The momentum and mass evolution equations are portrayed in Eq. 1 and 2, respectively, where u_i is the velocity vector components in the Cartesian x_i directions, η is the free surface elevation, υ is the turbulent viscosity and p_{atm} is the atmospheric pressure. p is the density and p' its anomaly, ρ_0 is the reference density, g is the acceleration of gravity, t is the time, h is the depth, Ω is the Earth velocity of rotation and ε is the alternate tensor.

$$\frac{\partial u_i}{\partial t} + \frac{\partial (u_i u_j)}{\partial x_j} = -\frac{1}{\rho_0}\frac{\partial p_{atm}}{\partial x_i} - g\frac{\rho(\eta)}{\rho_0}\frac{\partial \eta}{\partial x_i} - \frac{g}{\rho_0}\int_{x_3}^{\eta}\frac{\partial p'}{\partial x_i}dx_3 + \frac{\partial}{\partial x_j}\left(\upsilon\frac{\partial u_i}{\partial x_j}\right) - 2\varepsilon_{ijk}\Omega_j u_k \quad (1)$$

$$\frac{\partial \eta}{\partial t} = -\frac{\partial}{\partial x_1}\int_{-h}^{\eta} u_1 dx_3 - \frac{\partial}{\partial x_2}\int_{-h}^{\eta} u_2 dx_3 \quad (2)$$

3.2 Application to the study site

Simulation conditions were selected to represent the surroundings of Torre beach. The main forcing mechanisms for the circulation considered in the model were tide and Tagus river outflow. To minimize the open boundary constraints in the local current patterns, a three nested model system was implemented: first covering a part of the Portuguese west coast (37°N – 41°N), second encompassing all the Tagus estuary area (38.1°N – 39.9°N), and finally the third that covered the immediate zone of the study area. The adopted methodology for the model nesting followed the methodology proposed by other authors [18].

The first domain is characterized by a regular square grid with 223×168 computation points, each cell covering an approximated area of 4 km^2. The second nested domain, forced by the boundary conditions imposed by the first domain, has 162×162 computation points and a minimum resolution of 300 m. Third nested domain has 100×200 computation points,

having a minimum resolution of 20 m, and was forced by boundary conditions with detailed spatial and temporal variability. FES95.2 global tidal solution [19] was imposed at the open boundary of the first domain. It was assumed an intense vertical mixing implying a homogeneous water column in all three domains, and so only two spatial horizontal dimensions (2D) were considered.

3.3 Numerical drogues

The use of tracers in the study of sewage dispersion has been widespread in experimental scenarios but not so much in numerical ones. Bacterial and fluorescent tracers (e.g., rhodamine) can be used as indicators for the distribution of particles originated in brooks and rivers or entering any receiving water body [20]. Following the same rationale, a lagrangian model was used to simulate the dispersion of wastewater in the coastal area.

Tracers are transported by currents calculated by hydrodynamic model. Besides its spatial position, each tracer is characterized by volume and E. coli concentration, a commonly used indicator for which guidelines and mandatory standards have been specified in the EC Directive. In emission, each tracer has the same microbiological and physical characteristics of the Lage brook. Both volume and concentration vary in time, but in response to different parameters; volume is affected by turbulent mixing while microbiological indicators depend on environmental such as radiation, temperature and salinity.

A continuous discharge was set for the brook during the simulation period. Based on numerous water samples collected in the effluent (Lage brook) over some past years, the initial concentration (moment of discharge) of E. coli for each tracer was set as 10^5 MPN/100ml, a typical concentration found in local water samples. Tracers were released with an interval of 150 s, being the number of tracers a function of the initial box volume (given by grid area and batimetry) divided by the initial volume defined for the tracers (300 m^3). Brook flow was set to a constant value (0.04 $m^3\ s^{-1}$), measured with a flow meter in previous monitoring campaigns, and was considered explicitly in the hydrodynamic model. The initial tidal condition chosen for the simulations start, i.e. drogues emission start, was the end of high tide (at 19.00h on 12 May). A complete tidal cycle is achieved before early morning, the time of day when faecal counts are usually higher.

3.4 E. coli decay model

As stated before, we have adopted the Canteras et al algorithm [11] to account for the mortality rates of E. coli. The simultaneous combination of all factors is accounted as:

$$k = 2.533 \times 1.04^{(T-20)} \times 1.012^{S} + 0.113 i_z \tag{3}$$

where S and T are the surrounding water salinity and temperature (^{o}C), respectively, and i_z the radiation (watt m^{-2}) at depth$z$ (m). Radiation levels in the water ambient are estimated by the hydrodynamic model where the light extinction is a function of light absorption by water and suspended sediments concentration. The radiation is known for each vertical layer (depth integrated).

Bacterial decay is usually expressed as T_{90}, the time in which 90% of population is no longer detectable, meaning 1 log reduction in number of pathogens. Assuming a first-order loss, the 90% mortality time is obtained by:

$$T_{90} = 2.303/k \tag{4}$$

4 RESULTS

4.1 Field data

An identification of any possible source of contamination inside or in the vicinity of the Torre bay was performed before any interpretation of the field data. Despite all the efforts to eradicate faecal pollution sources in the past, two potential sources were recognized and investigated: the fort on the right side of the beach, and the marina on the left. Being an old construction and an actual residence, the fort was selected as the starting point to look up for any possible hidden discharge. After a thorough search along the fort walls, both above and below the water levels, it was possible to conclude that no such source was present.

Faecal pollution originated in coastal marinas have been a somewhat neglected example of contamination sources [21], but it was assumed as a potential threat for the water quality in Torre beach. After a detailed examination, the marina ended up by being excluded as a possible source of contamination because it only harbored small recreation and fishing boats. Water sampling for analysis was performed to verify this observation. The presence of other potential point and non-point sources was also excluded after a thoroughly inspection of the site.

Fecal distribution fields obtained from all campaign samples suggests the Lage brook (east from Torre beach) to be the source of contamination. In a total of 6 campaigns out of 8, E. coli counts above 100 MPN/100ml were observed (Table 1). Whenever contamination was found in the results, higher concentrations were always related with the brook (Fig. 3, panels A and B). No other source could be identified in the final analysis.

Usually, concentration decreased with increasing distance from the Lage brook. Except for the last campaign (C4), higher counts of fecal contamination occurred in the start of ebb, possibly caused by an increase in the Lage output as a consequence of tidal shift. Although the afternoon period of campaign C2 was characterized by the higher contamination values (5400 MPN/100ml), they were confined to the surroundings of the brook. The same pattern was observed with campaign C3, where despite low values observed in morning and afternoon periods, the higher counts of E. coli (peaking 400 MPN/100ml) where observed in the morning period in the middle of Oeiras bay.

All campaigns, despite different weather and tidal conditions, showed similar results. For this reason, only the results of campaign C1 will be discussed. The morning sampling period began during the starting period of ebb. From the results it is possible to identify a plume with its origin in the Lage brook, and spreading westward. This plume appears to have an influence on the waters inside Torre bay, with the higher observed value of E. coli around 700

Table 1. *Samples where faecal contamination was detected. Measurements were made inside Torre beach in early morning, during May and July (2003).*

Date	Time	E. coli	Tide(m)			Sampling	
		MPN/100ml	Amplitude	max	min	Level (m)	Phase
13 May	7.30	350	2.49 (average)	3.27	0.78	1.02	flood (start)
27 May	8.25	420	1.8 (average)	2.95	1.15	1.63	flood
28 May	8.10	170	1.96 (average)	3.04	1.08	1.26	flood (start)
18 Jun	8.10	900	1.8 (average)	2.91	1.11	2.02	mid-ebb
24 Jun	7.35	2000	1.31 (neap)	2.68	1.37	1.89	mid-flood
25 Jun	7.53	400	1.49 (neap)	2.78	1.29	1.72	flood (start)
01 Jul	7.55	300	1.98 (spring)	2.97	0.99	1.27	ebb (end)
08 Jul	8.05	120	1.67 (neap)	2.86	1.19	2.71	flood (end)
09 Jul	8.05	280	1.78 (neap)	2.93	1.15	2.31	mid-flood

MPN/100ml. Considerably high contamination values are also observed in the east side of Oeiras bay (around 1400 MPN/100ml). Assuming the Lage brook as the only source of contamination, this occurrence can be explained either by the cyclonic vortex (counter clockwise) developed during the previous flood period, or by the remains of the brook plume transported eastward during flood.

The contaminated plume can be traced as far as the east side of Carcavelos beach, where values reaching 390 MPN/100ml are observed. Another clear illustration of this far-reaching impact of the discharge at Lage brook is observed in the morning campaign C4 (Fig. 3, panel C). Values as high as 600 MPN/100ml were found in the east side of Carcavelos bay. The extension and persistence of high values of contamination on the surrounding areas of Lage brook found in the morning periods can be explained as a consequence of low mortality rates of coliforms during night periods [1, 22–24]. However, the lack of meteorological data for each campaign and sampling day does not allow to set a clear relation between atmospheric conditions (especially radiation levels) and E. coli counts. The results also imply the occurrence of discharge from the Lage brook during flood, given the lack of retention capacity in its final section. This hypothesis is validated by the numerical simulations presented below.

In the afternoon period of campaign C1 (Fig. 3, panel B), started during the beginning of flood, contamination values were low (309 MPN/100ml being the higher observed value) when compared to the morning period. Nevertheless, it is possible to identify a plume pointing east, associated with the Lage outflow. The plume direction follows the typical flow pattern (velocity field) under flood tidal period. Lower values in the afternoon can be explained by the conjugation of low brook discharge during flood and high mortality rates during daylight.

Results clearly show that the westward expansion of the Lage plume in Oeiras bay (eventually reaching Carcavelos bay) meets its favorable conditions under ebb regimes and with low solar radiation. Similar observation have been made in NW England beaches [25], leading them to suggest that whenever possible, all sampling of EU designated bathing waters should be carried out in the early morning period.

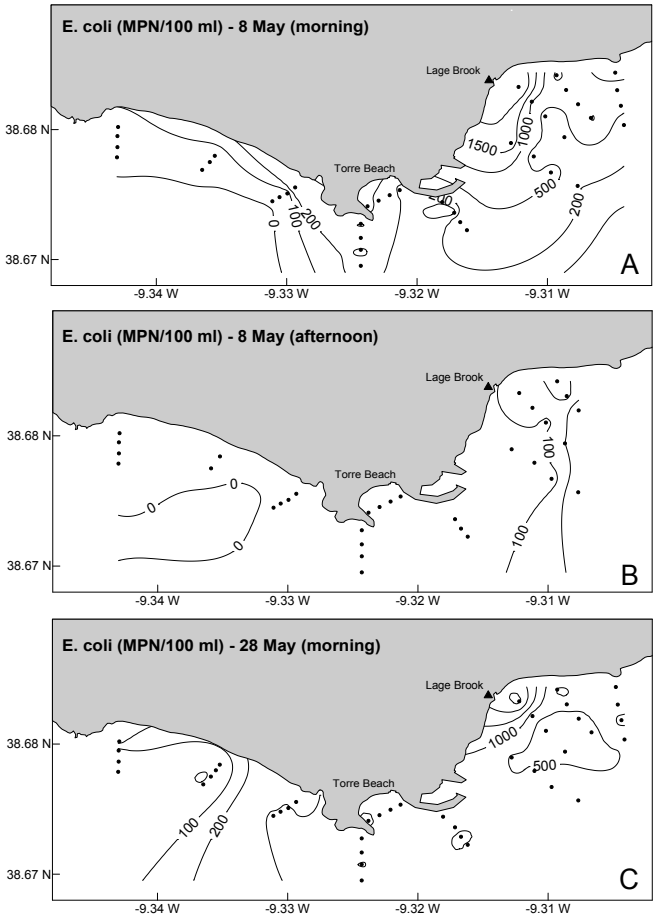

Figure 3. *Horizontal E. coli distribution (MPN/100ml) for Campaigns C1 and C4: A) in the starting period of ebb with samples taken in the morning; (B) in the starting period of flood with samples taken in the afternoon; (C) in the starting period of flood (samples taken in the morning).*

4.2 Model results

A proper representation of the hydrodynamic regime of the study area is imperative. Results for the second level hydrodynamic model that gives the boundary condition for the finer resolution model of the Torre beach area were previously validated. Model results for velocity fields seen in Figure 4 agree with the typical circulation pattern of the study area. While the dispersion pattern of particles is a consequence of the velocity-field determined by the hydrodynamic model, the extension and persistence of particles trapped near the coast is a function of T_{90} values. The ability to model both these processes is particularly relevant in settings like Torre beach, because of the high residence time inside the bay imposed by the hydrodynamic regime.

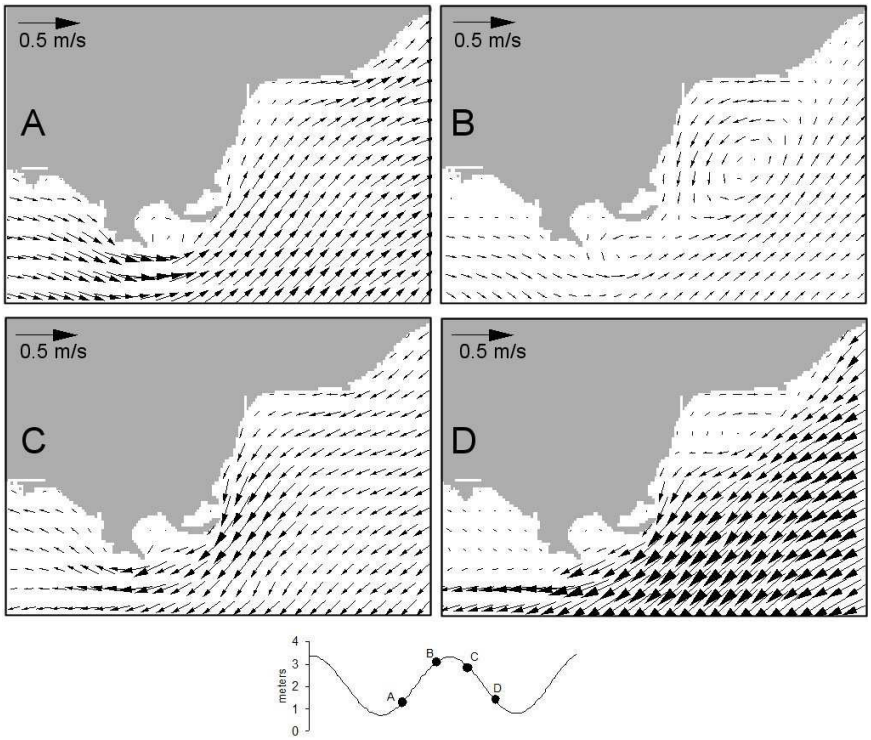

Figure 4. *Model results for the velocity field at four tidal instants indicated in the lower panel (sea surface height). Tidal conditions at each moment are: (a) flood start, (b) flood end, (c) ebb start, (d) mid-ebb.*

Figure 5 shows four instances of the simulation of the evolution of tracers with faecal concentrations. Five hours after the beginning of the simulation (at 0.00 a.m.) the plume has been carried along the coast by the ebb current, reaching the entrance of the marina. Under the absence of radiation influence on the mortality rate ($T_{90} > 15$ h), the observed 1 log unit decrease in E. coli concentration is explained on the basis of dilution and contribute of salinity and temperature. By 4 a.m., tracers reached Carcavelos bay with a concentration range of two log units ($10^3 - 10^4$ MPN/100ml). It is also possible to see some particles trapped inside Torre bay where higher concentrations are observed (10^5 MPN/100ml). Since a constant dilution rate is assumed, the differences seen so far are explained on the basis of the time passed since emission, with higher concentrations denoting a more recent emission.

Four hours later, (8 a.m.), with $T_{90} < 3$ h due to light radiation, only a few particles are noticed off Carcavelos bay and inside Torre bay. Simulated concentration (around 10^3) and results from samples made inside Torre bay are in the same range for this time of day (Table 2). Higher values seen near Lage brook represent recently emitted tracers transported by currents induced by tidal shift. Finally, at 12 a.m. contamination can only be observed in the surrounding area of the Lage brook. According to the simulation, no contamination occurs inside Torre bay from 9.30 a.m. onwards.

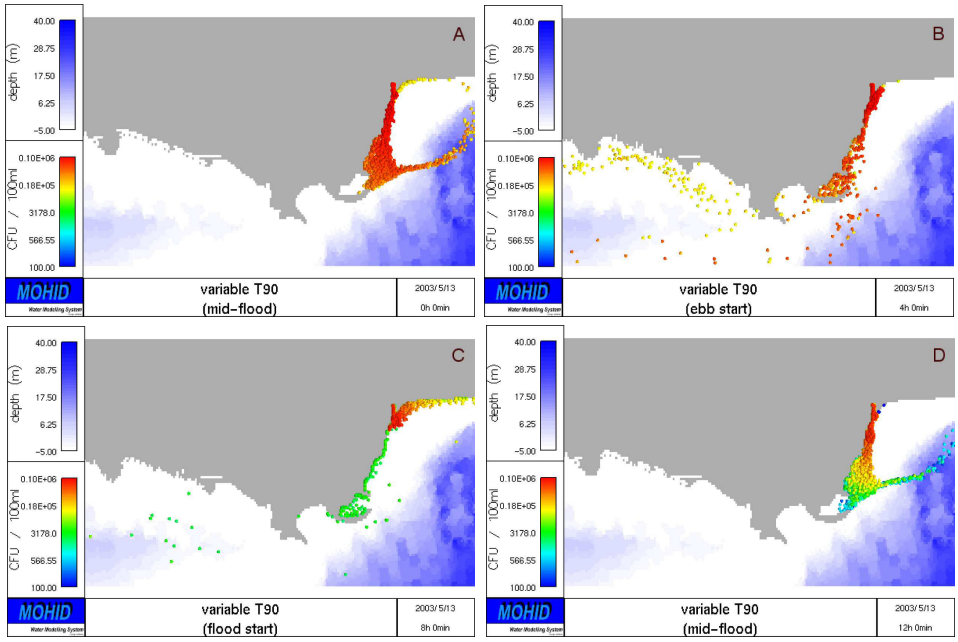

Figure 5. *Simulated dispersion of numerical drogues in the study area with the color code showing* E. coli *concentration in particles. Tidal conditions at each instant are: (a) mid-flood, (b) ebb start, (c) flood start, (d) mid-flood. The exact simulated time is mentioned in the figures.*

5 MAIN CONCLUSION FROM THIS STUDY

The study described in this chapter reports on a development made to equip the MOHID model with E. coli decay algorithms. This improvement made the model more versatile in the study of microbiological water quality, more specifically in the simulation of the dispersion and decay of faecal contamination in the receiving water bodies. With this upgrade in the code the model was able to simulate scenarios that previously modelling efforts failed to reproduce. Field data for contamination in the study area show that higher E. coli counts were:

- Found around the Lage brook area of influence;
- Associated with ebb starting period when brook discharge increases;
- Recorded mainly during the morning period, independent of the tidal regime. These observations suggested that the contamination might be locally induced by the Lage brook and that the role of solar radiation is a determinant in E. coli decay.

Model results have satisfactorily reproduced the observed patterns, validating the advanced hypothesis of Lage brook as the origin of contamination in the area. In addition, the model results provided a possible explanation for the observed patterns. It has been stressed that monitoring programs must take into account the diurnal variation of fecal indicators and should be able to explain it [26]. Hence, the modelling methodology used in this study was considered as useful as a management tool for other sites with similar pollution problems.

Table 2. *Summary of the results obtained in the May (2003) campaigns. Maximum and minimum values (range) measured in the samples.*

Campaign	Day		Tide	E. coli (MPN/100ml)
C1	8	morning	ebb (start)	14 – 2900
		afternoon	flood (start)	<1 – 309
C2	14	morning	flood (start)	<1 – 4300
		afternoon	ebb (start)	<1 – 5400
C3	21	morning	ebb (start)	<1 – 400
		afternoon	flood (start)	<1 – 80
C4	28	morning	flood (start)	2 – 2700
		afternoon	ebb (start)	<1 – 40

The present study comprising field data with model applications helped to solve a complex fecal pollution problem in one of the most attended bathing areas in Portugal. As an outcome of this study the discharge at Lage brook was eradicated. An overall improvement of the water quality of the studied area was achieved, leading to the classification of St. Amaro Beach (located in the Oeiras Bay) as a bathing area.

ACKNOWLEDGEMENTS

This work was financed by the Gabinete de Saneamento Básico da Costa do Estoril, SANEST, S.A., under the Project *Estudo de Monitorização Ambiental da Descarga no Mar do Efluente do Sistema de Saneamento Multimunicipal da Costa do Estoril*.

REFERENCES

1. D. Kay, C. M. Stapleton, M. D. Wyer, A. T. McDonald, J. Crowther, N. Paul, K. Jones, C. Francis, J. Watkins, J. Wilkinson, N. Humphrey, B. Lin, L. Yang, R. A. Falconer, and S. Gardner, "Decay of intestinal enterococci concentrations in high-energy estuarine and coastal waters: towards real-time t90 values for modelling faecal indicators in recreational waters," *Water Research*, vol. 39, no. 4, pp. 655–667, 2005.
2. M. G. Pereira and F. Alcantara, "Culturability of escherichia-coli and streptococcus-faecalis in batch culture and in-situ in estuarine water (portugal)," *Water Research*, vol. 27, no. 8, pp. 1351–1360, 1993.
3. H. Z. Sarikaya and A. M. Saatci, "Bacterial die-away rates in red-sea waters," *Water Science and Technology*, vol. 32, no. 2, pp. 45–52, 1995.
4. E. Serrano, B. Moreno, M. Solaun, J. J. Aurrekoetxea, and J. Ibarluzea, "The influence of environmental factors on microbiological indicators of coastal water pollution," *Water Science and Technology*, vol. 38, no. 12, pp. 195–199, 1998.
5. H. K. Bach, D. Orhon, O. K. Jensen, and I. S. Hansen, "Environmental-model studies for the istanbul master-plan .2. water-quality and eutrophication," *Water Science and Technology*, vol. 32, no. 2, pp. 149–158, 1995.
6. G. C. Christodoulou, I. Ioakeim, and K. Ioannou, "Modeling of pollution from the wastewater discharge of the city of limassol," *Water Science and Technology*, vol. 32, no. 9-10, pp. 197–204, 1995.
7. E. Garvey, J. E. Tobiason, M. Hayes, E. Wolfram, D. A. Reckhow, and J. W. Male, "Coliform transport in a pristine reservoir: Modeling and field studies," *Water Science and Technology*, vol. 37, no. 2, pp. 137–144, 1998.
8. A. U. Mahajan, C. V. Chalapatirao, and S. K. Gadkari, "Mathematical modeling - a tool for coastal water quality management," *Water Science and Technology*, vol. 40, no. 2, pp. 151–157, 1999.

9. C. Noutsopoulos, E. Gavalaki, and A. Andreadakis, "Evaluation of the impact from the discharge of treated sewage on the south-east saronicos gulf through mathematical water quality modelling," *Water Science and Technology*, vol. 39, no. 8, pp. 63–70, 1999.

10. A. Rodriguez, A. SanchezArcilla, J. M. Redondo, E. Bahia, and J. P. Sierra, "Pollutant dispersion in the nearshore region: Modelling and measurements," *Water Science and Technology*, vol. 32, no. 9-10, pp. 169–178, 1995.

11. J. C. Canteras, J. A. Juanes, L. Perez, and K. N. Koev, "Modeling the coliforms inactivation rates in the cantabrian-sea (bay-of-biscay) from in-situ and laboratory determinations of t-90," *Water Science and Technology*, vol. 32, no. 2, pp. 37–44, 1995.

12. S. Chapra, *Surface water-quality modeling*. Civil Engineering Series, New York: McGraw-Hill, 1997.

13. G. Kocasoy, "Waterborne disease incidences in the mediterranean region as a function of microbial pollution and t-90," *Water Science and Technology*, vol. 32, no. 9-10, pp. 257–266, 1995.

14. F. M. Salih, "Formulation of a mathematical model to predict solar water disinfection," *Water Research*, vol. 37, no. 16, pp. 3921–3927, 2003.

15. APHA, *Standard methods for the examination of water and wastwater*. Washington D.C.: American Public Health Association, 19th ed., 1995.

16. S. Chippada, C. N. Dawson, M. L. Martinez-Canales, and M. F. Wheller, "Finite element approximations to the system of shallow water equations, part ii: Discrete-time a priori error estimates," *Siam Journal on Numerical Analysis*, vol. 36, no. 1, pp. 226–250, 1998.

17. A. Arakawa, "Computational design for long-term numerical integration of the equations of fluid motion: Two-dimensional incompressible flow. part i," *Journal of Computational Physics*, vol. 1, pp. 119–143, 1966.

18. D. O. Hodgins, S. W. Tinis, and L. A. Taylor, "Marine sewage outfall assessment for the capital regional district, british columbia, using nested three-dimensional models," *Water Science and Technology*, vol. 38, no. 10, pp. 301–308, 1998.

19. C. Le Provost, F. Lyard, J. M. Molines, M. L. Genco, and F. Rabilloud, "A hydrodynamic ocean tide model improved by assimilating a satellite altimeter-derived data set," *Journal of Geophysical Research-Oceans*, vol. 103, no. C3, pp. 5513–5529, 1998.

20. O. Hadas, B. Shteinman, and R. Pinkas, "Distribution of fecal coliforms in the jordan river mouth originating from anthropogenic activities in the watershed," *Water Science and Technology*, vol. 42, no. 1-2, pp. 129–133, 2000.

21. M. D. Sobsey, R. Perdue, M. Overton, and J. Fisher, "Factors influencing faecal contamination in coastal marinas," *Water Science and Technology*, vol. 47, no. 3, pp. 199–204, 2003.

22. L. M. Evison and E. Tosti, "An appraisal of bacterial indicators of pollution in sea-water," *Water Science and Technology*, vol. 13, no. 1, pp. 591–599, 1981.

23. M. Pommepuy, J. F. Guillaud, E. Dupray, A. Derrien, F. Leguyader, and M. Cormier, "Enteric bacteria survival factors," *Water Science and Technology*, vol. 25, no. 12, pp. 93–103, 1992.

24. R. S. Fujioka and B. S. Yoneyama, "Sunlight inactivation of human enteric viruses and fecal bacteria," *Water Science and Technology*, vol. 46, no. 11-12, pp. 291–295, 2002.

25. K. Obiri-Danso, K. Jones, and N. Paul, "The effect of the time of sampling on the compliance of bathing water in nw england with the eu directive on bathing water quality," *Journal Coast Conservation*, vol. 5, no. 1, pp. 51–58, 1999.

26. D. G. Christoulas and A. D. Andreadakis, "Application of the eu bathing water directive to the design of marine sewage disposal systems," *Water Science and Technology*, vol. 32, no. 2, pp. 53–60, 1995.

AN OVERVIEW FOR SIMULATING THE BLOW OUT OF OIL SPILLS WITH A THREE-DIMENSIONAL MODEL APPROACH (CARIBBEAN COAST, COLOMBIA)

P. C. Leitão • M. S. Malhadas • J. Ribeiro • J. C. Leitão • J. Pierini • L. Otero

CHAPTER SYNOPSIS

Background

Oil spill modelling studies are usually focused in the first meters of the sea surface and consequently use a bi-dimensional (2-D) approach. The oil accidents are commonly associated with surface operations (e.g., ship accident, harbor activities) even in the case of blow ups in deep ocean majority of the oil released rise quickly to the surface. However, the works conducted in the DeepSpill Project show that for deep water blowouts dissolution potential of water-soluble oil components in seawater is an important factor when considering potential ecotoxicological effects from acute releases [1]. This is particularly relevant in connection to underwater releases.

In 2010, the Deepwater Horizon (DH) oil spill disaster (also referred to as the BP oil spill, the Gulf of Mexico oil spill, the BP oil disaster, or the Macondo blowout), trigger a great variety of in situ and remotely sensed observations and laboratory and numerical model studies on the oceanographic conditions in the gulf and their influence on the distribution and fate of the discharged oil [2]. One of the studies main focuses was the far-field subsurface and surface dispersal of different size classes of oil released from the DH. In the present work, a similar approach to the one presented in [3] is followed. A 3D coupled hydrodynamic and Lagrangian model system (MOHID) in the Caribbean Coast (Colombia) was applied.

Results

The 2-D model results show that the horizontal dispersion of oil spills at the surface is governed by wind, waves and surface currents. The oil thickness and track patterns depend on the oceanographic conditions of the simulated period. In case of extreme conditions, particularly persistent winds from the Northwest and West sectors, the oil plume could reach the Caribbean Coast Region and stay trapped along the shoreline of Rosario Islands.

The simulated droplet trajectories of the 3-D model at the Caribbean platform showed that droplets with a diameter of 50 μm formed a distinct subsurface plume, which was transported horizontally and could remain below the surface. This plume could have a very restricted area of impact because the dispersion is only controlled by the ocean currents which, at 1000 m depth, have a low intensity and are quite turbulent. In this case, the formed plume stayed trapped at 1000 m depth, not posing a risk to the Caribbean Coast. In contrast, droplets with diameters of 250 μm, 1 and 10 mm rose rapidly to the surface, even with different velocities (6, 10, 20 m s^{-1}).

Conclusions

Future oil-spill response models could use this approach to provide real-time forecasts of subsurface oil movement, and ongoing and planned improvements to this coupled model system will likely improve its predictive capabilities.

1 INTRODUCTION

The transport and fate of spilled oil in bodies of water are governed by physical, chemical, and biological processes that depend on the oil properties, hydrodynamics, meteorological and environmental conditions [4]. The processes include advection, turbulent diffusion, surface spreading, evaporation, dissolution and emulsification, and may influence the transport of the oil spill. When liquid oil is spilled on the sea surface, it spreads and forms a thin film,

the so-called oil slick [5]. Hence, oil spill models play a significant role in assessing risks and injuries to natural resources from actual and potential spills, and guiding the development of strategies for oil spill planning and response [6].

In spite of a great number of models available for oil spill simulation, most of them traditionally use the semi-empirical [7, 8] and are suitable mainly for oil slick tracking, evaluation of evaporation and generalized oil mass losses due to weathering [9].The new generation of the models has the ability to predict entrainment, subsurface transport and resurfacing of spilled oil [10, 11].

In the last three decades, many investigators have studied the transport and fate processes of oil spills based on the trajectory method [4, 12-19]. Such models have typically been two-dimensional surface models using constant or variable parameters to link wind and current velocities to the velocity of the surface oil slick [6]. Among these oil spill models, many of them focus on the surface movement of oil spills, since the traditional oil spill models have been used to describe horizontal plane dispersion [5]. Field, laboratory, and modelling studies [19-21] have clearly demonstrated the importance of the vertical dimension in oil movement. These studies have demonstrated that natural entrainment of oil can play an important role not only in mass balance calculations, but also in determining the spatial and temporal distribution of oil on the sea surface [6].

There has been little published research on the vertical distribution of oil but is well known that droplets of higher buoyancy spend proportionately more time on the surface layers and are advected further due to the surface currents than that smaller droplets [5, 3]. The spreading of the oil slick is a three-dimensional (3-D) process controlled by the droplet size distribution and shear diffusion processes [5, 3].

In this case of study the MOHID model was applied to the Caribbean Coast Region for simulating an oil spill associated with a blow out at 1000 m depth scenario. Two different model implementations were undertaken according to the processes addressed: i) horizontal transport at the surface and ii) vertical mixing of oil droplets. The first one is a two-dimensional numerical model application and have the main objective of simulating the transport and fate of the oil fraction able to rise quickly to the surface. This is based on the particle tracking model approach assuming that the amount of oil released is distributed among a large number of particles tracked individually. In a second stage, a Lagrangian discrete particle algorithm has been developed and applied to simulate movement of oil droplets in depth. This application is three-dimensional and consists of predicting vertical mixing assuming different size classes of oil droplets over time.

Performed simulations intend to understand the impact of an oil spill in protected areas along the Caribbean Coast (Rosario and Catalina Island), thus the importance of a 2-D or a 3-D model approach.

2 MATHEMATICAL MODEL

MOHID Water Modeling System, an integrated modelling tool, was applied to the study area. The hydrodynamic module of MOHID calculates and updates the flow information sol-

ving the primitive Navier–Stokes equations in the three-dimensional space for incompressible fluids and it is well described by [22]. The hydrodynamic information necessary to calculate the oil trajectories is then passed to the Lagrangian transport model, which computes their spatial evolution using the definition of velocity [23]. The oil weathering module (OWM) uses variables from the hydrodynamics and the Lagrangian transport module, and computes oil density, viscosity, and the weathering processes originally developed by [24].

For this particularly study was added a new vertical velocity component to the oil particles entitle buoyant velocity based in the formulation presented in [5].

2.1 Vertical mixing of oil droplets

The buoyant velocity of oil droplets is determined by their size, seawater viscosity and the density difference between seawater and oil droplets [4]. The critical diameter of oil droplets is calculated by the formula [25]:

$$d_c = \frac{(9.52v)^{\frac{2}{3}}}{g^{\frac{1}{3}}\left(1 - {}^{\rho_0}/_{\rho_w}\right)^{\frac{1}{3}}} \tag{1}$$

For small oil droplets $d_i < d_c$, Stokes law gives the steady buoyancy velocity depicted in Eq. 2:

$$u_{LS} = g d_i^2 \frac{\left(1 - {}^{\rho_0}/_{\rho_w}\right)^{\frac{1}{3}}}{18v} \tag{2}$$

For large oil droplets $d_i \geq d_c$, Reynolds law gives the steady buoyancy velocity showed in Eq. 3:

$$u_{LR} = \sqrt{\frac{8}{3} g d_i \left(1 - {}^{\rho_0}/_{\rho_w}\right)} \tag{3}$$

Where v is the seawater viscosity, while ρ_0 and ρ_w are the oil and seawater density, respectively. The rise velocity of droplets can have different orders of magnitude depending on diameters (e.g., for 30 and 300 μm corresponds 0.06 and 6 mm s^{-1}, respectively). These rise velocities fundamentally control whether the droplets reach the surface, if they form surface plumes (or sub-surface ones), and determine the direction and extent of horizontal dispersal.

For the oil type considered in this work (density = 920 kg m^{-3}), and assuming a water density of 1030 kg m^{-3}, the critical diameter is 210 μm (Figure 1). The velocities for diameters immediately above the critical one are on the order of 2.5 cm s^{-1} and immediately below on the order of 2.5 mm s^{-1}. Additionally, the ocean vertical velocities in this area and at this depth vary between 0.5-5 mm s^{-1}. This means that the droplets with a diameter below the critical diameter will have rising velocities lower or of the same order of magnitude than the environmental velocities, and will have the tendency to be dispersed, mainly due to the action of the ocean currents. The droplets with a diameter above the critical diameter will have rising velocities clearly higher than the hydrodynamic velocities, and will reach the surface quickly.

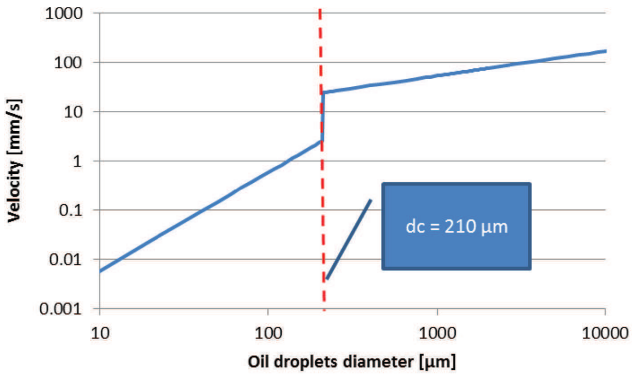

Figure 1. *Oil droplets rising velocity function of the oil droplets diameter with a 920* kg m^{-3} *density [4].*

3 APPLICATION OF THE OIL SPILL MODEL IN THE CARIBBEAN COAST

This section includes a description of 2-D and 3-D oil spill model implementation. The description includes the hydrodynamic and Lagrangian model configurations, model set-up and simulations performed. The 2-D implementation can be considered as the standard used in oil spill studies. The 3-D methodology followed here is similar to the one presented by [3] for the DH Spill.

The main goal of the 3-D model implementation was to illustrate the 3-D behavior of the oil plume in the near field function of the oil droplet dimension. The idea was to validate the hypothesis implicit to the 2-D approach that the plume raises very fast to the surface (order of minutes or a few hours). Another goal was to present a straightforward methodology to downscale a low frequency solution like RTOFS (http://polar.ncep.noaa.gov/ofs/) or MyOcean (http://www.myocean.eu.org/) [26].

3.1 Study site

The study site of the presumed oil spill (Figure 2, yellow polygon) is located on the Caribbean Coast of Colombia. The coast is about 1600 km long from Castilletes at the western border of Venezuela, to Cabo Tiburón at the eastern border of Panamá. The most important island areas are the coralline archipelagos of El Rosario Islands, 100 km south of Cartagena. The tidal range along the Caribbean Coast is a mixed semi-diurnal type, with maximum amplitudes of 60 cm [27]. The winds predominate from the east, north and northwest at the Guajira Peninsula, and from the northeast to northwest, south of the Sierra Nevada de Santa Marta [28].,

The climate of the Caribbean coast is generally characterized by two rainy periods (April-May and October-November) and two dry periods (December-April). Maximum annual precipitation for the Colombian Caribbean does not exceed 2500 mm. Minimum values are within the desert region of the Guajira Peninsula (yearly mean of about 267 mm), and maximum values are at the Sierra Nevada de Santa Marta massif (yearly mean of 2000 mm). Mean air temperatures for the Caribbean coast are less than 24 °C [28].

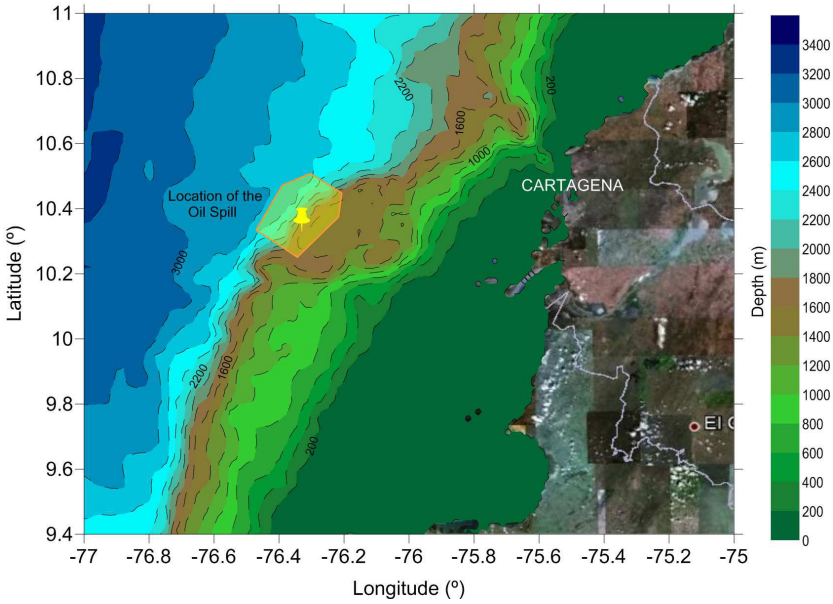

Figure 2. *Study site: Caribbean coast. Yellow polygon delineates the location considered for the oil spill.*

3.2 Input data

3.2.1 Bathymetries

The bathymetric data used in this study was extracted from the General Bathymetric Chart of the Oceans (GEBCO, http://www.ngdc.noaa.gov/mgg/gebco/) and local nautical charts. The main bathymetry characteristics are presented in Table 1 and model domains in Figure 3. The large scale model domain cover the Gulf of Mexico, regional scale the Colombia Coast and local scale Caribbean Coast region.

3.2.2 Oceanographic data

The oceanographic data includes wind, surface fluxes, currents, salinity, temperature and waves. The wind and surface fluxes data (temperature, humidity, pressure, solar radiation etc.) for the atmospheric forcing was gathered from NASA World Wind (http://worldwind.arc.nasa.gov/) and Global Forecast System (GFS, http://nomads.ncdc.noaa.gov/). NASA and GFS model solutions have 0.22º and GFS 0.5º resolution. Both of model predictions have 3-hourly frequency and 7 days forecast. The NASA World Winds solutions were gathered for the periods of January, August, September and November 2008 and GFS for 1 to 9 January 2012.

The currents, salinity and temperature data for the forcing of the hydrodynamic model comes from the Real Time Ocean Forecast System (RTOFS) managed by NOAA (http://polar.ncep.noaa.gov/ofs/) based in the Hybrid Coordinate Ocean Model (HYCOM, http://hycom.org/). The spatial resolution of the model solutions is about 1/12º. The surface (2-D solution) model predictions have an hourly frequency, while 3-D model solutions have daily one. The forecast extends for 6 days. ROFTS solution was gathered for 1 to 9 January 2012.

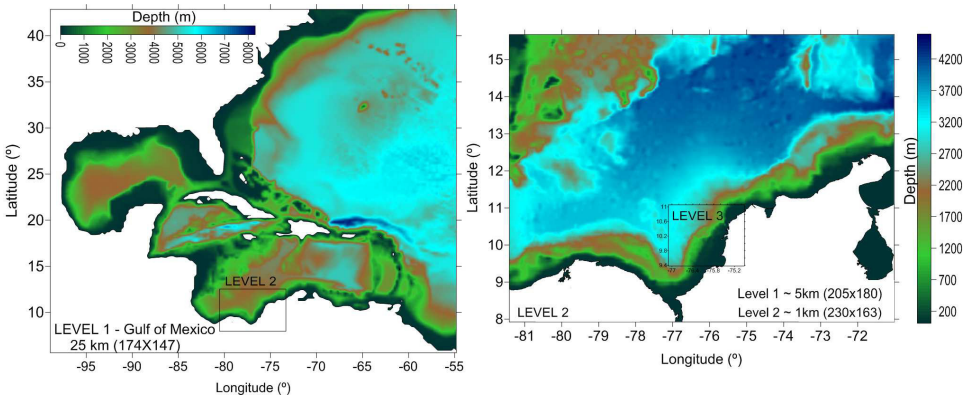

Figure 3. *Nested domains used in the 2-D and 3-D oil spill model configuration. Gulf of Mexico (large scale model domain) is the level 1, Colombia Coast (regional scale model domain) the level 2 and Caribbean Coast (local scale model domain) level 3.*

Table 1. *Main characteristics of domain bathymetries.*

Bathymetry	Coordinates	Dimension (dx/dy)	Resolution (km/º)
Gulf of Mexico	-99.0º W 5.5º S -54.7º E 42.9º N	174x147	25/0.22
Colombia Coast	-81.4º W 6.5º S -70.9º E 15.7º N	205x180	5/0.045
Caribbean Coast	-77.1º W 9.3º S -74.7º E 11.0º N	230x163	1/0.009

The wave data includes wave peak direction (Dp), wave peak period (Tp) and significant wave height (Hs). This was gathered through operational ocean wave predictions of NOAA/NWS/NCEP with WAVEWATCH III model (http://polar.ncep.noaa.gov/waves/). The model domain covers a longitude and latitude of 77º S to 77º N with 1.2ºx1º resolution. The model runs on the 00z, 06z, 12z and 18z model cycles, and starts with a 6h hindcast to assure continuity of swell, providing 5 days of forecast. The wave data was downloaded for the periods of January, August, September and November 2008.

3.3 Model configuration

3.3.1 2-D oil spill model

The model configuration for the 2-D oil spill model consists of two levels of nested grids (Figure 3): Colombia Coast and Caribbean Coast Region. Colombia Coast has 205×180 cells with 5 km×5 km of resolution and Caribbean Coast Region a model domain of 230×163 cells with 1 km×1 km of resolution. The hydrodynamic solution in both grids results from the interpolation of the high frequency (1 hour) RTOFS model surface solution.

Realistic meteorological and wave forcing are included in the model configuration. The wind (intensity, m s^{-1} and direction, °N) and wave data (Dp, Tp and Hs) were imposed in both nesting levels. Wind data was gathered from the NASA World Winds and wave data from WWIII model solutions.

A Lagrangian transport model was coupled with the hydrodynamic model to simulate the oil spill. A spill volume of about 3200 m^3 emitted at constant rate over 1 day is assumed. Particles were released in a continuous stream ($\sim$0.04 m^3 s^{-1}) at the location -76.33° W, 10.33° N (Figure 2) starting in the beginning of the simulation and ending after one day. During this period of time, 10,000 particles were released. The oil particle movement takes in consideration the effect of currents, waves and winds. Waves generate a drift velocity (stokes drift), and winds have direct drag effect over the floating oil. Processes such as surface spreading, evaporation, dissolution and emulsification were also simulated. For a detailed description of the MOHID oil spill model, see [23]. The oil type considered has an API of 21.3 and a density of 920 kg m^{-3} (for more details, see Table 2).

Table 2. *Main characteristics of oil.*

Type	Medium Crude Oil
Spill Rate (m^3/hours)	3200/24
API	21.3
Viscosity (cp)	33
σ (dyn/cm)	30
Water retention (%)	70
Emulsification Coefficient (s^{-1})	10^{-6}

Eight simulations were conducted, each for a specific period and assuming different forcing. Four of these correspond to real periods and aim to represent the seasonal variability, while the other four are considered as extreme conditions. Seasonality is introduced in the specific period of the input data - dry, wet and transition season. Extreme condition scenarios focus only on wind forcing, varying the intensities and directions according to typical values known in the area. In the scenrios of constant winds a random component of about 10% in the direction of the wind was associated. Model simulations performed in this work are presented in Table 3.

3.3.2 3-D oil spill model

To simulate the 3-D dispersion of an oil spill at 1000 depth on the Caribbean Coast, an off-line particle-tracking model using the 3-D hydrodynamic stored predictions was implemented. The off-line design was chosen to focus computational power on running a sufficient number of particles to ensure statistical robustness of model results [3]. The model configuration consists of providing hydrodynamic fields generated by a 3-D MOHID model of Caribbean Coast Region as an input to the Lagrangian model. In a first stage was implemented a 3-D model for predicting the hydrodynamic solution at the Caribbean Coast Region. This was simulated with MOHID model (www.mohid.com) using three levels of nesting (Figure 3): Level 1 (Gulf of Mexico), Level 2 (Colombia Coast) and Level 3 (Caribbean Coast Region).

Table 3. *Periods and main characteristics of the simulations performed.*

Scenario ID	Simulation Period	Characteristics	Hydrodynamic conditions	
1	18 to 28 January 2008	Wet Season	Currents Waves Wind	RTOFS WWIII NASA WW
2	17 July to 2 August 2008	Dry Season	Currents Waves Wind	RTOFS WWIII NASA WW
3	1 to 9 September 2008	Transition Season	Currents Waves Wind	RTOFS - NASA WW
4	9 to 20 November 2008	Transition Season	Currents Waves Wind	RTOFS WWIII NASA WW
5	96 hours	Extreme Conditions	Currents Waves Wind	- - North, 10 ms^{-1}
6	96 hours	Extreme Conditions	Currents Waves Wind	- - Northwest, 6 ms^{-1}
7	96 hours	Extreme Conditions	Currents Waves Wind	- - West, 6 ms^{-1}
8	96 hours	Extreme Conditions	Currents Waves Wind	- - Southwest, 10 ms^{-1}

The Gulf of Mexico has a dimension of 174×147 cells and resolution of 25 km and is a 2-D barotropic model. The sea level was assumed to be equal to the FES2004 tide global solution in the open boundary [29]. As initial conditions, a null free surface gradient and null velocity in all grid points were used. The time step is 240 s and the horizontal eddy viscosity is 250 $m^2\ s^{-1}$.

The Colombia Coast domain with 5 km x 5 km of resolution and 205x180 cell points is a 3-D baroclinic model with 40 Cartesian layers. Open Boundary Conditions (OBCs) were defined as a barotropic radiative condition (sea level and barotropic velocities) adding an exterior (or reference) solution equal to Level 1 plus RTOFS (daily average). In reality, the Level 1 corresponds to the high frequency component of the exterior solution and RTOFS to the low frequency. Salinity and temperature values relaxation (or nudging) along the open boundary are interpolated directly from the RTOFS solution. There is also relaxation to a 3-D velocity filed resulting from the interpolation of the RTOFS solution plus the Level 1 velocities. The time step used was 120 s and horizontal eddy viscosity 50 $m^2\ s^{-1}$.

The Caribbean Coast Region model domain (Level 3) has a model domain of 230×163 cells with 1 km×1 km of resolution and is also a 3-D baroclinic model nested in the Colombia Coast domain (Level 2). The same vertical discretization of Level 2 (40 Cartesian layers) was used. For the definition of OBCs, a similar methodology to the one followed in Level 2 was adopted. However, in this case, the barotropic exterior solution is only derived from Level 2, and the relaxation procedure is done for the salinity, temperature and velocity values

interpolated directly from the Level 2 model. In this case, Level 2 already incorporates the high and low frequency components. The time step is 40 s and the horizontal eddy viscosity is 10 $m^2\ s^{-1}$. This downscaling methodology is described in detail in [26].

The model was run for the period of 6 to 9 January 2012 being the first 6 days of simulation considered as a spin-up. The output includes 3-D fields of temperature, salinity, three components of velocity and sea surface height. An example of surface current velocities predicted by the 3-D Hydrodynamic Colombian Coast model can be found in Figure 4.

The second step consists of implementing the Lagrangian oil spill model. The predicted water level, three components of velocities, salinity, temperature, and diffusivities predicted by hydrodynamic model are interpolated for the grid where the particle model runs. It is assumed that particles were assigned characteristics of oil droplets, including diameter and density. Particles trajectories are tracked in three dimensions using advection, mixing and oil droplet rise velocities.

A continuous release ($\sim$0.04 $m^3\ s^{-1}$) with the same oil characteristics described for the 2-D model configuration is assumed (Table 2). Particles were released in a continuous stream at the location -76.33º W 10.33º N (Figure 2) at 1000 m depth over the 3 days of simulation. The discharge was connected along the entire simulation with the goal of integrating a larger set of conditions. The idea was to look at the oil plume 3-D structure, and not so much the impact of the blow out. A total of 7,000 particles were released during the simulation.

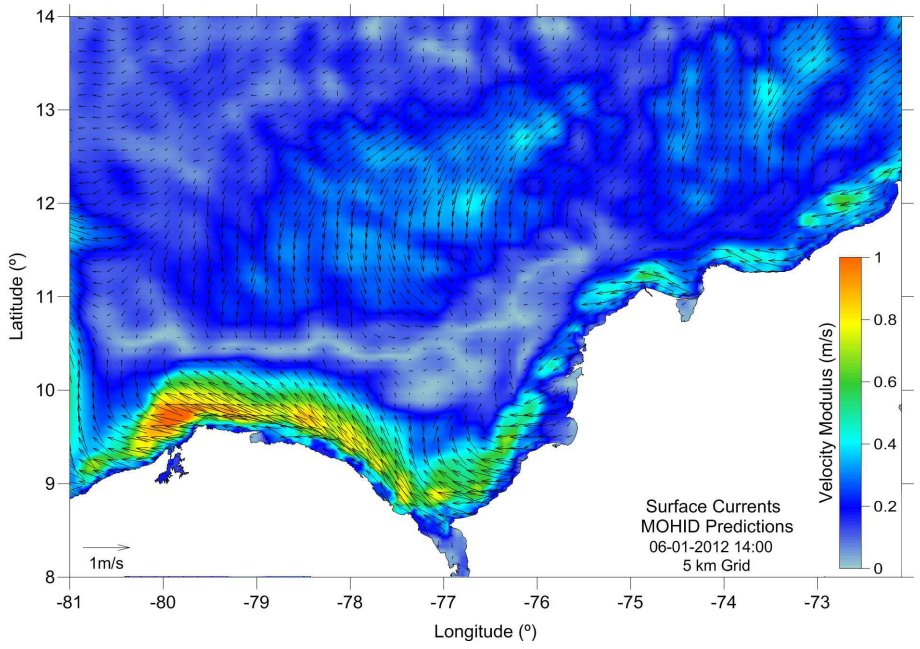

Figure 4. *Current velocities at the surface predicted by the 3-D hydrodynamic Colombia Coast model on 6 January 2012, 14:00h.*

Four simulations for the period of 6 to 9 January 2012 were conducted. The simulations set-up differ according to droplet diameter size and are presented in Table 4. The Lagrangian model input uses the hydrodynamic fields generated by the 3-D MOHID Caribbean Coast Region model. For this hydrodynamic set-up, several oil droplet diameters were simulated: 50 and 250 μm, 1 and 10 mm.

Table 4. *Periods and main characteristics of the simulations performed to analyze the vertical transport of oil droplets.*

Scenarios ID	Simulation Period	Droplets diameters	Hydrodynamic conditions	
1	6 to 9 January 2012	50 µm	Currents S and T	3-D Mohid Model 3-D Mohid Model
2	6 to 9 January 2012	250 µm	Currents S and T	3-D Mohid Model 3-D Mohid Model
3	6 to 9 January 2012	1 mm	Currents S and T	3-D Mohid Model 3-D Mohid Model
4	6 to 9 January 2012	10 mm	Currents S and T	3-D Mohid Model 3-D Mohid Model

4 RESULTS AND DISCUSSION

This section presents the most relevant model results obtained with the 2-D and 3-D oil spill model applications. For the 2-D model application, we present the evaporated mass in all scenarios and oil thickness. Results of 3-D model application include particle distributions along vertical depth.

4.1 2-D oil spill model

The curves of the evaporated rate in mass obtained for simulated scenarios with a 2-D oil spill model are presented in Figure 5. Results obtained for the scenarios that include seasonal variation in data (Scenario 1- wet season, Scenario 2- dry season, Scenario 3 and 4- transition seasons) are depicted in Figure 5a and different wind forcing (Scenario 5- North, 10 $m\,s^{-1}$, Scenario 6-Northwest, 6 $m\,s^{-1}$, Scenario 7-West, 6 $m\,s^{-1}$, Scenario 6-Southwest, 10 $m\,s^{-1}$) in Figure 5b.

In general, it is possible to conclude that crude oil reduces about 20-30% of its initial volume in the first 2 days. This reduction is affected mainly by wind, currents and seasonality (e.g., in summer evaporation is higher than that in winter). Figure 5 shows that higher evaporation rates ($\sim$35%) are achieved during the dry season simulated scenario, while lesser values are obtained in the others. Simulated scenarios considered wind forcing shows that evaporation rate values occur according to wind intensity (from 6 to 10 $m\,s^{-1}$). When wind speed increases the evaporation rates tend to be higher (about 30%).

Maximum oil thickness obtained at the surface with the 2-D model for the scenarios that include seasonal variation in data (e.g., Scenario 1- wet season, Scenario 2- dry season, Scenario 3 and 4- transition seasons) is shown in Figure 6 and reveals a different oil slick

pattern for each scenario. This can be explained by the current patterns of each simulated period. The results show a slick separated with relatively thick patterns and different thickness. A maximum thickness between 0.10 and 0.3 mm is predicted by the model, which is in line with other studies (U.S. Department of the Interior, 2006). Areas around oil spill seep slicks tend to be quite thin, with thickness values of about 0.10 mm.

The results of model simulations performed for the scenarios of wind are depicted in Figure 7. These scenarios are considered as extreme scenarios, assuming a situation where the wind is the only forcing. In this situation, a mean intensity and direction considered typical in the study area is assumed.

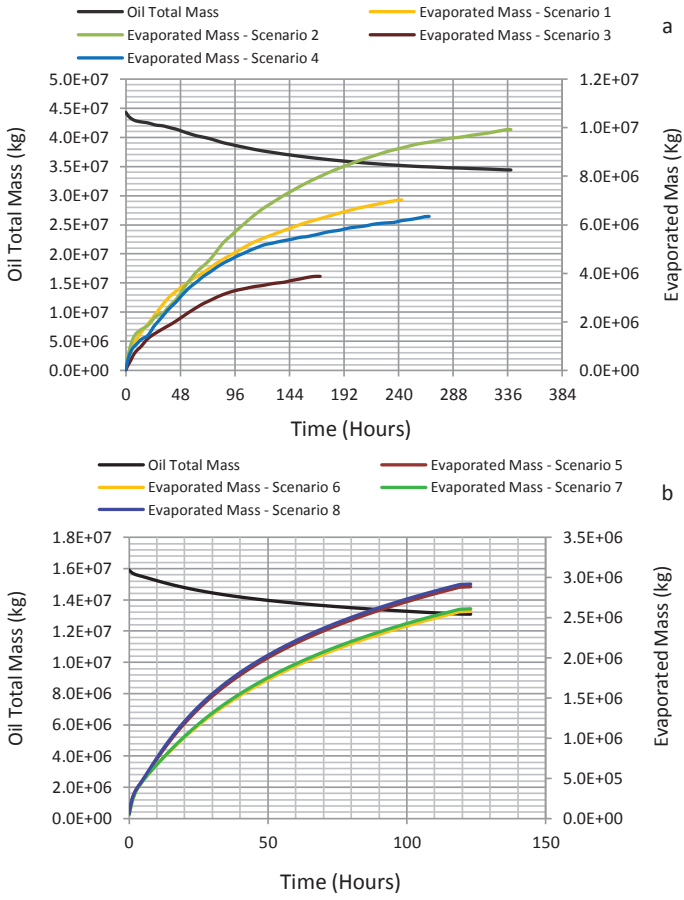

Figure 5. *Curves of evaporated rate in mass obtained for the scenarios that include a)seasonal variation in data (e.g., Scenario 1 – wet season, Scenario 2 – dry season, Scenario 3 and 4 – transition seasons) and b) different wind forcing (e.g., Scenario 5 – North, 10* $\mathrm{m\,s^{-1}}$*, Scenario 6 – Northwest, 6* $\mathrm{m\,s^{-1}}$*, Scenario 7 – West, 6* $\mathrm{m\,s^{-1}}$*, Scenario 8 – Southwest, 10* $\mathrm{m\,s^{-1}}$*).*

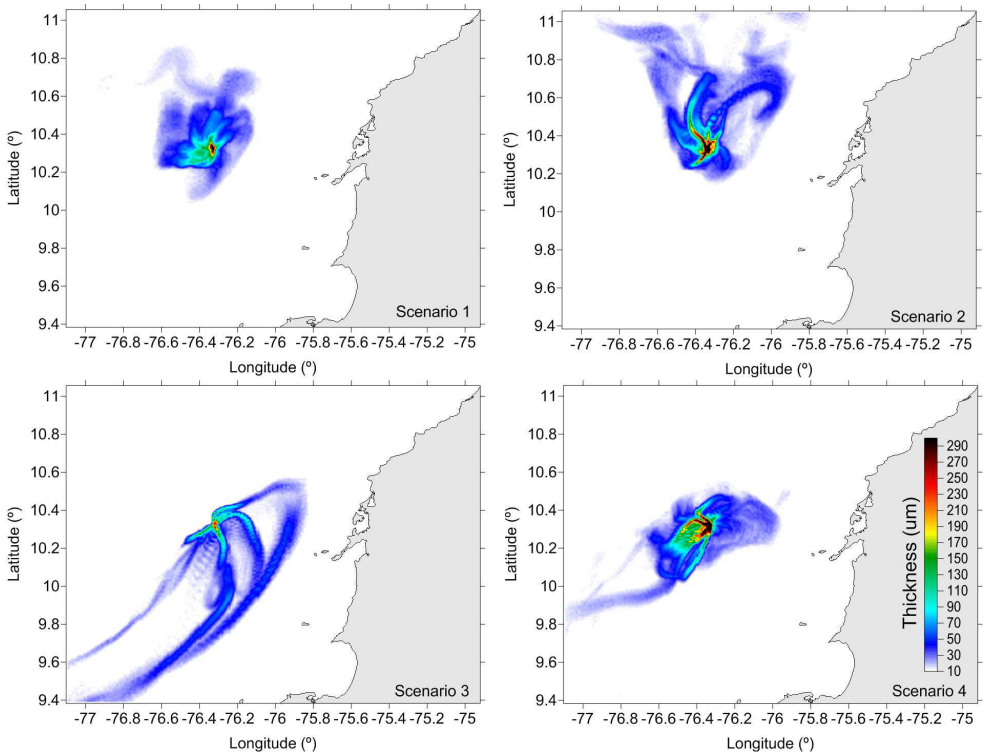

Figure 6. *Maximum oil thickness obtained at the surface with 2-D model for the scenarios that include seasonal variation in data (e.g., Scenario 1 – wet season, Scenario 2 – dry season, Scenario 3 and 4 – transition seasons).*

Simulations performed for the wind scenarios allow an evaluation of the surface oil plume for the areas of interest, Rosario Islands. The results reveal lower values of thickness (about 0.1 mm) when compared with the scenarios presented above. This is explained by the fact that, for these extreme cases, we assume that the only forcing is the wind (no waves and currents). Hence, the oil dispersion is more efficient, generating lower thickness values. Regarding the oil plumes in face of winds scenarios, it can be observed that Northwest and West are the most unfavorable situations. In these cases, the oil spill could reach the coast, and is seized along the coast.

4.2 3-D oil spill model

The particle position predictions for oil droplets sized 50 μm is depicted in Figure 8 (a - shelf front view and b - along shelf view). The same kind of results, but for 250 μm, 1 mm and 10 mm droplet sizes, are shown in Figure 9, Figure 10 and Figure 11.

The model simulations for fixed-diameter particles indicate that oil droplet diameter significantly influenced the transport of oil in water column. The predicted distributions of the particles in depth indicate that two types of plumes could be generated depending on the oil

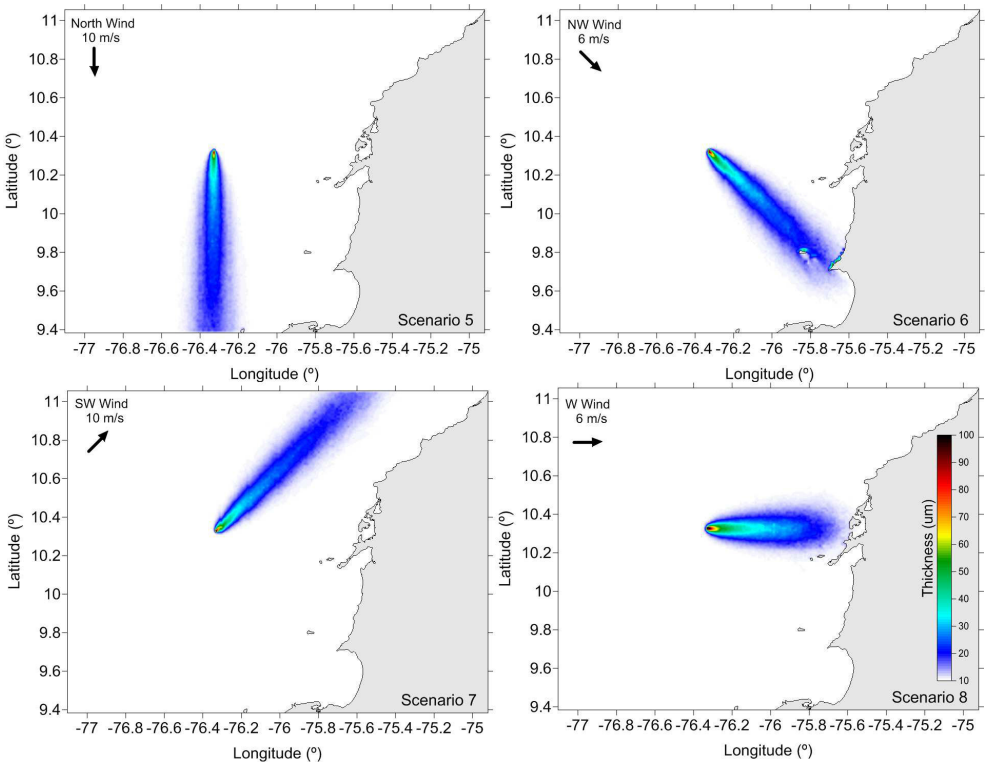

Figure 7. *Maximum oil thickness obtained at the surface with 2-D model for the scenarios with different wind forcing (e.g., Scenario 5 – North, 10* m s^{-1}*, Scenario 6 – Northwest, 6* m s^{-1}*, Scenario 7 – West, 6* m s^{-1}*, Scenario 8 – Southwest, 10* m s^{-1}*).*

droplets' size. Particles with diameters of 50 μm have low rising velocities ($\sim$0.08 mm s^{-1} vertical velocity) below typical velocities due to local hydrodynamics. In this situation, the subsurface plume tends to stay trapped around 1,000 m (Figure 8) in depth. The plume tends to disperse through the water column and be transported horizontally (Figure 6) due to physical processes (e.g., tide, internal waves and density currents). The oscillating movement at trapped depth ($\sim$1,000 m) could maintain the plume below surface for a long time (time scales on the order of months). The behavior of this kind of oil droplets is also predicted by the application of the SABGOM-LTRANS model to the Gulf of Mexico [3]. The predictions of the oil plume generated by droplets of 50 μm suggest a small risk for the Caribbean Coast Region. This could be explained by the fact that plumes remain at lower depths ($\sim$1,000 m) for long-time. Additionally, there are oil degradation processes, which in this present version of MOHID are only connected when the oil particles reach the surface.

Particles with diameters of 250 μm, 1 and 10 mm rose quickly to the surface (Figure 9, Figure 10 and Figure 11) with ascending velocities of about 6, 10 and 20 cm s^{-1}. The 250 μm particles take around 4 hours to reach surface. In the area of the oil spill, horizontal

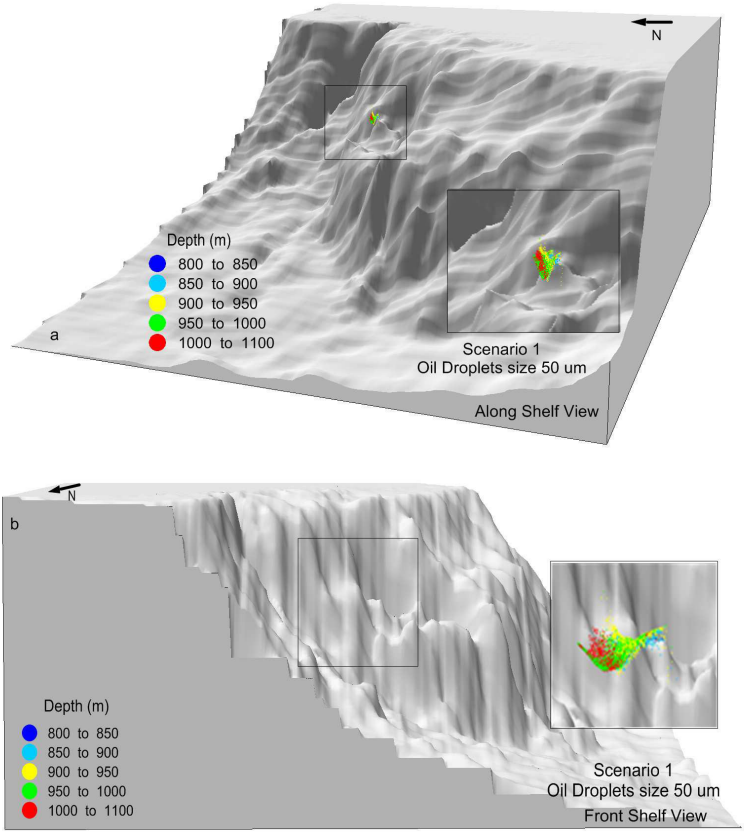

Figure 8. *Particle position along water depth for Scenario 1 – oil droplets size of 50 μm: a) along shelf view and b) shelf front view.*

velocities have typical intensities of 10 cm s^{-1}; this means for the 250 μm oil droplets, there is a horizontal displacement before reaching the surface on the order of 2 km. The analysis of the oil droplet velocity presented earlier (Figure 1) clearly predicts the two types of dispersion described above. For oil droplets with a diameter above 210 μm (critical diameter), the oil will reach the surface quickly. Droplets below the critical diameter would be dispersed mainly by the ocean 3-D current field.

At the surface, the plume is governed mainly by winds, waves and surface currents, and is highly dependent on instantaneous conditions; this means that the 2-D oil spill model is a valid methodology. After reaching the surface, particles remained there and started to be affected by horizontal dispersion induced by currents, winds and waves.

During the predicted time, the plume clearly deviates from the Caribbean Coast Region due to surface currents. However, since the surface plume is controlled by horizontal dispersion processes, as we saw in 2-D model application, in the case of extreme conditions of persistent winds, the oil plume could travel inshore and reach the Caribbean Coast region.

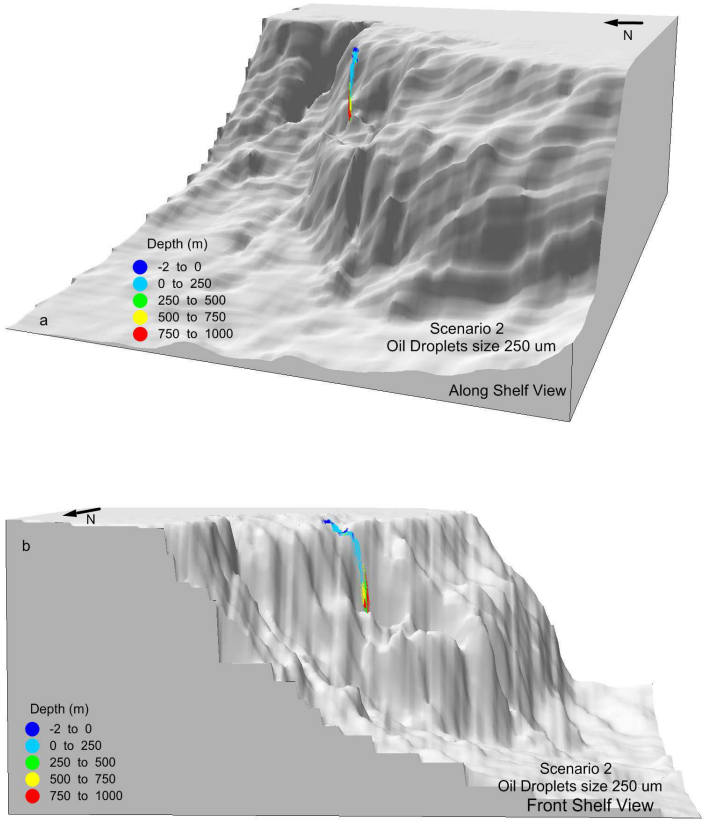

Figure 9. *Particle position along water depth for Scenario 2 – oil droplets size of 250 μm: a) along shelf view and b) shelf front view.*

5 CONCLUSIONS

The turbulent zone created at the release point causes the oil to fragment into droplets. Droplet sizes vary as a function of the exit conditions and velocities. Data presented by [30] based on field and laboratory work lead to the conclusion that the majority of the release droplets under a blowout situation have a diameter larger than 250 μm ($>$90% of the release volume). The same conclusion can be reached based in the DeepSpill project's experimental data [1]. This means that the majority of the oil released will rise quickly to the surface. However, this data should be confirmed with the company responsible for operating the infrastructure related to this study.

In conclusion, it can be stated that, in the case of blow outs, two types of dispersion analyses must be done:

1. Focus on the majority of the released oil ($>$90%) that reaches surface almost in the same horizontal point of the release depth ($\sim$2 km difference). In this case, the traditional 2-D approach is valid;

2. Focus in a small fraction of the released oil (<10%), but which is quite toxic. In this case, the dispersion is mainly controlled by the ocean's 3-D hydrodynamic structure. This means that this oil fraction will be dispersed quite slowly. At the release point, velocities are quite turbulent (do not have clear direction) and are small (horizontally 5–50 mm s^{-1} and vertically 0.5 – 5 mm s^{-1}). This can be clearly seen in the aerial view, side by side plot, of the oil spill plume for the 50 μm and 250 μm oil droplet diameter scenarios (Figure 10). The plume associated with 250 μm oil droplets covers a horizontal area at least two orders of magnitude greater than the 50 μm scenario. The area of impact of the more dissolved fractions will tend to be restricted. The impact over the web food of these more toxic oil components is the main point of concern.

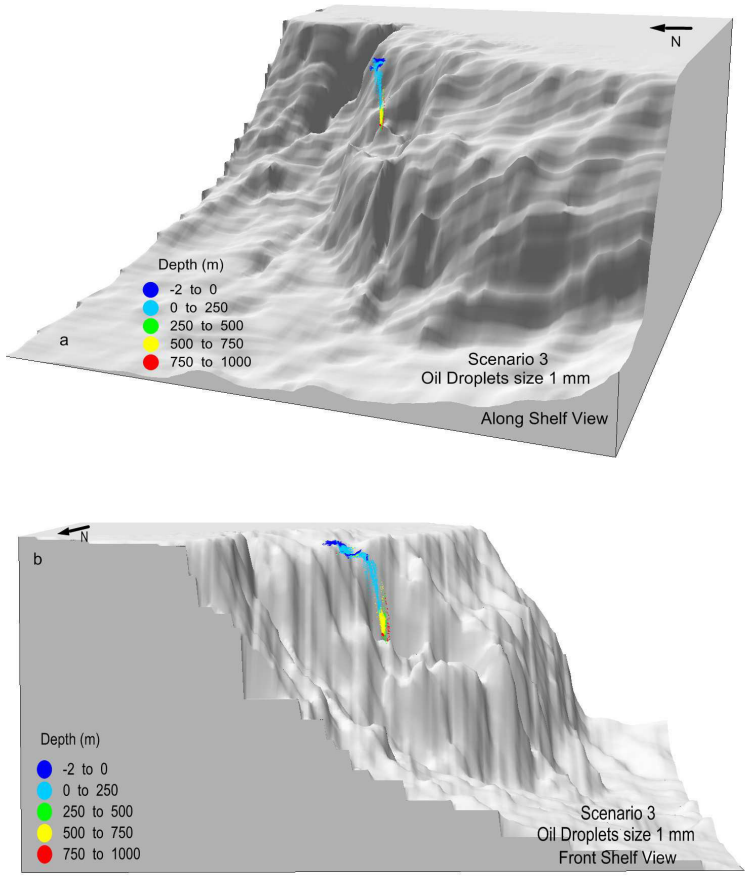

Figure 10. *Particle position along water depth for Scenario 3 – oil droplets size of 1 mm: a) along shelf view and b) shelf front view.*

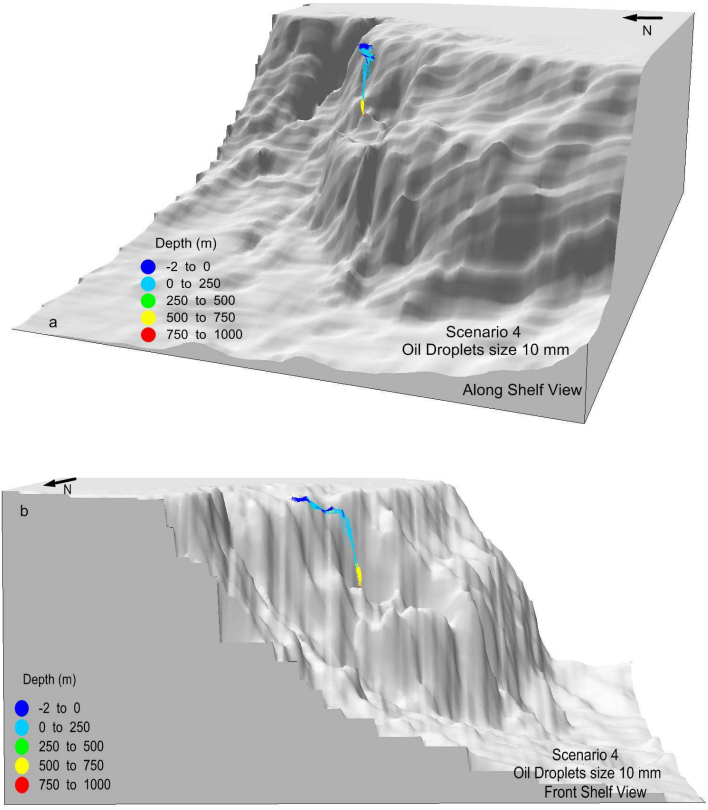

Figure 11. *Particle position along water depth for Scenario 4 – oil droplets size of 10 mm: a) along shelf view and b) shelf front view.*

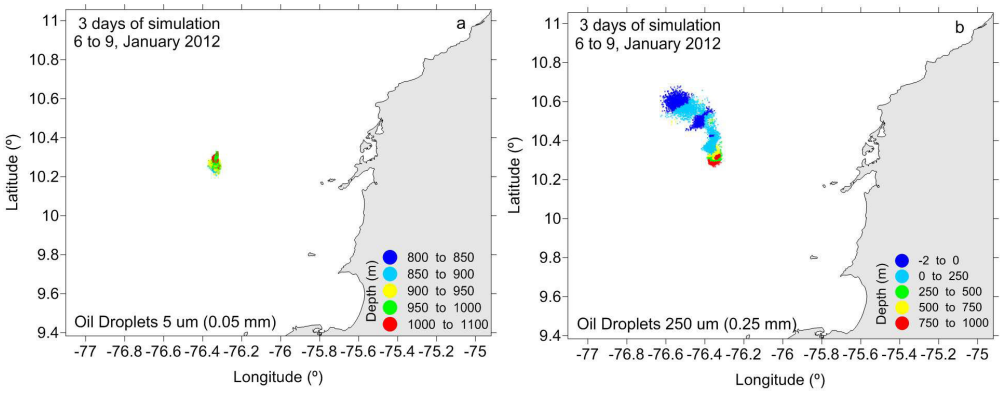

Figure 12. *Aerial view of the oil plumes after 3 days of simulation: a) 50 μm and b) 250 μm.*

ACKNOWLEDGEMENTS

The authors wish to thank ECOPETROL S.A (Columbian Oil Company) and GEOTEC Ingeniería Ltda.

REFERENCES

1. Johansen, O., Rye, H., Melbye, A., Jensen, H., Serigstad, B. and Knutsen, T. 2001. Deep Spill JIP Experimental Discharges of Gas and Oil at Helland Hansen, Parts I, II, and III – Technical Report, SINTEF Applied Chemistry, Norway.
2. Liu, Y., A. MacFadyen, Z.-G. Ji, and R. H. Weisberg (Eds.) 2011, Monitoring and Modeling the Deepwater Horizon Oil Spill: A Record-Breaking Enterprise, Geophys. Monogr. Ser., vol. 195, 271 pp., AGU, Washington, D. C., doi:10.1029/GM195.
3. North, E. W., E. E. Adams, Z. Schlag, C. R. Sherwood, R. He, K. H. Hyun, and S. A. Socolofsky 2011, Simulating oil droplet dispersal from the Deepwater Horizon spill with a Lagrangian approach, in Monitoring and Modeling the Deepwater Horizon Oil Spill: A Record-Breaking Enterprise, Geophys. Monogr. Ser., vol. 195, edited by Y. Liu et al., pp. 217–226, AGU, Washington, D. C., doi:10.1029/2011GM001102
4. Wang, S.D., Shen, Y.M., Zheng, Y.H., 2005. Two-dimensional numerical simulation for transport and fate of oil spills in seas. Ocean Engineering 32, 1556–1571.
5. Wang, S.D., Shen, Y.M., Zheng, Y.H., Guo, Y.K, Tang, J. 2008. Three-dimensional numerical simulation for transport of oil spills in seas. Ocean Engineering 35, 503–510.
6. Reed, M., Turner, C., Odulo, A., 1994. The role of wind and emulsification in modelling oil spill and drifter trajectories. Spill.
7. Fay, J.A., 1969. The spread of oil on a calm sea. In: D. Hoult (Ed.), Oil on the Sea. Plenum Press.
8. Fay, J.A., 1971. Physical processes in the spread of oil on a water surface. In: Proc. Conf. Prevention and Control of Oil Spills, 15-17 June. American Petroleum Institute, Washington, DC, pp. 463-467.
9. Tkalich P., Huda K., Gin K. 2003. A multiphase oil spill model. Journal of Hydraulic Research Vol. 41, No. 2, pp. 115–125.
10. Elliot, A.J., Hurford, N., Penn, C.J., 1986. Shear diffusion and the spreading of oil slicks. Mar. Pollut. Bull. 17, 308-313.
11. Spaulding, M.L., 1995. Oil spill trajectory and fate modelling: State-of-the art review. In: Proceeding of the Second International Oil Spill Research and Development Forum, IMO, London, UK.
12. Mackay, D., Paterson, S., Nadeau, S., 1980. Calculation of the Evaporation Rate of Volatile Liquids. Proceedings, National Conference on Control of Hazardous Material Spills, Louisville, Ky., pp. 364–368.
13. Huang, J.C., Monastero, F.C., 1982. Review of the State-of-the Art of Oil Spill Simulation Models. Final Report Submitted to the American Petroleum Institute, by Raytheon Ocean Systems Co., East Providence, R.I.
14. Shen, H.T., Yapa, P.D., Petroski, M.E., 1986. Simulation of oil slick transport in Great Lakes connecting channels. Report Nos.86–1 to 4, vols. I–IV, Department of Civil and Environmental Engineering, Clarkson University, Potsdam, NY.
15. Shen, H.T., Yapa, P.D., 1988. Oil slick transport in rivers. Journal of Hydraulic Engineering 114, 529–543.
16. Yapa, P.D., Shen, H.T., Angammana, K., 1994. Modeling oil spills in a river–lake system. Journal of Marine System 4, 453–471.
17. Lonin, S.A., 1999. Lagrangian model for oil spill diffusion at sea. Spill & Technology Bulletin 5 (5/6), 331–336.

18. Chao, X.B., Shankar, N.J., Cheong, H.F., 2001. Two- and three dimensional oil spill model for coastal waters. Ocean Engineering 28, 1557–1573.
19. Johansen, E., 1984. The Halten Bank experiment observations and model studies of drift and fate of oil in the marine environment. In: Proceedings of the 11th Arctic Marine Oil Spill Program (AMOP) Techn. Seminar. Environment Canada, pp. 18-36.
20. Delvigne, G.A.L., Sweeney, C.E., 1988. Natural dispersion of oil. Oil and Chemical Pollution 4, 281-310.
21. Singsaas, I., Daling, P.S., 1992. Meso-scale test for laboratory weathering of oil. In: Proceedings of the 158th Arctic and Marine Oil Spill Program Technical Seminar, Environment Canada, pp. 55-66.
22. Martins, F., Leitão, P., Silva, A., Neves, R., 2001. 3D modelling in the sado estuary using a new generic vertical discretization approach. Oceanologica Acta 24, S51–S62.
23. Janeiro J, Fernandes E, Martins F, Fernandes R. Wind and freshwater influence over hydrocarbon dispersal on Patos Lagoon, Brazil. Marine Pollution Bulletin. 2008; 56(4): 650-665.
24. Fernandes, R., 2001. Modelação de derrames de hidrocarbonetos. Trabalho de Final de Curso (Graduation Thesis). Relatório Final. Instituto Superior Técnico, Portugal.
25. Lou, A.G., Wu, D.X., Wang, X.C., Xi, P.G., 2001. Establishment of a 3-D model for oil spill prediction. Journal of Ocean. University of Qingdao 31 (4), 473–479 (in Chinese).
26. Leitão P, Coelho H, Santos A, Neves R. Modelling the main features of the Algarve coastal circulation during July 2004: A downscaling approach. Journal of Atmospheric & Ocean Science. 2005; 10(4): 421-462.
27. Tuchkovenko, Y.S. and Calero, L.A, 2003. Mathemathical modelo of the Ciénaga Grande de Santa Marta Ecosystem. Bol. Invemar 2003, vol.32, n.1, pp. 145-167. ISSN 0122-9761.
28. IGAC, 2002. 7th Scientific Conference of the International Global Atmospheric Chemistry Project. 18-25 September 2002 Crete, GREECE.
29. Lyard, L., F. Lefevre, T. Letellier and O. Francis, 2006: Modelling the global ocean tides: modern insights from FES2004. Ocean Dyn., 56, 394-415.
30. Ross, S. L. Environmental Research Ltd., Fate and Behavior of Deepwater Subsea Oil Well Blowouts in the Gulf of Mexico. Minerals Management Service, 1997.

COUPLING MOHID WITH OPTIMIZATION ALGORITHMS: PERSPECTIVES ON THE DEVELOPMENT OF AUTOMATIC CALIBRATION TOOLS

E. B. Lima • P. G. Watts Rodrigues • A. J. Silva Neto • J. Lugon Jr. • M. Irízar Mesa • O. Llanes Santiago

CHAPTER SYNOPSIS

Background
The mathematical formulation adopted in MOHID includes parameters that need to be defined or estimated This chapter presents the coupling of stochastic optimization methods and neural networks with the MOHID platform, in order to solve an inverse problem, here formulated as the better estimative of bed roughness height and turbulent diffusion coefficient, parameters that can be present in the mathematical formulation of hydrodynamic and transport models. The direct problem focused on here was the simulation of the hydrodynamics and salinity transport in an estuarine environment, the Macaé estuary, Brazil. The results presented here are part of ongoing investigation line, which has been conducted by researchers of the IPRJ/UERJ since 2008.

Results
All optimization methods tested here showed satisfactory performances, leading to error estimates lower than measurement errors. Whenever these errors were added to the experimental data, a longer simulation period was required to estimate the desired parameters. Regarding the neural network, the results highlighted the necessity to define a better training strategy.

Conclusions
The coupling of MOHID with optimization algorithms can considerably give agility to calibration procedures. Future researches should focus on water quality simulation, which are strongly dependent on a quite large number of parameters.

1 INTRODUCTION

The diagnosis of a given water body is based on the concentration analyses of a number of parameters. The water resources management can also include the simulation of scenarios, which could emerge as a consequence of man's interference in the environment. In this particular regard, mathematical models are useful tools, reducing time, costs and risks in the environmental impact evaluation. The mathematical formulation of these models includes a number of parameters that can assume a range of reasonable values, and a better estimative is crucial to the simulation accuracy. This estimative can be done through trial and error, what, besides being highly time consuming, can lead to values that allow to model calibration for a single and particular scenario only. Further, such strategy can lead to multiple and acceptable solutions. Alternatively, this calibration can be performed by algorithms, as those based on inverse problems techniques. These techniques have been used in different science fields. For water resources modelling purposes, however, not many applications can be found in the literature.

For example, [1] used a modified Newton method to estimate the nonpoint sources of fecal coliform, in order to establish allowable load for the Wye River, USA. Other studies have made use of the Gradient Method, Conjugate Direction Method and Variational Method to estimate parameters usually present in groundwater modelling [2-3]. On the other hand, instead of

parameters, the salinity boundary conditions was estimated by [4] for a three-dimensional tidal hydrodynamic and salinity transport model. In a similar way, [5] proposed a novel algorithm for the estimation of open boundary conditions in rivers systems where tidal forcing is present.

The solution of an inverse problem can be made through optimization algorithms, which attempt to minimize (or maximize) the value of a functional through the modification of its variables. Methods of optimization can be of two types: deterministics, which move with the setting in the sense of optimal, making use of particularities of the functional; and stochastic type, choosing random configuration with the goal of sweeping, stochastically, the entire search space, in the search for the optimum. These methods are usually compared regarding the computational time required to achieve the desired solution. From this point of view, the stochastic methods show advantages if compared with the deterministic ones. Another important feature of optimization methods is that they can be applied to any objective function, regardless the initial value assumed for it, beside the capability of avoid local minimums.

This chapter presents the coupling of optimization methods and neural networks with the MOHID platform, in order to solve an inverse problem, here formulated as the better estimative of bed roughness height and turbulent diffusion coefficient, parameters that can be present in the mathematical formulation of hydrodynamic and transport models. The direct problem focused on here was the simulation of the hydrodynamics and salinity transport in an estuarine environment, the Macaé estuary, Brazil.

1.1 MOHID simulator and the Direct Problem

In this work, the MOHID platform was used to simulate the hydrodynamics and salt transports of Macaé estuary, located at the Brazilian southeast coast (Figure 1). The Macaé basin, which has a population of around 141,000 people, has been submitted to some severe environmental impacts, especially in its estuarine zone. This has motivated the authorities to implement some actions, which includes the computational modelling of estuarine waters. The modelled domain included an extension of approximately 20 km, from the head to the outer region of the estuary, at the coast. It was adopted a spatial discretization of 40 m, based on quadratic cells. The bathymetry data of the coastal region was taken from the nautical chart 1507, edited by the Brazilian Navy in 1974, while the upper region bathymetry was obtained from [6]. Figure 2 shows the discretized domain and the adopted bathymetry implemented in MOHID.

Two boundary conditions were prescribed for the hydrodynamic model: (i) in the riverine boundary it was set a river discharge of 7.8 $m^3 s^{-1}$, typical of the dry season for the Macaé river close to estuarine region [6]; (ii) in the marine boundary it was simulated an astronomic tide with 17 components. A salinity of 0.037 PSU was set for the riverine boundary, and 36 PSU for the sea boundary. As the initial condition, a salinity of 20 PSU was set for the whole domain.

1.2 Formulation of the Inverse Problem

In most of the scientific disciplines, and particularly in engineering, there are problems characterized by differential equations with associated initial and boundary conditions. When

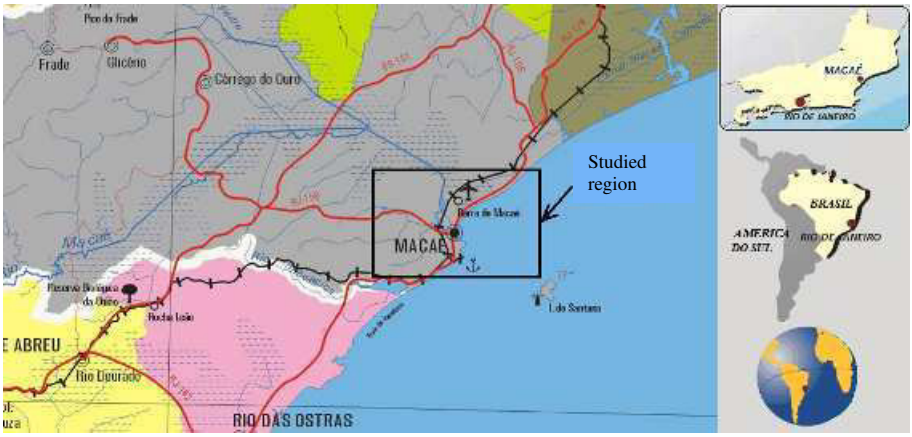

Figure 1. *Estuary location and detail of the simulated region.*

these problems are solved in a direct way, the result is generally a functional relationship or a system of equations, which can be used to calculate values of the dependent variable for given values of the independent variable. The inverse solution of systems of partial differential equations constitutes a complex problem, for which there are no universally accepted methods. Given an applicable direct solution to a system of partial differential equations, it is possible to propose an inverse problem as a problem of optimization. An algorithm to achieve such objective is [7]:

- Suppose a solution θ to the inverse problem. This can include the assumption of an initial or boundary condition, or a typical parameter for a given problem.
- Feed the supposed condition to the direct solution of the partial differential equation system, calculating in this way values of the dependent variable y. Here the output of the direct solution is a vector of values corresponding to the times in which the values of y are measured. This vector of solutions will be denoted as calculated and it will be represented as y'.
- Compare the calculated values y' with the observed ones, measured in consistent times.

The success of this approach is the mechanism through which the supposed condition is improved in the subsequent invocations of the first step. Optimization is the procedure used to upgrade the estimates for the unknown conditions in order to minimize the objective function, given by:

$$SSE(y', \theta) = \sum_{t_i=1}^{N_T} (y(t_i) - y'(t_i, \theta))^2 \tag{1}$$

where θ represents the parameters to be estimated and N_T is the total number of experimental data.

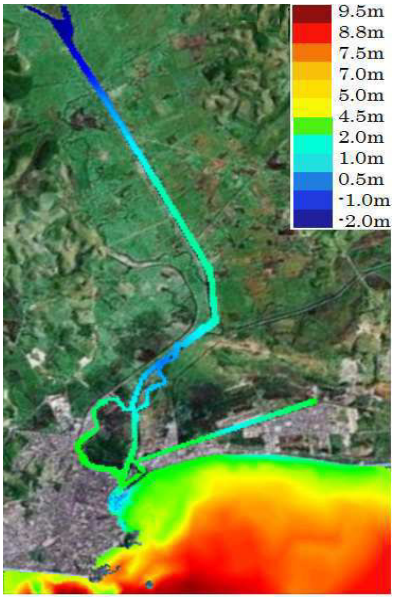

Figure 2. *Simulated domain and model bathymetry used.*

1.3 Parameter estimation in a model of estuarine hydrodynamics

The hydrodynamic and transport models built in the MOHID can be calibrated, for example, by adjusting, respectively, the bed roughness height (R) and the turbulent diffusion coefficient (D). On the other hand, the calibration procedure depends essentially on the field measurements. Regarding this aspect, there are two variables that are more easily obtained, the water level and salinity. Here a sensitivity analyses was performed to identify which of these variables would be more sensitive to the parameters of interest. The Macaé estuary bed is essentially dominated by sand sediments. According to [8], the bed roughness height in this case, must situate between 0.007 m and 0.05 m. On the other hand, the model configuration adopted here (time and space discretization) imposed a restriction regarding the turbulent diffusion coefficient, which might set between 0.01 m^2s^{-1} and 5.0 m^2s^{-1}, a quite large interval, anyway. Figure 3a compares the sensitivity coefficient of parameters in relation to the water level, where a much higher sensitivity in relation to R can be observed. Figure 3b shows the same results for salinity. Unlike water level, this variable is sensitive to both parameters. These results show that salinity simulation should be used in the parameters estimation.

1.4 Optimization Methods

The strategies described in Sub-sections 1.4.1 to 1.4.3 were employed to solve the inverse problem considered here. The Artificial Neural Network, described in 1.4.4 was also used for the inverse problem formulation and solution.

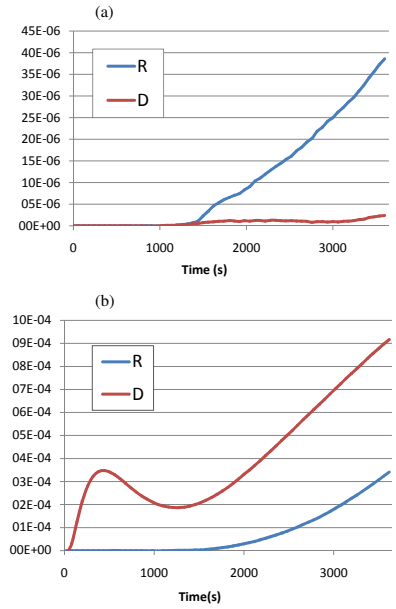

Figure 3. *Sensitivity coefficient of parameters in relation to water level (a) and salinity (b).*

1.4.1 Genetic Algorithm (GA)

The Genetic Algorithm (GA) is a method of Evolutionary Computation with several practical applications. The pseudocode 1 describes the general structure of an Evolutionary Algorithm.

Pseudocode 1: **GA**
$t = 0;$
Create an initial population $P(t);$
WHILE no stopping criterion is satisfied **DO**
Evaluate the fitness of population $P(t);$
Select reproducers from $P(t);$
Generate a new population $P(t+1);$
$t = t+1;$
END WHILE

The GA method is based in three basic operators, namely selection, crossover or recombination and mutation, detailed below:

Selection: selects chromosomes in the population for reproduction. The fitter a chromosome, more likely it is to be selected to reproduce;

Crossover: randomly chooses a locus in the string, which represents the parameters to be estimated. A new and different generation can be created from the exchange between two different strings. The crossover operator roughly mimics biological recombination between two single organisms chromosomes;

Mutation: randomly flips some of the bits in a chromosome. For example, the string 00000100 might be mutated in its second position to yield 01000100. As pointed out by [9], mutation can occur at any position in the string, with a given probability, usually very small (e.g., 0.001).

These algorithms should work in a wide interval range for the parameters values, but with differences in the efficiency, highlighting the importance of the programmer strategy. In the GA, the fitness function evaluates the accuracy of the solution candidates. This function together with execution parameters defines the algorithm completely. Selection, recombination and mutation processes form a generation in the execution of a GA, and are executed until a satisfactory solution – defined by a stopping criterion or a specified number of generations - is reached.

1.4.2 Particle Collision Algorithm (PCA)

The PCA structure resembles the Simulated Annealing structure: first an initial configuration is chosen, then, there is a modification of the old configuration into a new one. The accuracy of these two configurations is compared [10]. A decision is then made on whether the new configuration is ‘‘acceptable” or not. If that is the case, it serves as the old configuration for the next step. If it is not acceptable, the algorithm proceeds with a new change of the old configuration. PCA can also be considered a Metropolis algorithm, as a trial solution can be accepted with a certain probability. This acceptance may avoid the convergence to local optima. The main steps of the PCA are shown in the pseudocode 2 to 6.

Pseudocode 2: **Particle Collision Algorithms**

```
Generate an initial solution Old_Config;
Best_Fit ← Fit(Old_Config);
FOR n = 0 to number of iterations DO
    Perturbation;
    IF Fit(New_Config) < Fit(Old_Config) THEN
        IF Fit(New_Config) <Best_Fit THEN
            Best_Fit ← Fit(New_Config);
            Best_Config ← New_Config;
        END IF
        Old_Config ← New_Config;
        Exploration;
    ELSE
        Scattering;
    END IF
END FOR
```

Pseudocode 3: **Particle Collision Algorithms** (Cont.)

Function **Exploration**

```
FOR n = 0 untill the number of iterations DO
    Small_Perturbation;
    IF Fit(New_Config) < Fit(Old_Config) THEN
        IF Fit(New_Config) <Best_Fit THEN
            Best_Fit ← Fit(New_Config);
            Best_Config ← New_Config;
        END IF
        Old_Config ← New_Config;
    END IF
END FOR
```

Pseudocode 4: **Particle Collision Algorithms** (Cont.)

Function **Scattering**

$$P_{scattering} \leftarrow 1 - \frac{Best\_Fit}{Fit(New\_Config)};$$

```
IF P scattering <Random(0:1) THEN
    Old_Config ← Aleatory solution;
ELSE
    Exploration;
END IF
```

Pseudocode 5: **Particle Collision Algorithms** (Cont.)

Function **Perturbation**

```
FOR i = 0 Untill (dimension of problem − 1) DO
    Upper ← Upper limit [i];
    Lower ← Lower limit [i];
    Rnd ← Random(0:1);
    New_config[i] ← (3.old_config[i]+ (Lower + (Upper-Lower)Rnd))/4;
    IF New_Config[i] >Upper THEN
        New_Config[i] ← Upper limit [i];
    ELSE
        IF New_Config[i] <Lower THEN
            New_Config[i] ← Limite_Inferior[i];
        END IF
    END IF
END FOR
```

Pseudocode 6: **Particle Collision Algorithms** (Cont.)

Function **Small_Perturbation**

```
FOR i = 0 Untill (dimension of problem − 1) DO
    Upper ← Random(1,0:1,2)*Old_Config[i];
    IF Upper> Upper limit [i] THEN
        Upper ← Limite_Superior [i];
    END IF
    Lower ← Random(0,8:1,0)*Old_Config[i];
    IF Lower<Upper limit [i] THEN
        Lower ← Lower limit [i];
    END IF
    Rnd ← Random(0:10);
    New_config[i] ← old_config[i]+((Upper-old_config[i]).Rnd);
    New_config[i] ← New_config[i] - ((old_config[i]-lower).(1-Rnd));
END FOR
```

If the new configuration is better than the old one, the ‘’particle” is ‘’absorbed” and there is an exploration of the neighborhood, searching for an even better solution. Function “Exploration’‘ performs this local search, generating a small stochastic perturbation of the solution inside a loop (inner loop). In the PCA canonical version it is a one-hundred-iteration loop. (see “Small Perturbation’‘ in pseudocode 6). Otherwise, the “particle’‘ is “scattered’‘, which means that the new configuration receives random values within a given acceptable range. The scattering probability (pscattering) is inversely proportional to its quality. A high fitness particle will have a lower scattering probability.

1.4.3 Luus-Jaakola (LJ)

This method was introduced by [11] and its central idea consists on considering an initial broad search region for the parameters to be estimated. Random solutions are generated, whereas the search region becomes smaller as the iterations proceed. Pseudocode 7 describes the main steps of the method, where n_{out} and n_{in} are the numbers of iterations in the external and internal loops, respectively, chosen beforehand. R_j is a diagonal matrix of random numbers between [-0.5, 0.5] and ϵ is the coefficient of contraction of the search space.

1.5 Artificial Neural Network (ANN)

Artificial Neural Networks mimics biological neural networks, concerning their capability to learn and generalize. This is done through the basic structures of neural networks, the neurons. Eq. 2 shows the mathematical representation of a neuron:

$$out = f\left(\sum_{i=1}^{n} w_i d_i\right) \tag{2}$$

Where *out* is the output signal and d_i, is the neuron signals inputs, which are multiplied by weights, w_i, representing the synapses, and *f* is the activation function. The weights definition

is done by a process called training. In a supervised training, two sets are used, one for data entry, called pattern, and another to output, called targets. In this case, the patterns are passed over the network and the weights are adjusted, in a way that the result is the expected target. The most common type of neural network using this type of training is the perceptron [12], which consists of a layer of inputs connected by paths, with weights associated with each neuron, fixed. The training makes use of an iterative tuning, which is repeated until the convergence to the weights is reached, i.e., until the network returns the expected target, defined a *priori* within a given tolerance.

Pseudocode 7: **LJ**

Algorithm **Luus-Jaakola**

Choose an initial search space r^0

Generate an initial solution X^*

FOR i =1 **TO** n_{out} **DO**

FOR j = 1**TO** n_{in} **DO**

$X_j \leftarrow X^* + R_j r_{i-1}$

IF $\mathrm{Fit}(X_j) < \mathrm{Fit}(X^*)$ **THEN**

$X^* \leftarrow X_j$

END IF

END FOR

$r_i = (1-\varepsilon) r_{i-1}$

END FOR

2 RESULTS

Estimation of the parameters of interest was performed using synthetic data generated with MOHID, adopting D and R, respectively, as 2.5 $m^2 s^{-1}$ and 0.025 m. The objective function minimization was done by the GA, PCA and LJ methods.

2.1 Genetic Algorithm (GA)

As experimental data, a total of 60 salinity values generated over a period of one hour of simulation were considered. In the GA, 30 generations were used, with a population of five individuals and crossover and mutation probability of, respectively, 50% and 4%. The estimated values for D and R were respectively of 2.4921 $m^2 s^{-1}$ and 0.0259 m. In order to evaluate de results accuracy, the relative error – $E(t)$ – between simulation and "measured'' data was adopted. Figure 4a presents the time evolution of this error. This time profile motivated a 12 hours (real time) simulation, assuming the same values for the parameters. Figure 4b shows that, even for this larger period of time, the error did not exceed 1%.

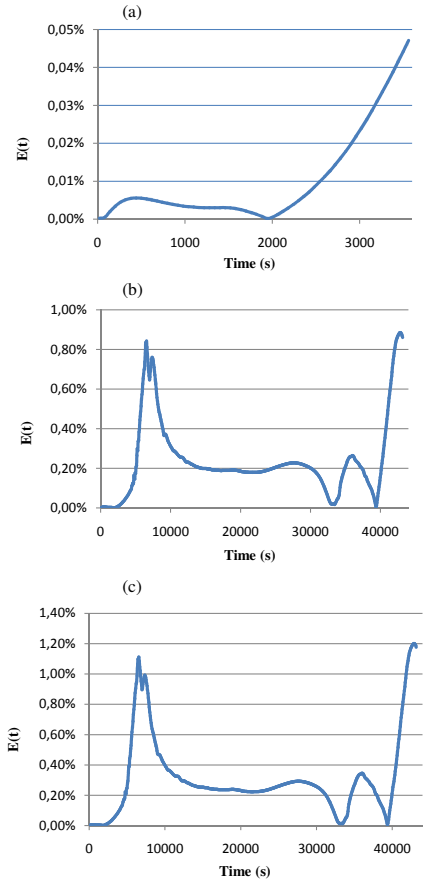

Figure 4. *Salinity relative error from GA estimative for: (a) 1 hour of simulation and considering experimental data acquired in the first hour; (b) 12 hours of simulation, considering experimental data acquired in the first hour; (c) 12 hours of simulation and considering noisy (4%) experimental data acquired in the first two hours.*

To assess the robustness of the method, a noise of 4% was added to the "experimental'' data. Firstly, the estimation was done considering the first hour of "experimental'' data, and poor estimates were obtained, of 1.7976 m^2s^{-1} and 0.0439 m, respectively for D and R. To improve these estimates, a period of 2 hour was considered, yielding to 2.4921 m^2s^{-1} and 0.0262 m, respectively. Figure 4c shows that, although the relative error trends to be larger than that observed with noiseless "experimental'' data, it did not exceed 1.20%.

2.2 Particle Collision Algorithm (PCA)

The same test case (considered in the previews section) was performed with the PCA, using 30 and 7 iterations, respectively for the outer and inner (exploration) loops. This roughly

corresponds to a simulation with the same number of objective function evaluations of those performed in the GA estimates. Figure 5a shows the time evolution of the relative error, considering noiseless "experimental'' data and one hour for estimation period. The worst, best and average results obtained with ten runs of the PCA are compared. It can be observed that even for the worst case, the maximum salinity relative error is of the order of 4.5%. Figure 5b presents the same comparison, with 4% of noise level and two hours for the estimation period. Here, much higher values for $E(t)$ can be observed.

2.3 Luus-Jaakola method (LJ)

In order to keep an equivalent number of objective function evaluations, the Luus-Jaakola method was run adopting internal and external loops of, respectively, 30 and 5, with a contraction coefficient of 0.05 for each test. Figure 6a shows the salinity relative error (worst, best and average) in 12 hours of simulation, considering "experimental'' noiseless data, one hour for estimation period and adopting the estimates after ten runs of LJ. Figure 6b shows the results for another test, when it was considered "experimental'' data with 4% of noise level acquired along the first two hours. The errors in both cases are less than 2.5%

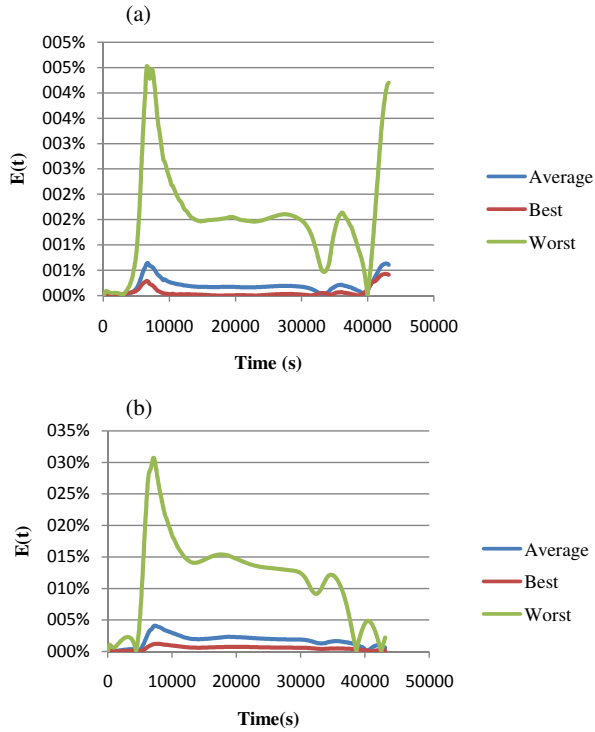

Figure 5. *Salinity relative error from PCA estimative, considering (a) noiseless experimental data and one hour for estimation period and (b) noisy (4%) experimental data and two hours for the estimation period.*

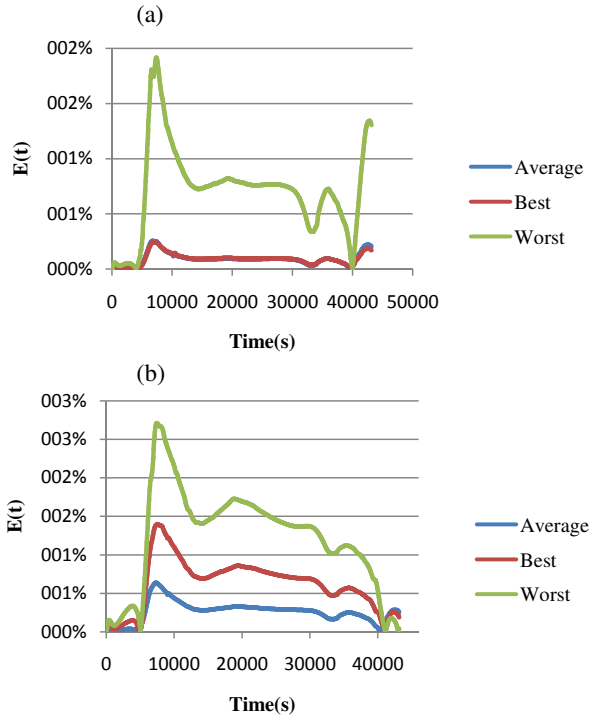

Figure 6. *Salinity relative error from LJ (ten runs) estimative in 12 hour of simulation considering (a) noiseless experimental data and one hour of estimation period and (b) noisy (4%) experimental data and two hours of estimation period.*

2.4 Artificial Neural Network (ANN)

Two ANNs were developed, one with three layers (one hidden), and the other with five layers (three hidden). For both ANNs, the input layer had 60 neurons, and the output layer had two neurons. The input data consisted of a 2 hours salinity time series "measured'' in a given station at low tide. Here the expected ANNs output should be estimated values for mean R and D. Table 1 gives details of test cases.

Table 1. *Adopted test cases for the inverse problem solution using ANNs.*

Test cases	R (m)	D ($m^2 s^{-1}$)
1	0.007	0.1
2	0.007	5.0
3	0.05	0.1
4	0.05	5.0
5	0.025	2.5

The ANNs were trained with 600 patterns. Ten discrete values for R and D, respectively between 0.007 and 0.05 m, and between 0.1 m^2s^{-1} up to 5.0 m^2s^{-1} were considered, generating the first set of 100 training patterns. The other 500 patterns were generated adding noise to the original patterns with respectively following levels: 1%, 2%, 3%, 4% and 5%. The ANNs were trained using 20,000 epochs and the Gradient descent with momentum backpropagation optimization method for weight updating and bias values. In all layers the hyperbolic tangent sigmoid activation function was used. Tables 2 and 3 show the ratios between estimated and exact values for the mean roughness height, R'/R, and the turbulent diffusion coefficient, D'/D, for the five test cases listed in Table 1, respectively, with and without noise (4%) addition. For all these tests an ANN with three layers was used. For comparison, the maximum error between simulation and "observation'', after a 12 hour simulation period, is showed.

The results show poor estimates for the mean R and/or D, with underestimation for both parameters. A marked improvement was observed with the application of a five layers ANN. Regardless this improvement, as a whole, the ANN approach method generated poor estimates for the parameters.

Table 2. *Three layers without noise.*

Test cases	R (m)	D (m^2s^{-1})
1	0.007	0.1
2	0.007	5.0
3	0.05	0.1
4	0.05	5.0
5	0.025	2.5

Table 3. *Three layers with noise of 4%.*

Test cases	R (m)	D (m^2s^{-1})
1	0.007	0.1
2	0.007	5.0
3	0.05	0.1
4	0.05	5.0
5	0.025	2.5

3 CONCLUSIONS

The present work dealt with a complex problem of estimating parameters in an estuarine simulation. The sensitivity analysis demonstrated the convenience of using the salinity as the observable variable. The inverse problem was then solved with three stochastic optimization methods, the Genetic Algorithm, the Particle Collision Algorithm and the Luus-Jaakola Method, coupled to hydrodynamic and transport models solved by MOHID. Artificial Neural

Networks were also used for the solution of the inverse problem. The optimization methods were implemented in a way to guarantee for all of them the same number of evaluations of the objective function, which is critical to define the computation time. With this regard, both GA and LJ had 150 evaluations to the objective function, whereas for the PCA this quantity was controlled by the probability associated with the exploration function calls, resulting in 163 evaluations in this present study.

Generally speaking, the optimization methods showed quite similar performances, with LJ presenting the best results with the lowest computational complexity. Although the GA method showed high efficiency as well, if compared to the other methods, it was disadvantageous due its binary approach, which imposes a limit to the search range (128 discrete values for each parameter in this study). It was also observed that, for all methods, noisy "measurements" required longer periods for estimation. The MOHID coupling with optimization algorithms seems to be a quite promising research area that can aid in the development of automatic calibration procedures.

REFERENCES

1. Shen, J., Jiab, J., Sissona and G. M., 2006. Inverse estimation of nonpoint sources of fecal coliform for establishing allowable load for Wye River, Maryland, Water Research (40): 3333-3342.
2. Sun, N.Z., 1994. Inverse Problems in Groundwater Modeling, Kluwer Academic Publishers, Dordrecht, The Netherlands.
3. Yeh, W.W.G., 1986. Review of parameter identification procedures in ground hydrology: The inverse problem, Water Resour. Res. (22): 95-108.
4. Yang, Z. and Hamrick, J. M., 2004. Optimal control of salinity boundary condition in a tidal model using a variational inverse method, Estuarine, Coastal and Shelf Science (62): 13-24.
5. Strub, I. S., Percelay, J., Stacey, M. T. and Bayen, A. M., 2009. Inverse estimation of open boundary conditions in tidal channels, Ocean Modelling (29): 85-93.
6. Amaral, K., 2003. Macaé River Estuary Computational Modeling as a Tool for the Integrated Management of Water Resources., COPPE/UFRJ /Rio de Janeiro. In Portuguese.
7. Karr, C.L., Yakushin, I. and Nicolosi, K., 2000. Solving inverse initial-value, boundary-value problems via genetic algorithm, Engineering Applications of Artificial Intelligence (13): 625-633.
8. Abbot, M. B. and Basco, D. R., 1989 Computational Fluid Dynamics, an Introduction for Engineers., Logan Group, UK Limited.
9. Melanie, M., 1999. An Introduction to Genetic Algorithms, A Bradford Book The MIT Press Cambridge, Fifth edition.
10. Sacco, W. F., Oliveira, C. R. E. and Pereira, C. M. N. A., 2006. Two stochastic optimization algorithms applied to nuclear reactor core design, Progress in Nuclear Energy (48): 525-539.
11. Luus, R. and Jaakola, T. H. I., 1973. Optimization by Direct Search and Systematic Reduction of the Size of Search Region, AIChE Journal (19): 760-766.
12. Fausett, L., 1994. Fundamentals of Neural Networks, Prentice-Hall, Englewood Cliffs, NJ.

NUMERICAL SIMULATION OF THE 2011 TOHOKU EARTHQUAKE TSUNAMI AND INUNDATION WITH MOHID

S.-K. Hyun • J.-Y. Choi • D.-Y. Lee • K.-H. Cho

CHAPTER SYNOPSIS

Background
From experiences on massive tsunami damages occurred in Indonesia on 25 October 2010 and Japan on 11 March 2011, we have learned that the development of a tsunami forecast system for the northwestern regions of the Pacific Ocean is required. We applied a multi-functional three-dimensional circulation model, MOHID, for the 2011 Tohoku earthquake tsunami and inundation simulations to determine if the model is appropriate to the forecast system.

Results
With three-level nested grids, we carried out tsunami and inundation simulations. In the tsunami simulation, MOHID represented reasonably the tendency of the observed tsunami with respect to tsunami height and arrival time of the maximum height. With the refined grids of 1/150º and 1/600º, the simulated inundation area and height were fairly well matched with a satellite image along the Japanese coast.

Conclusions
It is found that the increase of horizontal resolution in coastal regions up to 1/600º improved the result of coastal inundation showing the good agreement with the satellite image. Overall, it is concluded that MOHID is appropriately applied to the tsunami and inundation forecast system for the northwestern regions of the Pacific Ocean.

1 INTRODUCTION

Most of major tsunamis have been generated by undersea earthquakes. In deep water, tsunamis propagate very fast with long wavelengths and small amplitudes. A leading tsunami wave can be considered as a long wave with a propagating speed that is proportional to $(gh)^{1/2}$, where g is the gravitational constant ($m\,s^{-2}$) and h is the water depth (m). However, tsunami approaches shore where the water depth becomes shallow, the amplitude of the tsunami increases and the wavelength decreases. A tsunami can cause severe coastal flooding and property damages [1]. Historically tsunamis have rarely occurred around Korea peninsula. However, once the tsunamis happen in the East Sea, they make massive damages to the Korean, Japanese, and Russian coasts. Among the tsunamis occurred in the East Sea, the ones on 26 May 1983 and 12 July 1993 influenced the east coast of Korea. In particular, the tsunami in 1983 brought big inundation damages on Mukho and Imwon Harbors [2].

With increasing the activities of the earthquakes occurred in Chile on 27 February 2010, Indonesia on 25 October 2010, and Japan on 11 March 2011, we have learned that Korea is not a safe zone from the sea earthquakes and the corresponding tsunamis. It deserves to develop a tsunami forecasting system for the East Sea, the Yellow Sea, and the regional seas of Korea using an appropriate numerical model. Therefore, in the present study, the objectives are to investigate the propagation of the tsunami wave and inundation caused by the earthquake occurred in Japan on 11 March 2011 using a multi-functional three-dimensional

circulation model, MOHID, and to examine MOHID's applicability for the tsunami and inundation simulations. MOHID will be applied for the initial surface deformation estimated by elastic finite fault plane theory which represents the instantaneous seafloor rupture [3, 4].

2 INFORMATION OF SIMULATION

2.1 2011 Japan Earthquake and Tsunami

A massive earthquake of moment magnitude (M_w) of 9.0 occurred at 05:46 (UTC) on 11 March 2011, off the eastern coast of Japan (Tohoku region). This earthquake, 'the 2011 off the Pacific coast of Tohoku Earthquake' named by the Japan Meteorological Agency [5], is the largest one recorded in Japan. The focal area estimated from the distribution of aftershocks stretches about 500 km long and 200 km wide offshore [6]. Its epicenter was approximately 70 km east of the Oshika Peninsula, its hypocenter was located about 130 km east-southeast off Oshika Peninsula, and the observed maximum slip was approximately 24 m near the hypocenter [7]. The earthquake triggered the devastating tsunami waves which reached heights of up to 39.7 m in Miyako in Tohoku's Iwate Prefecture and caused the maximum inundation height (19.5 m) on the Sendai Plain, and the tsunami bore propagated more than 5 km inland [8]. The amplified tsunami can be formed through topographic refraction when tsunamis travel along ocean ridges and seamount chains in the Pacific Ocean [9]. The tsunami caused the tremendous loss of ten thousand lives and an astronomical damage cost (309 billion USD). JMA reported offshore tsunami heights recorded from wave height meter buoys were 6.3 m at Miyako, 6.0 m at Kuji, and 6.0 m at Miyagi.

2.2 MOHID modelling system and measurements

The MOHID Water Modeling System [10] was applied to estimate the tsunami wave propagation and inundation along the north-east coast of Japan during 2011 Tohoku earthquake. A three-level nesting scheme was used for tsunami simulations (Figure 1). As described in Table 1, the numerical experiments for 2011 Japan tsunami were carried out with three different level grids in horizontal. For the tsunami simulation, a resolution of $1/30^o$ ($\sim$3.6 km) is used at the Level-1 grid which is ranging from 25.0^o to 47.0^o N in latitude and from 127.3333^o to 157.0^o E in longitude. The result of the tsunami wave propagation computed at the Level-1 grid will be compared with the tsunami data observed by NOAA National Data Buoy Center (NDBC) and UNESCO/IOC Sea Level Station Monitoring Facility.

The experiment for tsunami inundation is performed at the Level-3 grid which resolution is $1/600^o$ ($\sim$180 m) in latitude and longitude because the inundation simulation requires much higher resolution to resolve the wetting and drying areas. The interfacial resolution at the Level-2 grid is $1/150^o$ ($\sim$720 m) which is 5 times finer than Level-1 and 4 times coarser than Level-3. To generate Level-1 and Level-2 grids, we utilize ETOPO-1 bathymetry dataset obtained from NOAA's National Geophysical Data Center (NGDC) and shoreline data from NOAA coastline extractor. For the Level-3 grid generation, we combined 30-arc second bathymetry data from the General Bathymetric Chart of the Oceans (GEBCO) of the British Oceanographic Data Center (BODC) with 90-m resolution digital elevation model (DEM) data

Table 1. *Information of constructed model system.*

Model	Modeled Area	Resolution	Number of Grid cells		Δt(sec)
			x	y	
Level-1	25.0000~47.0000 °N 127.3333~157.0000 °E	1/30 °	890	660	10
Level-2	37.0~38.7333 °N 140.6000~141.7333 °E	1/150 °	170	260	5
Level-3	37.6467~38.4867 °N 140.7933~141.2666 °E	1/600 °	284	504	5

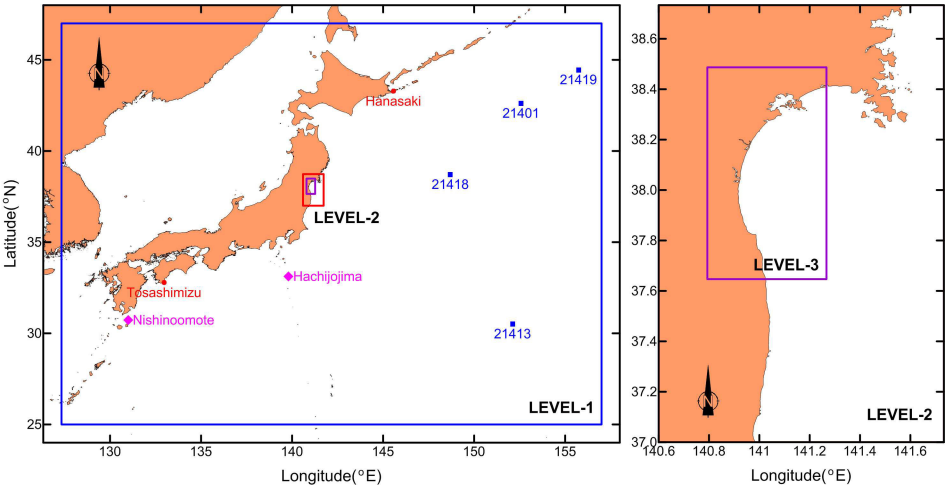

Figure 1. *Simulation domain with three-level nesting grid system including observation stations: DART buoy (blue squares), IOC (red circles), and JCG (pink diamonds).*

from the Shuttle Radar Topography Mission (SRTM3) operated by the U.S. Geological Survey (USGS) (Figure 2). For the tsunami simulation, we considered initial water surface displacement obtained from an elastic fault plane model as an initial condition and simulated until 5 hours after the earthquake occurred. Detailed information on MOHID can be found in [11].

2.3 Tsunami source: Initial water surface displacement

Initial water surface displacement caused by Tohoku earthquake is calculated by the elastic fault plane model [4] which is included in the Cornell Multi-grid Coupled Tsunami model version 1.7 (COMCOT) [12]. The fault model assumed that the water surface displacement is the equivalent of the seafloor deformation since the uplift motion is much faster than the wave propagation. To compute the deformation, fault parameters are necessary to be defined [12]. The definition of fault parameters is depicted in Figure 3. The detailed procedure of elastic fault plane theory can be found in the [3, 4]. In this experiment, fault parameters are determined from double fault data calculated by Geospatial Information Authority of Japan [7]

as described in Table 2. The initial epicenter is located in the position released from JMA (142.861° E, 38.104° N). It is assumed that two rectangular faults are slipped uniformly. Total fault length is approximately 380 km (northern segment: 186 km, southern segment: 194 km) and total moment magnitude is M_w 8.9 (northern segment: M_w 8.8, southern segment: M_w 8.3). Consideration of double faults is suggested to be more reasonable than that of a single fault [13]. Besides, horizontal and sectional distributions of initial water surface displacement calculated by [4] fault model are shown in Figure 4. In the AA' section, the predicted maximum and minimum water heights are approximately 11.2 m and -3.8 m, respectively.

Table 2. *Fault parameters for the 2011 Tohoku earthquake.*

	Lat. (°)	Lon. (°)	Depth (Fault Top, km)	Length (km)	Width (km)	Strike (°)	Dip (°)	Rake (°)	Slip (m)	M_w
Fault 1	38.80	144.00	5.1	186	129	203	16	101	24.7	8.8
Fault 2	37.33	142.80	17.0	194	88	203	15	83	6.1	8.3

3 RESULTS OF SIMULATION

3.1 Tsunami simulation with the first level grid

The tsunami predicted at MOHID Level-1 is compared with sea surface elevation data obtained from three resources: 1) Deep-ocean Assessment and Reporting of Tsunamis (DART) Buoys operated by NOAA National Data Buoy Center (NDBC), 2) UNESCO/IOC seal level station monitoring facility, and 3) Japan Coast Guard (JCG). Tidal signals in observation data were removed through a 3-h high-passed filter [14] to fairly compare with the predicted tsunami. At eight stations (21401, 21413, 21418, 21419, Hanasaki, Tosashimizu, Hachijojima, and Nishinoomote, see Figure 1), the time series comparisons between the predicted and observed tsunamis are plotted in Figure 5. The prediction has a reasonable agreement with the observation showing 10∼45 cm of root-mean-squared-error. Especially, the predicted tsunamis reproduced the observed tsunamis well at offshore stations (21401, 21413, 21418, and 21419) where are less influenced by geometry and topography.

At the Hachijojima and Nishinoomote stations, the model results were reasonably well compared with the observations. However, the comparisons at Japan coastal stations (Hanasaki and Tosashimizu) represented the increase of bias between model result and observation data. This bias seems to be induced by the use of 1/30° resolution in ETOPO-1 topographic data. It seems that wave propagation and deformation induced by depth change were inaccurately computed in the grid generated with low resolution topographic data. Thus, it is expected that the usage of higher resolution bathymetry data may improve the accuracy of tsunami prediction. As shown in Figure 6, horizontal distributions of tsunami height at Level-1are plotted on 5 minutes, 10 minutes, 30 minutes, and 60 minutes after tsunami occurred. The maximum height is generated from the northern segment and spreads to the coastal areas and to the Pacific Ocean.

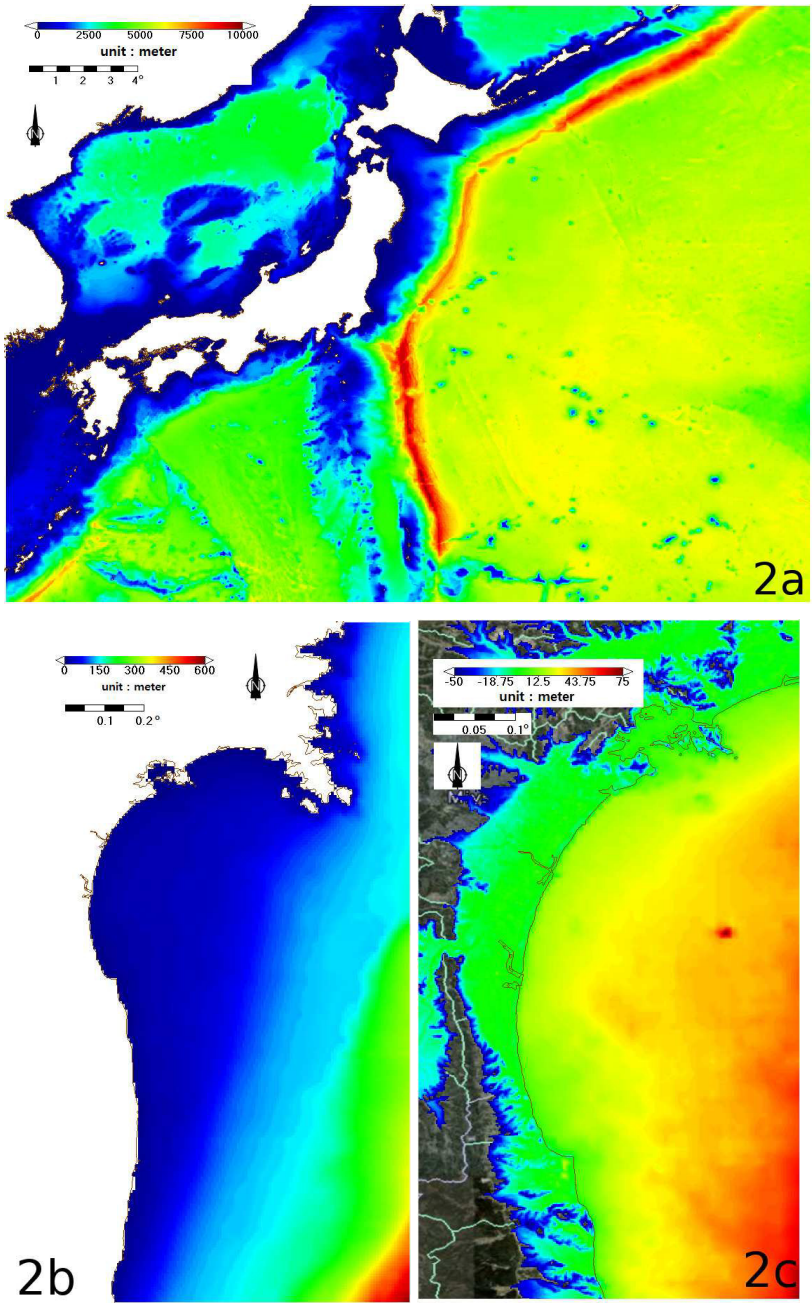

Figure 2. *Applied bathymetry and topography to the three-level nesting grid system: (a) Level-1, (b) Level-2, and (c) Level-3.*

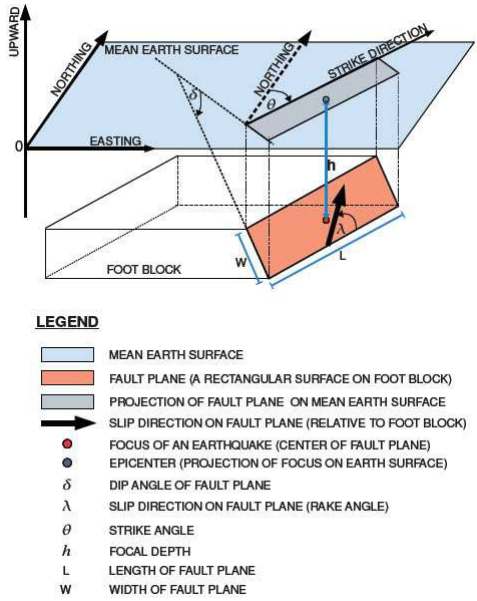

Figure 3. *Sketch of a fault plane and fault parameter definitions [12].*

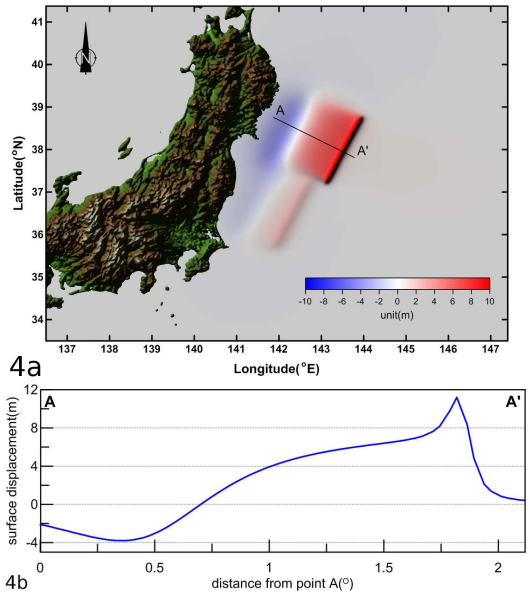

Figure 4. *Tsunami source estimated by a fault plane model. (a) Horizontal initial water surface displacement and (b) Surface displacement from A to A'.*

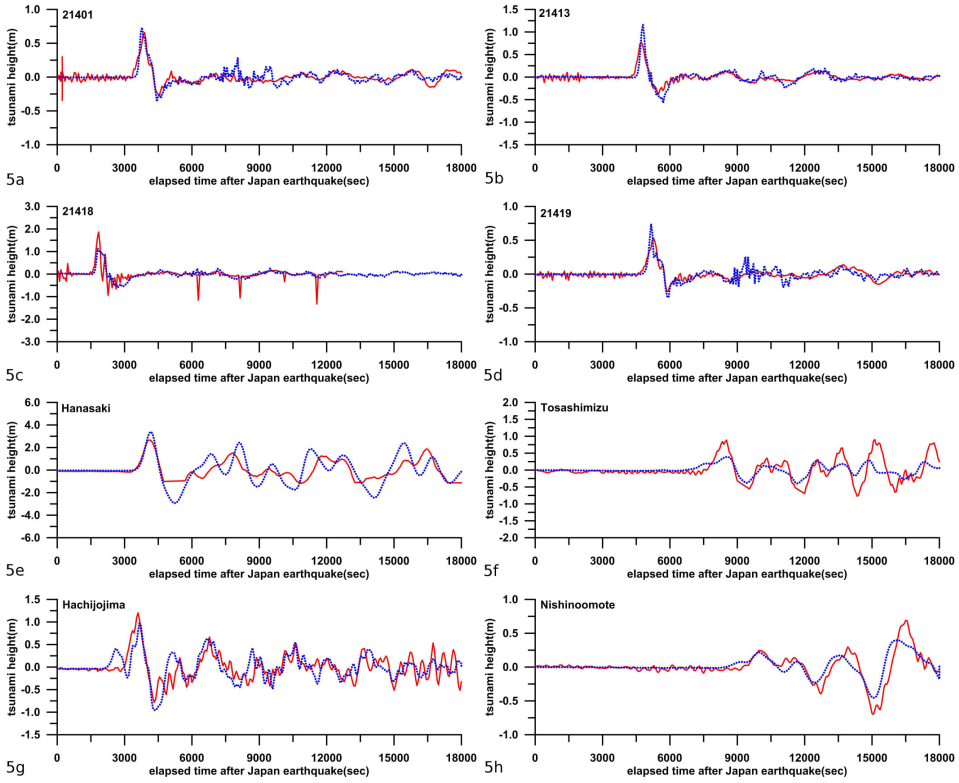

Figure 5. *Comparisons of tsunami height between the observed data (red) and computed results (blue).*

We estimated the arrival time of the first maximum tsunami peak to individual stations to evaluate the model performance. As shown in Table 3, the peak time differences between the observed and the predicted at all stations were within two minutes and it is confirmed that the corresponding tsunami wave speeds were computed reasonably well. A snapshot of the maximum tsunami height predicted at Level-1 during 5-hour simulation period is depicted in Figure 7. The maximum tsunami heights are concentrated on the northern segment of faults and the eastern coast of Japan. In the coastal region of Miyako, the highest maximum value is approximately 23.8 m which is nearly 40% less than the observation.

3.2 Inundation simulation with higher level grids

To predict the influence of inundation induced by tsunami on the Japanese coast, the second-level nesting experiments are implemented using the refined grids of 1/150 ^{o} (Level-2) and 1/600^{o} (Level-3). Figure 8 represents the inundation areas with tsunami height compared with the TerraSAR-X image taken by the Center for Satellite Based Crisis Information (ZKI) on 12 March 2011. We overlapped the model result onto the satellite image. The simulated inundation areas (purple) are fairly well matched with the TerraSAR-X inundation areas (blue) along the Japanese coast. The along-shore distribution of the inundation height in the

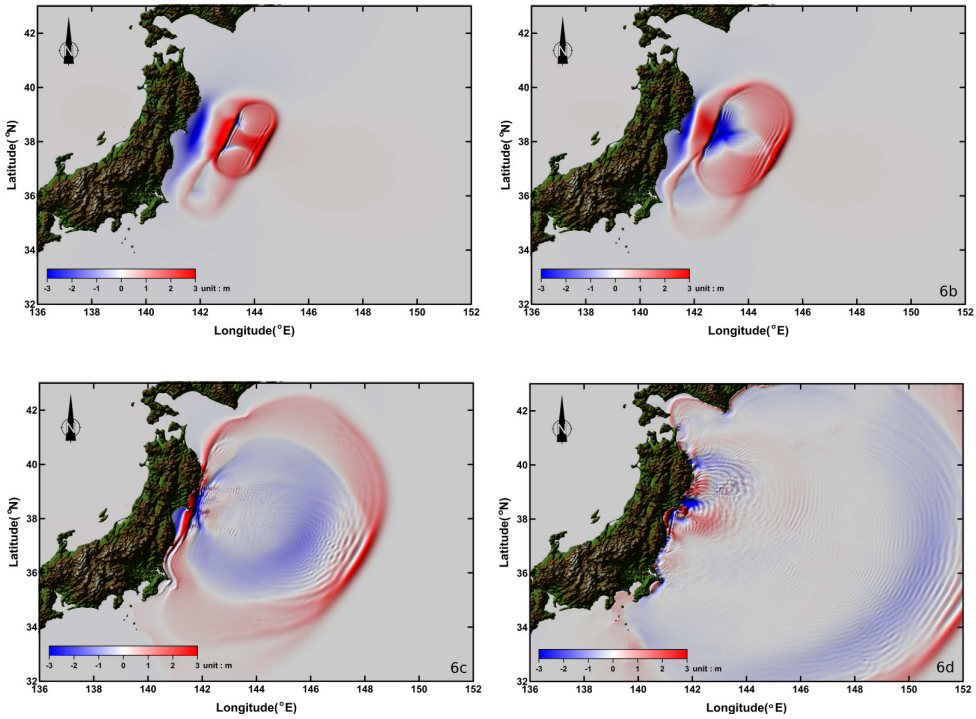

Figure 6. *Horizontal distributions of the modelled tsunami height snapshotted at (a) 5 minutes, (b) 10 minutes, (c) 30 minutes, and (d) 60 minutes after the earthquake.*

uppermost water cells is depicted in Figure 9. The inundation heights were estimated at the survey locations (Figure 9a). The survey data are obtained from The 2011 Tohoku Earthquake Tsunami Joint Survey Group [15] and available at ftp://ftp.agu.org/apend/gl/2011gl049210 [8]. The predicted inundation heights (blue in Figure 9b) were compared with the measured inundation heights (red in Figure 9b). The inundation heights around Natori, Iwanuma, Watari, and Arahama areas were fairly well matched with measurements even though those near Miyagi and Sendai areas were underestimated. It is expected that the use of much higher resolution of bathymetry and geometry data can improve the model results.

4 DISCUSSION AND SUMMARY

In the tsunami simulation for the Japan Tohoku Earthquake in 2011, the MOHID represented reasonably the tendency of the observed tsunami. In Level-1 (1/30^o) simulation, tsunami bias at onshore stations is larger than that at offshore stations due to the coarse grid which may not accurately resolve the bathymetry and coastline. However, the predicted arrival time of the first maximum tsunami wave is well matched with the observation record lagged within only 2 minutes. The increase of horizontal resolution in coastal regions up to 1/600^o (Level-3) improved the result of coastal inundation induced by tsunami waves showing the good agreement with the satellite image.

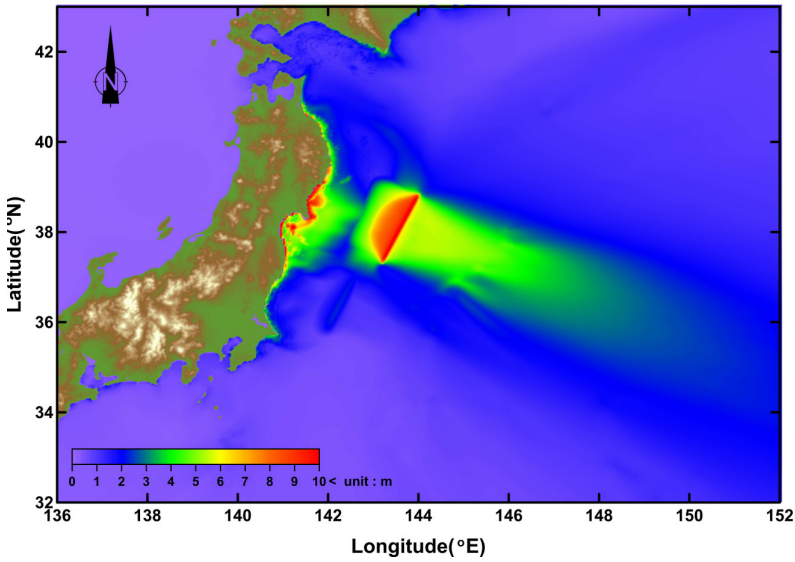

Figure 7. *Maximum tsunami height during 5 hours computed in Level-1 simulation.*

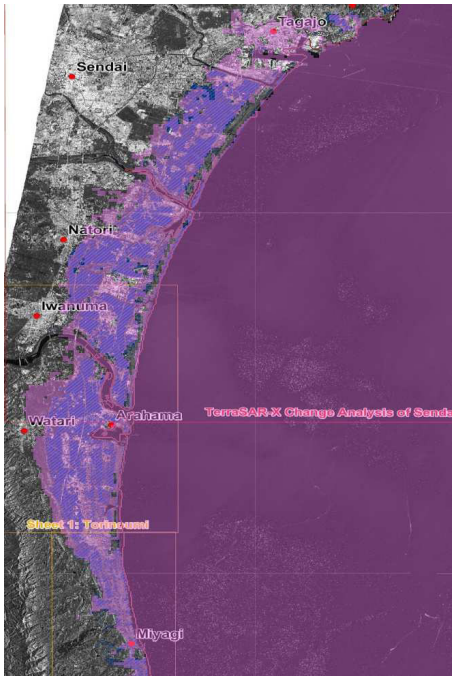

Figure 8. *Comparison of the computed inundation area (purple) with the TerraSAR-X satellite image (blue-shaded).*

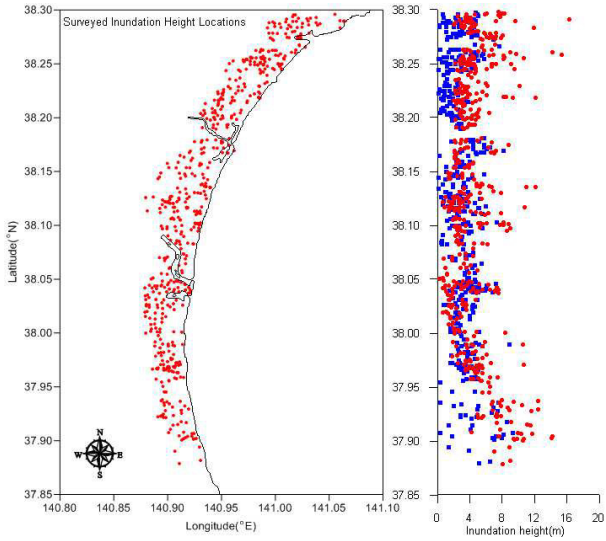

Figure 9. *Survey locations for inundation height (left) and comparison of inundation height (right) between observations (red dots) and computed results (blue squares).*

Table 3. *Arrival time of the first maximum tsunami wave heights at the stations with comparisons between observations and predictions.*

station	Arrival time in minutes	
	observed	calculated
21401	65	63
21413	79	80
21418	31	30
21419	88	86
Hanasaki	68	69
Tosashimizu	142	142
Hachijojima	60	61
Nishinoomote	166	166

A further study is required to quantitatively analyze the model skill comparing the inundation areas and inundated water volume. The inundation height comparison with observation suggests that a higher resolution grid model with more accurate coastal bathymetry and topography data improves the tsunami height and inundation prediction. It is notable that a model grid which does not resolve the barriers and structures to protect tsunami waves is insufficient to predict inundation height and run-up height on the local areas, because sea walls, barriers, structures, and debris may play important roles in changing local tsunami propagation. Furthermore, the tsunami and inundation prediction needs to be combined with the external forcing such as tides, currents, and winds in a real-time oceanic forecast system to warn the tsunami coming immediately.

ACKNOWLEDGEMENTS

This research is a part of the project titled ‘’Development of Korea Operational Oceanographic System (KOOS)” funded by the Ministry of Land, Transport and Maritime Affairs, Korea.

REFERENCES

1. Liu, P. L.-F., S.-B. Woo, and Y.-S. Cho, 1998. Computer programs for tsunami propagation and inundation, Cornell University.
2. Choi, B.-H., S.-J. Hong, S.-B. Woo, and E. Pelinovsky, 2000. Computation of Tsunamis in the East Sea using Dynamically Interfaced Nested Model. Korean Society of Coastal and Ocean Engineers, 11, pp. 47-54.
3. Mansinha, L. and D. E. Smylie, 1971. The displacement fields of inclined faults. Bulletin of Seismological Society of America, 61, pp. 1433-1440.
4. Okada, Y., 1985. Surface deformation due to shear and tensile faults in a half-space. Bulletin of Seismological Society of America, 75, pp. 1135-1154.
5. Japan Meteorological Agency (JMA), 2011: `www.jma.go.jp/jma/en/2011_Earthquake.html`.
6. Sato, M., T. Ishikawa, N. Ujihara, S. Yoshida, M. Fujita, M. Mochizuki, and A. Asada, 2011. Displacement above the hypocenter of the 2011 Tohoku-Oki Earthquake. Science, 332, 1395
7. Geospatial Information Authority of Japan (GSI), 2011: `www.gsi.go.jp/cais/topic110422-index-e.html`.
8. Mori, N., T. Takahashi, T. Yasuda, and H. Yanagisawa, 2011. Survey of 2011 Tohoku earthquake tsunami inundation and run-up. Geophysical Research Letters, 38, L00G14, doi:10.1029/2011GL049210.
9. Song, Y.T, I. Fukumori, C.K. Shum, and Y. Yi, 2012. Merging tsunamis of the 2011 Tohoku-Oki earthquake detected over the open ocean. Geophysical Research Letters, 39, L05606, doi:10.1029/2011GL050767.
10. Cancino L, Neves R. 1999. Hydrodynamic and sediment suspension modelling in estuarine systems. Part I: Description of the numerical models. Journal of Marine Systems, 22, pp. 105-116.
11. Ribeiro, J., A. Silva, and P. Leitão, 2011. High resolution tsunami modelling for the evaluation of potential risk areas in Setúbal (Portugal). Natural Hazards and Earth System Science, 11, pp. 2371-2380.
12. Wang, X., 2009. User manual for COMCOT version 1.7. Cornell University.
13. Bae, J.S., Y.J. Cho, S.J. Kwon, and S.B. Yoon, 2012. Numerical analyses of 2011 East Japan tsunami propagation towards Korean peninsula. Journal of Korean Society of Coastal and Ocean Engineers, 24, pp. 66-76 (In Korean).
14. Rabiner, L. and B. Gold, 1975. Theory and application of digital signal processing. Prentice-Hall, Englewood Cliffs, New Jersey.
15. The 2011 Tohoku Earthquake Tsunami Joint Survey Group, 2011. Nationwide field survey of the 2011 off the Pacific coast of Tohoku earthquake tsunami, Journal of Japan Society of Civil Engineers, 67, pp. 63-66.

MOHID AS A TOOL TO EVALUATE THE IMPACT OF WATER DISCHARGE FROM DAMS ON THE ADVECTION OF ESTUARINE FISH LARVAL STAGES

P. Morais • F. Martins • M. A. Chícharo • J. Lopes • L. Chícharo

CHAPTER SYNOPSIS

Background
The impoundment of rivers by dams is the biggest direct anthropogenic impact on the hydrological cycle. The utility of dams, as providers of water for human consumption, irrigation and electrical production, is undeniable. However, the price to pay, weighting benefits versus ecological impacts caused by dams, is enormous and often questionable. The deleterious ecological impacts caused by dams are detected at the dam's site are and at hundreds of kilometers downstream from dams, even in estuaries and coastal areas.
The uncontrolled water discharge from dams, both high volumes of water and inappropriate timing, compromise fish recruitment because eggs are flushed from estuarine spawning and nursery areas. Thus, our goal was to develop an hydrodynamic modelling approach that evaluates the impact of water discharge from dams on the advection of fish larval stages off estuaries and into coastal areas. This goal was accomplished by merging the abundance of anchovy eggs along the Guadiana estuary in MOHID.

Results
MOHID hydrodynamic model for the Guadiana estuary was able to replicate the spawning and nursery areas of anchovy, as well as the general distribution pattern of younger anchovy larvae observed in this estuary in June 2002. Seven river discharge scenarios, each lasting for 10 days, were tested. Scenarios B (Q_{max} = 20 $m^3 s^{-1}$) and C2 (Q_{max} = 50 $m^3 s^{-1}$, sudden end at day 5) reduce the abundance of anchovy larval stages in their spawning and nursery areas by 17% and 47%, respectively.
Theoretically, these two scenarios can solve the eutrophication problem in the upper Guadiana estuary and, simultaneously, do not flush a significant quantity of fish eggs to the coast. Scenario C2 is preferable to scenario C1(Q_{max} = 50 $m^3 s^{-1}$ slow end) because it requires 30% less water.

Conclusions
MOHID was decisive to choose among the river discharge scenarios defined to solve or mitigate eutrophication problems in the upper Guadiana estuary, and without compromising the nursery function of the estuary. The definitive choice between the two best scenarios for solving the eutrophication problem will depend on the degree of the eutrophication and on the effectiveness of an inexistent monitoring program. This work's approach developed an easy-to-use management tool for Guadiana managers, serving as an example to other basin managers around the world.

1 INTRODUCTION

Estuaries are highly dynamic systems, where complex interactions occur linking the physical, chemical, geological and biological components [1, 2]. Estuaries undergo anthropogenic impact along their path, and also from the disturbances occurring in the entire basin [3]. Dams are one of such disturbances that cause meaningful deleterious changes to downstream ecosystems [4, 5], forcing estuarine managers to re-act to an upstream-originated event rather than acting on a problem together with dam managers.

The achievement of sustainable water management, i.e. to manage water resources taking into account the needs of present and future users, is being attained with the implementation of UNESCO International Hydrological Programmes (UNESCO-IHP) [6]. The joint efforts of UNESCO-IHP and the Man and Biosphere Programme set the concepts and principles of Ecohydrology, and defined as the study of functional inter-relations between hydrology and biota [7]. Ecohydrology advocates that sustainable management and development of water resources is possible by restoring and maintaining evolutionary established processes of water and nutrient circulation and energy flow at the basin scale [8].

The ecohydrological approach was initially applied in freshwater ecosystems [9-11], and then expanded to estuarine and coastal ecosystems [12]. In the Guadiana estuary (SW Iberian Peninsula) (Figure 1), the ecohydrological approach is pursued since 1996 [13-16]. The ecosystem health of this estuary is regulated by bottom-up and top-down processes [14], which are threatened by dam's river flow regulation [16].

Successful estuarine and coastal management demands an Ecohydrology-based and basin-wide management, focused on how to adapt, mitigate and restore the functioning of estuaries and coastal areas impacted by dams [15]. For example, controlling eutrophication and preventing harmful algal blooms may occur when the magnitude and periodicity of dams' hydraulic flushing and nutrient loading are large [17]. In the Guadiana basin, water discharged from dams might be a useful tool to prevent or mitigate eutrophication in the upper estuary [18, 19]. However, unsuitable management practices may cause ecological impacts in the estuary [20], particularly when frequency and intensity of hydraulic flushing are neglected. The prescription of flow pulses should also consider the impact on estuarine fish recruitment, because estuaries are the spawning and nursery areas of many coastal and estuarine fishes [21].

High flow pulses increase the advection of fish eggs off an estuary [16] and compromise fish recruitment, mainly of species with reduced reproductive periods and non-competent larvae (i.e. larvae are unable to regulate their position in the water column) [22]. As an example, the overall abundance of anchovy eggs decreased 99.9% in the Guadiana estuary after an intense river discharge from the Alqueva dam [16]. Thus, our goal was to develop an easy-to-use approach in MOHID to allow dam managers to evaluate the impact of water discharge from dams on fish larval stages advection off estuaries. Fish eggs are excellent natural lagrangian tracers and for validating lagrangian models. In return, these models allow the definition of spawning [23] and nursery areas [24] and infer on larval transport mechanisms [25]. However, finding an appropriate model species and incorporate data on their abundance and distribution in a lagrangian transport model is difficult (consult the next chapter).

In the Guadiana estuary, the most appropriate species to use in lagrangian modelling is the European anchovy (Pisces: Engraulidae - *Engraulis encrasicolus* (Linnaeus, 1758)) (anchovy hereafter). The eggs and larvae of anchovy are identified unambiguously and are an excellent indicator of river flow impacts in the Guadiana estuary [16]. Moreover, anchovy is the most abundant planktivorous fish in this estuary [26], it has a wide reproductive period (March to November) [27], a central position in Guadiana's trophic web [28] and was designated as a potential key species in detecting ecosystem changes [29, 30].

1.1 Requisites that fish larval stages have to comply to be used in lagrangian modelling

Not all larval stages can be used for lagrangian modelling. Field surveys ought to aim to collect data on fish larval stages with pelagic eggs and larvae, undoubtedly identified to species level, abundant and broadly distributed along the study site.

Fish eggs must be pelagic because data on its abundance and distribution has to be used in a lagrangian model. It is also relevant to determine how egg's buoyancy change with salinity, particularly if the study site is deep, if halocline or picnocline exist [31] and if a 3D model is to be implemented. Any species with non-pelagic eggs (e.g. eggs laid on rocks, shells, algae, marine plants) are unsuitable for lagrangian modelling. Recently hatched non-competent larvae are passive tracers, as they only perform micro-adjustments in their position [32, 33]. Larvae's buoyancy change as the yolk sac is absorbed, and larvae might then tend to sink. Larvae become fully competent, i.e. larvae are able to regulate their position in the water column, when the gas bladder and the fin rays are formed. The time until larvae become competent varies within the same population due to temperature-dependent development [34-36]. Competent larvae are unsuited for lagrangian modelling because they exhibit migratory strategies to counter-act currents and tides [37, 38], or because they settle and remain in their preferred habitat [39].

The identification of fish larval stages until species level is difficult and often impossible; particularly the identification of fish eggs [40]. The incorrect identification of fish larval stages compromises the success of the project for disabling correct calibration and interpretation of impacts on a species or population.

The abundance of fish larval stages have to be high enough and with a broad distribution to allow accurate model predictions. Otherwise, the model will not capture the small and abrupt variations observed in nature. Ideally, the species' reproduction period should occur along a broad range of river discharges to allow better model calibration.

Finding a species fulfilling all these requisites is difficult. The European anchovy *E. encrasicolus* is the most suited species to use in the lagrangian models of Portuguese estuaries. This species has pelagic eggs, both eggs and larvae are easily identifiable, larval stages are abundant and present for at least six consecutive months in many Portuguese estuaries [27, 41, 42], therefore comprising distinct river inflow regimes. Other European anchovy populations [43, 44] and other anchovy species are abundant in many European and world estuaries and respective offshore ecosystems [45-49].

1.2 Characteristics of European anchovy larval stages

Anchovy eggs are slightly positive buoyant [50] and its development is temperature dependent [34]. The time elapsed from spawning to hatching vary between 24 h and 67 h in the Guadiana estuary [27].

Anchovy larvae hatch from pelagic eggs and recently hatched larvae ($\sim$3.5 mm) tend to have neutral floatability, due to its huge yolk sac. The yolk sac causes drag and any movement is highly expensive in terms of energy. At this stage, larvae just perform regular short bursts to adjust their position and search for microhabitats with oxygen saturation higher than 60%,

since oxygen is exchanged by cutaneous diffusion until the gills are developed. Anchovy larvae move by active swimming when smaller than 5 mm, because viscosity and drag will force them to stop when they beat-and-glide. Larvae tend to have negative floatability as the yolk sac is consumed. The yolk sac is fully absorbed at day 5 ($\sim$5 mm) and intermittent motion becomes the more efficient way of swimming [32, 33]. The development of the dorsal fin and the gas bladder occurs at days 11 and 13, respectively. The gas bladder is completely formed at day 20 (10 mm), allowing larvae to control their position and perform diel rhythms of vertical migration [51]. Thus, lagrangian tracers released in a hydrodynamic model and set to run for 10 days would correspond to anchovy larvae with ages ranging from 7.2 to 9 days, i.e. before larvae develop the morphological characteristics that allow them to regulate actively their position in the water column [51].

2 STUDY AREA

The Guadiana estuary (SE-Portugal/SW-Spain) (Figure 1) is approximately 76 km long, with an area of 22 km^2 and an average depth of 6.5 m. It is a mesotidal estuary, tide amplitudes range from 1.3 to 3.5 m, and partially stratified at the entrance of the estuary [27], where an average river flow of 150 m^3s^{-1} and tidal prism ($\sim$3 x 10^7 m^3) are observed [52]. The estuary is not stratified, both at high and low tides, during periods of low river inflow [27]. River flow has a striking variability between and within years, since the majority of the basin is under the influence of a climate with Mediterranean characteristics. The annual average temperature varies from 14 °C to 18 °C. Rainfall is irregular among seasons, $\sim$80% occurs during autumn and winter, while summers are very dry. The annual average rainfall fluctuates from 561 mm to 600 mm in the Portuguese basin, however higher variations are expected among years. Climate variability imposes a similar trend to river flow; thus, the average river flows are as follows: dry years, 8 – 63 m^3s^{-1}; average years, 170 – 190 m^3s^{-1}; humid years, 412 – 463 m^3s^{-1} [53].

The main ecological constraints observed in the Guadiana basin are damming, water abstraction from aquifers and water pollution. Even so, the estuary is one of the best preserved estuaries of the Iberian Peninsula. Nevertheless, nowadays it has to deal with i) the impact caused by one of the major European dams, the Alqueva dam, ii) the creation of 110,000 ha of irrigation areas in the surroundings of this dam and iii) the destruction of vast natural areas along the estuary margins to build tourist resorts [3].

The Alqueva dam was inaugurated in 8 February 2002, it is located approximately at 150 km from the river mouth. The Alqueva reservoir is one of the biggest in Europe, with a maximum area of 250 km^2, a perimeter of more than 1000 km and a total capacity of 4150 hm^3 [54]. A proper water management is undoubtedly a challenging task to accomplish in this reservoir, due to the multiple uses that water has, e.g. hydroelectric production and river flow regularization. The major concern that dam managers must have regarding water discharge is to comply with the international political agreement made between Portugal and Spain. This agreement states that the average daily flow in Badajoz (Spain) and Pomarão (Portugal) cannot be lower than 2 m^3s^{-1} and the minimum annual inflow in Badajoz has to vary from 300

Figure 1. *Location of the Guadiana basin in the Iberian Peninsula (Europe).*

hm^3 $year^{-1}$ to 600 hm^3 $year^{-1}$ (except during drought years), but depending on the volume of water stored in dams and precipitation [55]. From the ecological point of view, this agreement does not have into account the dynamics of biota, which depends on the natural variability of river inflow [56].

3 METHODS

Anchovy larval stages were collected monthly in the Guadiana estuary from March 2002 to February 2003, during new moon spring tides at low and high tides. Nine sampling stations were sampled, seven inside the estuary and two in the coastal area. Sampling started at the beginning of the flood in station 1 and continued upstream, towards station 9. Station 1 was re-sampled at the beginning of the ebb; the remaining stations were sampled afterwards (Figure 2). Sub-superficial zooplankton trawls were made with a 250 μm net mesh, equipped with a flowmeter (General Oceanics). Samples were preserved with buffered formaldehyde (4% final concentration) until processing. In each station, vertical profiles of temperature and salinity were recorded with an YSI 6600 probe. In the laboratory, anchovy eggs and larvae were sorted from the zooplankton samples to estimate their abundance.

Data on anchovy eggs abundance and distribution determined in June 2002, when the highest abundance of anchovy eggs was registered, were incorporated in MOHID's lagrangian module.

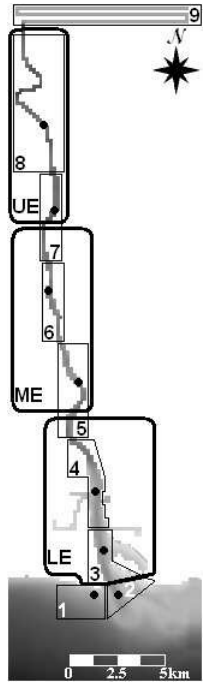

Figure 2. *Grid used in MOHID hydrodynamic model for hydrodynamic simulation of the Guadiana estuary. Legend: Black dots: discharge points and sampling stations; Thick lines: release and monitor boxes used in simulation 1; Thin lines: monitor boxes used in simulation 2.*

3.1 MOHID hydrodynamic model for the Guadiana estuary and simulations' setup

The grid defined to model the hydrodynamic processes in the Guadiana estuary begins in the coast at 5 km from the estuary mouth, ending few kilometers downstream of Alcoutim (station 9). This grid holds ∼45% of the estuary and comprises the area where anchovy eggs were collected (Figure 2). The domain of calculus is made by 205 x 53 cells with a spatial step of 180 x 180 m. The bathymetry was crafted on the grid and one sigma layer was used for the vertical discrimination; thus the model behaves as a 2D depth integrated model. Field measurements of hydrodynamic parameters (water level, velocity and direction) and water properties (salinity and cohesive sediments) were used for calibration purposes [57]. River discharge was determined at 16 km above the tidal limit of the estuary, in Pulo do Lobo hydrometric station (code: 27L/01) [54], where ∼90% of the water going to the estuary passes [58].

A constant river discharge of 5 $m^3 s^{-1}$ (average Guadiana river discharge between the samplings of April and June 2002) was used to stabilize hydrodynamics and salt transport. Then, two simulation setups were set (Figure 3) and tested in seven river discharge scenarios (scenarios A, B, C1, C2, D, E and F) (Figure 4) and two tidal situations, during the weaker neap tides and strongest spring tides of late May and early June 2002, respectively. Scenario A has

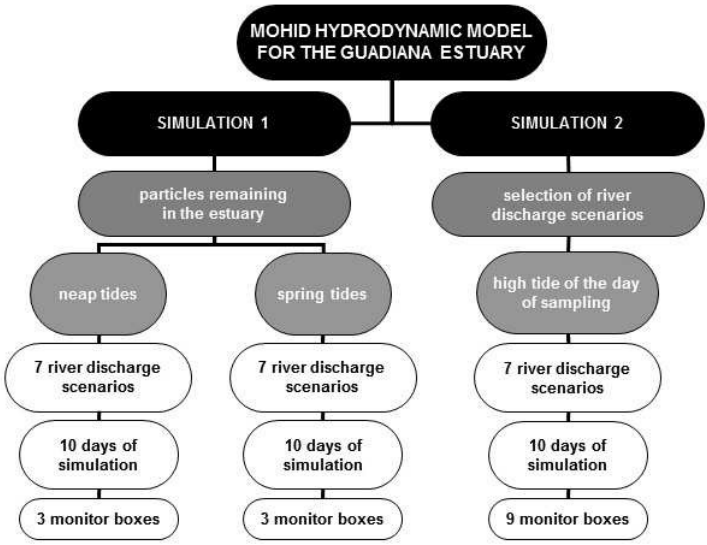

Figure 3. *Summary of the two simulation setups.*

a constant river discharge of 5 m^3s^{-1}, while the remaining six scenarios have maximum river discharges of 20 m^3s^{-1} (scenario B), 50 m^3s^{-1} (scenarios C1 and C2), 100 m^3s^{-1} (scenario D), 250 m^3s^{-1} (scenario E) and 500 m^3s^{-1} (scenario F). In scenarios B to F, the discharge increases steadily during 4 days until reaching the maximum discharge, remains constant for 2 days and then decreases progressively until reaching 5 m^3s^{-1} at day 10, except for scenario C2. This scenario has an abrupt decrease at day 6, from 50 m^3s^{-1} to 5 m^3s^{-1} (Figure 4). Two simulations were set to: Simulation 1) determine the percentage of particles released from the upper, middle and lower Guadiana estuary remaining in the estuary along 10 days and for seven river discharge scenarios; Simulation 2) select the discharge scenario(s) that do not compromise the presence of anchovy eggs and non-competent larvae inside the Guadiana estuary, by merging the abundance of anchovy eggs in the hydrodynamic model.

3.2 Simulation 1 – Percentage of particles remaining in the estuary

Three release and monitor boxes were set, corresponding to the upper, middle and lower estuary (Figure 2). This subdivision was made according to the hydrology, sedimentology and biology of the estuary [13, 40, 59]. The number of particles released in each box was proportional to its volume; thus, 1140, 1110 and 1610 particles were released in the upper, middle and low estuary, respectively. The duration of each simulation was 10 days (Figures 3 and 4). The effect of tides on the number of particles in the estuary at day 10, for each river discharge scenario, was evaluated with a t-test. This analysis compares the means of two groups. Mann-Whitney rank sum test will be used when the Kolmogorov-Smirnov test (with Lilliesfors' correction) reveals that data has not a normal distribution [60].

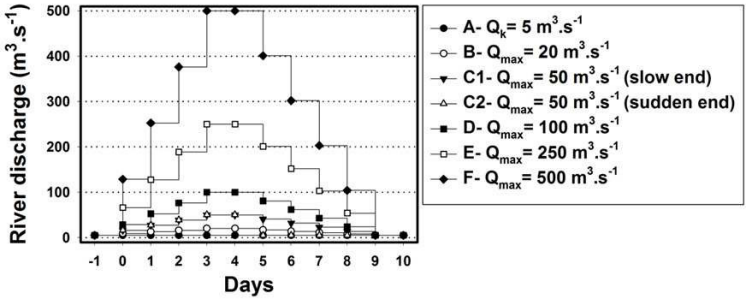

Figure 4. *River discharge scenarios applied in MOHID hydrodynamic model for the Guadiana estuary.*

3.3 Simulation 2 – Selection of river discharge scenarios

The seven river discharge scenarios were tested to select those that do not compromise the presence of anchovy larval stages inside the estuary. The number of particles released in each releasing point was proportional to the abundance of anchovy eggs registered in the survey made during the high tide of June 2002 [27]. Thus, 1, 111, 175, 614, 21064, 6202, 2782 and 13 lagrangian tracers were released in releasing points 1 to 8, respectively. Simulation started at the high tide of the sampling day and lasted for 10 days. The number of particles was calculated in nine monitor boxes, at the high tide of days 5 and 10. Boxes boundaries were set at the half way between stations (boxes 3 to 8) or comprising a particular area (boxes 1, 2 and 9). No particles were released in box 9, but the number of particles entering the box was monitored (Figure 2). The median was calculated because it is less sensitive to extreme scores than the mean, thus providing a better measure of highly skewed distributions [60].

4 RESULTS

4.1 Anchovy eggs and larvae

In June 2002, anchovy eggs were distributed from stations 2 to 7 and were more abundant in the low estuary (stations 3 and 4) during the low tide. At the high tide, the distribution ranged from stations 2 to 8 and were more abundant in the middle estuary (stations 5 to 7). The maximum abundance of anchovy eggs was registered in station 4 at the low tide (1883 eggs 100 $m^{-}3$) and in station 5 at the high tide (2106 eggs 100 $m^{-}3$) (Figure 5A). Maximum larvae abundance was registered in station 5 during the low tide (218 larvae 100 $m^{-}3$) and in station 6 during the high tide (151 larvae 100 $m^{-}3$). Anchovy larvae were collected from stations 4 to 9, but were more abundant in the middle estuary at both tides (Figure 5B). Younger larvae (8.2 ± 0.5 days) were collected in the middle estuary, while older larvae (15.1 ± 4.7 days) were in the upper estuary at station 9 (data not shown) [27].

4.2 Percentage of particles remaining in the estuary (Simulation 1)

The median percentages of particles inside the estuary for each scenario and tide, along 10 days, are summarized in table 1. The number of particles remaining in the estuary after 10

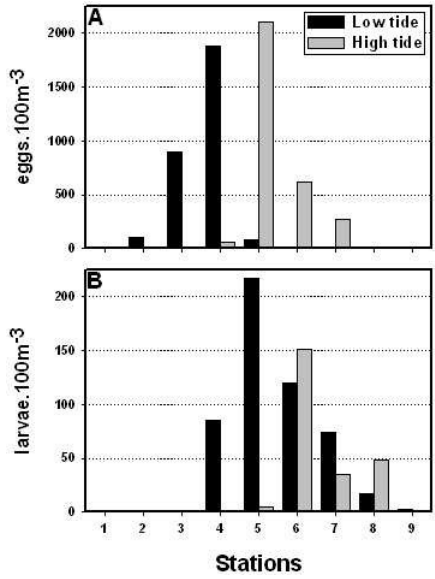

Figure 5. *Abundance of anchovy eggs (A) and larvae (B), in each sampling station, at the low and high tides of June 2002.*

days was significantly lower during spring tides, except for scenario F (Q_{max} = 500 m^3s^{-1}) (for all comparisons, $P \leq 0.001$). Hereafter, the analyzed scenarios correspond only to the spring tide. Thus, in scenario A (Q_k = 5 m^3s^{-1}), 53.3% of the particles remained in the estuary after 10 days. The number of particles in the estuary decreased, as maximum river discharge increased, down to 3.7% in scenario F (Q_{max} = 500 m^3s^{-1}), corresponding to a water residence time of 3.7 days. Scenarios C1 (Q_{max} = 50 m^3s^{-1}slow end) and C2 (Q_{max} = 50 m^3s^{-1} sudden end) are significantly different ($P \leq 0.001$), for the period when river discharge pattern started to differ. The median values were 39.2% (scenario C1) and 39.7% (scenario C2) (Figure 6). The water residence time of the low estuary was 9.5 days in scenario A, decreasing to 1.6 days in scenario F (Figure 7). Also for scenario F, the middle and upper estuary had residence times of 3.8 days and 4.7 days, respectively (Figure 7). For scenarios D, E and F, the particles in the estuary after 10 days correspond to 28.7%, 5.8% and 1.5% of those in the estuary for scenario A, respectively (Figure 6).

4.3 Selection of river discharge scenarios (Simulation 2)

For scenario A (Q_k = 5 m^3s^{-1}), 76.2% and 63.2% of the particles released in each station remained in the estuary after 5 and 10 days, respectively. Particles remained largely in the middle estuary. The distribution pattern of particles along the estuary observed in scenarios B (Q_{max} = 20 m^3s^{-1}), C1 (Q_{max} = 50 m^3s^{-1} slow end) and C2 (Q_{max} = 50 m^3s^{-1} sudden end) was similar to that of scenario A, despite their reduction in the estuary. For scenarios C1 and C2, 67.8% of particles were in the estuary after 5 days, decreasing to 42.6% and 47.6%

after 10 days, respectively. In scenario D (Q_{max} = 100 m^3s^{-1}), 22.5% of particles were in the estuary after 10 days, but their distribution pattern was more even than for the previous scenarios. For scenarios E (Q_{max} = 250 m^3s^{-1}) and F (Q_{max} = 500 m^3s^{-1}), only 5.0% and 4.8% of the particles remained in the low estuary after 10 days, respectively (Figure 8).

Table 1. *Median percentage of particles in the estuary for each tidal condition, throughout the 10 days of simulation.*

Scenarios		Neap	Spring
A	5 m^3s^{-1}	57.8%	53.3%
B	20 $m^3 s^{-1}$	56.5%	50.4%
C1	50 $m^3 s^{-1}$ (slow end)	53.1%	47.0%
C2	50 $m^3 s^{-1}$ (sudden end)	52.3%	47.5%
D	100 $m^3 s^{-1}$	45.3%	39.9%
E	250 $m^3 s^{-1}$	17.4%	14.6%
F	500 $m^3 s^{-1}$	2.6%	3.7%

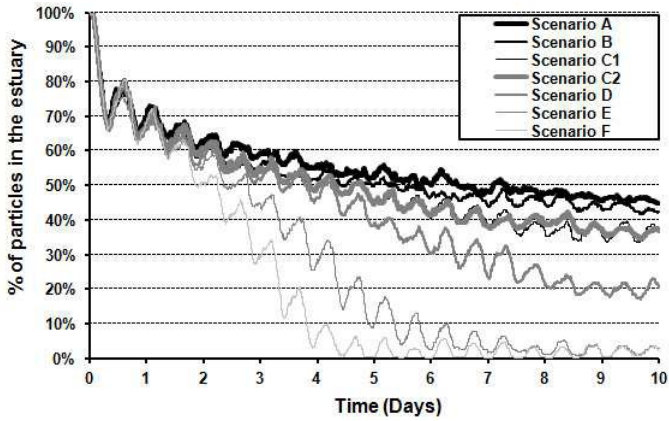

Figure 6. *Percentage of particles remaining in the estuary for each discharge scenarios, throughout the 10 days during the spring tide simulation (Simulation 1).*

5 MANAGING RIVER FLOW IN THE LOWER GUADIANA BASIN

Water and ecosystem management policies are often based on economic decisions, with little concern towards fish conservation [61]. In the Guadiana basin, the political treaties between Portugal and Spain on minimum river flow and annual inflow have also to be considered during management [55]. The ecosystem services provided by the Guadiana to humans are broad and management programs, based on the preservation of these services, require a full

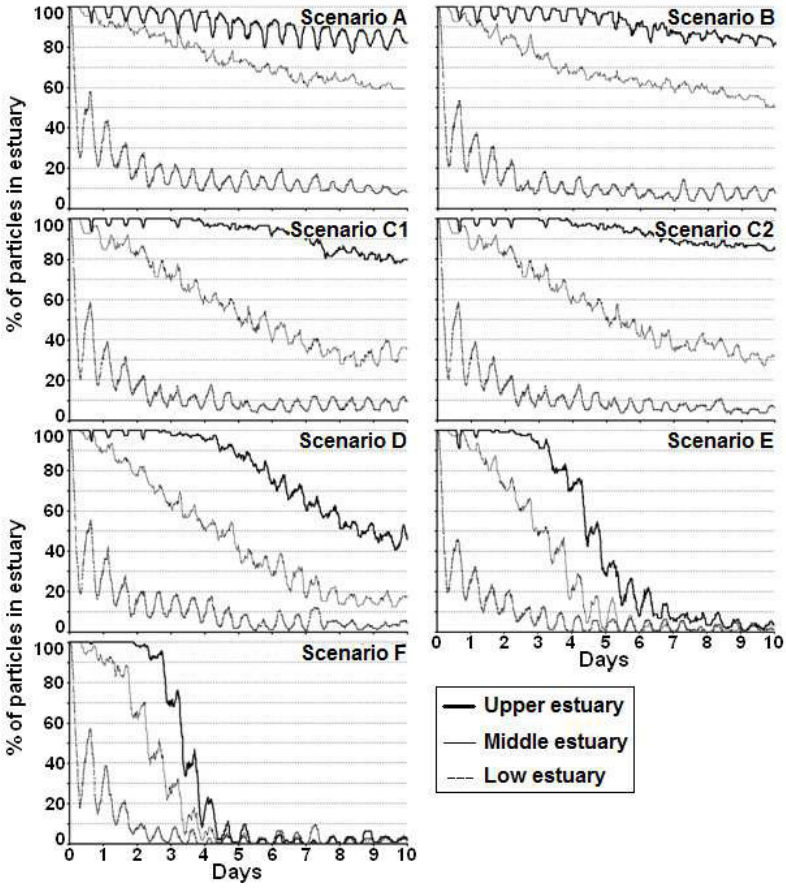

Figure 7. *Percentage of particles in each estuarine section for each discharge scenario, throughout the 10 days of simulation (Simulation 1).*

knowledge of the complexity in which they benefit humans [62]. However, the inexistence of long term monitoring programs in the Guadiana basin, as well as in many worldwide aquatic ecosystems, difficults the proposal of scientific based management policies [63] and the evaluation of how these measures protect nature and benefit humans [62].

The prescription of flushing flows is one of the most important river management tools [64, 65]. Thus, a wise prescription of flushing flows can be made with the approach we developed with MOHID, which take into account the locations of fish spawning and nursery areas. Field observations showed that anchovy was the most abundant pelagic fish in the Guadiana estuary, with one spawning area located in the transition between the low and middle estuary [27]. The approach we applied with MOHID corroborated field observations, since particles released in station 5 (in the transition between the low and middle estuary) were those that better reproduced the distribution pattern of anchovy eggs in the estuary (data not shown)

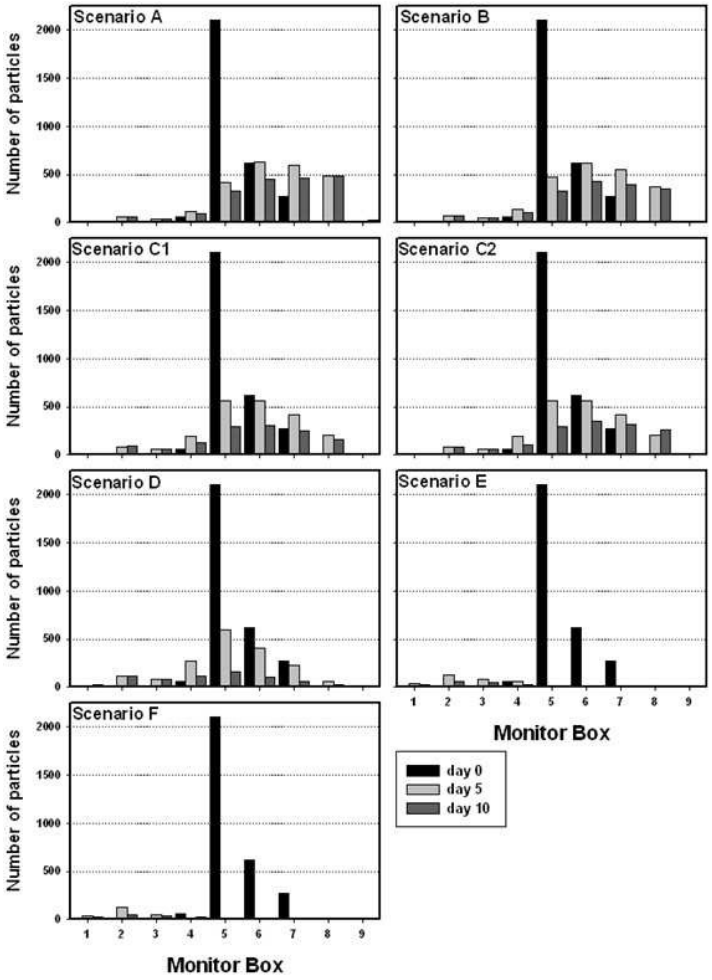

Figure 8. *Number of particles, in each monitor box, at the high tide of days 0, 5 and 10, for each river discharge scenario (Simulation 2).*

[27]. The transition between the low and middle estuary seems to be the best spawning area for anchovy, since circulation patterns and residence times of this area allow larval stages to fulfill their need for exogenous food and develop their capability to actively control their distribution [23, 66]. In this transition zone, the estuary has pronounced S shape morphology, forming secondary flows that enable the retention of particles [77]. This hypothesis explains the marked difference between the number of particles remaining in the low and middle estuary, after 5 and 10 days at $Q = 5\ m^3s^{-1}$. Moreover, there is an upstream residual transport of particles, because the length of the ebb is longer than the flood, even if water velocity is higher during the flood and in periods of low river flow [68, 69].

The distribution pattern of particles obtained with a $Q = 5\ m^3s^{-1}$ after 10 days of simulation is comparable with the one observed for anchovy larvae [27], which had an average age of 8 days and without active swimming abilities [51]. A more analogous pattern could have been obtained if egg and larvae mortality were integrated in the model and if more samples were collected along the estuary. The elder anchovy larvae were found in the upper estuary [27], indicating that they used active retention strategies, other than passive retention mechanisms, to reach this area and remain there [37, 38]. The active retention mechanisms used by anchovy could be: (a) selective tidal stream transport and residual bottom inflow, which might be synchronized with vertical migrations of larvae with formed gas bladder [51]; and (b) lateral migrations to the margins, where the river flow is lower, or to take advantage of the residual up-estuary flow near the margins of the low Guadiana estuary [70]. On the other hand, passive retention mechanisms are exemplified by tidal and wind advection; however in narrow estuaries, as the Guadiana estuary, inert particles seem to be under little effect by these agents [71].

Significant differences in the number of particles remaining in the estuary were calculated between neap tides and spring tides. This means that setting one of the chosen river discharge scenarios should occur during neap tide, because the chances of anchovy larval stages to remain inside the estuary are higher. Scenarios D ($Q_{max} = 100\ m^3s^{-1}$), E ($Q_{max} = 250\ m^3s^{-1}$) and F ($Q_{max} = 500\ m^3s^{-1}$) flush anchovy larval stages from their spawning and nursery areas. In contrast, scenario A ($Q = 5\ m^3s^{-1}$), the low and continuous inflow provides a stationary state of the different biological compartments unlikely to trigger the mitigation/prevention of eutrophication [20]. Thus, depending on the magnitude of the eutrophication in the upper estuary, scenarios B ($Q_{max} = 20\ m^3s^{-1}$), C1 ($Q_{max} = 50\ m^3s^{-1}$ slow end) or C2 ($Q_{max} = 50\ m^3s^{-1}$ sudden end), could be set during the neap tides. The two similar scenarios, scenarios C1 and C2 ($Q_{max} = 50\ m^3s^{-1}$), imply the loss of $\sim$50% of the anchovy larval stages from the estuary, therefore the timing of the pulse (i.e. if it coincides or not with anchovy spawning) and the benefits resulting from this action have to be ecologically and economically evaluated [62, 64]. Scenario C2 is more conservative, i.e. the number of particles remaining inside the estuary is greater, and requires 30% less water. This is a crucial aspect to consider in a region with reduced water resources and highly variable supply [54]. A final choice between scenarios has also to rely on conclusions obtained with plankton experiments [17].

The management tool we developed with MOHID has fish and fisheries conservation into account, it is easy and fast to implement and is a step-forward in modelling the dispersion of fish eggs in estuarine ecosystems. This tool can be applied in estuaries of different structures, circulation patterns and climatic regions, as long as the hydrodynamic model is calibrated and the requisites assigned for fish larval stages to be used in lagrangian models are fulfilled.

The prescription of flow pulses is not restricted to mitigate/prevent eutrophication. The utility of our approach using MOHID can be adapted to test the impact of flow pulses and the simulation of natural flow regimes in refraining the invasion success of non-indigenous species, since invasiveness success is facilitated by the alteration of flow regimes [56]. In the Guadiana estuary, flow pulses or setting natural flow regimes could be useful to refrain

the invasiveness success of the hydromedusae *Blackfordia virginica* (Cnidaria, Hydrozoa), the oriental shrimp *Palaemon macrodactylus* (Crustacea, Decapoda) [72] and the asian clam *Corbicula fluminea* (Bivalvia, Corbiculidae) [73]. Regarding non-indigenous fish, it was shown that natural flow regime per se is unlikely to ensure persistence of native fish assemblages, being necessary a combination of active management of natural flow regimes with concurrently suppressing or excluding the non-indigenous fishes from the fish population [74].

In conclusion, the work we developed with MOHID is an important contribution for the ecohydrological knowledge on the Guadiana estuary. With MOHID, we set river discharge scenarios that would not jeopardize the presence of fish larval stages inside the estuary, in order to solve or mitigate eutrophication in the upper estuary. The results obtained with MOHID are encouraging us to develop a new MOHID module, specifically designed to study the lagrangian transport of fish eggs. The ultimate ecohydrological model has to compulsory merge physical, chemical, biological and hydrological processes in one dynamic model, which ought to be social and economical contextualized. Thus, MOHID has also an important role to play in the ecohydrological management of the Guadiana estuary. The current management paradigm of the Guadiana river flow is primarily based on economical and political premises. However, just a management program guided by robust ecological studies and adequate sociological framework will ensure conservation of the Guadiana estuary and the maintenance of ecosystem services.

ACKNOWLEDGEMENTS

We are grateful to Ana Faria, Anabela Venâncio, Alberto Brito, Antero Fernandes, Isabel Marques, João Janeiro, Luís Cristóvão and Selma Gabriel for their help during this work. Fundação para a Ciência e a Tecnologia (Portugal) funded this work through project ERIC (FCT/P/MAR/15263/1999) and through the scholarships granted to Pedro Morais (SFRH/BD/5187/2001, SFRH/BPD/40832/2007).

REFERENCES

1. Struyf, E., Van Damme, S., Meire, P., 2004. Possible effects of climate change on estuarine nutrient fluxes: a case study in the highly nutrified Schelde estuary (Belgium, The Netherlands). Estuarine, Coastal and Shelf Science, 60: 649-661.
2. Trigo, R.M., Vázques, D.P., Osborn, T.J., Castro-Díez Y., Gámiz-Fortis S., Esteban-Parra M.J., 2004. North Atlantic Oscillation influence on precipitation, river flow and water resources in the Iberian Peninsula. International Journal of Climatology, 24: 925-944.
3. Morais, P., 2008. Review on the major ecosystem impacts caused by damming and watershed development in an Iberian basin (SW-Europe): Focus on the Guadiana estuary. Annales de Limnologie-International Journal of Limnology, 44: 105-117.
4. Ly, C.K., 1980. The role of the Akosombo Dam on the Volta river in causing coastal erosion in central and eastern Ghana (West Africa). Marine Geology, 37: 323-332.
5. Nixon, S.W., 2004. The artificial Nile. American Scientist, 92: 158-165.
6. IHP (International Hydrological Programme), 2007. Updated draft strategic plan for the 7th phase of the IHP (2008-2013). UNESCO, Delft, The Netherlands, 34 p.
7. Zalewski, M., Janauer, G.A., Jolánkai, G., 1997. Ecohydrology- a new paradigm for the sustainable use of aquatic resources. UNESCO International Hydrological Programme- V Technical Documents in Hydrology. UNESCO, Paris, France, 58 p.
8. Chícharo, L., Chícharo, M.A., 2006. Applying the ecohydrology approach to the Guadiana estuary and coastal areas: Lessons learned from dam impacted ecosystems. Estuarine, Coastal and Shelf Science, 70: 1-2.

9. Boruah, S., Biswas, S.P., 2002. Ecohydrology and fisheries of the upper Brahmaputra basin. The Environmentalist, 22: 119-131.
10. Porporato, A., Odorico, P., Laio, F., Ridolfi, L., Rodriguez-Iturbe, I., 2002. Ecohydrology of water-controlled ecosystems. Advances in Water Resources, 25: 1335-1348.
11. Luz, L.D., Loucks, D.P., 2003. Developing habitat suitability criteria for water manage-ment: A case study. International Journal of River Basin Management, 1: 283-295.
12. Wolanski, E., Boorman, L.A., Chícharo, L., Langlois-Saliou, E., Lara, R., Plater, A.J., Uncles, R.J., Zalewski, M., 2004. Ecohydrology as a new tool for sustainable manage-ment of estuaries and coastal waters. Wetlands Ecology and Management, 12: 235-276.
13. Chícharo, M.A., Chícharo, L., Galvão, H., Barbosa, A., Marques, M.H., Andrade, J.P., Esteves, E., Miguel, C., Gouveia, I., 2001. Status of the Guadiana Estuary (south Portugal) during 1996-1998: An ecohydrological approach. Aquatic Ecosystem Health and Management Society, 4: 73-89.
14. Wolanski, E., Chicharo, L., Chicharo, M.A., Morais, P., 2006. An ecohydrology model of the Guadiana Estuary (South Portugal). Estuarine, Coastal and Shelf Science, 70: 132-143.
15. Chícharo, L., Ben Hamadou, R., Amaral, A., Range, P., Mateus, C., Piló, D., Marques, R., Morais, P., Chícharo, M.A., 2009. Application and demonstration of the Ecohydrology approach for the sustainable functioning of the Guadiana estuary (South Portugal). Ecohydrology and Hydrobiology, 9: 55-71.
16. Morais, P., Chícharo, M.A., Chícharo, L., 2009. Changes in a temperate estuary during the filling of the biggest European dam. Science of the Total Environment, 407: 2245-2259.
17. Roelke, D., Augustine, S., Buyukates, Y., 2003. Directing the fall of Darwin's "Grain in the balance": Manipulation of hydraulic flushing as a potential control of phytoplankton dynamics. Texas Water Resources Institute, College Station, USA, 14p.
18. Chícharo, L., Chícharo, M.A., Ben-Hamadou, R., 2006. Use of a hydrotechnical infrastructure (Alqueva Dam) to regulate planktonic assemblages in the Guadiana estuary: Basis for sustainable water and ecosystem services management. Estuarine, Coastal and Shelf Science, 70: 3-18.
19. Sobrino, C., Matthiensen, A., Vidal, S., Galvão, H. 2004. Occurrence of microcystins along the Guadiana estuary. Limnetica, 23: 133-144.
20. Small, M., Bonner, T., Baccus, J., 2009. Hydrologic alteration of the lower Rio Grande terminus: a quantitive assessment. River Research and Applications, 25: 241-252.
21. Blaber, S.J.M., Brewer, D.T., Salini, J.P., 1995. Fish communities and the nursery role of the shallow inshore waters of a tropical bay in the Gulf of Carpentaria, Australia. Estuarine, Coastal and Shelf Science, 40: 177-193.
22. Strydom, N.A., Whitfield, A.K., Paterson, A.W., 2002. Influence of altered freshwater flow regimes on abundance of larval and juvenile *Gilchristella aestuaria* (Pisces: Clupeidae) in the upper reaches of two South African estuaries. Marine and Freshwater Research, 53: 431-438.
23. Page, F.H., Sinclair, M., Naimie, C.E., Loder, J.W., Losier, R.J., Berrien, P.L., Lough, R.G., 1999. Cod and haddock spawning on Georges Bank in relation to water residence times. Fisheries Oceanography, 8: 212-226.
24. Parada, C., van der Lingen, C.D., Mullon, C., Penven, P., 2003. Modelling the effect of buoyancy on the transport of anchovy (*Engraulis capensis*) eggs from spawning to nursery grounds in the southern Benguela: an IBM approach. Fisheries Oceanography, 12: 170-184.
25. Allain, G., Petitgas, P., Grellier, P., Lazure, P., 2003. The selection process from larval to juvenile stages of anchovy (*Engraulis encrasicolus*) in the Bay of Biscay investigated by lagrangian simulations and comparative otolith growth. Fisheries Oceanography, 12: 407-418.
26. Chícharo, M.A., Chícharo, L., Morais, P., 2006. Inter-annual differences of ichthyofauna structure of the Guadiana estuary and adjacent coastal area (SE Portugal/SW Spain): Before and after Alqueva dam construction. Estuarine, Coastal and Shelf Science, 70: 39-51.
27. Morais, P., 2007. The life cycle of *Engraulis encrasicolus sensu lato* in the Guadiana estuary: Ecology, Ecohydrology and Biology. PhD Thesis. Univ. do Algarve, Faro, Portugal, 238 p.

28. Canário, A., 2001. Estudo das condições ambientais no estuário do rio Guadiana e na zona de Vila Real de Santo António. Componente ecosistemas. Diagnóstico da situação actual e definição da situação de referência. CCMAR, Faro, Portugal, 168 p.

29. Chícharo, L., Chícharo, M.A., Esteves, E., Andrade, J.P., Morais, P., 2001. Effects of alterations in fresh water supply on the abundance and distribution of *Engraulis encrasicolus* in the Guadiana estuary and adjacent coastal areas of south Portugal. Ecohydrology and Hydrobiology, 1: 341-345.

30. Chícharo, L., Chícharo, M.A., Morais, P., 2003. Effects of Guadiana river inflow on coastal fisheries. Thalassas, 19: 99-100.

31. Mullon, C., Fréon, P., Parada, C., van der Lingen, C., Huggett, J., 2003. From particles to individuals: modelling the early stages of anchovy (*Engraulis capensis / encrasicolus*) in the southern Benguela. Fisheries Oceanography, 12: 396-406.

32. Weihs, D., 1980. Energetic significance of changes in swimming modes during growth of larval anchovy, *Engraulis mordax*. Fishery Bulletin, 77: 597-604.

33. Weihs, D., 1980. Respiration and depth control as possible reasons for swimming of northern anchovy, *Engraulis mordax*, yolk-sac larvae. Fishery Bulletin, 78: 109-117.

34. Lo, N.C.H., 1985. A model for temperature-dependent northern anchovy egg development and an automated procedure for the assignment of age to staged eggs. NOAA Technical Report NMFS, 36: 43-50.

35. Bernal, M., Borchers, D.L., Valdés, L., Lago de Lanzós, A., Buckland, S.T., 2001. A new ageing method for eggs of fish species with daily spawning synchronicity. Canadian Journal of Fisheries and Aquatic Sciences, 58: 2330-2340.

36. Fox, C.J., Geffen, A.J., Blyth, R., Nash R.D.M., 2003. Temperature-dependent development rates of plaice (*Pleuronectes platessa* L.) eggs from the Irish Sea. Journal of Plankton Research, 25: 1319-1329.

37. Kimura, R., Secor, D.H., Houde, E.D., Piccoli, P.M., 2000. Up-estuary dispersal of young-of-the-year bay anchovy *Anchoa mitchilli* in the Chesapeake Bay: inferences from microprobe analysis of strontium in otoliths. Marine Ecology Progress Series, 208: 217-227.

38. Hare, J.A., Thorrold, S., Walsh, H., Reiss, C., Valle-Levinson, A., Jones, C., 2005. Biophysical mechanisms of larval fish ingress into Chesapeake Bay. Marine Ecology Progress Series, 303: 295-310.

39. Borges, R., 2006. Composition, temporal and spatial patterns of very-nearshore larval fish assemblages at the Arrábida Marine Park. PhD Thesis. Univ. do Algarve, Faro, Portugal, 341 p.

40. Faria, A., Morais, P., Chícharo, M.A., 2006. Ichthyoplankton dynamics in the Guadiana estuary and adjacent coastal area (SE-Portugal/SW-Spain). Estuarine, Coastal and Shelf Science, 70: 85-97.

41. Ré, P., 1984. Ictioplâncton da região central da costa portuguesa e do estuário do Tejo. Ecologia da postura e da fase planctónica de *Sardina pilchardus* (Walbaum, 1792) e de *Engraulis encrasicolus* (Linné, 1758). PhD Thesis. Univ. de Lisboa, Lisboa, Portugal, 425 p.

42. Ribeiro, R., 1991. Ecologia do ictioplâncton e reprodução da anchova *Engraulis encrasicolus* (L.) (Pisces, Engraulidae) no estuário do rio Mondego. PhD Thesis. Univ. de Coimbra, Coimbra, Portugal, 356 p.

43. Sinovčić, G., 2004. Growth and length-weight relationship of the juvenile anchovy, *Engraulis encrasicolus*, in the nursery ground (Zrmanja River estuary-eastern Adriatic Sea). Journal of Applied Ichthyology, 20: 79-80.

44. Drake, P., Borla, A., González-Ortegón, E., Baldó, F., Vilas, C., Fernández-Delgado, C., 2007. Spatio-temporal distribution of early life stages of the European anchovy *Engraulis encrasicolus* L. within a European temperate estuary with regulated freshwater inflow: effects of environmental variables. Journal of Fish Biology, 70: 1689-1709.

45. Viñas, M.D., Negri, R., Ramírez, F.C., Hernández, D., 2002. Zooplankton assemblages and hydrography in the spawning area of anchovy (*Engraulis anchoita*) off Río de la Plata estuary (Argentina-Uruguay). Marine and Freshwater Research, 53: 1031-1043.

46. Wang, Y.-T., Tzeng, W.-N., 1999. Differences in growth rates among cohorts of *Encrasicholina punctifer* and *Engraulis japonicus* larvae in the coastal waters off Tanshui River Estuary, Taiwan, as indicated by otolith microstructure analysis. Journal of Fish Biology, 54: 1002-1016.

47. Iseki, K., Kiyomoto, Y., 1997. Distribution and settling of Japanese anchovy (*Engraulis japonicus*) eggs at the spawning ground off Changjiang River in the East China Sea. Fisheries Oceanography, 6: 205-210.

48. Olney, J.E., 1983. Eggs and early larvae of the bay anchovy, *Anchoa mitchilli*, and the weakfish, *Cynoscion regalis*, in lower Chesapeake Bay with notes on associated ichthyoplankton. Estuaries, 6: 20-35.

49. Yang, J., Arai, T., Liu, H., Miyazaki, N., 2006. Environmental signature in the otolith elemental fingerprint of the tapertail anchovy, *Coilia mystus*, from the Changjiang estuary, China. Journal of Applied Ichthyology, 22: 459-462.

50. Blaxter, J.H.S., 1969. Development: eggs and larvae. In: Fish Physiology, Hoar WS, Randall DJ (Eds). Academic Press, New York, USA, 177-252 pp.

51. Ré, P., 1986. Otolith microstructure and the detection of life history events in sardine and anchovy larvae. Ciência Biológica, 6: 9-18.

52. Michel, D., 1980. Synthese des donnes physiques mesures dans le Rio Guadiana. Evaluation de l'intrusion saline dans l'estuaire. Univ. de Bruxelles, Bruxelles, Belgium.

53. Bettencourt, A., Gomes, V., Dias, J.A., Ferreira, G., Silva, M.C., Costa, L., 2003. Estuários Portugueses. Instituto da Água, Lisboa, Portugal, 300 p.

54. INAG (Instituto Nacional da Água), 2005. http://www.inag.pt.

55. Diário da República, 1999. Resolução da Assembleia da República nº 66/99. Convenção sobre cooperação para a protecção e o aproveitamento sustentável das águas das bacias hidrográficas Luso-Espanholas. Diário da República, 191: 5410-5430.

56. Bunn, S.E., Arthinghton, H., 2002. Basic principles and ecological consequences of altered flow regimes for aquatic biodiversity. Environmental Management, 30: 492-507.

57. Lopes, J., 2004. Modelação matemática do transporte de sedimentos no Estuário do Guadiana. MSc Thesis. Universidade do Minho, Braga, Portugal, 92 p.

58. Ribeiro, O., Lautensach, H., Daveau, S., 1988. Geografia de Portugal. II- O ritmo climático e a paisagem. Edições João Sá da Costa, Lisboa, Portugal, 288 p.

59. Morales, J.A., 1993. Sedimentología del Estuário del Río Guadiana. PhD Thesis. Univ. de Huelva, Huelva, Spain, 322 p.

60. Sokal, R.R., Rolph, F.J., 1981. Biometry. 2nd Edition. W.H. Freeman and Co.: San Francisco.

61. Huckstorf, V., Lewin, W.-C., Wolter, C., 2008. Environmental flow methodologies to protect fisheries resources in human modified large lowland rivers. River Research and Applications, 24: 519-527.

62. Farber, S., Constanza, R., Childers, D.L., Erickson, J., Gross, K., Grove, M., Hopkinson, C.S., Kahn, J., Pincetl, S., Troy, A., Warren, P., Wilson, M., 2006. Linking ecology and economics for ecosystem management. Bioscience, 56: 121-133.

63. Souchon, Y., Sabaton, C., Deibel, R., Reiser, D., Kershner, J., Gard, M., Katopodis, C., Leonard, P., Poff, N.L., Miller, W.J., Lamb, L., 2008. Detecting biological responses to flow management: missed opportunities; future directions. River Research and Applications, 24: 506-518.

64. Chi, J.-H., Chang, N.-B., 2005. Risk assessment for optimal freshwater inflow in response to sustainability indicators in semi-arid coastal bay. Stochastic Environmental Research and Risk Assessment, 19: 111-124.

65. Batalla, R.J., Vericat, D., 2008. Hydrological and sediment transport mechanisms of flushing flows: implications for management in large Mediterranean rivers. River Research and Applications, 25: 297-314.

66. Brown, C.A., Jackson, G.A., Holt, S.A., Holt, G.J., 2005. Spatial and temporal patterns in modelled particle transport to estuarine habitat with comparisons to larval fish settlement patterns. Estuarine, Coastal and Shelf Science, 64: 33-46.

67. Martins, F., Leitão, P., Neves, R., 2002. Simulating vertical water mixing in homogeneous estuaries: the Sado Estuary case. Hydrobiologia, 475/476: 221-227.

68. Fortunato, A.B., Oliveira, A., Alves, E.T., 2002. Circulation and salinity intrusion in the Guadiana estuary. Thalassas, 18: 43-65.

69. Pinto, L.L., Oliveira, A., Fortunato, A.B., Baptista, A.M., 2003. Analysis of the stratification in the Guadiana estuary. Estuarine and Coastal Modelling, 8: 1094-1113.

70. Oliveira, A., Fortunato, A.B., Pinto, L., 2006. Modelling the hydrodynamics and the fate of passive and active organisms in the Guadiana estuary. Estuarine, Coastal and Shelf Science, 70: 76-84.

71. Braunschweig, F., Martins, F., Chambel, P., Neves, R., 2003. A methodology to estimate renewal time scales in estuaries: the Tagus Estuary case. Ocean Dynamics, 53: 137-145.

72. Chícharo, M.A., Leitão, T., Range, P., Gutierrez, C., Morales, J., Morais, P., Chícharo, L. 2009. Alien species in the Guadiana Estuary (SE-Portugal/SW-Spain): *Blackfordia virginica* (Cnidaria, Hydrozoa) and *Palaemon macrodactylus* (Crustacea, Decapoda): potential impacts and mitigation measures. Aquatic Invasions, 4: 501-506

73. Morais, P., Teodósio, J., Reis, J., Chícharo, M.A., Chícharo, L., 2009. The Asian clam *Corbicula fluminea* (Müller, 1774) in the Guadiana River Basin (southwestern Iberian Peninsula): Setting the record straight. Aquatic Invasions, 4: 681-684.

74. Gozlan, R.E., Britton, J.R., Cowx, I., Copp, G.H., 2010. Current knowledge on non-native freshwater fish introductions. Journal of Fish Biology, 76: 751-786.

SARDINE LARVAE VERTICAL MIGRATION AND HORIZONTAL DISPERSION PATTERNS RELATED TO LIGHT INTENSITY IN THE DYNAMIC WESTERN PORTUGUESE COAST: A NUMERICAL STUDY

J. Nogueira • F. J. Campuzano • R. Neves

CHAPTER SYNOPSIS

Background
Sardine is an important traditional fishery in Portugal which recruitment could be affected, among other factors, by oceanographic and atmospheric conditions. Their annual spawning period generally extends between November and April, coinciding with the period when the upwelling episodes are less intense. The sardine larvae present vertical migration strategies that could generally be explained by predatory and survival behaviour. In this work, larvae vertical migration was parameterized using a relation with light availability and implemented into a lagrangian tracers model. A parameterization for sardine was modelled in the Western Portuguese coast using the 3D PCOMS model results to determine the different horizontal dispersion scenarios.

Results
The lagrangian model was applied in two realistic upwelling and downwelling simulations, obtaining the continental shelf retention index with and without vertical migration activation. Modelling results showed that vertical migration increased larvae retention in both scenarios. Thus, indicating a relationship between the spawning period and the typical oceanographic scenarios associated to the dominant atmospheric regimes in this coastal area.

Conclusions
Vertical migration strategies are important for the sardine larvae survival in the Portuguese continental coast, not only because of food abundance or protection from predators, but also because it increases their retention in coastal areas. Modelling tools could contribute on the study of fish larvae mechanistic behavioural providing aid to fisheries management and larvae sampling campaigns design.

1 INTRODUCTION

The significant European sardine *Sardina pilchardus* (hereafter referred only as sardine) recruitment decrease off the Portuguese coast during the 90's [1] led to several studies trying to determine the possible causes. In addition to the overfishing, some oceanographic phenomena were pointed out to explain the problem [2-4]. Ekman offshore transport caused by unusual winter upwelling events, showed an inverse correlation with the sardine and horse mackerel recruitment in the Portuguese Atlantic coast [2], but the interaction between costal currents and river plumes could also provide a vertical retention mechanism responsible for some of the recruitment variability [3]. A numerical study analysing the sardine larvae survival off the Atlantic Portuguese coast pointed out that the intense upwelling conditions during the winter of 1994 could lead to a recruitment decrease [4]. This study suggested that the transport to oligotrophic zones could not only be the reason for the recruitment decrease as changes on temperature patterns could infer some of this variability.

The larva transport along its growth is naturally affected by its own capacity of movement. These movements come from the development of their capacity of horizontal swimming or from its capacity of vertical movements due to the inflation and deflation of the swim bladder.

The locations where the propagules are found at the end of the larval phase are determinant for the juvenile recruitment success [5]. For this reason, it is extremely important that both the hydrodynamic model and the larvae model employed are as realistic as possible [6]. The knowledge about larvae movement is scarce and in most species is limited to the vertical migration movements, justifying its inclusion in most IBMs (Individual Based Models). Vertical migration parameterisation in numerical models has been an important research topic in recent years [7-15].

The sardine spawning season in the Western Portuguese coast usually takes place between November and April [16]. In general during this period, wind predominantly blows from the South inducing downwelling conditions whereas in summer months wind usually blows from the Northeast and coastal circulation is dominated by an upwelling regime. The early phases, eggs and yolk-sac, of the Pacific Sardine *Sardinops sagax* life are around 5.6 days long being followed by the early and late larvae phases that in the sardine case take approximately 11 and 35 days respectively [17]. Prior to the swim bladder activation the sardine larvae could be regarded as part of the planktonic life, and its dispersion is dominated by the oceanic currents.

A functional swim bladder allows active depth selection in the water column in order to find particular physical conditions, high prey density and to protect of eventual predators [18]. Diel swim bladder inflation/deflation rhythm initiates in sardine around age 17 days [19]. This diel migration could be related to phototropism phenomena as the bladders are generally found full of gas during the night period and empty at daytime. The filling process takes place during the twilight by atmospheric air intake [20]. During a research cruise in May 2002, the sardine vertical migration strategy was observed and correlated with daytime and night-time [21].

Due to the vertical migration importance and bearing in mind that the determining factor of these vertical movements is light-related, in this work an atmospheric model was coupled providing instant light intensities to the lagrangian model along the water column. In this approach, during dense cloud cover conditions, larvae could remain for longer at surface after dawn. This hypothesis agrees with the suggestion pointed out by Vikebø et al. [15], where the fish larvae has information related to growth and mortality conditions in the water column. The incorporation of realistic atmospheric values could provide a closer approximation to reality in fish larvae dispersion studies, in particular in the present study to the sardine larvae off the Portuguese coast.

The present work objectives include: to integrate a vertical migration model, based on the light availability computed by an atmospheric model, into a lagrangian model; to verify the influence of the vertical migration in the sardine larvae horizontal dispersion patterns and to associate the sardine vertical migration to their seasonal spawning strategy.

2 METHODS

2.1 PCOMS circulation model

The PCOMS (Portuguese Coast Operational Modelling System) model consists on a fully 3D baroclinic circulation model covering the Iberian Western Atlantic region (Figure 1) that

runs the Mohid model (http://www.mohid.com) with a horizontal resolution of 5.6 km and with 50 vertical layers, 43 in Cartesian coordinates and the top 7 in sigma coordinates, with a resolution of down to 1 m near the surface. The PCOMS model is a downscaling of the Mercator-Océan PSY2V4 [22] and its water levels are obtained from the global tide model FES2004 [23].

The MOHID Water is an open source numerical model included in MOHID Water Modelling System [24] developed since 1985 mainly at the Instituto Superior Técnico (IST) from the Technical University of Lisbon. The model adopted an object oriented philosophy model for surface water bodies which integrates different scales and processes. The core of the model is a fully 3D hydrodynamic model which is coupled to different modules comprising water quality, atmosphere processes, discharges, oil dispersion, mixing zone model for point source discharges, catchment area. The Mohid Water model has been applied to several coastal and estuarine areas and has shown its ability to simulate successfully very different spatial scales from large coastal areas as the northern European Atlantic front or the Western Iberia coast to estuaries and coastal structures [4, 25-28].

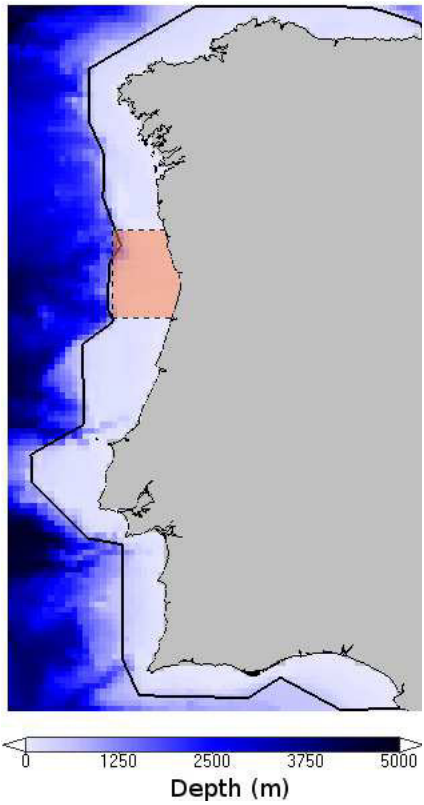

Figure 1. *Bathymetry (color scale) and boxes for the initial larvae particles distribution (broken line)and for calculating the continental shelf particle retention (continuous line).*

The MOHID model is programmed in ANSI FORTRAN 95 using an object orientated philosophy able to simulate eulerian and lagrangian processes. Lagrangian transport model manages the evolution of water parcels and has been used to simulate different processes as near field outfall dispersion, oil spills trajectories and during this work was adapted to include the fish larvae vertical migration as explained in the next section.

The PCOMS is a Mohid application that simulates hydrodynamics since 2009 and biogeochemistry since 2011 in the Western Iberia region. Every day the model hindcasts the previous day, in order to optimize the meteorological forcing, and obtain the following three days forecasts providing a solution which is also used as open ocean boundary conditions for local higher spatial resolution models [29].

The atmospheric forcing for the hydrodynamic model is provided by MM5 model application with 9 km of horizontal resolution running at IST [30]. The forcing includes air temperature, wind intensity and direction, atmospheric pressure, solar radiation and cloud coverage. From the last two properties is obtained the solar radiation that reaches the water surface. The Mohid water model would compute from these values the light extinction in the water column for each grid cell.

2.2 Larvae model

In order to study the larvae dispersion due to the interaction of their movement with the hydrodynamics a larvae lagrangian model was coupled off-line using results from the PCOMS model. Archived hindcasts results for the area shown in Figure 1 were the basis for the simulations of the present work. The time resolution of the PCOMS hindcasts was 15 minutes in order to represent the tidal variations accurately while the lagrangian model was computed using a time step of 180 seconds.

In order to simulate larvae dynamics, the lagrangian larvae model developed by Nogueira [31] was upgraded to compute the vertical migration. Larvae movements were restricted to the vertical direction, thus a vertical velocity term was added to the local vertical advective and diffusive term obtained from the hydrodynamic model while larvae horizontal velocity was given by the PCOMS model velocity.

Bearing in mind that vertical movement is obtained from the balance between the body weight and buoyancy and due to the reduced larvae dimension, it could be assumed that larvae vertical velocity was constant, in other words larvae would reach instantly the terminal velocity. It was assumed for this work that larvae vertical swimming velocity is constant along this life-story stage.

To determine the sardine larvae vertical velocity value, results from an oceanographic cruise conducted in May 2002 were used [21]. Sardine larvae were mainly distributed in the upper 20–25 m and - presented a negative relation with solar radiation, being located during the night near the surface and swimming down began around dawn. Based on this information, it was assumed that during the dusk larvae would swim to a defined minimum depth of 5m and during the dawn larvae would swim away from light to a maximum depth of 30 m. These limits were not rigid as the hydrodynamic model vertical advection could force the lagrangian particles out of these limits; however the particles would swim against these currents to return inside these depth limits.

This conceptual model was parameterised using a scheme related to the light radiation intensity. In absence of light, fish larvae were assumed to swim to the defined top depth limit of 5 meters and when light radiation over the particle exceeded a defined radiation intensity larvae would swim down until a maximum defined depth of 30 m. Since the main spawning period takes place during winter and the maximum defined deep was 30 m, the radiation limit value was considered as the mean light intensity value of at midday during winter (50 W m^{-2}). This value would determine the time spent by fish larvae at different depths. The light radiation at the lagrangian particle depth were obtained from the PCOMS model. According to the permanence time at surface, it was considered that fish larvae could not spend more than 7 hours in swimming the distance between both depth limits corresponding to a vertical swimming speed of 1 mm s^{-1}. This value was also used for different fish species larvae by van der Molen et al. [14].

3 MODEL SIMULATIONS

During wintertime sardine spawn takes place in the entire Western Portuguese coast [16], for this study is was chosen the area studied in Santos et al. [4] that corresponds to the ICES Subdivision IXa – Central North. This area is characterised by a wide continental shelf of around 40 km and gentle slopes until the shelf break, reaching maximum depths around 5000 m in the model domain (Figure 1). Using as reference the larval stage duration estimated of 46 days for the Pacific Sardine *Sardinops sagax* [17] and that the swimming bladder is fully functional for performing vertical migrations at the age of 17 days [19], the simulations consisted on 29 days periods.

To represent realistic upwelling and downwelling scenarios, two different periods for the year 2011 were selected. The first simulation included the period between the 19th May 2011 and the 17th June 2011 that corresponded to a typical summer scenario in the Western Iberia coast with predominant northern winds (see figure 2-top), hereafter referred as the May-June period. This wind regime is associated with upwelling conditions as could be observed in the model horizontal residual velocity (Figure 3-left). This period was characterised by low cloud cover as can be observed in the uniformity of the solar radiation peaks obtained from the MM5 atmospheric model (figure 4-top).

The second simulated period was between the 9th November 2011 and the 8th December 2011 coinciding with winds blowing predominantly from the South (see figure 2-bottom) inducing downwelling conditions (see figure 3-right), hereafter referred as the November-December period. On contraposition with the May-June period, it was registered a high variability of cloud coverage that would severely affect the solar radiation reaching the sea surface (Figure 4-bottom).

The residual velocities are the net velocities obtained after balancing velocities in different directions and they are of particular importance with regard to transport of particulate matter defining persistent currents during the whole simulated period. The horizontal residual velocities for the simulations performed during November-December period show a typical downwelling pattern with a strong poleward current (Figure 4-left). In the May-June period,

the pattern changed dramatically showing an offshore current, typical of an upwelling regime (Figure 4-rigth). These patterns could also be observed in the horizontal residual velocity near the seabed (Figure 5).

For each period, two identical simulations were performed, one with the diel vertical migration implemented, adding the extra vertical velocity to the lagrangian tracers respect to the advection given by the hydrodynamic model and a second simulation with passive lagrangian particles where the vertical velocity was entirely determined by the PCOMS model. All simulations began with 8580 particles uniformly distributed between 10 and 30 m depth released in the box represented in Figure 1. For each simulation, the retention percentage in the continental shelf between the water surface and 100 m deep was obtained using the monitor box defined in Figure 1. The Portuguese continental shelf was assumed to have enough food to avoid larvae starvation during their planktonic life stage.

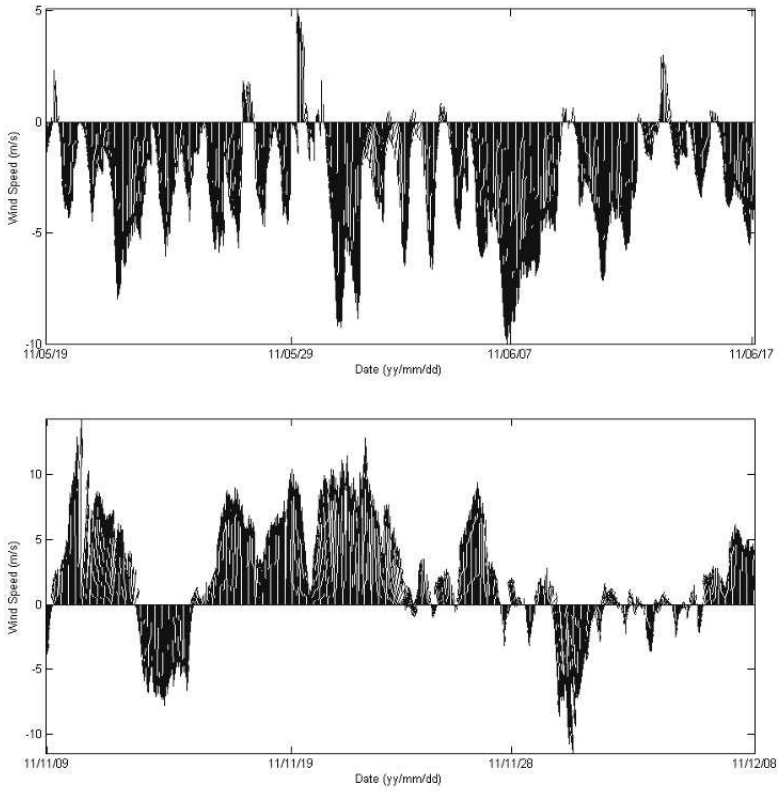

Figure 2. *Wind velocity and direction for the two simulated periods: May-June period (top) and November-December period (bottom).*

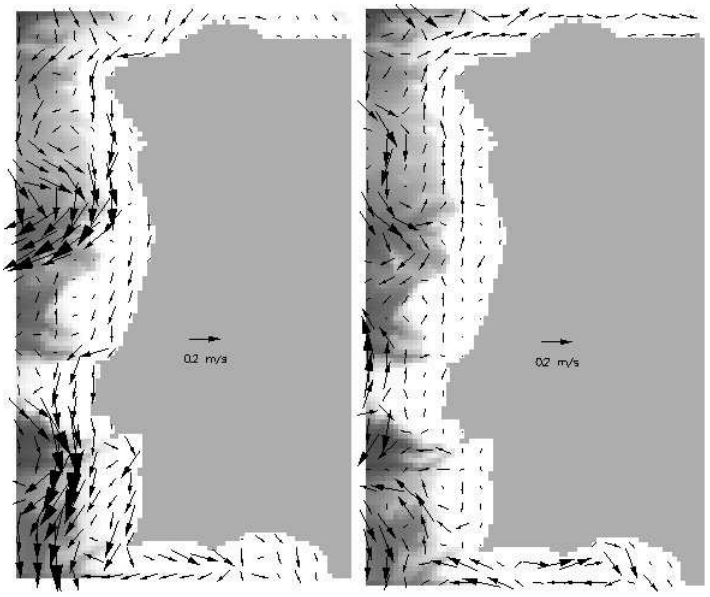

Figure 3. *Horizontal residual velocity from the PCOMS model at the surface: May-June period (left) and November-December period (right). Note that vectors are represented each four model cells to allow a clearer visualisation.*

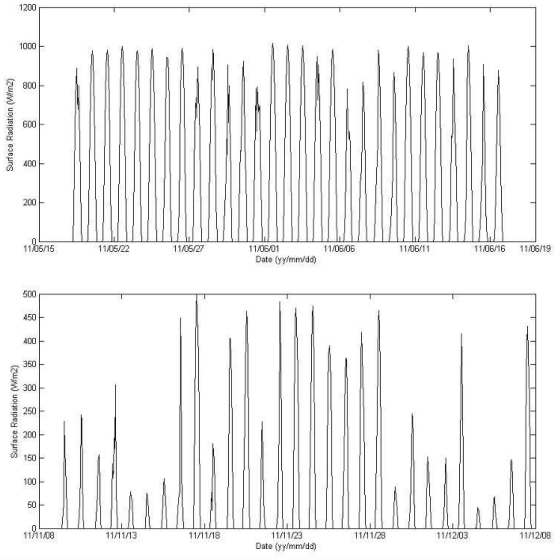

Figure 4. *Surface radiation from the MM5 model at the initial particle release: May-June period (top) and November-December period (bottom).*

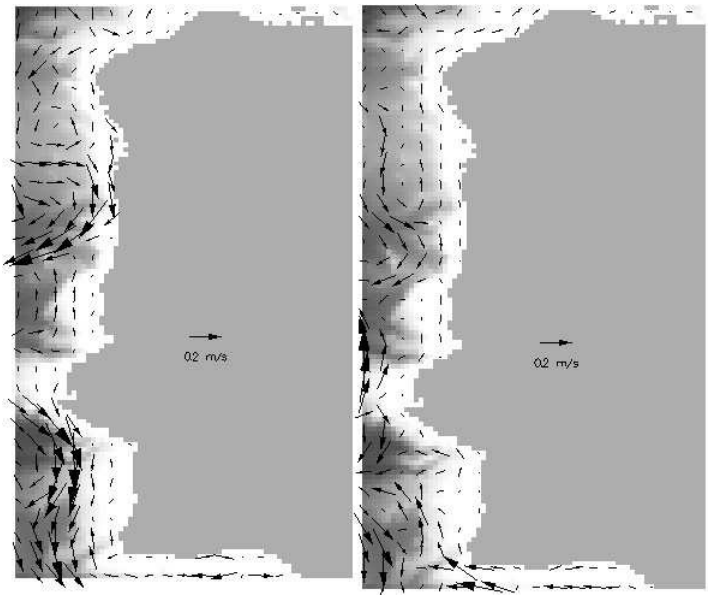

Figure 5. *Horizontal residual velocity from the PCOMS model at 150 m deep: May-June period (left) and November-December period (right). Note that vectors are represented each four model cells to allow a clearer visualisation.*

4 MODELLING RESULTS

The horizontal larvae distribution at the end of the simulated periods reflected the influence of the hydrodynamic conditions and the larvae vertical movement in the larvae dispersion patterns. In one side the upwelling simulations, May-June period, showed a strong Ekman transport offshore in whether or not the vertical migration was active (Figure 6). On the other hand, the downwelling simulations, November-December period, showed higher larvae coastal retention capacity regardless of the vertical migration (Figure 7). Simulations including the larvae vertical migration obtained higher retention values for both periods (Table 1).

Modelling results also showed that vertical migration during both periods increased the larvae retention in the continental shelf (Table 1). In the November-December period, the vertical migration increased the larvae retention in around 20%, being the particles inside the monitored box of more than 99% of the total particles released in the model domain. In the May-June period, the vertical migration also reduced the offshore larvae export in more than 10%, however both simulations with and without vertical movement showed lower values when compared with the November-December period.

The horizontal residual currents obtained close to the seabed (figure 5-left) could explain the decrease in lagrangian particles retention for the simulation with no larvae vertical migration. It could be observed a zonal current that would transport the larvae reaching transported by the hydrodynamic model to those depths offshore. It should be noted that during downwelling periods, the vertical velocity tend to be mostly negative and a passive particle would sink, which implies its offshore transport.

Figure 6. *Larvae lagrangian tracers position at the end of the May-June simulation: without vertical migration (left) and with vertical migration (right).*

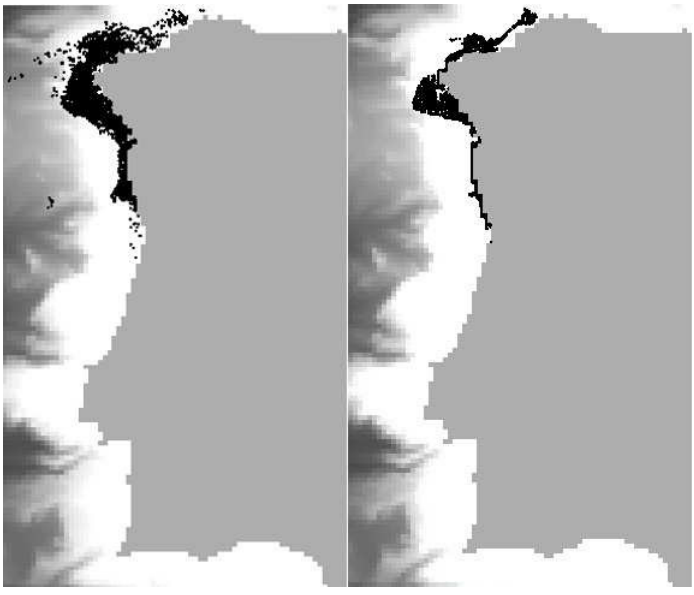

Figure 7. *Larvae lagrangian tracers position at the end of the November-December simulation: without vertical migration (left) and with vertical migration (right).*

Table 1. *Percentage of larvae retention in the first 100 m of the continental shelf at the end of the simulations respect the total particles remaining in the domain.*

	Without vertical migration	**With vertical migration**
May-June	67.50 %	79.70 %
November-December	81.39 %	99.88 %

According to the defined parameterisation and the light radiation limit in the larvae model and regarding the MM5 model radiation values, it was verified that during the November-December simulation the larvae would swim towards the surface between 16h and 17h and would dive between 9h and 10h in a relatively clear day. During the May-June simulation, fish larvae would swim to the surface between 18h and 19h and swim down between 6h and 7h. These values are in agreement with the migration times observed in the May 2002 cruise [21].

5 DISCUSSION

In recent times, larvae dispersion has been studied through numerical modelling using lagrangian particles in 3D hydrodynamic models and its diel vertical migration related to particular timings. These studies have been performed in different coastal areas, from the Arctic coasts [15] to South Africa [11]. This kind of applications have become common for coastal managers and scientists, being developed generic tools as Ichthyop where the modeller was able to determine the timing for diel vertical migration [9]. The latter tool has been applied in several studies focused in larvae retention in nursery areas showing all of them the importance of these larvae movements in the dispersion patterns of the analysed species [7,8,10,12].

In this work, a conceptual model based on the light availability and an optimum depth interval was implemented in an existing open source model. The main singularity in this model was the definition of diel migration related to light intensities obtained from realistic meteorological simulations instead of defined fixed timings. The combination of the meteorological light radiation and its propagation through the water column would impact the position of the fish larvae depending of the season of the year and the cloud coverage. The coupling of the meteorological model with the 3D hydrodynamic-biogeochemical model for the Western Iberian coast and the vertical migration behaviour of the fish larvae would be able to support some possible explanations in recruitment variability applied for the sardine in the Portuguese coast.

From the performed simulations it could be concluded that vertical migration had a significant importance in the horizontal dispersion of fish larvae. This conclusion was supported by model results (figure 6-right and figure 7-right) in which it could be seen that during both periods lagrangian particles remain more spatially structured when the vertical migration was active and particles presented a greater horizontal dispersion for passive particles, as pointed out by similar works [7,15]. Regarding the two simulated periods (Table 1), a clear relationship between the sardine spawning period and the typical oceanographic scenarios associated to the dominant atmospheric regimes could be observed. The downwelling period increased

the coastal retention, even for passive particles the coastal retention increased around 15% compared to the values obtained during the upwelling period. These results are in agreement with the inverse correlation between the winter upwelling index and the sardine recruitment described by Santos et al. [2]. In fact, an increase on upwelling events during the spawning season would lead to a decrease of larvae recruitment.

The obtained results are in agreement with the hypothesis formulated by Parada et al. [11] that states that vertical migration could oppose the offshore transport, thus increasing the retention in the nursery areas. While the formulated hypothesis was not proven on that work, in the present work this hypothesis seems to be verified as the May-June scenario results shows that vertical migration increased 12% the continental shelf retention under a strong upwelling scenario. Bearing in mind that the May-June simulated period would correspond to a spawn by the end of April, model simulations would support the idea that main spawning peak would take place during wintertime [16] while during springtime spawning would be located in other areas, as the Cantabric Sea [32].

During the November-December period, simulations showed a northern migration along the continental shelf towards the North. These results would agree with the South-North age gradient observed by Carrera and Porteiro [33] and would support these authors' idea of an Ibero-Atlantic sardine metapopulation.

Another interesting outcome from the modelling results was the longer permanence of the sardine larvae near surface waters during the November-December simulation in comparison with the May-June period. This fact was related with the different solar radiation reaching the surface waters in both periods (Figure 3). In addition to the daylength differences between the two periods, it should be noticed the radiation reduction due to cloud coverage as pointed out by the MM5 model results. From these results and considering as daytime any moment with any solar radiation, it was obtained an average day length of 9.30 hours for the period November-December and 15 hours for the May-June period. As could be observed in Figure 3, the surface radiation intensity in the May-June period is almost twofold the obtained for the November-December period.

During the during the day central hours of May-June period, these solar radiation levels would influence larvae survival, as, even at the maximum defined depth, larvae would be exposed to solar radiation intensities higher than the defined limit radiation and would be more vulnerable to predation. During winter, the clouds coverage would allow larvae to remain longer at the surface and its movement and dispersion would be more related to the surface currents.

Summarising, vertical migration strategies are important for the sardine larvae survival in the Portuguese continental coast, not only because of food abundance or protection from predators, but also because it increases their retention in coastal areas as was described by Heath [18] in his study of the marine fish early life stages.

At last, it should be highlighted the contribution of modelling tools on the study of fish larvae mechanistic behavioural and the high adaptability of the numerical models used in the present work to the different fish species and coastal study areas.

ACKNOWLEDGEMENTS

This work was supported by the EASYCO Project, financed by the Atlantic Area Transnational Programme of the European Commission (EC), priority 2, through the European Regional Development Fund (ERDF), contract nr. 2008-1/002.

REFERENCES

1. Stratoudakis, Y., Bernal, M., Borchers, D.L., Borges, M.F., 2003. Changes in the distribution of sardine eggs and larvae off Portugal, 1985–2000. Fisheries Oceanography, 12(1): 49–60.
2. Santos, A.M.P., Borges, M.F., Groom, S., 2001. Sardine and horse mackerel recruitment and upwelling off Portugal, ICES Journal of Marine Science, 58(3): 589–596.
3. Santos, A.M.P., Peliz, A., Dubert, J., Oliveira, P.B., Angélico, M.M., Ré, P., 2004. Impact of a winter upwelling event on the distribution and transport of sardine eggs and larvae off western Iberia: a retention mechanism. Continental Shelf Research, 24: 149–165.
4. Santos, A.J.P., Nogueira, J., Martins, H., 2005. Survival of sardine larvae off the Atlantic Portuguese coast: a preliminary numerical study. ICES Journal of Marine Science, 62: 634–644.
5. Cowen, R. K., Paris, C.B., Srinivasan, A., 2006. Scaling of connectivity in marine populations. Science 311(5760): 522–527.
6. Gallego, A., North, E.W., Petitgas, P., 2007. Introduction: status and future of modelling physical–biological interactions during the early life of fishes. Marine Ecology Progress Series, 347: 121–126.
7. Brochier, T., Lett, C., Tam, J., Fréon, P., Colas, F., Ayón, P., 2008. An individual-based model study of anchovy early life history in the northern Humboldt Current system. Progress in Oceanography, 79(2-4): 313–325
8. Brochier, T., Colas, F., Lett, C., Echevin, V., Cubillos, L.A., Tam, J., Chlaida, M., Mullon, C., Fréon, P., 2009. Small pelagic fish reproductive strategies in upwelling systems: A natal homing evolutionary model to study environmental constraints. Progress in Oceanography 83: 261–269
9. Lett, C., Verley, P., Mullon, C., Parada, C., Brochier, T., Penven, P., Blanke, B., 2008. A Lagrangian tool for modelling ichthyoplankton dynamics. Environmental Modelling & Software 23: 1210–1214
10. Nicolle, A., Garreau, P., Liorzou, B., 2009. Modelling for anchovy recruitment studies in the Gulf of Lions (Western Mediterranean Sea). Ocean Dynamics, 59: 953–968.
11. Parada, C., Mullon, C., Roy, C., Fréon, P., Hutchings, L., van der Lingen, C.D., 2008. Does vertical migratory behaviour retain fish larvae onshore in upwelling ecosystems? A modelling study of anchovy in the southern Benguela. African Journal of Marine Science, 30(3): 437–452.
12. Soto-Mendoza, S., Parada, C., Castro, L., Colas, F., Schneider, W., 2012. Modeling transport and survival of anchoveta eggs and yolk–sac larvae in the coastal zone off central-southern Chile: Assessing spatial and temporal spawning parameters. Progress in Oceanography 92–95: 178–191.
13. Sundelöf, A., Jonsson, P.R., 2012. Larval dispersal and vertical migration behaviour – a simulation study for short dispersal times. Marine Ecology, 33(2): 183–193.
14. Van der Molen, J., Rogers, S.I., Ellis, J.R., Fox, C.J., McCloghrie, P., 2007. Dispersal patterns of the eggs and larvae of spring-spawning fish in the Irish Sea, UK. Journal of Sea Research, 58: 313–330.
15. Vikebø, F., Jørgensen, C., Kristiansen, T., Fiksen, Ø., 2007. Drift, growth, and survival of larval Northeast Arctic cod with simple rules of behaviour. Marine Ecology Progress Series, 347: 207–219.
16. Ré, P., Silva, R.C., Cunha, E., Farinha, A., Meneses, I., Moita, T., 1990. Sardine spawning off Portugal. Boletim do Instituto Nacional de Investigação das Pescas, 15: 31–44.
17. Lo, N., Smith, P., Butler, J., 1995. Population growth of northern anchovy and Pacific sardine using stage-specific matrix models. Marine Ecology Progress Series, 127: 15–26.
18. Heath, M., 1992. Field investigations of the early life stages of marine fish. Advances in Marine Biology, 28, 1–174.

19. Ré, P., 1986. Ecologia da postura e da fase planctónica da Sardina pilchardus (Walbaum 1792) na região central da costa Portuguesa. Boletim da Sociedade Portuguesa de Ciências Naturais, 23: 5–81. (In Portuguese).

20. Ré, P., 1999. Ictioplâncton estuarino da Península Ibérica. Câmara Municipal de Cascais, 163pp. (In Portuguese).

21. Santos, A.M.P., Ré, P., Santos, A., Peliz, A., 2006. Vertical distribution of the European sardine (Sardina pilchardus) larvae and its implications for their survival. Journal of Plankton Research, 28: 523-532.

22. Drillet, Y., Bourdalle-Badie, R., Siefridt, L., Le Provost, C., 2005. Meddies in the Mercator North Atlantic and Mediterranean Sea eddy-resolving model. Journal of Geophysical Research 110(C3): C03016.

23. Lyard, F., Lefevre, F., Letellier, T., Francis, O., 2006. Modelling the global ocean tides: modern insights from FES2004. Ocean Dynamics 56: 394 – 415.

24. Braunschweig, F., Martins, F., Leitão, P., Neves, R., 2003. A methodology to estimate renewal time scales in estuaries: the Tagus Estuary case. Ocean Dynamics, 53: 137–145.

25. Santos, A., Martins, H., Coelho, H., Leitão, P., Neves, R., 2002. A circulation model for the European ocean margin. Applied Mathematical Modelling, 26(5): 563-582.

26. Coelho, H., Neves, R., White, M., Leitão, P., Santos, A., 2002. A model for ocean circulation on the Iberian Coast. Journal of Marine Systems, 32(1-3): 153-179.

27. Riflet, G., Leitão, P.C., Fernandes, R., Neves, R., 2007. Assessing the quality of a pre-operational model for the Portuguese coast. In European Geosciences Union 2007, number 09979 in 1607-7962/gra/EGU2007-A-09979.

28. Saraiva, S., Pina, P., Martins, F., Santos, M., Braunschweig, F., Neves, R., 2007. Modelling the influence of nutrient loads on Portuguese estuaries. Hydrobiologia 587: 5–18.

29. Mateus, M., Riflet, G., Chambel, P., Fernandes, L., Fernandes, R., Juliano, M., Campuzano, F., de Pablo, H., Neves, R., 2012. An operational model for the West Iberian coast: products and services. Ocean Science, 8: 713–732.

30. Trancoso, A. R., 2012. Operational modelling as a tool in wind power forecast and meteorological warnings. PhD Thesis, Instituto Superior Técnico, Universidade Técnica de Lisboa, 146p.

31. Nogueira, J. 2005. Estudo numérico do recrutamento de pequenos peixes pelágicos na Costa Ibérica. MSc dissertation thesis. Technical University of Lisbon. (Portuguese)

32. Solá, A., Motos, L., Franco, C., Lago, A., 1990. Seasonal occurrence of pelagic fish eggs and larvae in the Cantabrian Sea (VIIIc) and Galicia (IXa) from 1987 to 1989. ICES, C.M 1990/H: 25.

33. Carrera, P., Porteiro, C., 2003. Stock dynamic of the Iberian sardine (Sardina pilchardus, W.) and its implication on the fishery off Galicia (NW Spain). Scientia Marina, 67: 245–258.

MODELLING MUSSEL GROWTH IN TAGUS ESTUARY: A PRELIMINARY APPROACH

L. Pinto • M. Mateus • I. Ascione • G. Franz • R. Neves

CHAPTER SYNOPSIS

Background
In recent years, considerable research has been carried out on the application of the DEB theory to simulate growth and bio-energetics of bivalve species. DEB theory describes the individual in terms of two state variables, structural body and reserves, describing energy flow through organisms from assimilation to allocation to growth, reproduction and maintenance. The advantages of DEB model lies in its versatility and generality, with its applications to other species only requiring a new set of parameters. DEB models have been successfully applied to several shellfish species including *Mytilus edulis* and *Crassostrea gigas*.

Results
A model based on the DEB theory was integrated in MOHID model and applied to the Tagus estuary. The model was applied to the Tagus estuary to simulate the potential growth potential of the *Mytilus edulis* in the system. In order to identify the preferential growth zones of the bivalves, the discussion of the results were focused on the shell allometry (structural volume, shell length, dry weight) and mussel bioenergetics (energy in the reserves, reproductive energy).

Conclusions
A model capable of examining environmental sustainability and productivity of a system is a powerful tool to support sustainable management of shellfish culture. The present model can reproduce a system behavior and is capable to assess the impact of mussel culture on the dynamics of the system. Therefore it can be used to estimate the potential for growth, the ecological and the capacity of a system to support shellfish production.

1 INTRODUCTION

Growth of bivalve species with economic value has been widely studied due to their role in aquaculture and other ecosystem services such as water filtration [1]. The need for tools to understand ecological interactions and processes of relevance for estimating carrying capacity in shellfish aquaculture has promoted the development of individual bivalve growth models. Individual bivalve growth has been modelled using a range of energetic models, from empirical based net-production models [2] to the recent use of more mechanistic models based on the Dynamic Energy Budget (DEB) theory [3].

In recent years, considerable research has been carried out on the application of the DEB theory [4] to simulate growth and bio-energetics of bivalve species. DEB theory describes the individual in terms of two state variables, structural body and reserves [5], describing energy flow through organisms from assimilation to allocation to growth, reproduction and maintenance. The advantages of DEB model lies in its versatility and generality, with its applications to other species only requiring a new set of parameters. DEB models have been successfully applied to several shellfish species including *Mytilus edulis* [6,7] and *Crassostrea gigas* [3,8]. Also, some authors have coupled DEB models with biogeochemical models to supply feedbacks from aquaculture farms to phytoplankton and nutrient dynamics [9,10,11].

Dabrowski et al. [11] developed a Fortran 90 implementation of the DEB algorithm for *Mytilus edulis*. The developed model includes physiological interactions with the ecosystem and it has been coupled with a Nutrient-Phytoplankton-Zooplankton-Detritus (NPZD). Afterwards, the coupled model was subsequently embedded within a numerical physical model for hydrodynamics and transport of passive tracers. The modelling system was applied to Bantry Bay (Ireland) and successfully reproduced the biogeochemical cycles and growth of mussel cultures in the system. The DEB model developed by [11] is generic and it can be coupled to any hydrodynamic model for estuarine, coastal and ocean waters.

In the present study, the DEB model developed by [11] was integrated by the authors in MOHID water modelling system (http://www.mohid.com), and applied to the Tagus estuary (Portugal), to simulate the potential growth of *Mytilus edulis* in the system. The aim of the study was to identify the preferential potential growth zones of the bivalves in the modelled domain.

2 DEB MODEL INTEGRATION WITH MOHID

In this section, a brief description of the integration in MOHID model of the DEB model developed by [11] is given. The detailed description of the DEB model formulation and validation is not reported in this study, but it can be found in [11].

The DEB model was integrated in MOHID model through the module BenthycEcology. To run the DEB model with MOHID the user has to turn on at least the modules Hydrodynamic, WaterQuality, BenthicEcology and InterfaceSedimentWater. The DEB model parameters handled by ModuleInterfaceSedimentWater and by ModuleBenthicEcology, are listed in Table 1 and Table 2, respectively.

A schematic diagram of the integrated model is presented in Figure 1. The DEB model calculates bivalve's volume, energy, reproductive energy, individual dry weight and total dry weight. The model accounts of feedbacks to the ecosystem (Chlorophyll-a consumption, oxygen consumption, ammonia excretion, nitrogen egestion). The biogeochemical fields are updated by taking into account the following processes: Oxygen (O_2) is consumed by bivalves' respiration, Phytoplankton (Phyto) is consumed by benthic grazing, ammonia (NH_4) increases due to excretion, Particulate Organic Matter (POM) increases due to mortality and egestion processes.

3 MODEL APPLICATION

3.1 Study area

The Tagus estuary is the largest estuary in Portugal and one of the largest in Europe, covering an area of 320 km^2 (Figure 2). The Tagus estuary is a semi-diurnal mesotidal estuary, with tidal range varying from 1 m during neap tides up to almost 4 m in the spring tides. The tide propagates up to almost 80 km upstream and the estuary mean resident time is 25 days [12]. In this area the wind blows predominantly from south and southwest during winter, rotating progressively to northwest and north during spring and maintaining this direction during summer.

Table 1. *List of parameters required for the initialization of DEB model.*

Parameter	Unit	Description
bivalve volume	m^3	Individual bivalve volume
bivalve energy	J	Energy reserve of individual bivalve
bivalve reproductive energy	J	Reproductive energy of individual bivalve

Table 2. *Input parameters required for the chosen species.*

Parameter	Unit	Description
NINDM2	-	Number of individuals per m^2
EGCC	J m^{-3}	Energetic growth cost per unit growth in structural body volume
MAXSAING	J m^{-2} s^{-1}	Max. surface-area-specific ingestion rate
ASSEFFIC	-	Assimilation efficiency (= Pam/Pxm)
SOMACOST	J m^{-3} s^{-1}	Somatic maintenance cost
FLUXRESFRAC	-	Fraction of flux from reserve spent on somatic maintenance
SATCOEF	mg (chl-a) m^{-3}	Saturation coefficient - food density at which ingestion rate is half the maximum
REPOREFFIC	-	Reproduction efficiency
ENERCONT	-	Energy content of 1g of reserve
WWTODW	-	WW to DW converter
SPAWEFFIC	-	proportion of the reproductive buffer emptied at each spawning
TSPAWN	ºC	temperature threshold trigeering spawning
GSOMINDEX	-	Gonado-somatic index triggering spawning (fraction)
NSPAWND		Number of spawning days in a year (MUST be same as SpawnDay array dimension)
JDAYSPAWN	D	Julian day
VOLADULT	m^3	Volume specifying a change from juvenile to adult
SHAPEPARAM	-	shape parameter
REFTEMP	K	Ref. temp. for rate constants
TEMPARRH	K	Arrhenius temperature
TEMPLOW	K	Lower boundary of tolerance range
THRESP	K	Upper boundary of tolerance range for respiration
THING	K	Upper boundary of tolerance range for ingestion
TAL	K	Arrhenius temp. for rate of decrease at lower boundary
TAHRESP	K	Arrhenius temp. for rate of decrease at upper boundary for respiration
TAHING	K	Arrhenius temp. for rate of decrease at upper boundary for ingestion
FECALDECAY	s^{-1}	Corresponds to T_{90} of 0
ENERGPHY	J mg^{-1} C	energetic value of phyt C
ENERGO2		energetic value of oxygen (J mg^{-1} O_2)
CCHLABIV		C to Chla ratio used to convert Phyto to Chla
NH4EXCFRAC		define NH4 excretion as a fraction of N ingested
BILENINIC	m	Initial bivalve length

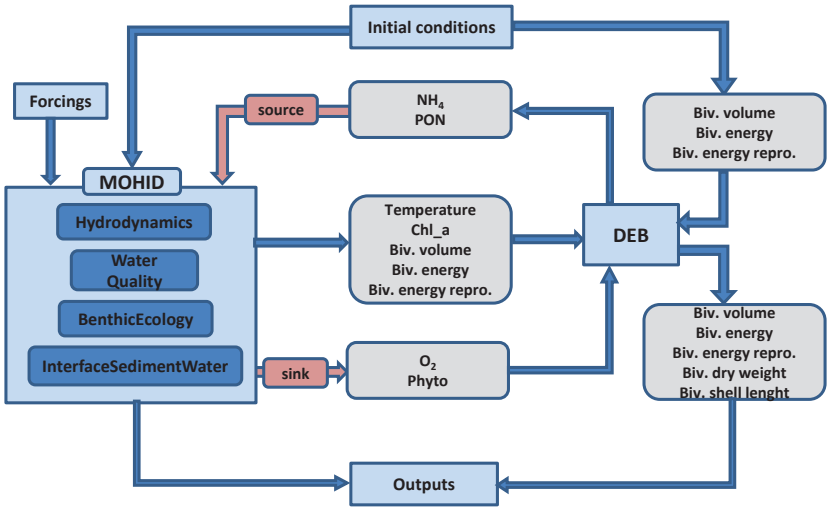

Figure 1. *Flowchart presenting the integration of the DEB model with the MOHID model.*

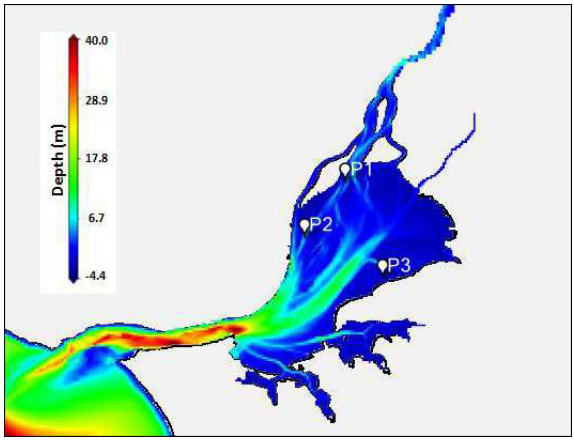

Figure 2. *Tagus estuary bathymetry.*

Morphologically the estuary can be divided into three main areas: a straight narrow and deep W-E oriented channel with about 16 km long and 2 km wide, with maximum depths of about 45 m; an inner bay with 25 km long and 15 km wide SW-NE oriented with depths between 5 and 10 m and; an upper shallow estuary with an area of 100 km^2, encompassing large mudflats and salt marshes separated by shallow channels.

The main freshwater source to the estuary is the Tagus River, with flow rates varying typically between 50 and 2000 $m^3\ s^{-1}$, showing a strong seasonality and the actual discharge is also controlled by dam releases. The Sorraia and the Trancão rivers are the second and third main estuarine tributaries with mean discharges of 39 and 6 $m^3\ s^{-1}$, respectively.

The combined effect of low average depth, strong tidal currents and low freshwater input make Tagus a globally well-mixed estuary, with significant stratification occurring only during specific situations such as neap tides or after heavy rains.

Until the 1970's Portugal and specifically the Tagus estuary, was the major exporter of oysters in Europe. Factors like TBT and oysters gill disease caused the end of the shellfish aquaculture in the Tagus estuary. Mesotidal estuaries, like Tagus, are favorable areas for shellfish culture, offering good trophic conditions due to strong tidal currents that ensure an intensive food renewal within the area [13]. Thus, the Tagus estuary provides the conditions to implement the aquaculture of bivalves, as existed for decades, until the collapse 40 years ago of the fishery of the Portuguese oyster *Crassostrea angulate*.

3.2 Numerical model

The MOHID modelling system was applied to the Tagus estuary by using a 2-D configuration, with a downscaling scheme with three nested domains was used (Figure 3). The first domain covers the entire Portuguese coast with a 0.06^{o} horizontal resolution and is forced with the FES2004 global tide solution [14]. To obtain a smooth grid variation, an intermediate domain with 0.02^{o} resolution was created to supply hydrodynamic ocean open boundary conditions to the Tagus estuary model. The third domain encompasses the Tagus estuary with a variable horizontal resolution ranging from 0.02^{o} off the coast up to 0.002^{o} inside the estuary. Figure 2 shows the bathymetry of the Tagus estuary used in the simulations.

For the atmospheric conditions, the system is one-way coupled offline with the MM5 atmospheric forecast model for the west Iberian coast, running at IST (http://meteo.ist.utl.pt). This model provides wind speed, air temperature, mean sea level pressure, surface humidity, cloud cover, downward long wave radiation and solar radiation hourly data with a 9 km spatial resolution. Water proprieties were simulated only on the Tagus estuary model (third domain) and constant values were imposed in the ocean open boundary, considering a low seasonal variation of these proprieties in the ocean. The simulated proprieties were: water temperature, salinity, oxygen, ammonia, nitrite, nitrate, phosphorus, phytoplankton, zooplankton, and cohesive sediment.

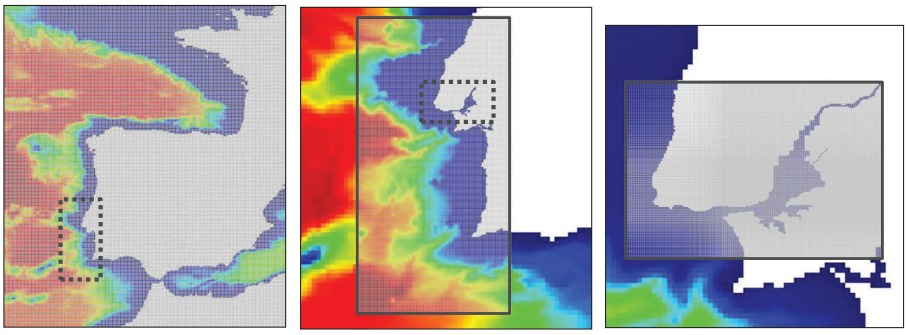

Figure 3. *Downscaling scheme used for the Tagus estuary model with three nested domains: a) first domain; b) second domain; c) third domain the Tagus estuary.*

Tagus river freshwater discharges measured at the Almourol hydrometric station were used as the main river boundary conditions (http://snirh.pt). For Sorraia and Trancão rivers, flow and water properties were obtained from climatological data. Other 15 discharges related with urban waste water treatment plants were included in the model.

The DEB model was applied only for the Tagus estuary model (third domain) and the same parameterization used by [11] for the *Mytilus edulis* simulations was employed. A value of 100 individuals per m^2 was applied in all the domain cells and the initial values of bivalve volume, energy and reproductive energy was set to 2.95×10^{-6} m^3, 5177 J and 1000 J, respectively.

The model was executed over a time period of 1 year from January 2009 to January 2010. The validation of hydrodynamic and biogeochemical model for this period can be found in [15].

4 RESULTS AND DISCUSSION

The model was applied to the Tagus estuary to simulate the potential growth of the *Mytilus edulis* in the system. In order to identify the preferential growth zones of the bivalves, the discussion of the results were focused on the shell allometry (structural volume, shell length, dry weight) and mussel bioenergetics (energy in the reserves, reproductive energy).

Figure 4 shows the spatial distribution of predicted structural volume and energy in the reserves of an individual bivalve after one year of simulation. Results obtained for the structural volume shows two distinct regions: an offshore area and the lower estuary where the potential mussel growth is almost null, and the upper estuary as a preferential zone for the potential mussel growth. Initially the mussel volume was 2.95 cm^3 (shell length of 5 cm) and in the upper estuary after one year of simulation the volume reached values of 8 cm^3 (shell length of 7 cm). Shell allometry and mussel depend on the consistent supply of high quality food, particularly phytoplankton [16]. Thus the level of shellfish production that can be sustained in a body of water is determined by the level and supply of primary production.

The upper estuary is the area with higher phytoplankton concentrations and consequently the area with more potential for the mussel growth. However, salinity can also be a limitation factor for the *Mytilus edulis* growth. This species is euryhaline and occurs in marine as well as in brackish waters down to 4‰, although it does not thrive in salinities of less than 15‰ and its growth rate is reduced below 18‰ [17]. This factor was not considered in the simulation and in the case of the present application the results can be affected, due to the range of salinities that can occur in the system. Another growth limiting factor not considered in the model is the sediment concentration. In some way these are model limitations that should be solved in the future.

The time series of predicted shell length and mussel dry weight (DW) in three stations (P1, P2, P3) located in the upper estuary (Figure 2) are shown in Figure 5. Results of the phytoplankton concentration are also represented in the mussel dry weight plot. The model recreated the annual pattern of growth: growth in the spring and summer and little or no growth in the autumn and winter. However, after one year different potential growth rates are predicted for the three stations, with the maximum rate at P1 and similar rates at P2 and P3. The final shell length varies from 7.0 cm in P1 and 5.68 cm in P3, showing a significant variation in the potential growth depending on the zone of the upper estuary.

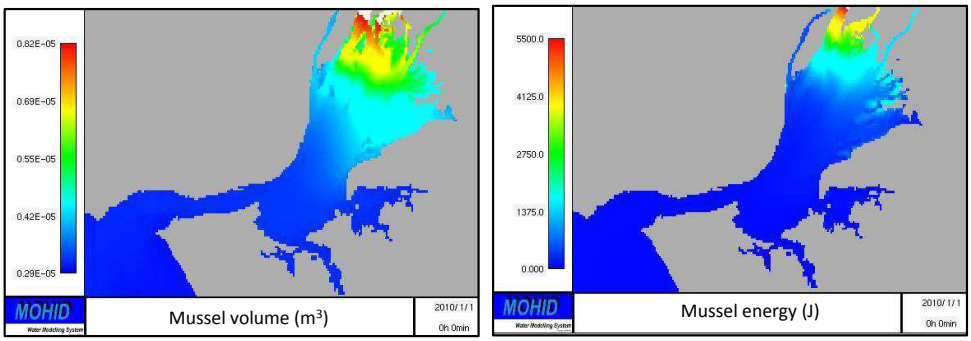

Figure 4. *Results after one year of simulation: a) potential mussel volume, and b) potential mussel energy.*

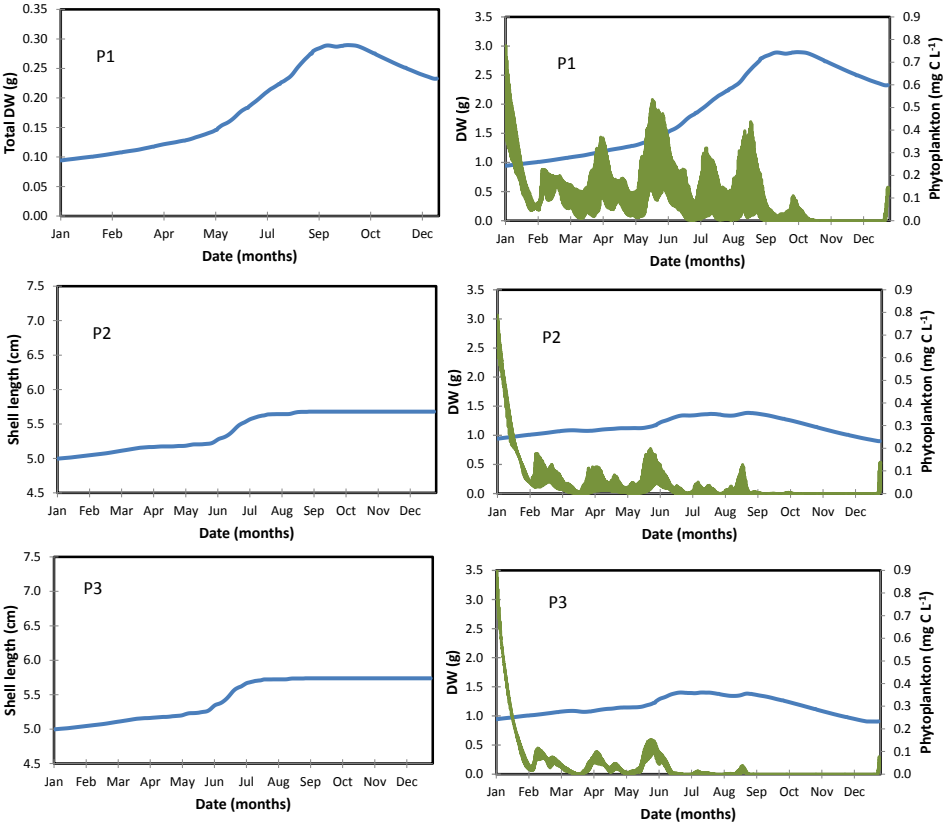

Figure 5. *Time series of simulated shell lengths, dry weights and phytoplankton concentration (green line) in three stations located in the upper estuary area (see Figure 2 for stations location).*

In terms of dry weight (DW), the model results shows an increase from 1.0 g to between 2.9 g at P1 and to 1.4 g in P2 and P3, and a reduction of DW in autumn and in winter in the three stations. This reduction is associated with starvation (very low phytoplankton concentration). The time series of the phytoplankton concentration show high values of phytoplankton concentration in station P1 than in stations P2 and P3 and consequently, high final shell length and dry weight are predicted in P1.

5 CONCLUSIONS

A model based on the DEB theory was coupled with the MOHID model and applied to the Tagus estuary. The one year simulation results showed that the upper estuary is the area with more potential for mussel growth. However, within the upper estuary different potential growth rates are obtained depending on the phytoplankton concentration. Results also showed that some improvements can be done to the model, namely the inclusion of salinity and sediment concentration as limiting factors for *Mytilus edulis* growth.

A model capable of examining environmental sustainability and productivity of a system is a powerful tool to support sustainable management of shellfish culture. The present model can reproduce a system behavior and is capable to assess the impact of mussel culture on the dynamics of the system. Therefore it can be used to estimate the potential for growth, the ecological and the capacity of a system to support shellfish production.

ACKNOWLEDGEMENTS

This work is partially supported by EASYCO Project, financed by the Atlantic Area Transnational Program of the European Commission (EC), Priority 2, through the European Regional Development Fund (ERDF), contract nr. 2008-1/002.

REFERENCES

1. Officer, C.B., Smayda, T.J., Mann, R., 1982. Benthic filter feeding: a natural eutrophication control. Mar. Ecol. Prog. Ser. 9: 203–210.
2. Gangnery, A., Chabirand, J.M., Lagarde, F., Le Gall, P., Oheix, J., Bacher, C., Buestel, D., 2003. Growth model of the Pacific oyster, *Crassostrea gigas*, cultured in Thau Lagoon (Méditerranée, France). Aquaculture 215: 267–290.
3. Bernard, I., de Kermoysan, G.Pouvreau, S., 2011. Effect of phytoplankton and temperature on the reproduction of the pacific Oyester *Crassostrea gigas*: Investigation through DEB theory. Journal of Sea Research 66(4): 349-360.
4. Kooijman, S.A.L.M, 2010. Dynamic Energy Budget Theory for Metabolic Organisation, 3rd edition. Cambridge University Press, Cambridge, 514 pp.
5. van der Meer, J., 2006. An introduction to Dynamic Energy Budget (DEB) models with special emphasis on parameter estimation. Journal of Sea Research 56: 85-102.
6. Handå, A., Alver, M., Edvardsen, C.V., Halstensen, S., Olsen, A.J., Øie, G., Reitan, K.I., Olsen, Y., Reinertsen, H., 2011. Growth of farmed blue mussel (*Mytilus edulis* L.) in a Norwegian coastal area; comparison of food proxies by DEB modeling. Journal of Sea Research, 66(4): 297-307.
7. Saraiva, S., van der Meer, J., Kooijman, S.A.L.M., Sousa, T., 2011. DEB parameters estimation for *Mytilus edulis*. Journal of Sea Research 66(4): 289-296.
8. Alunno-Bruscia, M., Bourlès, Y., Maurer, D., Robert, S. Mazurié, J.Gangnery, A., Goulletquer, P., Pouvreau, S., 2011. A single bio-energetics growth and reproduction model for the oyster *Crassostrea gigas* in six Atlantic ecosystems. Journal of Sea Research 66(4): 340-348.

9. Ren, J.S., Ross, A.H, Hadfield, M.G., Hayden, B.J., 2010. An ecosystem model for estimating potential shellfish culture production in sheltered coastal waters. Ecological Modelling 221: 527-539.
10. Guyondet, T., Roy, S., Koutitonsky, V.G., Grant, J., Guglielmo, T., 2010. Integrating multiple spatial scales in the carrying capacity assessment of a coastal ecosystem for bivalve aquaculture. Journal of Sea Research 64: 341-359.
11. Dabrowski, T., Lyons, K., Curé, M., Berry, A., Nolan, G., 2012. Numerical modelling of spatio-temporal variability of growth of *Mytilus edulis* (L.) and influence of its cultivation on ecosystem functioning. Journal of Sea Research, in press (http://dx.doi.org/10.1016/j.seares.2012.10.012).
12. Braunschweig, F., Martins, F., Chambel, P., Neves, R., 2003. A methodology to estimate renewal time scales in estuaries: the Tagus Estuary case. Ocean Dynamics, 53(3): 137-145.
13. Raillard, O., Ménesguen, A., 1994. An ecosystem box model for estimating the carrying capacity of a macrotidal shellfish system. Mar. Ecol. Prog. Ser. 115: 117–130.
14. Lyard, F. , Lefevre, F., Letellier, T., Francis, O., 2006. Modelling the global ocean tides: modern insights from FES2004. Ocean Dynamics, 56(5-6):394-415.
15. Franz, G., Neves, R., Neto C., de Pablo, H., Trancoso, R., Pinto, L., Fernandes, R., Mateus, M., 2012. Validação do modeo do estuário do Tejo para 2006 a 2009. Relatório do projecto ENVITEJO, 82pp (in portuguese).
16. Meeuwig, J.J., Rasmussen, J.B., Peters, R.H., 1998. Turbid waters and clarifying mussels: their moderation of empirical chl:nutrient relations in estuaries in Prince Edward Island, Canada. Mar. Ecol. Prog. Ser. 171: 139–150.
17. FAO, 2004-2012. Cultured Aquatic Species Information Programme. *Mytilus edulis*. Cultured Aquatic Species Information Programme. In: FAO Fisheries and Aquaculture Department [online]. http://www.fao.org/fishery/culturedspecies/Mytilus_edulis/en.
18. Nunes, J.P., Ferreira, J.G., Gazeau, F., Lencart-Silva, J., Zhang, X.L., Zhu, M.Y., Fang, J.G., 2003. A model for sustainable management of shellfish polyculture in coastal bays. Aquaculture 219: (257–277).

A NUMERICAL STUDY OF CO_2 DYNAMICS IN THE TAGUS ESTUARY

M. Mateus • A. P. Oliveira

CHAPTER SYNOPSIS

Background
Among the most important current issues in marine and freshwater geochemistry are the fluxes, sources, and mechanisms of CO_2 transport and transformation. Data of water-air CO_2 fluxes are available for some Portuguese estuarine systems. However, a numerical modelling approach was never implemented in these systems. This chapter reports on the development of an algorithm to simulate CO_2 exchanges at the water-air interface, and its application in a study case in the Tagus estuary.

Results
The modelling approach can be considered successful, inasmuch as the CO_2 dynamics has been modelled in a realistic way. The major spatial and seasonal patterns of CO_2 dynamics (CO_2 partial pressure and fluxes across the water-air interface) were adequately reproduced.

Conclusions
Based on the results exposed in this study and the comparison between them and field data, it can be stated that the major objectives of this modelling exercise have been achieved, namely, the simulation of the basic patterns of CO_2 dynamics in the estuary and the magnitude of values found in nature. So, even with some limitations, the model as it is can be used in coastal management context for studies of CO_2 export/import flux across the water-air interface.

1 COASTAL AND ESTUARINE DYNAMICS OF CO_2

Carbon entering the estuaries can be transported by various means and has different fates. A fraction will be emitted to the atmosphere in the form of CO_2, other will remain in the water column and in the sediment and other fraction will be exported to the nearby coastal area. The flux and/or residence of carbon in each of these compartments depend on the characteristics of each estuary as well as on the season of the year and time of the day the study is carried out. For example, in Scheldt estuary approximately 60% of the respiratory CO_2 is released to the atmosphere, 26% is transferred to the sediment and only 14% remains in the water column [1]. Moreover, within the estuary, spatial variability plays an important role due to the hydrodynamic and geomorphological complexity of these littoral zones. Thus, among the most important current issues in marine and freshwater geochemistry are the fluxes, sources, and mechanisms of CO_2 transport and transformation.

An aspect of the recent compilation of available water-air CO_2 fluxes in inner estuaries [2], is that the west European inner estuaries have been the more extensively studied, representing 47% of the total results presented. Still, inter-annual and decadal variability of water-air CO_2 fluxes is, so far, undocumented in some estuarine environments. Concerning Portugal, a country localized at the eastern boundary of the Subtropical North Atlantic, few studies have been undertaken [3]. As a matter of fact, data of water-air CO_2 fluxes are available for four Portuguese estuarine systems, the Aveiro Lagoon and the estuaries Douro, Sado and Tagus [3]. However, none of these studies uses a numerical modelling approach.

This chapter reports on the development of an algorithm to simulate CO_2 exchanges at the water-air interface, and its application in a study case in the Tagus estuary (Figure 1). The skill of the model to reproduce the CO_2 dynamics is qualitatively assessed by comparing the results with field data. This was the first attempt to model CO_2 dynamics in the water and its fluxes at the water-air interface with the MOHID modelling system.

2 ACCOUNTING FOR DISSOLVED CO_2 IN THE MODEL

CO_2 concentration in the water is controlled by a variety of physical, chemical and biological processes. The role of biological processes in CO_2 concentration, namely photosynthesis and cellular respiration, is already parameterized in the biogeochemical model as sink and source terms in the mass balance equation for the functional groups (producers, consumer and decomposers). As such, this section describes the new processes added to the model, and the algorithms that have been implemented to account for the role of physical processes in the dynamics of CO_2. The chemical reactions that influence DIC concentration were not considered under the assumption that in most estuarine and coastal systems the CO_2 dynamics is mostly controlled by biological processes.

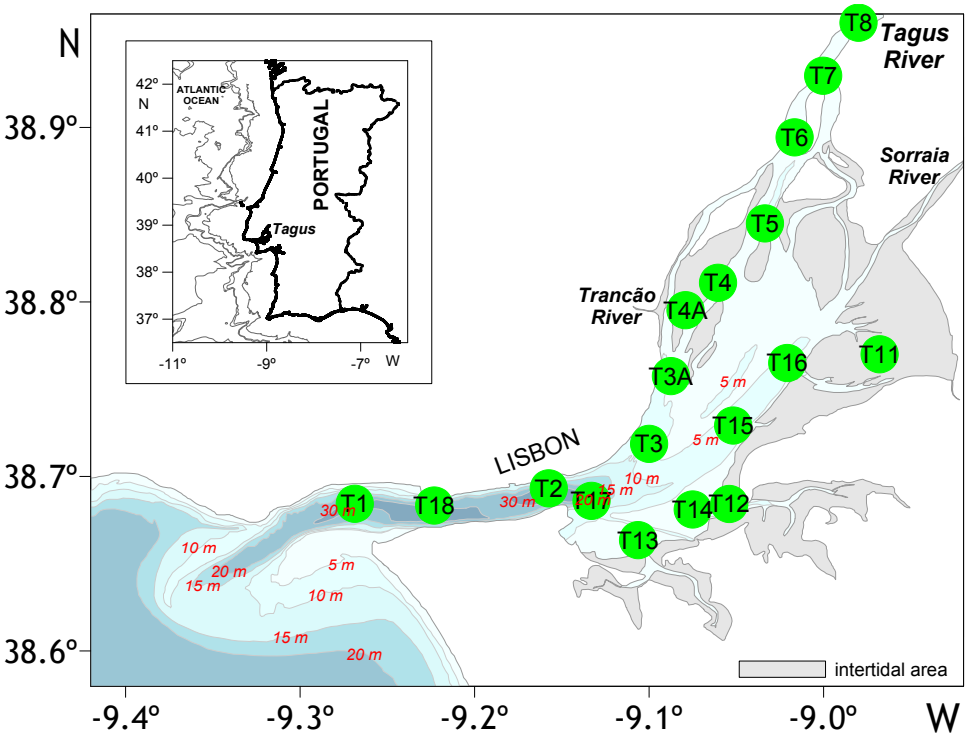

Figure 1. *Study site and the location of the sampling stations monitored.*

2.1 Modeling CO_2 fluxes in the water-air interface

As an integrated modelling system, the MOHID model has been used to study several processes in the Tagus estuary, including hydrodynamics, sediment dynamics, water quality, pollution and biogeochemical cycles in the water column [4-6]. However, the dynamics of CO_2 in the water and the fluxes of this gas across the water-air interface as never been studied before using MOHID. To accomplish this, the model had to be updated with new processes to link CO_2 dynamics in the water managed by the ecological/biogeochemical modules with the modules responsible for handling the gas fluxes in water-air interface.

The biogeochemical module at the base of this study consists in an algorithm that simulates the cycles of several elements such as nitrogen, phosphorus, silica and oxygen [7]. The module has 12 major components: producers, consumers, decomposers, organic matter (particulate, dissolved labile and semi-labile), nutrients (nitrate, ammonium, phosphate and silicate acid), biogenic silica and oxygen. Trophic interactions are expressed in terms of flux of carbon and nutrients by the model.

Borges et al. [8] constructed an empirical relationship to compute the gas transfer velocity of CO_2 (k, cm h^{-1}) that accounts for the contribution of wind and water current:

$$k = k_{OCD} + (1.0 + 2.58 \cdot u_{10}) \cdot \left(\frac{Sc(T,S)}{600}\right)^{-1/2} \tag{1}$$

where k_{OCD} is the conceptual relationship of O'Connor and Dobbins [9] for the water current, u_{10} (m s^{-1}) is the wind speed at 10 m above mean sea level, and $Sc(T,S)$ is the Schmidt number for CO_2 defined as a function of temperature and salinity.

O'Connor and Dobbins [9] formulation (k_{OCD}, cm h^{-1}) estimates the contribution of water current:

$$k_{OCD} = \left(1.719 \cdot \sqrt{\frac{v}{d}}\right) \cdot \left(\frac{Sc}{600}\right)^{-1/2} \tag{2}$$

where v (cm s^{-1}) is the water current, d (m) the mean depth of the water column, and Sc the Schmidt number determined using the polynomial relationship of Wanninkhof [10]:

$$\mathrm{Sc} = 2073.1 - 125.62 \times \mathrm{T} + 3.6276 \times \mathrm{T}^2 - 0.043219 \times \mathrm{T}^3 \tag{3}$$

Wind speed was referenced to a height of 10 m (u_{10}) using the algorithm given by Johnson [11]:

$$u_{10} = u \cdot \left(\frac{10}{z}\right)^{1/7} \Rightarrow \quad z \leq 20\,\mathrm{m} \tag{4}$$

where z (m) is the elevation above mean sea level at which the wind speed was measured.

The Schmidt number, a dimensionless ratio of the transfers of momentum and mass, was computed for a given salinity from the formulations for salinity 0 and 35 [10], and assuming that Schmidt number varies linearly with salinity:

$$Sc(T,S) = \frac{Sc(T,35) - Sc(T,0)}{35} \cdot S + Sc(T,0) \tag{5}$$

The $Sc(T,35)$ and $Sc(T,0)$ parameters are defined as:

$$Sc(T,35) = 1953.4 - 128.0 \cdot T + 3.9918 \cdot T^2 - 0.050091 \cdot T^3 \quad (6)$$

$$Sc(T,0) = 1800.6 - 120.10 \cdot T + 3.7818 \cdot T^2 - 0.047608 \cdot T^3 \quad (7)$$

2.2 Model setup

The geographic area of the model implementation is bounded by the coordinates 38°30' – 39° N and 8°51' – 9°51' W, stretching from the lower Tagus river section in the north, to the coastal area of the estuary mouth in the south. The modelled domain is composed of a variable step grid with 73×94 computation points, having higher resolution inside the estuary where the cells correspond to an approximated area of 372 km^2.

A two-dimension vertically integrated configuration was used, assuming that the intense mixing and shallowness of the estuary prevents the formation of vertical stratification. As such, only one vertical layer is used, having variable thickness depending on the bathymetry. Hydrodynamic and ecological models run with a time step of 60 s and 3600 s, respectively, during a 4-year period with repetitive annual forcing conditions.

2.2.1 Open boundary conditions and model forcing

Real wind conditions (direction and intensity) where prescribed as surface forcing, along with solar radiation and air relative humidity and temperature. Realistic river flow was used for rivers Tagus, Sorraia and Trancão. The effluent discharge of the waste water treatment plants (WWTP) inside the estuary is also considered in the application. All water inputs (rivers and WWTP) are characterized by flow, temperature, cohesive sediment concentration, and ecological parameters such as nutrients, organic matter, chlorophyll a (Chla), etc.

The values used to characterize water inputs and the open boundary conditions (OBD) were taken by similar previous studies of application of the model to the Tagus estuary [6, 12]. Given the importance of the wind regime in the gas fluxes at the water-air interface, a high-resolution forcing was adopted with hourly means calculated from a data set covering the period from 2001 and 2007 (Figure 2), measured at Portela Airport meteorological station in Lisbon.

2.2.2 Sampling

From 1999 to 2007 ten samplings were performed in Tagus estuary covering in an irregularly way the four seasons (Table 1). Nevertheless such samplings allowed characterizing the seasonal patterns of the estuary. Along the estuary a total of 18 stations were selected in order to study the spatial CO_2 distribution along the system (Figure 1). Surface seawater samples were collected during ebb conditions and along a salinity gradient with Niskin bottles.

In 2007 sampling was also performed at a fixed station (T18, see Figure 1) also covered four seasons and included two tide conditions (neap and spring). Surface water sampling was carried out at neap and spring tide every hour, for both tidal cycles (approximately 13 h). A total of 101 observations were recorded.

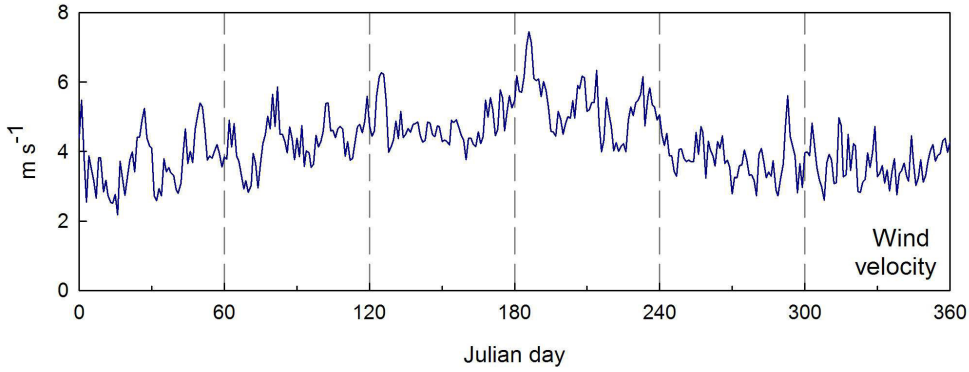

Figure 2. *Time-series for wind velocity prescribed as surface forcing in the model application. Hourly means calculated from a continuous time-series from 2001 to 2007, measured at the Portela Airport meteorological station in Lisbon.*

Table 1. *Sampling periods. Upwelling was present at the adjacent coastal shelf in the marked (*) periods.*

Season	Sampling periods	Season	Sampling periods
Winter	March 2001 February 2004	**Summer**	September 1999 * July 2001 * June 2002 *
Spring	May 2000 May 2003 * May 2006 * May 2007 *	**Autumn**	November 2006

3 MODEL RESULTS

The main purpose of this modelling experiment was to evaluate the skill of the model in reproducing the most relevant features and dynamics of CO_2 fluxes at the water-air interface in the estuary. As such, the results outlined here focus on the parameters and state-variables that determine or have a strong influence in this gas exchange. Accordingly, there is a significant quantity of results that are not addressed, considering that at the base of this application there is a rather complex biogeochemical model. Model validation for ecological and biogeochemical variables is also not presented here, since it is already presented in previous studies dealing with the modelling study of ecological processes in the Tagus [6, 12].

3.1 Nutrients and chlorophyll

Model results show a seasonal trend in nutrient concentration inside the estuary (Figure 3), as well as a distinct longitudinal pattern characterized by a decrease in concentration seaward. Higher values (> 1 mgN L^{-1}) in the upper and middle estuary are a consequence

of the Tagus river discharge and its variation throughout the year. The contribution from the river is also relevant for phosphorus and silica concentrations in the estuary, thus making possible to define as a general rule that nutrient concentrations decreases with increasing distance from the river.

Together, nutrient and light availability exert a strong control on primary production and, consequently, Chla concentration. Since both nutrients and light radiation have a clear seasonal pattern, Chla concentration also has a similar pattern, as seen in Figure 4. River flushing also determines Chla concentration by regulating the residence time inside the estuary. The results also show a spatial pattern described by higher mean concentration in the mid and lower estuary.

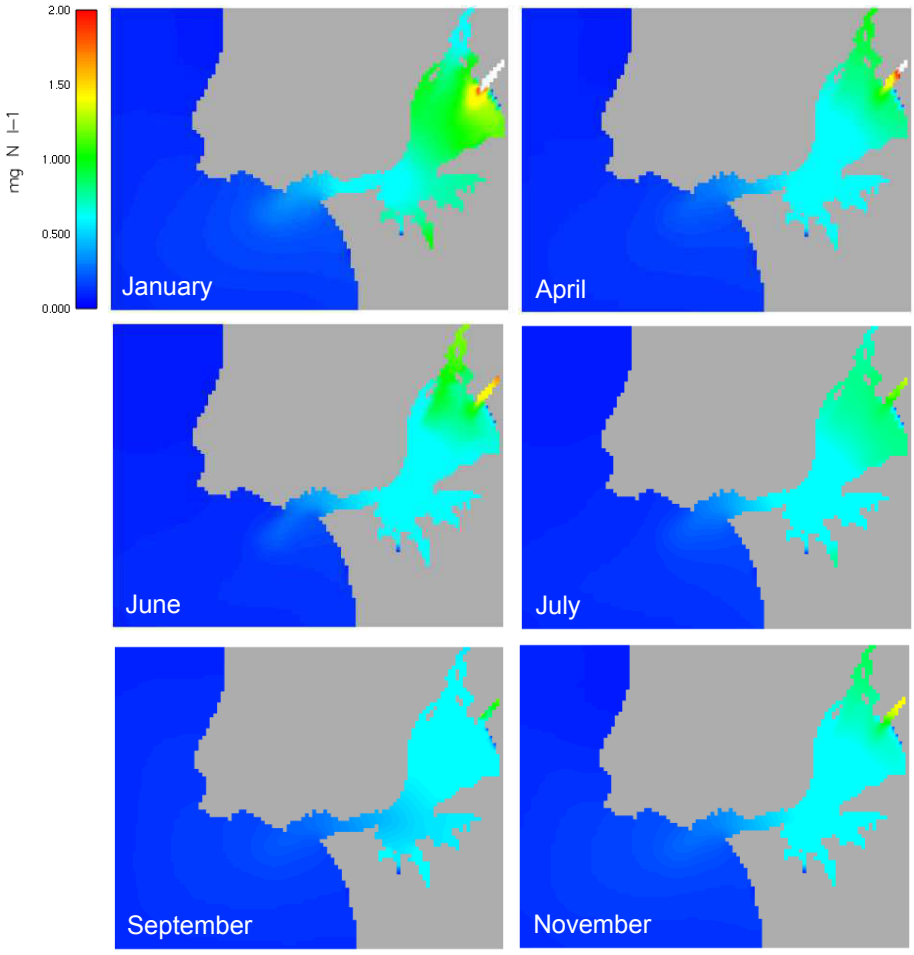

Figure 3. *Monthly means for nitrate concentration (mgN L^{-1}) calculated by the model from outputs with a temporal resolution of one hour.*

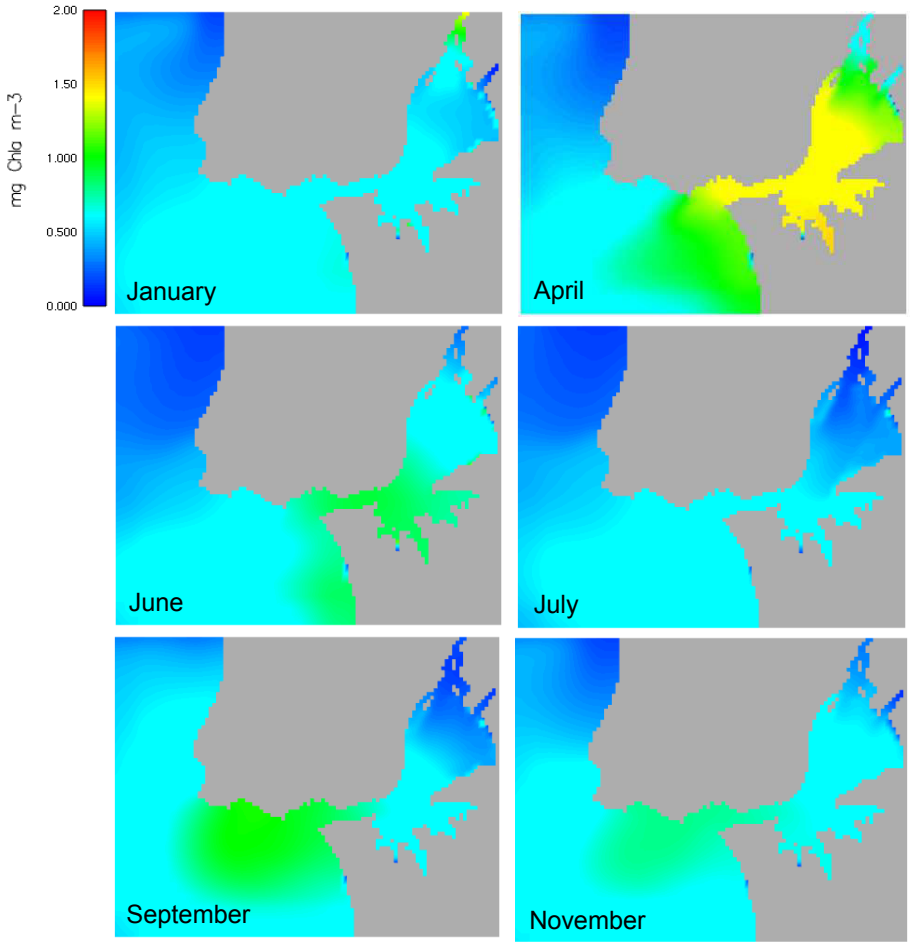

Figure 4. *Monthly means for Chla concentration (mg Chla m^{-3}) calculated by the model from outputs with a temporal resolution of one hour.*

Field data show that Chla concentration inside the estuary frequently peak at values around 12 to 15 mgChla m^{-3}. The values seen in Figure 4 are significantly lower because they correspond to monthly means, and not to discrete events. According to the results, higher values are observed in April, suggesting that the model may be anticipating optimal conditions for the growth of primary producers.

3.2 CO_2 partial pressure

Model predictions for the CO_2 partial pressure (pCO_2) in water are shown in Figure 5. There is a clear temporal and spatial variation in this property, with higher values ($\sim$500 μatm) usually found in upper estuarine areas all year around. In some parts under the direct influence of the Tagus river these concentrations are even higher. These results also show that

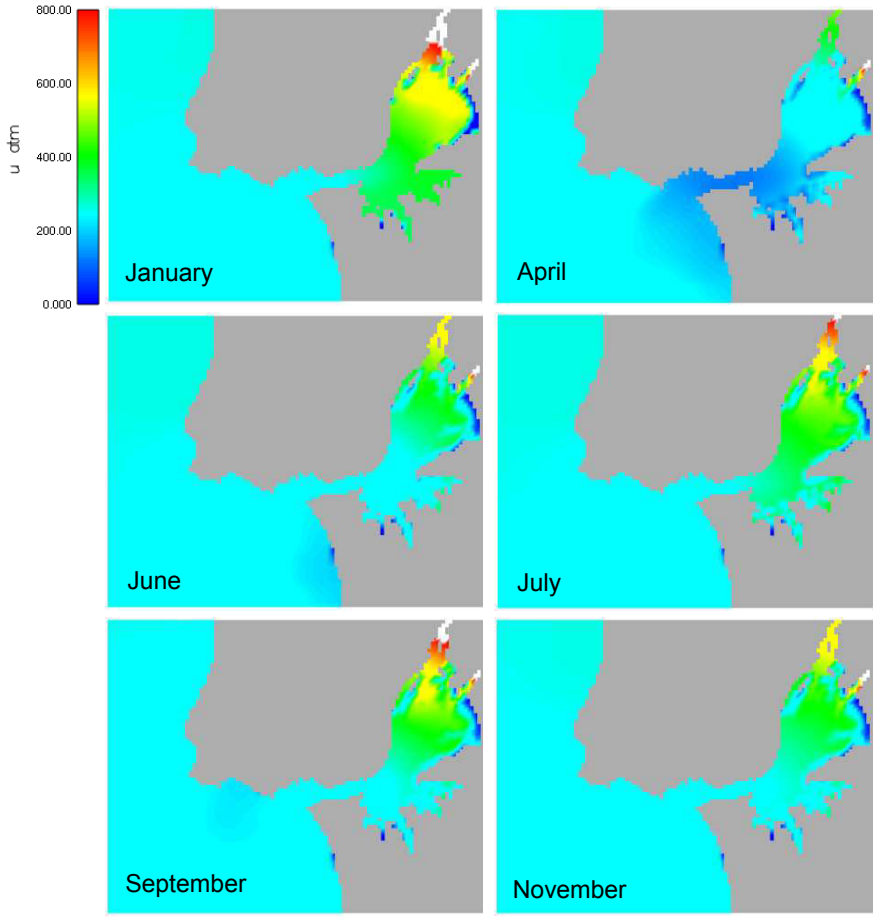

Figure 5. *Monthly means for CO_2 partial pressure (μatm) calculated by the model from outputs with a temporal resolution of one hour.*

the pCO_2 has its lower values ($<$400 μatm) during spring and early summer months in all estuarine range. The range of values seen in the model results are within the magnitude of values found in natural aquatic systems, denoting that the model is able to reproduce real CO_2 concentrations in water, both qualitatively and quantitatively.

The results for pCO_2 show that this property has an inverse relation with Chla concentrations. This inverse relation is particularly obvious during spring months, when the mean Chla concentration is higher and pCO_2 is lower. CO_2 and O_2 dynamics are both strongly conditioned by biological activity, specifically by means of primary production, cellular respiration and organic matter degradation (bacterial activity). During winter months, when respiration and organic matter degradation processes dominate, there is a surplus of CO_2 that is not absorbed by primary producers because ambient conditions are not favorable for growth. This

explains the higher pCO_2 seen during those months. Primary production is eventually boosted in spring with the increase of light radiation, and since CO_2 is removed from the water during this process, consequently, pCO_2 decreases.

pCO_2 is also conditioned by water temperature, since the increase in temperature induces an increase in the metabolic rates (respiration) of organisms, thus intensifying O_2 consumption and CO_2 release. These processes may explain the pCO_2 values that are higher during July in the inner estuary, when compared with the values for September and December. The higher pCO_2 observed in the upper areas of the estuary can be the result of mineralization processes, given the higher concentrations of organic matter in this region. Finally, wind plays a decisive role in gas exchanges over the water-air interface, having a direct effect on pCO_2 in water. This process is addressed in the next section.

3.3 CO_2 fluxes in the water-air interface

Selected results for the CO_2 fluxes at the water-air interface are illustrated in Figure 6 for some of the monitored stations. Station selection for comparison purposes was based on their spatial distribution, in such a way to cover distinct zones of the estuary in terms of ambient conditions. These zones are the estuary mouth (T1), the north channel (T4A), the south margin (T12) and the river influence upper estuarine area (T6).

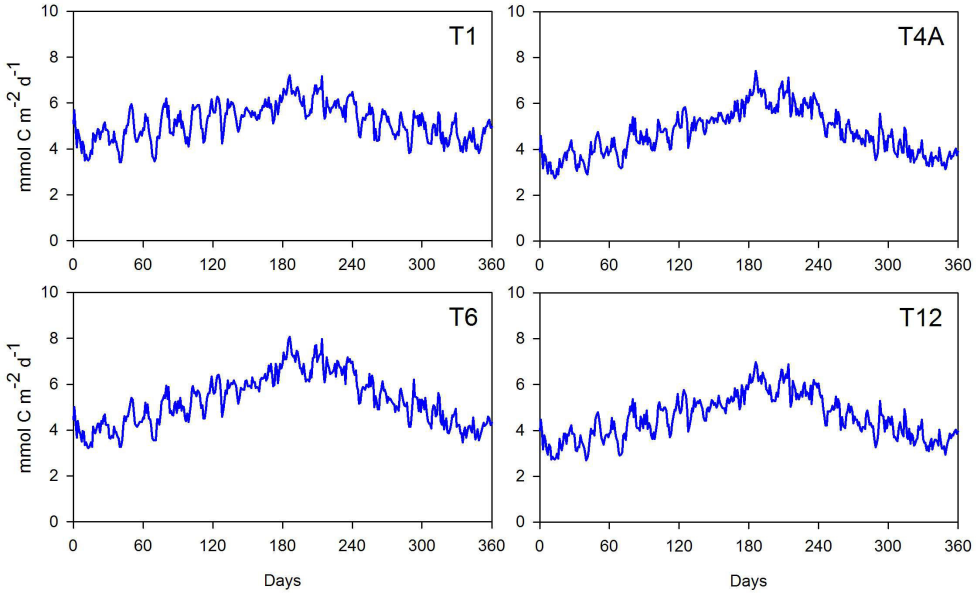

Figure 6. *Model results for mean water-air CO_2 fluxes (mmol C m^{-2} d^{-1}) at the estuary mouth (T1), the north channel (T4A), the south margin (T12) and the river influence upper estuarine area (T6) during an year of simulation.*

An inter-station comparison shows low spatial variation with values ranging between 3 and 8 mmol C m^{-2} d^{-1} (mean daily values) at all station. Nevertheless, station T6 has higher mean values when compared to others, which can be attributed to the higher pCO_2 and lower salinity in this section of the estuary. Station T1, at the mouth of estuary, also has higher comparative values during winter, an occurrence that can be explained by the higher current velocities in this area, a factor that is determinant in the parameterization used to calculate the fluxes at the interface [8, 13].

Field data show marked differences between stations, not coinciding with model results. Among the factors that may help to explain this difference, the most important are:

1. Differences in the physical conditions;
2. In situ fluxes were calculated based on instantaneous salinity, temperature and wind values, while in the model the fluxes are calculated with daily means for wind, and estimates of temperature and salinity;
3. Lack of realism in the estimative of the organic loads that reach the estuary via Tagus river and waste water treatment plants effluents;
4. Limitations inherent to the model parameterization.

The strong correlation between wind intensity and the CO_2 fluxes is evident in all stations. Higher values for the flux (>6 mmol C m^{-2} d^{-1}) occur during the period when the wind intensity is also higher, between the Julian days 150 and 240 (June – August). This correlation is corroborated by field data, highlighting the significant weight of wind contribution in the algorithm used to estimate the flux [13].

The model calculates instant CO_2 fluxes, accounting for the marked variations throughout the day that characterize both wind and currents regime. The results presented here, however,

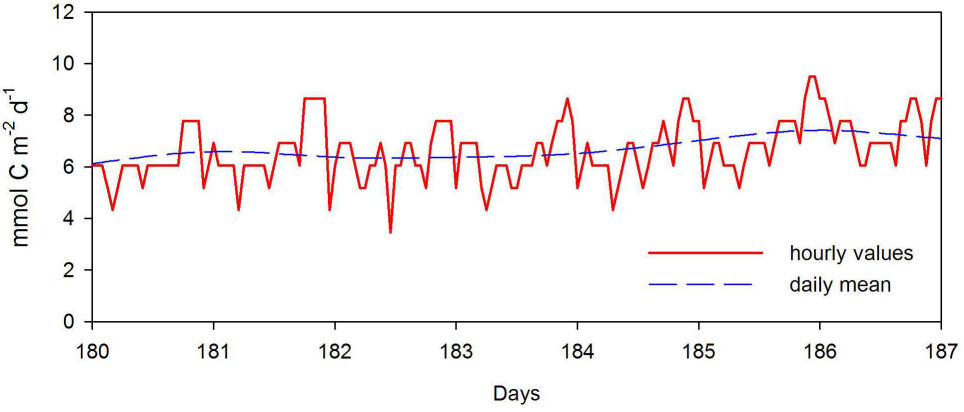

Figure 7. *CO_2 water-air flux variability at instant and hourly values (station T4A).*

correspond to daily mean values so that the daily variation is filtered, thus simplifying their analysis. This is illustrated in Figure 7 for a period of one week, where instant values (hourly resolution) for the flux are plotted together with daily mean values (Station T4A).

In some cases this variation can be even more accentuated, with fluxes varying between positive (water-air direction of the flux) and negative (air-water direction of the flux). This is observed in Figure 8, in which the flux varies between -15 and >35 mmol C m^{-2} d^{-1}. The results support the idea that, in respect to CO_2 dynamics, there are distinct zones in the estuary and adjacent coastal area, with some acting as both sources and sinks of CO_2 to the atmosphere. Given the relation between pCO_2 and the magnitude of CO_2 fluxes to and from the atmosphere, the distribution of pCO_2 is superimposed to all other processes affecting CO_2 fluxes. Model predictions show this relation in a clear way.

4 THE MODEL AS IT STANDS AND THE NEXT STEPS

The limitations of this initial attempt to model CO_2 dynamics in a coastal system are significant, as already discussed. Several code developments and model application improvements are needed for a more comprehensive and realistic modelling exercise of CO_2 fluxes in the Tagus estuary. Among the most relevant there is the:

- Development of a module to explicitly account for the kinetics of chemical reactions in the water and its control on pH variation;
- Increase of resolution and adequate temporal coverage in the forcing conditions, since the lack of adequate data imposed the application of mean conditions and not the values observed at the time of the campaigns;
- Inclusion of alternative parameterization and algorithms to calculate CO_2 fluxes;
- Simulate the temporal window of field campaigns using realistic forcing.

Despite all the limitation, this modelling approach can be considered successful, inasmuch as the CO_2 dynamics has been modelled in a realistic way. Based on the results exposed in this study and the comparison between them and field data, it can be stated that the major objectives of this modelling exercise have been achieved, namely, the simulation of the basic patterns of CO_2 dynamics in the estuary and the magnitude of values found in nature.

As a concluding remark from this work it can be said that even with the limitations, the model is adequate to be used for studies of CO_2 dynamics in coastal waters. In a coastal management context, the model may provide relevant information on the export/import flux across the water-air interface.

ACKNOWLEDGEMENTS

This work was funded by the European Commission, Programa POpesca MARE project 22-05-01-FDR-0015 and the Portuguese Science Foundation (FCT) with which A. P. Oliveira had a Ph.D. grant. The work of M. Mateus was supported by project DyEPlume (PTDC/MAR/107939/2008) funded by the FCT and co-funded by COMPETE/QREN/UE.

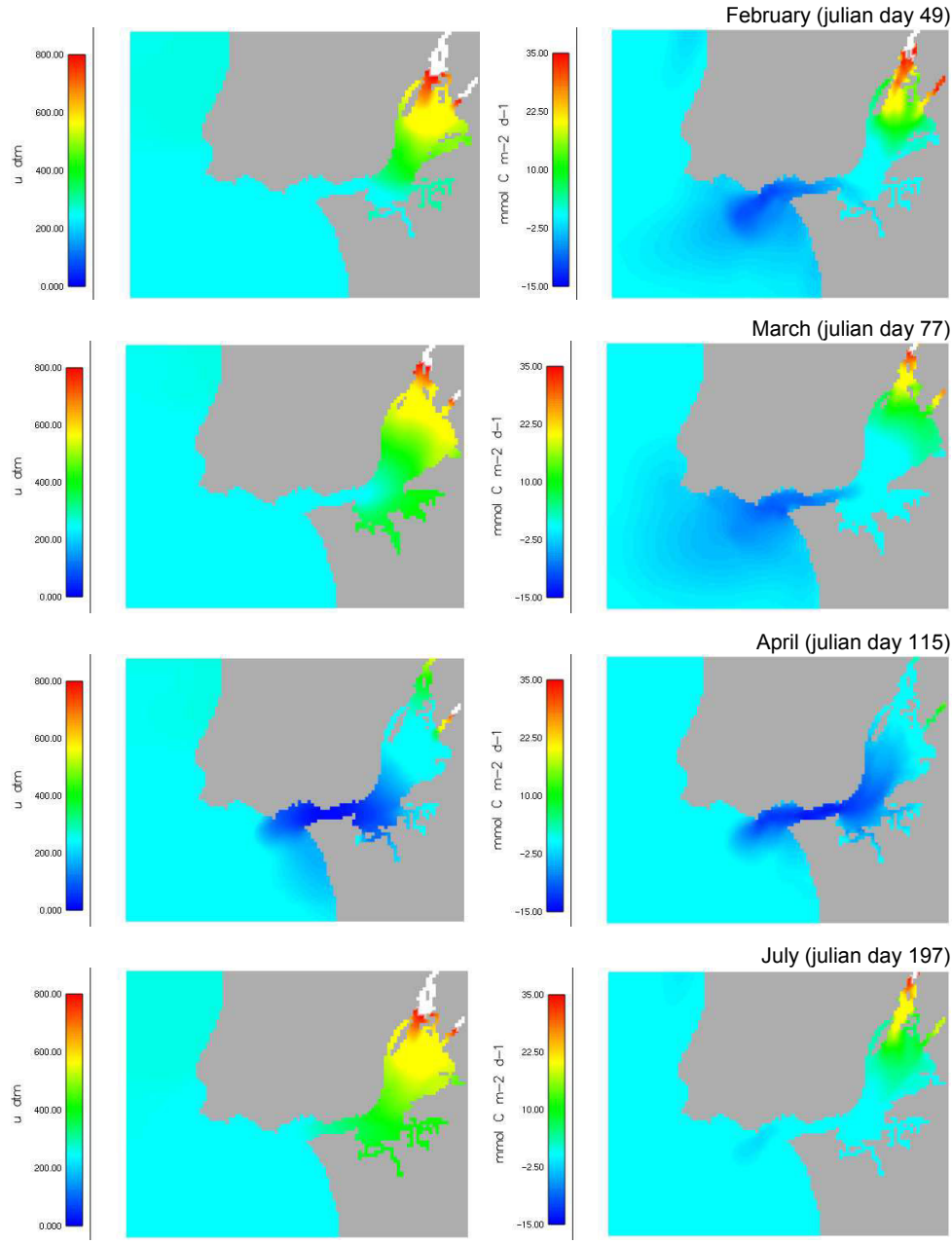

Figure 8. *Model results for instantaneous values of CO_2 partial pressure (μatm) and of CO_2 water-air fluxes (mmol C m^{-2} d^{-1}).*

REFERENCES

1. Gattuso JP, Frankignoulle M, Wollast R: Carbon and carbonate metabolism in coastal aquatic ecosystems. Annual Review of Ecology, Evolution, and Systematics 1998, 29.
2. Chen C-TA, Borges AV: Reconciling opposing views on carbon cycling in the coastal ocean: continental shelves as sinks and nearshore ecosystems as sources of atmospheric CO_2. Deep-Sea Research II 2009, 56.
3. Oliveira AP, Cabeçadas G, Pilar-Fonseca T: Iberia Coastal Ocean in the CO_2 Sink/Source Context: Portugal Case Study. Journal of Coastal Research 2012, 28:184-195.
4. Braunschweig F, Martins F, Chambel P, Neves R: A methodology to estimate renewal time scales in estuaries: the Tagus Estuary case. Ocean Dynamics 2003, 53:137-145.
5. Saraiva S, Pina P, Martins F, Santos M, Braunschweig F, Neves R: Modelling the influence of nutrient loads on Portuguese estuaries. Hydrobiologia 2007, 587:5-18.
6. Mateus M, Vaz N, Neves R: A process-oriented model of pelagic biogeochemistry for marine systems. Part II: Application to a mesotidal estuary. Journal of Marine Systems 2012, 94, Supplement: S90-S101.
7. Mateus M: A process-oriented model of pelagic biogeochemistry for marine systems. Part I: Model description. Journal of Marine Systems 2012, 94:S78-S89.
8. Borges A, Vanderborght J-P, Schiettecatte L-S, Gazeau F, Ferrón-Smith S, Delille B, Frankignoulle M: Variability of the gas transfer velocity of CO_2 in a macrotidal estuary (the Scheldt). Estuaries 2004, 27:593-603.
9. O'Connor DJ, Dobbins WE: Mechanism of reaeration in natural streams. Trans American Soc Civil Eng 1958, 123:641–684.
10. Wanninkhof R: Relationship between wind speed and gas exchange over the ocean. Journal of Geophysical Research 1992, 97:7373-7382.
11. Johnson HK: Simple expressions for correcting wind speed data for elevation. Coastal Engineering 1999, 36:263-269.
12. Mateus M, Neves R: Using a process-oriented ecological model to evaluate light limitation and nutrient limitation in the Tagus estuary. Journal of Marine Engineering and Technology 2008, 12:43-54.
13. Borges AV, Delille B, Schiettecatte L-S, Gazeau F, Abril S, Frankignoulle M: Gas transfer velocities of CO_2 in three European estuaries (Randers Fjord, Scheldt, and Thames). Limnology and Oceanography 2004, 49:1630-1641.

ASSESSMENT OF PRIMARY PRODUCTIVITY AND NUTRIENTS FOR A COASTAL LAGOON IN SOUTHERN BRAZIL

L. M. N. Seiler • E. H. L. Fernandes

CHAPTER SYNOPSIS

Background

The present study was applied to a coastal lagoon, the Patos Lagoon, located in southern Brazil. Considered the largest strangled-type coastal lagoon in the world, it presents on its shores a population of approximately 7,000,000 inhabitants. The Port of Rio Grande, one of the most important in the Americas, is installed in its estuarine portion. The lagoon is home to fish and shrimp species of great commercial importance. Thus, the lagoon is an important water resource in economic and environmental terms. These activities provide the Patos Lagoon importance and prominence, but also make it susceptible to a large number of environmental damages, resulting from waste of domestic, industrial and agricultural activities. Several initiatives aimed at preserving the waters of this system have been performed, but most of these studies were carried out by means of field collection and / or as focus on the estuary portion of the Lagoon. Therefore, this paper presents a study on the Patos Lagoon water quality as a whole (using the numerical model MOHID as a tool) and the front differential to the other water quality works already done to the region using the same numerical model.

Results

Even with the complex dynamic of water quality parameters in the water column, the model showed that it can represent the reality well, with validations qualified between excellent and reasonable. Bidirectional winds parallel to the coast along with the river discharge, operating in the transport of freshwater to the coast and coastal water to the interior of the lagoon. The highest variations in salinity and ecological parameters (nitrate, ammonium, phosphate and chlorophyll-a) were found in the estuarine region. The lowest values of salinity and the highest concentrations of the ecological parameters are near the river mouths due to the high concentration of waste by river discharges. The analysis of the flows of such properties has shown that an input flow of dissolved inorganic nutrients and chlorophyll-a to the lagoon, by river discharge, is higher than the output from the lagoon to the coastal area.

Conclusions

The study has achieved the goals set besides contributing to the understanding of the main factors that control the water quality in the Lagoon. This study allowed quantifying flow properties, to characterize different sub-areas and to present more realistic results as well due to the use of a bathymetry consistent with the current morphology. The ecological parameters variations that rule the water quality are strongly influenced by the hydrodynamics of the system, which interferes in their releases for the water column. The decrease of flows of properties along the lagoon (from the north area of the lagoon to the coastal region) may be explained by flocculation processes and by grazing on phytoplankton which causes a reduction of chlorophyll-a and nutrients.

1 NUMERICAL MODELLING AND ITS APPLICABILITY IN WATER QUALITY

The ecological parameters governing the water quality of water bodies, such as biomass and dissolved inorganic nutrients have a short-scale temporal variation (few hours). The complexity of the interaction between physical, chemical and biological processes of water body, coupled with the difficulty of analyzing the parameters of water quality in the field indicates the need to work with tools that can overcome these difficulties, such as the numerical models.

Prognostic numerical models provide the possibility to simulate different scenarios and predict the short and long-term environmental response. The use of differential equations and empirical relations to represent the quantitative and qualitative aspects of the hydrological cycle is widely used technique for the simulation of hydrological processes and water quality [1].

Patos Lagoon is a water resource of high importance to the State of Rio Grande do Sul (RS), both ecologically (it generates high productivity in the coastal zone of the southern region, besides being an environment of high fishing activity) and economically (in its estuarine portion there is the Port of Rio Grande, the most southern seaport of Brazil, considered one of the most important in the Americas [2]). The growing development of the RS implies the need for better understanding of the processes occurring in the lagoon and influencing the degradation of its waters.

Since 1986 several initiatives aimed at studying the water quality of the Patos Lagoon have been developed in southern Brazil. However, these studies do not address the lagoon as a whole, focusing on specific stations due to the operating difficulty of sampling. In 2000 the project “Mar de Dentro” (Inside Sea) was developed – Program for Rational Development, Environmental Rehabilitation and Management of the Patos/Mirim Lagoon. Therefore, the first model of simplified water quality was applied taking the lagoon as a whole [2].

In 2003 a larger study was carried out aimed at assessing the water quality of the Patos Lagoon involving physical, chemical and biological events as well as their interactions, using the Delft 3D numerical model [2]. However, the study used a morphology that is inconsistent with the current configuration of the Patos Lagoon and does not provide an assessment of biomass transport and production. More recently there was an ecological modelling study of the Patos Lagoon [3] in which the water quality simulation period was very short (few months), preventing the stabilization of the ecological parameters in the system.

Therefore, it is clear the need to continue numerical studies on the water quality of the Patos Lagoon, taking into account the time required for stabilization of the ecological parameters and the new configuration of its access channel. Such a distinguishment makes it possible to obtain more representative values of nutrient concentrations and their variations throughout the year as well as to estimate the flow of ecological parameters between different regions of the lagoon and the overall ecological balance.

The numerical model chosen for this study was the MOHID (Water Modelling System), developed to support the management of aquatic ecosystems [4]. Besides having already been successfully used in numerous studies involving hydrodynamics and water quality of coastal environments, MOHID has the concept of integration boxes, designed to measure the flow of properties between different areas of the water body under study.

Through the MOHID numerical model this study presents an important ecological analysis of a lagoon located in the south of Brazil (Figure 1), based on varying concentrations of phytoplankton and dissolved inorganic nutrients governing water quality of such a water body over one year. Moreover, from the concept of flow measurement drawing on integration boxes it is possible to understand the importance of each area in the system’s ecological balance [6].

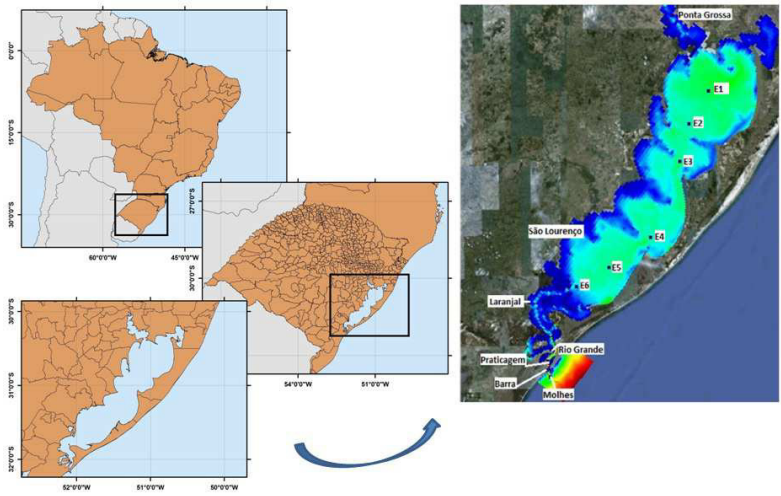

Figure 1. *Location of the Patos Lagoon; bathymetric mesh and stations for results analysis.*

1.1 Objectives

The main objective of this study is to understand the key events controlling the water quality in the Patos Lagoon. This will focus on an analysis of Biogeochemical Cycles (oxygen, nitrogen, and phosphate), Primary and Secondary Production, flow properties among different regions of the lagoon, and the determination of limiting factors for phytoplankton growth.

2 METHODOLOGY

2.1 Bathymetric mesh

In order to discretize the domain for the numerical model of the Patos Lagoon, a bathymetric mesh representative of the new configuration of the Port of Rio Grande was generated for this study. This new mesh included the extension of 500 and 900 m at the East and West breakwaters, respectively, as well as the progressive deepening of the access channel [5]. As this study focuses on the lagoon as a whole, the new mesh no longer used the nesting concept of a parent model (lower resolution) with a child model (of higher resolution) [3, 7, 8]. Instead it created a single varied resolution domain. This modification enabled integration boxes to be created along the field to measure the flow properties of the lagoon from the northern to the coastal region.

For creating the bathymetric mesh, data were used in UTM coordinates of scanned letters of the Directorate of Hydrography and Navigation (DHN) [9] as well as recent data from the region of the Access Channel and Porto Novo obtained from the bathymetric survey conducted by the company *Jan de Nul do Brazil Dragagem Ltda*. The spatial domain has a mesh of irregular cell spacing, ranging from 90,000 m^2 (the highest resolution in the estuary region) and 4,000,000 m^2 for the rest of the lagoon, and a declination of 37^o to the North (to follow the inclination of the lagoon in relation to the Geographic North). In total, the grid has 210 cells in the x direction and 100 cells in the y direction.

2.2 Hydrodynamics

For the hydrodynamic simulation, time series of wind, sea level rise and river discharge in the open border of system were used. Data on level variation were obtained from the Meteorological Station of Pilots at Barra do Rio Grande [10]. The series of wind speed and direction were obtained from the Project Reanalysis of the Earth System Research Laboratory, NOAA, through the Monitoring System of Oceanographic Data from the Southern Brazil Coastal Zone (SISCONSUL) [11] of the Universidade Federal do Rio Grande – FURG, which makes this type of data available for the coastal region of southern Brazil. These data consist of u and v wind components every 6 h. After processing the data for its time variation, the wind stress was calculated using the Bulk equation that determines the transfer between wind and water/water properties.

Data on river discharge were obtained from the Brazilian National Water Agency (ANA) [12], which provides gauged stations with time series of flow. Two hourly time series have been imposed as initial conditions of the model, one representing the discharge of Guaíba River, a composition of the discharge of Taquari-Jacuí system, and another representing the discharge of Camaquã River. For this study the following considerations were made: the role of the Coriolis force; horizontal initial velocity of 0 m/s; horizontal turbulent viscosity of 10 m^2s^{-1} and vertical one of 0.0010 m^2s^{-1}; and sediment roughness coefficient of 0.0025. The output of results calculated by the model was established for certain sites along the lagoon (Ponta Grossa, E1, E3, E4, E6, São Lourenço, Laranjal, Rio Grande, Barra, and Molhes – Figure 1).

2.3 Water quality

The initial conditions of the water quality module were: constant salinity of 8 psu, concentration of nitrite (0.02 mgN L^{-1}), nitrate (0165 mgN L^{-1}), ammonia (0.11 mgN L^{-1}), phosphate (0.07 mgP L^{-1}), oxygen (8 mg L^{-1}), phytoplankton (0.125 mgC L^{-1}), zooplankton (0.01 mgC L^{-1}), particulate organic nitrogen (0.05 mgN L^{-1}), dissolved organic nitrogen non-refractory (0.002 mgN L^{-1}), dissolved organic phosphorus non-refractory (0.019 mgP L^{-1}), dissolved organic phosphorus refractory (0.008 mgP L^{-1}), organic phosphorus particles (0.011 mgP L^{-1}). Values of salinity, temperature, nitrite, nitrate, ammonia, dissolved oxygen, and phosphate were provided by the Laboratory of Hydrochemistry at the Universidade Federal do Rio Grande (FURG). These data were obtained by quarterly sampling of surface, half and bottom water. In this study only the superficial means are used. The remaining parameters were obtained from previous studies.

Due the required time for that the biogeochemical cycles be completed, the modelling of ecological processes needs a long simulation time (about one year) to be stabilized and in fact represent the environment.. As the proposed duration of the study was the year 2006, both simulations were made consecutively. The first one enabled ecological parameters to be inserted in the water column and had a chance to interact, i.e. time enough for the stabilization of phytoplankton and zooplankton variations in biogeochemical cycles. The second one was for the period of interest and had as initial condition the results from the first.

In both simulations, the domain was divided into compartments called integration boxes. Each box is the averaging concentration of the properties of all cells inserted therein, resulting in flows (defined as the mean velocity multiplied by the mean concentration of border cells) that allow to infer the areas which are producers or carriers, an important aspect for assessing the total ecological balance. Furthermore, the integration boxes enable instantaneous variation of these properties to be monitored over time.

3 HYDRODYNAMIC ANALYSIS

3.1 Hydrodynamic Model Validation

Model validation was made on comparisons of actual data on rising sea levels obtained from ANA, and results were calculated by the model at the stations of Ponta Grossa, São Lourenço, Laranjal, and Rio Grande. The results showed that the model simulates the actual data as it tracks the changes in sea level, but cannot keep up with the maximum and minimum elevation. For assessing the quality of results thereof, the Relative Mean Absolute Error statistical method was applied according to Walstra classification [13]. In this classification, errors below 0.2 are considered 'excellent'; 0.2 to 0.4 'good'; 0.4 to 0.7 'reasonable'; and 0.7 to 1 'poor'. Ponta Grossa station showed an error of 0.183, classified as 'excellent', while the reproduction model was rated as 'good' for the stations of São Lourenço, Laranjal, and Rio Grande, with errors of 0.397, 0.295, and 0.338, respectively.

3.2 Hydrodynamic Assessment

From the hydrodynamic perspective, the Patos Lagoon is governed by a system of bidirectional winds, parallel to the coast, as well as by river discharge. The effect of the tide is negligible because the estuary is of hyposynchronic type, i.e. the effect of friction is greater than that of the channel convergence, causing the tidal wave to be attenuated inside the channel [14]. Guaíba is the main river flowing into the lagoon, where the Jacuí-Taquari system is responsible for 85% of total freshwater average input [7] (Figure 2). The seasonal movement of air masses implies a system of NE-SW winds acting along the lagoon. SE/SW winds of greater intensity occur more frequently between between March and August (autumn and winter). When operating on a scale of 3-15 days associated with a low discharge, they force the water inlet from the ocean into the lagoon, causing salinity to increase. Moreover, N/NE winds of greater intensity occur more frequently between September and February (spring and summer), forcing the output of fresh water from the lagoon to the ocean. The sum of the local and remote wind effects generate gaps of 0.3-0.4 m along the lagoon [15, 16], which together with the river discharge effect interfere with salinity and variation in sea level. The river discharge behaviors differently throughout the year, showing high discharge in late winter and early spring, and low to moderate discharge during summer and autumn (Figure 2).

The results of the model indicate that the discharge strongly influences the salt water inlet so that salinity decreases exponentially with increasing the river discharge. Since the stations of Ponta Grossa, E1, and E3 are far from the region where the saline intrusion occurs and close to the discharge from Guaíba, they have the lowest salinity values compared to the stations of E6, Laranjal, Rio Grande, and Molhes (Figure 3). From the results it is also possible

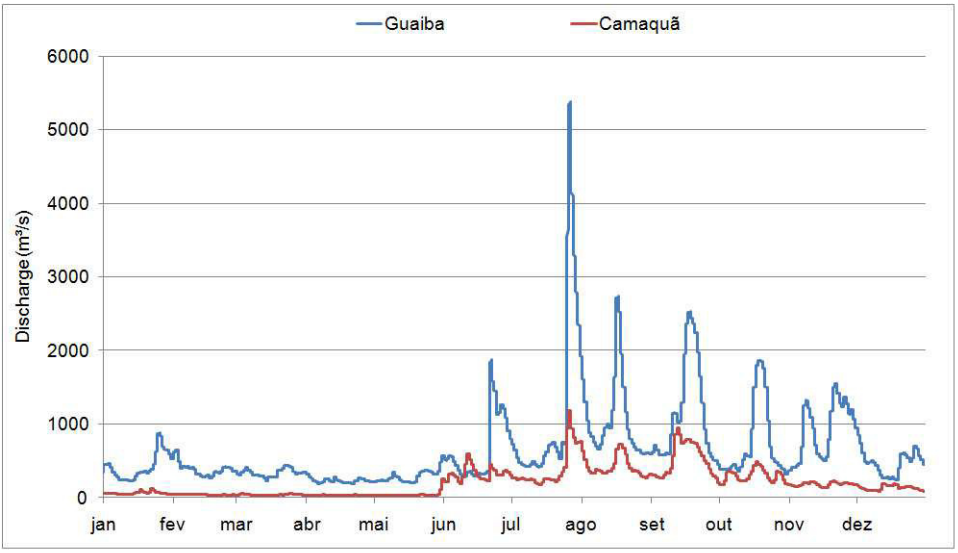

Figure 2. *River discharge from Camaquã and Guaíba Rivers.*

to observe the strong influence of the performance of bidirectional winds parallel to the coast, forcing the entry of saline water (Figure 4) and forcing the output of fresh water (Figure 5), which confirms the findings of previous studies.

4 FLOWS QUANTIFICATION AND VARIATION OF ECOLOGICAL PARAMETERS

4.1 Water Quality Model Validation

Assessment of results from the water quality module was based on a comparison of salinity, chlorophyll-a, ammonia, nitrate and phosphate, all of which refer to Barra station and were calculated by the model with field data. The salinity data were provided by the Laboratory of Estuarine and Coastal Oceanography at FURG. It is possible to see that the model follows the variation of salinity given by actual data, but does not reach the maximum and minimum values, showing sometimes a difference of up to 12 psu. The same behavior was also observed for sea level elevation.

In order to verify that the correlation between the measured and calculated values of salinity was significant, the correlation coefficient (R^2) and the hypothesis test (P) were calculated. Results showed $R^2 = 0.73$ and $P = 0$. Correlation coefficients greater than 0.70 are considered to have strong correlation: so the correlation of salinity data is significant. The Relative Mean Absolute Error calculation for salinity data indicated a value of 0.29, which describes the model result as 'good'. The next step was to evaluate the behavior of solar radiation, which showed that low values of solar radiation are found between June and September, corresponding to winter, with peaks between December and March for the summer, a situation that is consistent with the expected to temperate regions of the Southern Hemisphere. Other properties were validated using data from the Laboratory of Phytoplankton at FURG, which held monthly

cruises to collect physical and chemical parameters and nutrients. The Relative Mean Absolute Error method for chlorophyll-a, nitrate, ammonia and phosphate provided RMAE values of 0.43, 0.60, 0.20, and 0.43, respectively. These values indicate that the reproductive behavior of ammonia was classified as excellent, while for others it was reasonable.

4.2 Water Quality

The water quality module outputs indicate that changes in phytoplankton concentration and hence the primary production is associated with changes in concentration of inorganic nutrients dissolved in water, namely: ammonia, nitrite and phosphate. In general larger variations and concentrations are found during spring and summer, probably due to uptake by primary producers, salinity and the interaction with sediment.

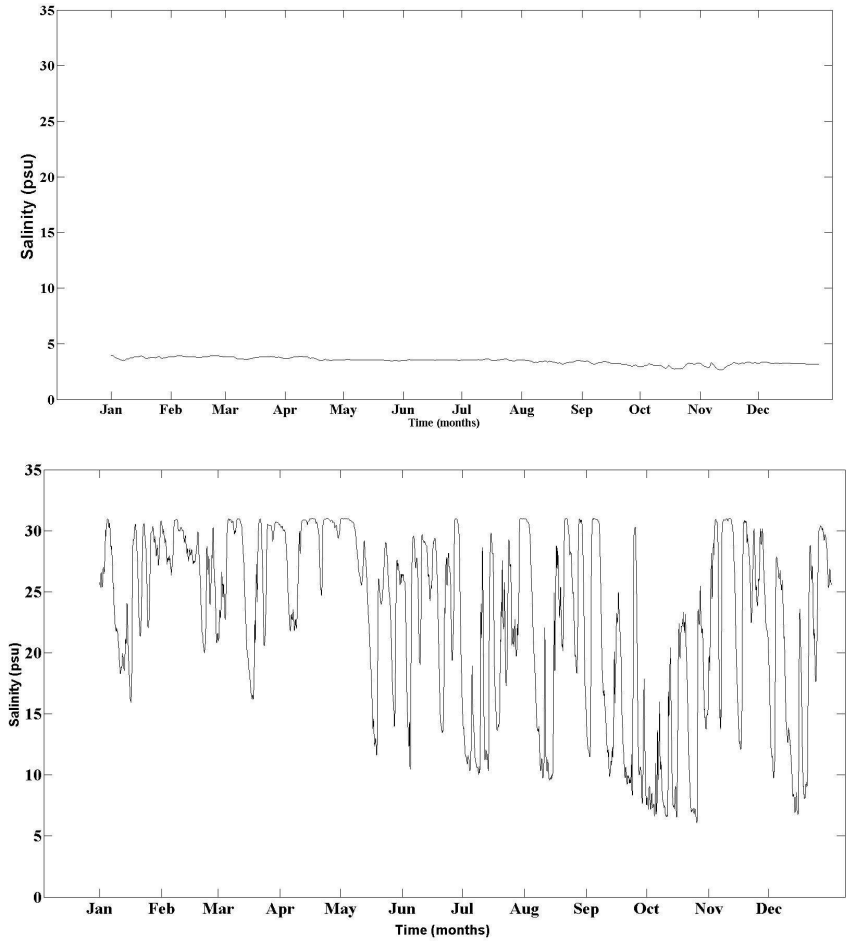

Figure 3. *Time series of salinity: (A) E1; (B) Rio Grande.*

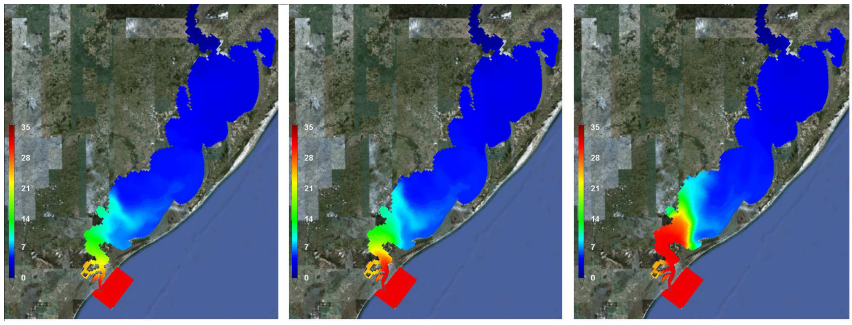

Figure 4. *Salinity variation with SW winds with low river discharge (April).*

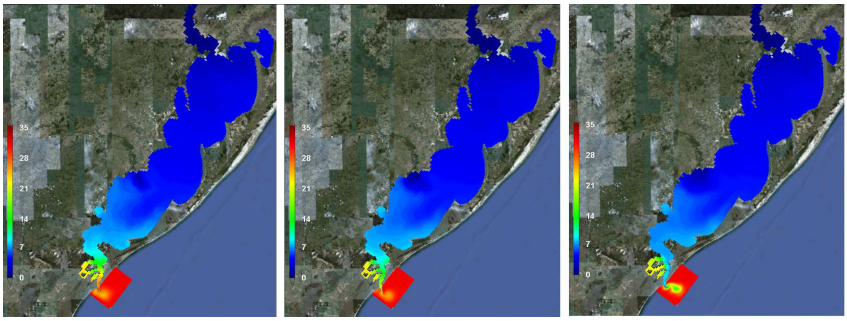

Figure 5. *Salinity variation with NE winds with high discharge rates (September)*

These inorganic forms are produced from organic matter remineralization. According to [17], there are several factors leading to changes in concentration of phytoplankton in the Patos Lagoon, such as: precipitation - which transports more dissolved inorganic nutrients by the continental discharge and changes salinity and ionic strength, influencing the flocculation of particles; saline wedge input - which causes the elevation of dissolved inorganic nutrients which may be caused by return of estuarine water still containing high levels of nutrients; wind action - at low hydrodynamic an potential gradient redox in the sediment is formed. This makes that reductive conditions occurs over the sediment, facilitating the production and retention of dissolved inorganic nutrients near the bottom. With the action of the winds, there is an increase of the local hydrodynamic and redox gradient is disrupted, causing the release of dissolved inorganic nutrients to the water column; and human activities - which are responsible for the main sources of phosphate and the main cause of eutrophication in the estuary.

A representation of the behavior of environmental parameters is shown in Figure 6. The maximum values of chlorophyll-a were found in the northern portion of the lagoon (Ponta Grossa: 44.9 μg L^{-1}) and the minimum at E1 (1.56 μg L^{-1}). The largest variations in chlorophyll-a followed the saline intrusion; thus above the maximum reach of salt in the lagoon (stations E1 and E3) the variation in chlorophyll-a is minimal. As an exception to this

situation, the station of Ponta Grossa even without any interference of salt has large variations in chlorophyll-a, related to continental discharge. The mean concentration of the lagoon was approximately 9.0 μg L^{-1}, which is equivalent to a primary production of 0.45 mgC L^{-1}.

The maximum and minimum concentrations of nitrate were found at Ponta Grossa (21.09 μmol L^{-1} and 0.007 μmol L^{-1}). The mean values for the lagoon as a whole was 2.14 μmol L^{-1}. Ponta Grossa station also had the maximum and minimum concentrations of ammonia (90.4 μmol L^{-1} and 0.74 μmol L^{-1}). The mean concentration of ammonia for the entire lagoon was 3 μmol L^{-1}. At all stations the increase in chlorophyll-a was find to cause a decrease in ammonia. At Ponta Grossa station the maximum and minimum concentrations of phosphate were found (1.6 μmol L^{-1} and 0.137 μmol L^{-1}). The mean value for the lagoon was 0.9 μmol L^{-1}.

a) Ponta Grossa

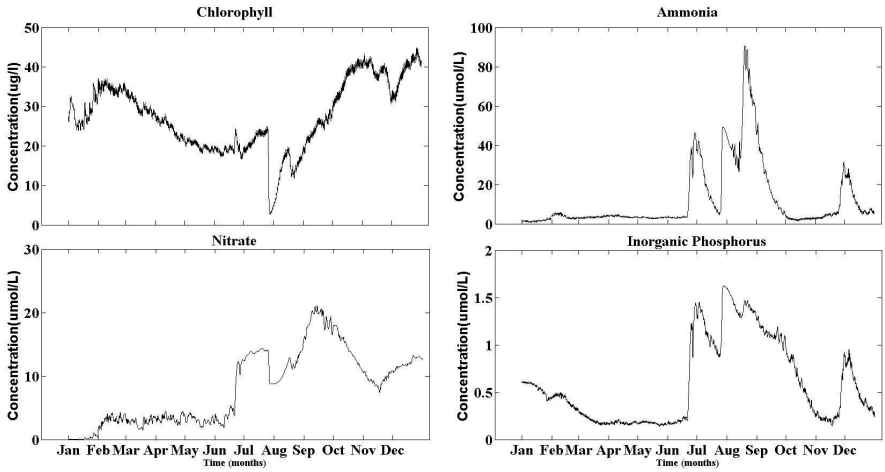

b) E3

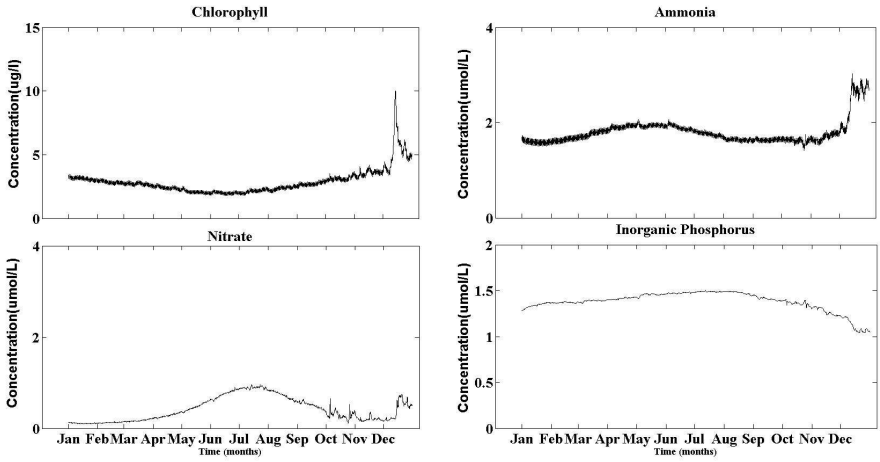

Fig 6. *Cont.*

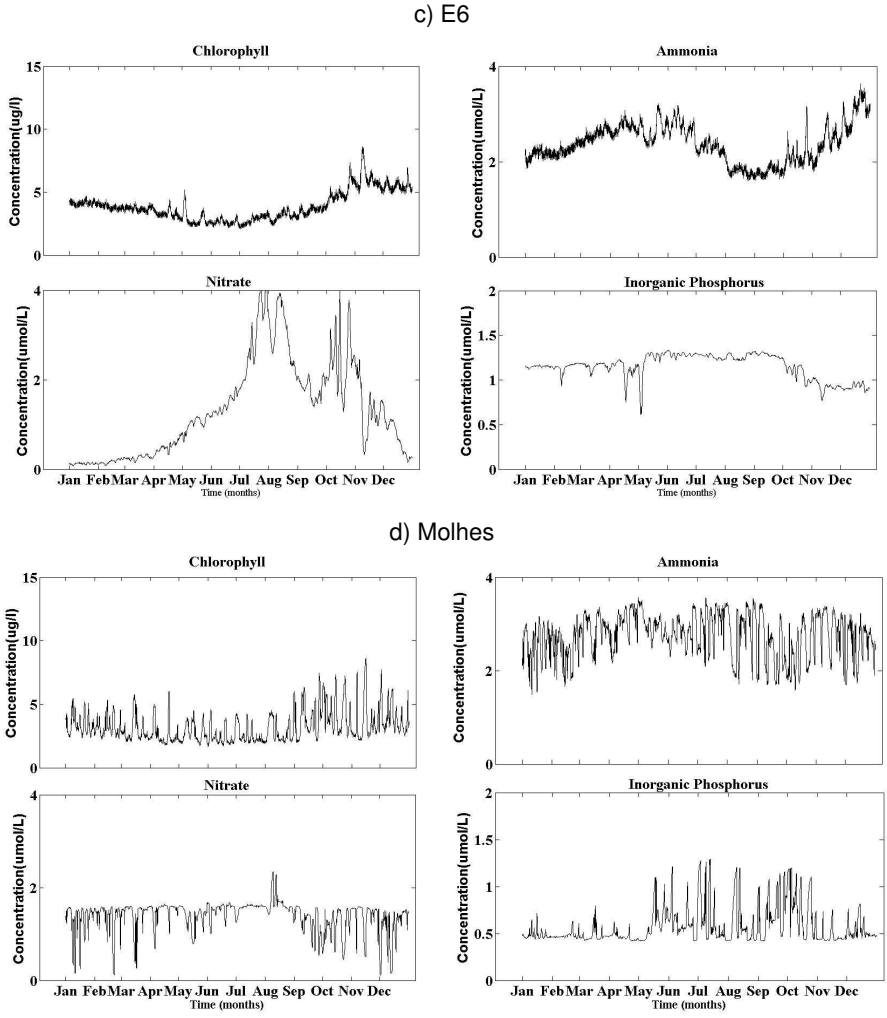

Figure 6. *Variation in ecological parameters for the stations of: a) Ponta Grossa; b)E3 ; c)E6 e d) Molhes.*

Low concentrations of phosphate and ammonia are related to long-stay fresh water within the lagoon, which leads to lower nutrient release from sediments [17]. This behavior was verified for all stations in November. The high values of dissolved inorganic nutrients in the north of the lagoon are related to land supply as transported by rivers to the lagoon. These high values are also observed near the discharge of Camaquã River.

There is a tendency for higher values of nitrite, nitrate and phosphate as the water goes fresher in the low estuary [17], and this can be verified by comparing the behavior of the stations E6 and Molhes. Flocculation and uptake by primary producers are the two reasons which may lead dissolved inorganic nutrients to removal from the water column in areas of

salinity level lower than 5 psu. In the limnic region of Patos Lagoon phytoplankton depletes nutrients in the water when they form large biomass, making this nutrient-poor water to reach the estuarine portion [17]. Such behavior was verified at Ponta Grossa, which though being close to the river discharge shows low nutrient levels during summer and spring, when there is high rate of phytoplankton growth.

Large variations of dissolved inorganic nutrients and chlorophyll-a in the estuary may be related to wind action and the entry of saline water. The action of winds and the entry of saline water disrupt the redox gradient and release great amounts of nutrients into the water column [17]. The interference of salinity was observed at E6, Laranjal, Rio Grande, and Molhes, where salinity variations occurred in a short time, causing a large change in ecological parameters over the year. This behavior was not standard for the entire lagoon and may be related to the proximity of some stations to the river discharge (Ponta Grossa and E1, for example), which consequently causes the nutrient concentration in the water column to increase and thus prevents the sediment from spreading.

Studies [17] indicate that periods of high river discharge and precipitation turn light into the major limitation of phytoplankton growth, since the high river discharge increases the concentration of suspended matter in water and reduces the penetration of light. As observed for Ponta Grossa in August the decreased chlorophyll-a concentration may have been caused by high river discharge. Previous studies on the evolution of chlorophyll-a and dissolved inorganic nutrients in the Patos Lagoon found that in the limnic region, north of the lagoon, there is a high mean chlorophyll-a concentration; as for the oligohalina region (salinity from 0.5 to 5 psu) a biomass phytoplankton was found controlled not only by light but by nitrogen as well. Over the year E3 and E4 stations showed low values of nutrients when compared to other stations, agreeing thus with the study. This still indicates that relatively high values of phosphate, greater than 1 μmol L^{-1}, prevail along the lagoon and virtually throughout the year. Such behavior was also found in the model results.

Analyzing the flow of properties among the boxes along the lagoon (Figure 7) the estuary was found to receive yearly approximately 13,240 tons of chlorophyll-a (in terms of carbon), while 6,093 tones are exported to the coast. Thus there appears to be a significant death of phytoplankton in the lagoon. In general there is an annual flow of ammonia, nitrate, chlorophyll-a and phosphate from inside the lagoon to the coast. However the highest flows were observed in the estuarine portion. This behavior can be explained by the intrusion of sea water, which carries a portion of the estuarine water previously discharged on the coast containing large amounts of dissolved inorganic nutrients.

The flow of sediment nutrients meets the needs of primary production by phosphorus, whereas only 25% of the nitrogen needs are met [17]. This statement may justify the behavior of ammonia and nitrate between boxes 6 and 7. The low concentration of these in box 6 induces the phytoplankton to import them from an area of high concentration. As the area of box 7 includes the Camaquã River discharge it has higher concentrations of nitrogen than box 6 and generates the observed flow.

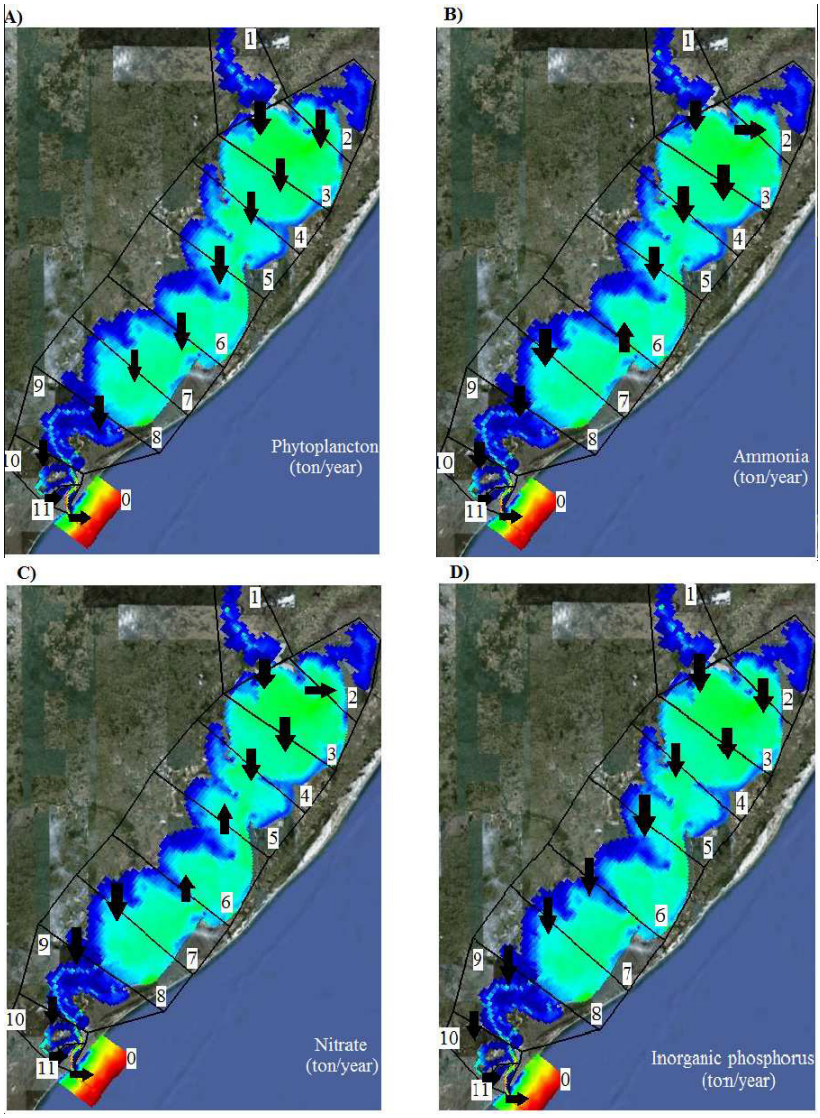

Figure 7. *Flow of properties among the boxes along the lagoon: Phytoplancton (A); Ammonia (B); Nitrate (C), Inorganic Phosphorus*

5 CONCLUSION

Results represent a few more important steps in understanding the key processes controlling the water quality of the Patos Lagoon. Taking into account the time required for the stabilization of environmental parameters, the long numerical simulations (one year) were important in the reproduction of data measured in the field, whereas considering the new configuration of its access channel brought model results closer to the environment reality.

However, the reproduction of data measured in the field was not perfect due to a series of approximations and limitations of numerical models. This was evidenced by the failure of the model to reproduce the maximum and minimum peaks of the calculated parameters. The model used was two dimensional, i.e. the result calculated by the model represents the integration of the parameter along the water column, regardless of stratification, and this was one of the factors that contributed to this behavior. Furthermore, there is a great need for water quality data on temporal and spatial scale suitable for the model.

There is a great lack of water quality data in temporal and spatial scale adequate to feed the model. As phytoplankton activity fluctuations occur on a small scale (hours or days) and with non-standard behavior and the field data used for validation has a monthly time scale, the comparison between simulated results (hourly time scale) and the field data is limited. Thus, the fact that the model does not follow the peak of dissolved inorganic nutrients and chlorophyll-a, as was observed in field datas, may not be an error of the model.

Even within this context, the model validation exercises have resulted in ratings ranging from ‘excellent’ to ‘good’, which indicates it is suitable for the proposed study. Moreover, the results also indicate that the variation of ecological parameters is complex and directly linked to climatic variations, mainly river discharge, wind action and salinity. Therefore, a similar ecological behavior across the lagoon was not observed: some parts of the lagoon are strongly influenced by river discharge, while others are strongly influenced by seawater intrusion. Furthermore, the results indicate that the main limiting factors for primary productivity are the shortage of nutrients and/or light.

Analyzing the results of ecological properties flow, it was noted that even though these are more intense in estuarine portion what is exported from the lagoon to the coast is less than that entering it via river discharge, i.e. there is an indication of loss of phytoplankton biomass and nutrients along the lagoon. The hypotheses that could explain such a behavior is that the phytoplankton was used as food, and hydrodynamic events which makes the lagoon water almost entirely fresh intensify the flocculation processes, thus eliminating the dissolved inorganic nutrients from the water column. In this same analysis it was also observed that in the region of the lagoon between the boxes 5 and 6 there was intense sediment deposition, which reduced the concentration of sediment and environmental parameters in this area, so that such may be characterized as areas low productivity.

Overall this work contributed to an assessment of the key ecological parameters controlling the water quality of the Patos Lagoon, considering its short time scale (time variation). Based on the evaluation of transport and production of biomass, it is possible that studies related to other economic activities such as aquaculture understand what period and region of the Patos Lagoon may have the best ecological conditions for the enterprise.

ACKNOWLEDGEMENTS

The authors would like thank Rodrigo da Rosa Pereira (FURG’s official English Translator) for the English version of this manuscript, which was carried out with the linguistic support of PAPCD-NuTra (English Language Support to Student Scientific Production) at FURG.

REFERENCES

1. Braga Jr., B. P. F,1987. Técnicas de otimização e simulação aplicadas em sistemas de recursos hídricos. In: Barth, F. T. et al. Modelos para gerenciamento de recursos hídricos. São Paulo, Nobel/ABRH, 1987. P.427-518. (Coleção ABRH de recursos hídricos). In: Braga Jr., B. P. F, Ferraz, A. R. G. Modelo decisório para a outorga de direito ao uso da água no Estado de São Paulo. Revista Brasileira de recursos hídricos. Volume 3 N.1. Jan/Mar 1998, 5-19.
2. Porto do Rio Grande. Available at: http://www.portoriogrande.com.br, Accessed on: 13/10/2010.
3. Pereira, R. S.; Niencheski, Luis Felipe Hax, 2003. Processos que regem a qualidade da água da Lagoa dos Patos segundo o modelo Delft 3D. Dissertação de mestrado em Engenharia Oceânica - Universidade Federal Do Rio Grande,RS.
4. Pearson, M., 2007. Programa Costa Sul - Manejo costeiro integrado do baixo estuário da Lagoa dos Patos e região costeira adjacente. Universidade Federal do Rio Grande,RS.
5. Neves, R.J.J., Silva, A.J.R., Braunschweig, F.; Leitão, P. C., 2001. Hidroinformática e optimização da gestão de ecossistemas aquáticos, a hidroinformática em Portugal, Lisboa. (Edição em CD).
6. Saraiva, A. S., 2001. Produção primária de biomassa no estuário do Tejo – Estudo da variabilidade das descargas. Trabalho final de curso em engenharia do ambiente. Universidade Técnica de Lisboa. Instituto superior Técnico.
7. Schiller, R. V., 2004, Influência de alterações morfológicas sobre a hidrodinâmica do estuário da Lagoa dos Patos. Monografia de Graduação, Laboratório de Oceanografia Física, FURG, Rio Grande, Rio Grande do Sul, Brasil, 84p.
8. Janeiro, J., Fernandes, E., Martins, F. and Fernandes, R., 2008. Wind and freshwater influence over hydrocarbon dispersal on Patos Lagoon, Brazil, Marine Pollution Bulletin, 56:650–665
9. Martinho, V., 2010. Estudo da dispersão de manchas de óleo na área de atuação do porto de Rio Grande –RS. Trabalho de Conclusão de Curso. Universidade Federal do Rio Grande. Programa de recursos humanos Nº 27 – ANP/MME/MCT Estudos Ambientais Nas Áreas De Atuação Do Petróleo. DHN- Diretoria de Hidrografia e Navegação.
   Available at: www.mar.mil.br/dhn/dhn/index.html, Accessed on: 01/08/2010.
10. DHN- Diretoria de Hidrografia e Navegação. Available at: www.mar.mil.br/dhn/dhn/index.html, Accessed on: 01/08/2010.
11. Praticagem – Estação Meteorológica Dos Práticos De Rio Grande.
    Available at: www.praticagemriogrande.com.br, Accessed on: 15/09/2010.
12. SISCONSUL – Sistema de controle de dados oceanográficos da zona costeira do sul do Brasil. Available at: www.sisconsul.furg.br, Accessed on: 12/09/2010.
13. ANA – Agência Nacional de Águas. Available at: www.ana.gov.br, Accessed on: 01/09/2010.
14. Leonardo, N. F., Dourado, M. S., 2010. Variabilidade diurna dos fluxos turbulentos de calor no Atlântico Equatorial. XVI Congresso Brasileiro de Meteorologia. Belém, Brasil.
15. Ribeiro,C. R., 2008. Processos de alteração da maré astronômica na Lagoa dos Patos. Dissertação de mestrado em engenharia oceânica - Universidade Federal do Rio Grande,RS
16. Fernandes, E.H.L., Dyer, K.R., Möller, O.O. and Niencheski, L.F.H., 2002. The Patos Lagoon hydrodynamics during an El Niño event (1998). Continental shelf research 22, 1699-1713.
17. Möller, O.O., Castaing, P., Salomon, J.C. and Lazure, P. 2001. The influence of local and non-local forcing effects on the subtidal circulation of Patos Lagoon. Estuaries 24,275-289.
18. Seeliger, U., Odebrecht, C., 2010. O Estuário da Lagoa dos Patos: um século de transformações. Universidade Federal do Rio Grande – FURG. Rio Grande,RS. 4: 43-45.

AN INTEGRATION METHODOLOGY TO ESTIMATE WATER FLUXES AND CONSTITUENTS BUDGETS IN COASTAL AREAS: APPLICATION TO THE TAGUS COASTAL AREA

H. de Pablo • D. Brito • M. Mateus • A. R. Trancoso • F. J. Campuzano • L. Pinto • R. Neves

CHAPTER SYNOPSIS

Background
Coastal models use fine vertical and horizontal grids for accuracy and, consequently, the output files contain large volumes of information. The interpretation analysis effort of these data is simplified if integration tools are employed. This is particularly important for long simulation periods. This chapter describes the strategy followed in the case of Tagus Estuary mouth, where a three dimensional (3D) operational model is used to simulate the flow generated by the tide, the density currents and the atmospheric forcing, and the biogeochemical processes controlled mostly by vertical transport and by the Tagus Estuary discharge.

Results
The hydrodynamic model was validated using tidal data collected at the mouth and inner estuary. Instantaneous results of the biogeochemical model in the vicinity of the outfall were validated using field data from the submarine outfall monitoring program. Fluxes were temporally and spatially integrated using three layers of five boxes. Results are presented for two contrasting situations, respectively during upwelling and downwelling conditions. Results show that in both scenarios the tidal flow associated to the estuary flood/ebb dynamics dominates the transport processes in the Tagus inlet vicinity and that the effect of the wind and global circulation role increase as one moves of the inlet.

Conclusions
With this methodology integration boxes may show the influence of systems with different hydrodynamic and biogeochemical properties (river, estuary, mouth, coastal area) to the circulation/property patterns of a particular area. The spatial and temporal versatility of boxes in MOHID implementation allows also differentiating periods in which each of the forcing actors are more significant. The use of integration boxes with vertical discretization of the water column also reproduced the effect of upwelling or downwelling, typical of this coastal area.

1 INTRODUCTION

Climatological data or monitoring campaigns allow instantaneous characterization and describe the main trends of coastal systems. However, this is insufficient to understand the processes that determine the spatial and temporal patterns. Thus, model results can provide continuous information about the system status and aid in the interpretation of observed data values.

The hydrodynamic of coastal areas influences the biogeochemical processes and determines the fate of both incoming constituents to that area and of materials produced locally. Since the velocity fields provided by these models presents a great spatial and temporal variability, which renders the hydrodynamic characterization and analyses difficult, most of the times their integration (residual circulation) provides significant information. In this context, mathematical models are essential tools for a spatial and temporal integrated characterization. The use of integration boxes with vertical discretization of the water column also reproduces the effect of upwelling or downwelling, typical of this coastal area. A way to obtain results for

areas that have distinct hydrodynamic and ecological patterns is to consider each zone as individual volumes, but nevertheless allowing the interaction between them. MOHID model allows such approach, making possible to set a number of boxes with variable shapes and sizes in function of the objectives.

Recently modelling approaches and integration boxes have been used to describe the fluxes of the main constituents between areas of interest [1], as a complement to field data estimations. As an example, Hydes et al. [2] studied seasonal nutrient and sediment patterns in North Sea using measurements, and their work was followed by Skogen and Moll [3] using a three dimensional model for the same area to estimate the role of river inflow and modelled physics on primary production.

2 STUDY AREA

The study area is located in the West Iberian coast (Figure 1), and is under the influence of one of the largest estuaries in the Europe, the Tagus Estuary, with an approximately area of 320 km^2. Residual circulation in this coastal area depends mainly on four main forces: alongshore coastal currents, tides, the Tagus Estuary outflow and local wind. The interaction between these four factors determines the dominant regime at any given moment.

The Western Iberian currents systems present a seasonal variability, with distinct summer and winter regimes. In the surface layer, a current towards south associated to the wind regime (the Portugal current [4]) occurs predominantly during the upwelling the May-September period creating upwelling conditions. At the end of the summer and during winter, the predominant wind inverts (towards east and north) and surface currents to north occur. At intermediate depths, a poleward current (slope current) persists during all the year [5].

The Tagus Estuary outflow is forced mainly by tides and therefor is oscillatory. The maximum velocities occur in the estuary mouth, with spring tide ebb values around of 2 $m\,s^{-1}$ are reached. The Tagus River is the main freshwater source of the estuary with a mean flow rates of 300 $m^3\,s^{-1}$. During winter, river flow can eventually reach around 2000 $m^3\,s^{-1}$ while summertime river flows of around 50 $m^3\,s^{-1}$ are common. The instantaneous values are strongly controlled by several dams in the Tagus River. The estuary fresh water affluence is determinant for the estuary residence time. However, only in extreme river flows conditions the circulation pattern and consequently the water characteristics that reach the estuarine mouth.

3 METHODOLOGY

3.1 Tagus Estuary mouth operational model

MOHID model was first implemented for the Tagus Estuary and adjacent areas in the early 1990s to provide answers to coastal management issues, such as residual water discharges, eutrophication sensible areas, bathing waters protection, etc. Along the years, the model has been continuously validated and improved through calibration with *in situ* data collected in several monitoring campaigns. Both monitoring programs and modelling efforts provide a significant knowledge of the system, in terms of hydrodynamics and biogeochemical processes in this coastal area.

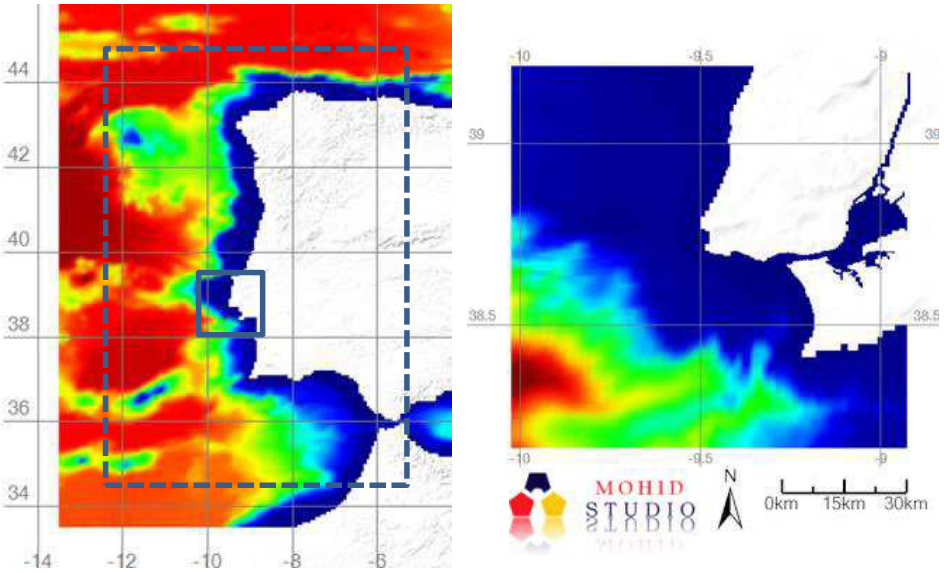

Figure 1. *Modelled domains in this study: regional model for the Portuguese coast (left) and nested model domain for the Tagus Estuary and adjacent coastal area (right).*

Recently, results were greatly improved with open boundary conditions obtained from the Portuguese Coast Operational Model System (PCOMS) (www.mohid.com/operational) [6, 7]. Velocity fields, water level, density, temperature, salinity, nutrients concentration and other parameters needed by the biogeochemical model are obtained with a 15 minutes time step (Figure 1). In the open boundary, PCOMS is forced by results from Mercator-Océan PSY2V4 [8] and its water levels are obtained from the global tide model FES2004 [9]. Both PCOMS and Tagus Mouth models are forced in the surface by operational meteorological models also running at IST (http://meteo.ist.utl.pt, [10]) which provide hourly fields of surface wind, temperature, relative humidity, pressure and solar radiation. PCOMS is forced with MM5 meteorological model with 9 km of spatial resolution, while the Tagus Mouth model is forced by the WRF meteorological model with 3 km of spatial resolution, allowing for a better differentiation of land use within the estuary and adjacent areas.

Rivers discharging into the estuary (Tagus, Sorraia and Trancão) and the submarine outfall from Guia WWTP are imposed as discharges in Tagus Mouth model with time series for flow and nutrients concentration values. The Tagus discharge has hourly values obtained in real time from hydrometric station, while the other affluent rivers values and WWTP correspond to monthly means from historical records.

The Tagus Mouth model has a 3D setup, thus allowing to study of the vertical stratification of density and coastal upwelling. The model runs operationally with 50 vertical layers (43 Cartesian and 7 sigma at the surface), in a similar configuration to the large-scale PCOMS model. The layers vary in thickness according to depth, increasing from 1 m at the surface

to 450 m at a depth of 5000 m. The model horizontal resolution is irregular with a higher discretization around the estuarine mouth and the submarine outfall area with values around 300 m while in the open ocean the resolution is around 2 km. This horizontal grid was defined in this manner to optimize computation time while keeping the necessary spatial resolution for the areas of interest.

3.2 Model validation

PCOMS model validation [6] is made using real-time with data from satellite imagery (temperature and chlorophyll-a from http://oceancolor.gsfc.nasa.gov/), tidal gauge data, currents and temperatures measured in buoys along the Iberian coast and data from ARGOS buoys, an ocean monitoring international network (www.argos-system.org) [6].

Tagus Mouth model was validated using data from monitoring campaigns. Figure 2 shows the temperature and chlorophyll-a concentration model results compared with *in situ* data from laboratorial samples and multiparametric probe, at three different water depths in the water column (surface, middle and bottom water column) from a sampling station in the study area (the emission point of the outfall). In this example it is possible to observe that the model was able to reproduce the more important seasonal tendency patterns as well as small time scale variations deriving from wind and river flow variations, which determine the influence area of the estuary plume.

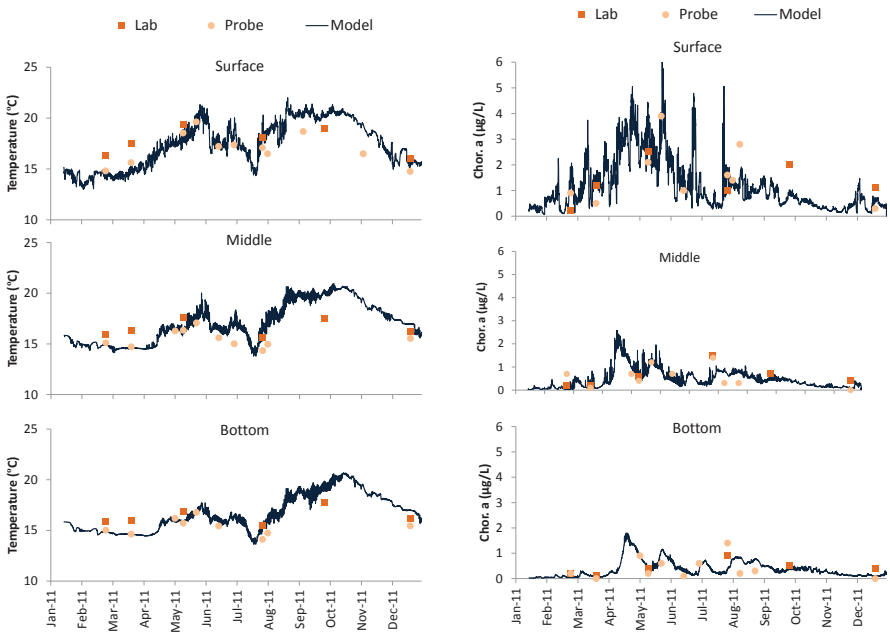

Figure 2. *Validation of model results with field data for temperature and chlorophyll-a during 2011 (outfall station).*

3.3 Fluxes

The model results comparison with field data, obtained at discrete locations, is a useful procedure for validation, but these results correspond to a specific cell in the model grid and to a given time instant. When the goal is to study areas or volumes as a whole, the representation of a specific area by a single cell make the model results simplistic and therefore unrealistic. Boxes definition is particularly useful to delimit zones or water masses with different characteristics and thereby to define and quantify processes within and between each other. In the MOHID model, the users can define boxes that could serve to determine the concentrations and the fluxes in the areas or volumes defined by them. Each box can be regarded as a finite volume where changes of proprieties exchanges between adjacent faces can take place. These exchanges are called fluxes, and can be defined as the product of the box interface flow rate and the concentration in each volume. Boxes concentrations mainly depend on the transport and transformation processes that occur in each box (mineralization of organic matter, consumption and excretion of phytoplankton, etc.).

The boxes are parallelepipeds that contain one or more cells, horizontally and vertically. Each box concentration results from the masses integration of all the cells that constitute the box. The flux between boxes is calculated by the sum of the fluxes between the adjacent cells that share a common face. An example of the MOHID box concept is shown in Figure 3. In the model each cell is defined by *i*, *j*, *k* coordinates.

To simplify the calculations, the regular or irregular polygon that defines each box is forced so that their faces coincide with the sides of the adjacent cells, that is, a cell cannot belong to two different boxes. Each box concentration results from the sum of the masses calculated at the center of each cell (green dots in Figure 3). The fluxes are calculated for all cells, partial fluxes, but for calculating the flux between the boxes, the model only considers the fluxes between cells that share one of the polygons faces (orange arrows oranges in Figure 3). The final flux results of the integration of the partial flows of each face. Water flux is calculated as:

$$\Phi_{a-b}^{water} = \int \int \left(\vec{v} \cdot \vec{n}\right) \cdot dA \tag{1}$$

Where *a* and *b* are the boxes, *v* is the velocity and *n* the normal.

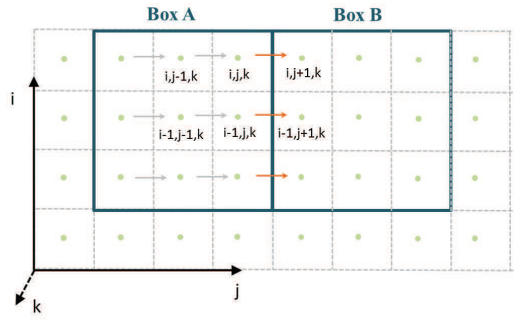

Figure 3. *Illustration of box fluxes calculated by the MOHID model.*

The flux of a given propriety is:

$$\Phi_{a-b}^{\beta} = \int_t \left(\int \int \beta \left(\vec{v} \cdot \vec{n} \right) \cdot dA + \int \int \gamma \left(\vec{\nabla} \beta \cdot \vec{n} \right) \cdot dA \right) \cdot dt \tag{2}$$

Where β is a given property and γ is the diffusion coefficient and ∇ the property gradient.

In dimensional form:

$$\left[\frac{M}{T} \right] = \left[\frac{M}{L^3} \right] \left[\frac{L}{T} \right] \left[L^2 \right] + \left[\frac{L^2}{T} \right] \left[\frac{M}{L^4} \right] \left[L^2 \right] \tag{3}$$

The number and size of the boxes result from the compromise between the computational process and the resolution of the process under study. A higher spatial resolution, horizontally and vertically, requires more computational time but the local scale phenomena are better represented, i.e., recirculation, punctual discharges.

Other studies [11, 12] used this box methodology to calculate residence times or nutrient and phytoplankton fluxes in several Portuguese estuaries. In both studies, a 2D model was used, since vertical stratification was not significant. When the upwelling process and the seasonal stratification or thermohaline are significant it is necessary to use a water column discretization approach. In the present study were considered five horizontal boxes, each discretized into three or four vertical layers, depending on the local depth. The study area was divided into three main areas namely: the estuarine, coastal and ocean areas. To understand the water column dynamics, the effort was centred in the coastal zone, which was represented by a total of nine boxes, three horizontal and three vertical (Figure 4). The analysed properties were water fluxes (flow), phytoplankton and nitrate, for being one of the key nutrients and for having a great variability depending on the Tagus River loads.

3.4 Upwelling Index

One way of quantifying the upwelling phenomenon is through the upwelling index [13, 14]. This index is a measure of the volume of water that upwells along the coast; it identifies the amount of offshore transport of surface waters due to geostrophic wind fields. Indices are in units of cubic meters per second along each 100 meters of coastline.[1]

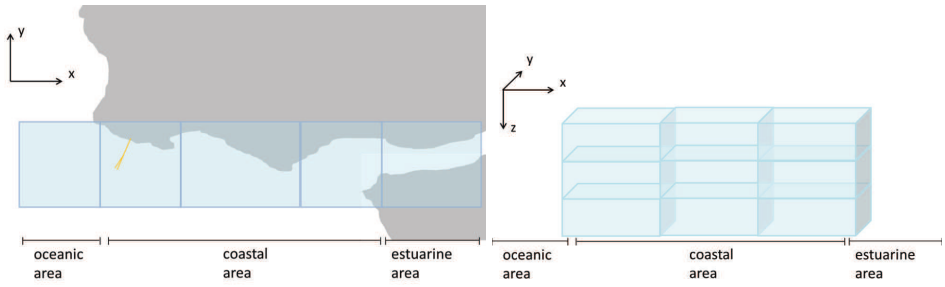

Figure 4. *Horizontal (left) and vertical (right) boxes used in the simulations.*

[1] Available at: www.indicedeafloramiento.ieo.es

4 RESULTS

The analysis focused on the first two weeks of September and November. These periods were selected based on the distinct coastal hydrodynamic patterns resulting mostly from rather different wind regimes [4]. Northerly winds dominated during September, while in November the wind regime was mostly dominated by south winds. In both periods, the Tagus River flow was relatively low ($\sim$40 $m^3\ s^{-1}$ and $\sim$180 $m^3\ s^{-1}$, respectively). As previously mentioned, vertical movements in the water column are strongly induced by local wind direction and intensity. Upwelling is a common occurrence under northern winds regimes and the upwelling index calculated for 2011 is presented in Figure 5. Values were in the same order of magnitude in both months but opposite signals were recorded: 325 $m^3\ s^{-1}\ km^{-1}$ in September and -324 $m^3\ s^{-1}\ km^{-1}$ in November. This can be attributed to the upwelling and downwelling dominance, respectively. The study area shows significant variation in the upwelling index, with maximum values peaking $\sim$3000 $m^3\ s^{-1}\ km^{-1}$ [15].

Figure 6 presents wind directions and velocities and residual surface field velocity for September and November 2011. During September the dominant north wind induced a southward surface current, setting a pattern that characterized the general surface circulation during that period. Fresh water intrusion in the coastal area induced an E-W along shore transport. Together these two processes model the estuarine plume. River discharges determined the amount of water reaching the coastal area, and the upwelling current transported the plume outwards and induced its dispersion. Local topography is also known to play an important role in the general circulation patterns [16]. An opposite scenario was seen during November, when in general the dominant southern winds induced a surface general pattern of water transport towards north.

Figure 7 and 8 show the integrated fluxes obtained from the model results for the analysed months. It must be stressed that the values shown in this figures were the result of an in-depth integration, which might explain the similar fluxes patterns for both months. This pattern is characterized by a net transport of water from south into the coastal area, followed by an outflow towards west. However, when looking at individual surface boxes (results not showed), it is possible to observe that the general circulation in the upper layers is mostly determined by the wind pattern.

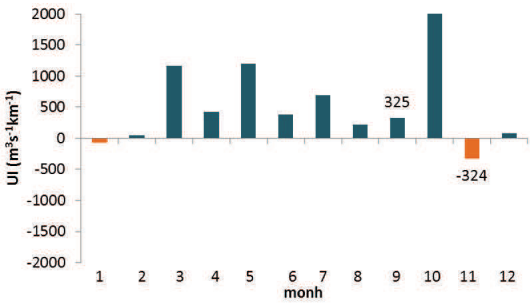

Figure 5. *Upwelling index for 2011.*

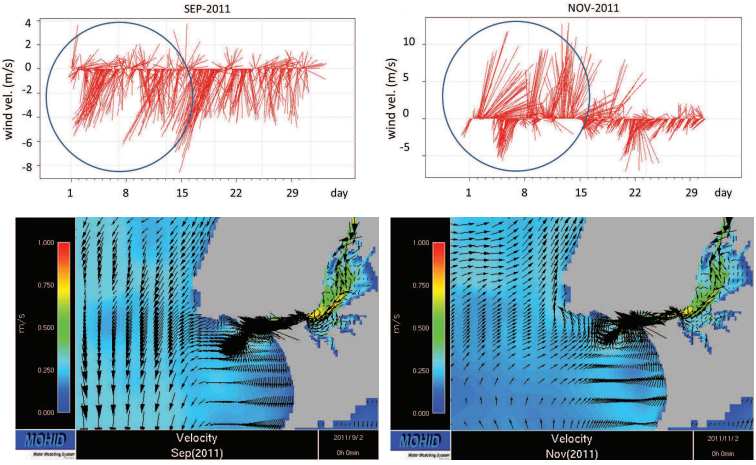

Figure 6. *Wind directions and velocities (top) and residual surface field velocity (bottom) for September (left) and November (right) 2011.*

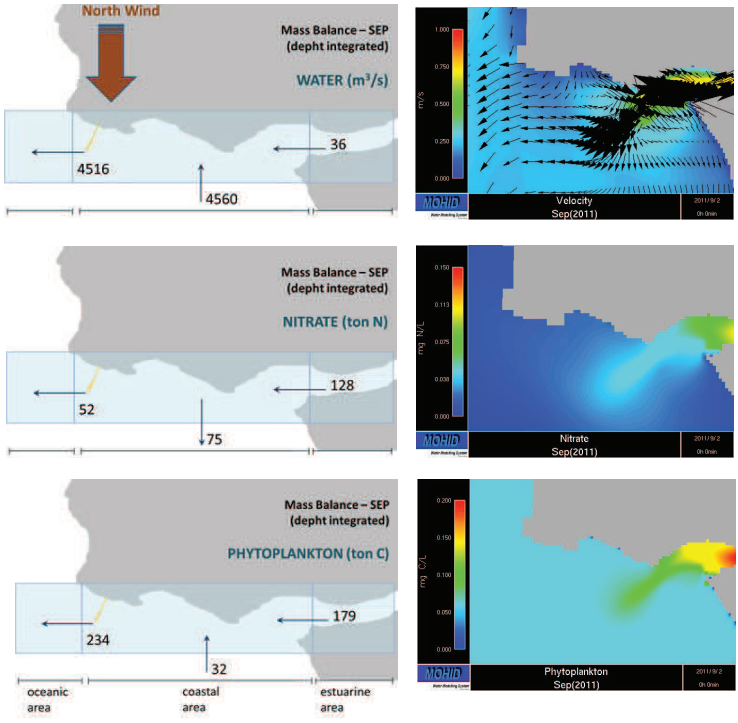

Figure 7. *Water, nitrate and phytoplankton fluxes (left) and respective residual field (right) from 2 to 15 September 2011.*

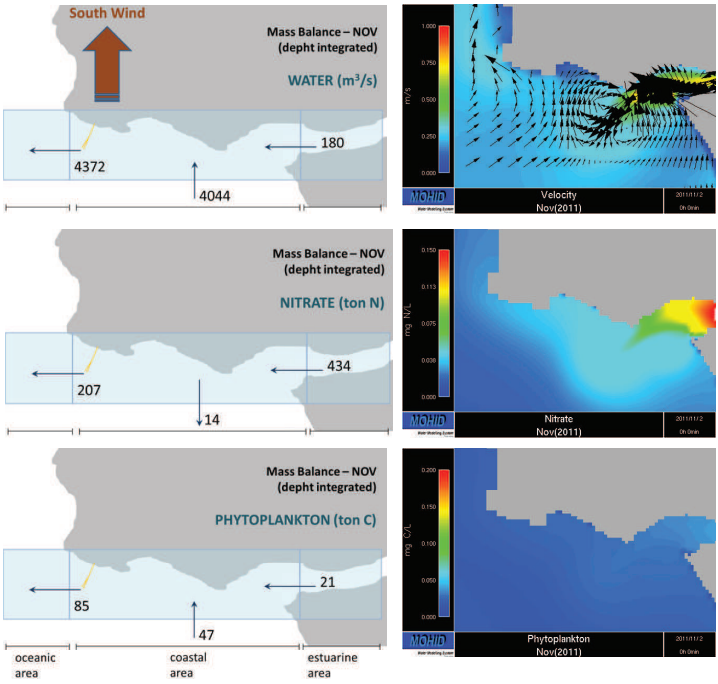

Figure 8. *Water, nitrate and phytoplankton fluxes (left) and respective residual field (right) from 2 to 15 November 2011.*

The nutrient flux is rather similar in both months, with a positive flux from the estuary to the coastal area and exportation of nutrients from this area into the open ocean. Nevertheless, the flux was higher in November, probably due to increased loads associated with the river discharge intensification and also because phytoplankton consumption decreased in response to lower light levels. The estimated values calculated in this work agree with previous data [12].

In general, phytoplankton (expressed in ton C) presented the same pattern found in the water fluxes. During the two analysed periods there was an export of phytoplankton from the estuary to the coastal zone. The low river flow caused a longer residence time within the estuary which could favour the growth of microorganism [17]. The difference lied in the balance for each of the periods, contrary to what was found for nutrients. During September, inside the estuary, the microorganisms still had favourable conditions for growing, therefore, the export from the estuarine area to the coastal area was around 10-fold higher than in November.

For a better understanding of the vertical fluxes in the water column, results for the near-coast boxes are shown in Figure 9. Flux direction suggests that upwelling condition predominated during September, with the exception of the estuarine mouth area, where the flux was downwards, most probably as a consequence of the effect of local topography. In the opposite situation, when the predominant wind was from south (Figure 10), downwelling occurred and the predominant flux was downwards for water and all the analysed properties.

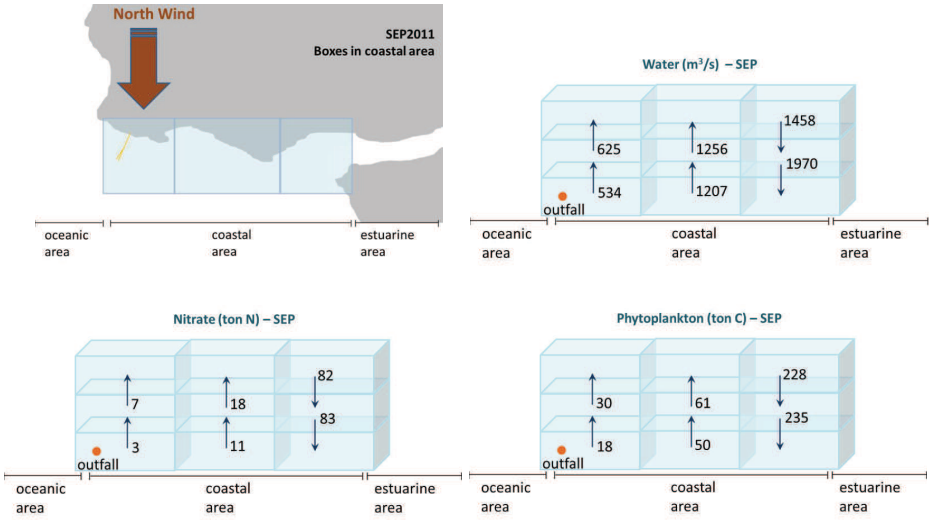

Figure 9. *Water, nitrate and phytoplankton fluxes in coastal area from 2 to 15 September 2011.*

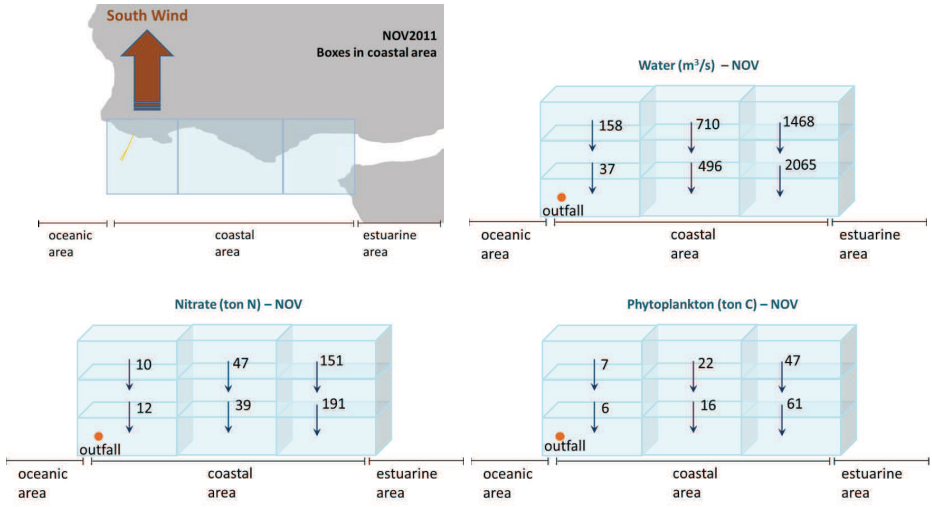

Figure 10. *Water, nitrate and phytoplankton fluxes in coastal area from 2 to 15 November 2011.*

5 CONCLUDING REMARKS

MOHID model runs operationally in forecast mode at the Tagus mouth and is validated using remote sensing data and field *in situ* data collection is continuously being performed. Field data sampled both on the Tagus Estuary influence area and on the coastal zone show that MOHID was able to reproduce both hydrodynamic circulation and water quality main processes.

The 3D biogeochemical model MOHID model reproduced the three-dimensional structure of the studied water masses. A 3D integration box approach was carried out and the model reproduced very satisfactorily the expected behaviour of circulation patterns. When the entire water column was integrated the expected north-south general circulation along the Portuguese coast was observed. When analysed only the surface boxes that cover the first few meters of the water column, flows were a function of the prevailing winds during the studied period, with circulation towards south with north wind and vice-versa. The use of integration boxes with vertical discretization of the water column also reproduced the upwelling or downwelling effect, typical of this coastal area.

Integration boxes may show the influence of systems with different hydrodynamic and biogeochemical properties (river, estuary, mouth, coastal area) to the circulation/property patterns of a particular area. The spatial and temporal versatility of boxes in MOHID implementation allowed also differentiating periods in which each of the forcing actors prevailed. For instance, in episodes with high river flow, the Tagus Estuary plume would be the most dominant factor in the physicochemical properties of the coastal zone, especially in the surface layers; episodes with intense winds would define the plume dispersion and possible redistribution of properties either at surface or in depth in upwelling / downwelling areas.

The possibility of different spatial boxes arrangements allows isolating smaller scale phenomena such as coastal recirculation or the submarine outfall effluent discharges local effects, making this a robust and versatile methodology for backing coastal management decisions.

ACKNOWLEDGEMENTS

This work was financed by SANEST, S.A. (Saneamento Básico da Costa do Estoril) under the project Guia Submarine Outfall Monitoring Program. Part of this work was included in the DyEPlume project – PTDC/MAR/107939/2008 – supported financially by the Portuguese Foundation for Science and Technology in the terms of the III Community Support Framework.

REFERENCES

1. Proctor, R., Holt, J.T., Allen J.I., Blackford, J., 2003. Nutrient fluxes and budgets for the North West European Shelf from a tree-dimensional model. Science of the Total Environment (314-316): 769-785
2. Hydes, D.J., Kelly-Gerreyn, B.A., Le Gall, A.C., Proctor, R., 1999. The balance of supply of nutrients and demands of biological production and denitrification in a temperate latitude shelf sea - A treatment of the southern North Sea as an extended estuary. Mar Chem (68): 117-131
3. Skogen, M.D., Moll, A., 2000. Interannual variability of the North Sea primary production: comparison from two model studies. Continental Shelf Research (20): 129-151
4. Fiúza, A.F.G., Macedo, M.E., Guerreiro, M.R., 1982. Climatological space and time variation of Portuguese coastal upwelling. Oceanol. Acta 5, 31-40
5. Coelho, H., 2002. Modelação de Processos Físicos Relacionados com a circulação oceanic na Margem Continentl Ibérica. Ph. D. Thesis, Instituto Superior Técnico, Universidade Técnica de Lisboa, Lisboa
6. Mateus, M., Riflet, G., Chambel, P., Fernandes, L., Fernandes, R., Juliano, M., Campuzano, F., de Pablo, H., and Neves, R., 2012. An operational model for the West Iberian coast: products and services. Ocean Science 8(4): 713-732
7. Riflet, G.F., 2010. Downscaling large-scale Ocean-basin solutions in coastal tri-dimensional hydrodynamical models. Ph. D. Thesis, Instituto Superior Técnico, Universidade Técnica de Lisboa, Lisboa, 273 pp

8. Drillet, Y., Bourdalle-Badie, R., Siefridt, L., Le Provost, C., 2005. Meddies in the Mercator North Atlantic and Mediterranean Sea eddy-resolving model. Journal of Geophysical Research 110(C3): C03016
9. Lyard, F., Lefevre, F., Letellier, T., Francis, O., 2006. Modelling the global ocean tides: modern insights from FES2004. Ocean Dynamics 56: 394 – 415
10. Trancoso, A. R., 2012. Operational Modelling as a Tool in Wind Power Forecasts and Meteorological Warnings. Ph. D. Thesis, Instituto Superior Técnico, Universidade Técnica de Lisboa, Lisboa
11. Braunschweig F., Martins, F., Leitão, P., Neves, R., 2003. A methodology to estimate renewal time scales in estuaries: the Tagus Estuary case. Ocean Dynamics, 53: 137-145
12. Saraiva, S., Pina, P., Martins, F., Santos, M., Neves, R., 2007. Modelling the influence of nutrient loads on Portuguese estuaries. Hydrobiologia, 587: 5-18.
13. Bakun, A., 1973. Coastal upwelling indices west coast North America. 1946-71 NOAA Tech. Rept. NMFS SSRF-671. 103pp
14. Ekman, V.W., 1905. On the influence of the earth's rotation on the ocean currents. Arkiv for MAthematik, Astronomi och Fysik, 2 (11), 52pp
15. Palma, S., Mouriño, H., Silva, A., Barão, M.I., Moita, T., 2010. Can Pseudo-nitzschia blooms be modeled by coastal upwelling in Lisbon Bay?. Hamful Algae 0: 294-303
16. Vaz, N., Fernandez, L., Leitão, P.C., Dias, J.M., Neves, R., 2009. The Tagus estuarine plume induced by wind and river runoff: Winter 2007 case study. Journal of Coastal Research, SI 56 (Proceedings of the 10th International Coastal Symposium), 1090 – 1094
17. Mateus, M., Vaz, N., Neves, R., 2012. A process-oriented model of pelagic biogeochemistry for marine systems. Part II: Application to a mesotidal estuary. Journal of Marine Systems 94, Supplement: S90-S101

MODELLING THE WATER QUALITY OF THE COASTAL WATERS ALONG THE AVEIRO REGION USING A MOHID-3D MODEL SETUP

J. L. Sobrinho

CHAPTER SYNOPSIS

Background
Since a proposal has been made to improve the level of treatment in three Waste Water Treatment Plants (WWTP) and a paper factory in the Aveiro region (Portugal), all of which are discharged through a submarine outfall into the ocean, about 3 km from the shore line, there is the need to build a model that can predict the influence of this proposal in the water quality in this coastal area. The model was, thus, applied to this region in order to estimate the importance of three different sources of nutrients and phytoplankton, the ocean, Ria de Aveiro, and a submarine outfall located 3 km away from the shore line.

Results
Three scenarios where built in a 3D-ecological model which includes: (1) no discharges; (2) discharge of Ria de Aveiro and (3) discharges of Ria de Aveiro and submarine outfall. The results show that of both discharges, only Ria de Aveiro has a significantly high influence in the hydrodynamics and nutrient fluxes near its mouth and a notable importance almost 40 km from its mouth, and the importance of the submarine outfall in nitrate and phytoplankton concentrations is never higher than 2% in all the time series implemented.

Conclusions
This work suggests that the implementation of a higher level of treatment in the WWTP and paper factory, in terms of nitrate and phytoplankton concentrations would have a very low impact on water quality in the Aveiro coastal region, as the ocean and the estuary are two much more important features.

1 INTRODUCTION

The Portuguese coastal area is a very complex region to study, not only from a hydrodynamic point of view but also from an ecological point of view, and especially because it is influenced by upwelling events during the spring/summer months [1]. These hydrodynamic events are caused by the combination of northerly winds and the Coriolis effect, pushing the surface water to the ocean and consequently bringing cold, saltier, nutrient-rich, to the surface. These events provide the primary producers enough food for a rapid growth during this time and are also responsible for an increase of the concentration of all the trophic levels above them, and a seasonal variation of the phytoplankton concentration.

This makes the Portuguese coast a very productive area, where fishing activities benefit. The Aveiro Coastal area is a particular case of the Portuguese coastal waters, where the hydrodynamics and primary production are difficult to model realistically [2], thus making the implementation of 3D ecological and hydrodynamic numerical models necessary to better understand and predict the influence of these upwelling events, variations of the discharges from the Vouga estuary (also called Ria de Aveiro) and the S. Jacinto submarine outfall in the primary production. In the case of coastal areas such as the Aveiro coast, the limiting factor is usually nitrogen, as is normally in the ocean, which explains the influence of the nutrients brought by upwelling events, river discharges and point sources such as submarine outfalls in

the in primary production. The main focus of this work is the study of the contribution of these 3 sources of food for the primary producers in the coastal waters of Aveiro, in order to give a formal opinion on the need to implement a stronger treatment process to the water discharged by the S. Jacinto outfall.

2 THE STUDY AREA

The coastal waters of the Aveiro region studied in this paper are located between 40° N and 41° N (Figure 1), and its length extends until 66 km from the coast line at about 9° W with a low slope, at which point the slope of the continental shelf becomes very steep [3]. There are two sources of direct fresh water input to the area, the Ria de Aveiro and a submarine outfall which discharges treated wastewater from 3 WWTP and a paper factory. Regarding the climate, the study area is located in the northern part of the northern-hemisphere subtropical high pressure belt, and the location of the anti-cyclone determines the climate over the region [1]. Due to this anti-cyclone, winter is dominated by weak southerly and westerly winds, and in summer the atmospheric current changes, where strong northerly and north-westerly winds with mean velocity of 5 – 6 m s-1 are registered [4]. Throughout the winter when the wind blows northward, the currents, forced by the wind, and intensified by the density gradient and the water discharges along the Portuguese coast, flow northward with higher speed. During Spring/Summer months when the wind blows southward, the density gradient is not strong enough to maintain a superficial northward flow and its direction is inverted. The upwelling events occurring during these seasons push surface water to the open ocean and cool deep water is forced to emerge close to the coast, which generates a baroclinic jet flowing in the same direction as the wind [5].

Figure 1. *Location of the study area.*

3 BATHYMETRY

There were two grids applied to the study area, one from the regional model – PCOMS-BIO model which is an external model to this work and the local one, built specifically for this work (Figure 2). The regional and local model cell's dimensions are 6×6 km and 2×2 km, covering an area of 11×16 and 30×42 cells, respectively. Throughout this study, several different bathymetries were used, due to hydrodynamic instability problems originated by them. The final bathymetries used were built using bathymetric points obtained from EMODnet (European Marine Observation and Data Network), which provides points in a 350 m grid.

4 WATER AND NUTRIENTS DISCHARGED

The discharges from Ria de Aveiro and the submarine outfall were provided by an external 2-dimension model implemented inside the Estuary and SIMRIA, respectively. The latter had to be estimated, since the results were relative to the WWTP entrance instead of the effluent. This estimate was made using efficiency data present in [6], and the concentration values for each of the nitrogen and phosphorus forms were obtained. Since these waters are later mixed before being discharged in the ocean, the final concentrations were calculated, using the Equation 1, were C_A(final) represents the concentration of property A in the month i, j is the index of the three WWTP and $M_A^{PORTUCEL}$ represents the mass average for each month being discharged by Portucel. In terms of nutrients, and due to lack of data, it is assumed that Portucel discharges the equivalent of 40% of all the three WWTP. The results obtained and used in the model are presented in and, and the average hourly flow for the outfall is 1 $m^3\ s^{-1}$.

$$C_A^i(final) = \frac{\sum_{j=1}^{3} (C_A^j \times V^j + M_A^{PORTUCEL})}{Vtotal} \tag{1}$$

As for the discharges from Ria de Aveiro, these were obtained using an integration box at the mouth of the Ria, and this box gives, as an output, mean hourly values for water (and all of its properties) flux coming in and out of the Ria. The concentrations of all nutrients considered in the discharge of the submarine outfall are presented in Table 1 where the most important nutrient discharge is the nitrate which also has the highest concentration due to oxidation of organic and inorganic matter in the WWTP. The average monthly flow of this discharge is 1 $m^3\ s^{-1}$.

5 ECOLOGICAL MODEL

In this project the following forms of nitrogen were simulated: ammonia (NH_4), nitrate (NO_3), nitrite (NO_2), dissolved refractory organic nitrogen (DONre), dissolved non-refractory organic nitrogen (DONnr) and particulate organic nitrogen (PON). As to the phosphorus compounds, the following are included in the model: Phosphate (PO_4), dissolved refractory organic phosphorus (DOPre), dissolved non-refractory organic phosphorus (DOPnr) and particulate organic phosphorus (POP). Regarding primary and secondary producers, phytoplankton and zooplankton were included.

Table 1. *Concentration of the various nutrients considered in the discharge of the outfall.*

	$N\text{-}NH_4$	$N\text{-}NO_3$	PON	DONre	P-PO4	POP	DOPre
Jan	1.95	10.67	4.68	8.46	1.27	0.13	0.46
Feb	3.00	16.42	7.21	13.03	1.91	0.20	0.70
Mar	2.32	12.67	5.56	10.05	1.52	0.16	0.55
Apr	2.83	15.47	6.79	12.28	1.69	0.18	0.62
May	3.65	19.98	8.77	15.85	2.00	0.21	0.73
Jun	3.78	20.66	9.07	16.4	1.59	0.17	0.58
Jul	3.67	20.06	8.81	15.92	2.35	0.25	0.86
Aug	3.87	21.21	9.31	16.83	2.74	0.29	1.00
Sep	1.70	9.33	4.10	7.40	1.53	0.16	0.56
Oct	2.18	11.94	5.24	9.47	1.70	0.18	0.62
Nov	2.15	11.78	5.17	9.35	1.96	0.21	0.72
Dec	2.94	16.08	7.06	12.76	2.01	0.21	0.74

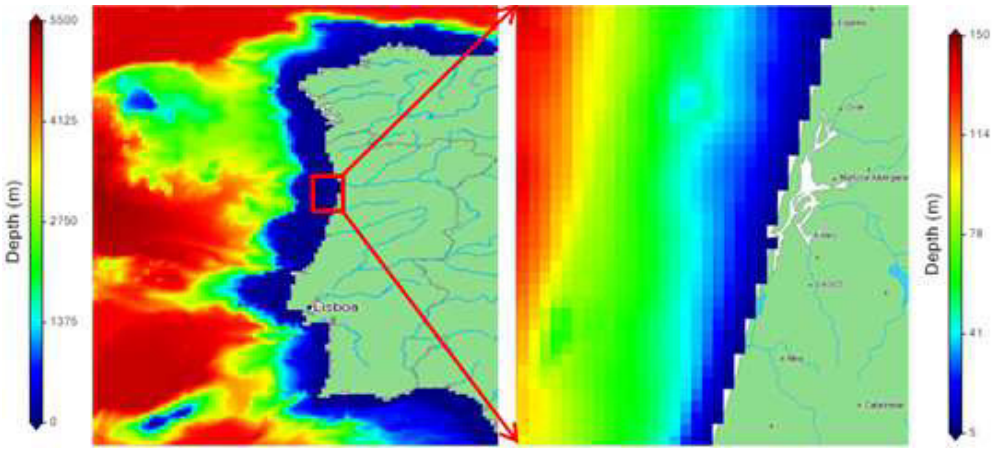

Figure 2. *Regional model (external) and local model (built for this project) bathymetries.*

For the maximum growth and mortality rates of phytoplankton, a value of 2 d^{-1} and 0.02 d^{-1} were assumed with nitrogen and phosphorus half-saturation concentrations of 0.014 mgN L^{-1} and 0.001 mgP L^{-1}, respectively.

6 RESULTS

In order to study the importance of each source near the mouth of the estuary, six integration boxes and four surface output time series were implemented, as shown in Figure 3. It was assumed that the number of time series would be enough to evaluate the influence of the submarine emissary far from its discharge point. The integration boxes were used to calculate the amount of nutrients and water flowing North, South and West, from the center cell near the mouth of the estuary.

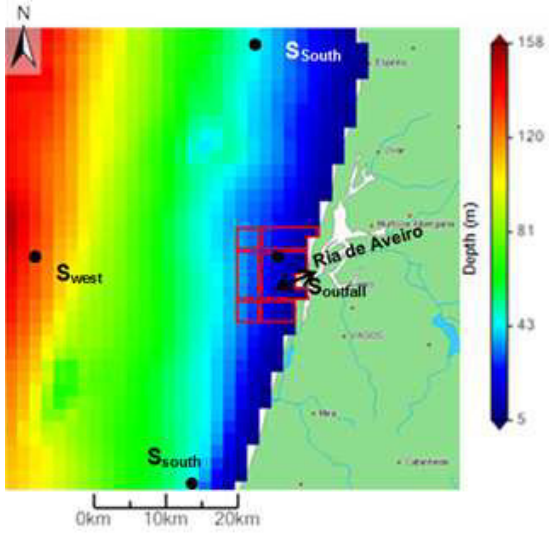

Figure 3. *Location of the time series (black, 2D integration boxes (red boxes), location of Ria de Aveiro and the submarine outfall' discharges (red dot and red double arrow).*

Furthermore, three different scenarios were created in order to determine the importance of each nutrient source. The first one considers the ocean to be the only contribution of water and nutrients to the coastal waters, the second includes Ria de Aveiro which enables to quantify its importance in comparison to the ocean, and the third considers all the sources (ocean, Ria de Aveiro and the S. Jacinto submarine outfall). The results provided by these integration boxes (Table 2) show a strong influence of Ria de Aveiro's discharge in the costal currents near its mouth, considerably changing the local hydrodynamics.

All fluxes considered were inverted when this discharge was included, with values changing from 1448×10^6 m^3 flowing North to 2332×10^6 m^3 flowing South for the scenario with no discharges and the scenario with the discharge of the estuary, respectively. The remaining fluxes have the same trend, with the discharge of the Ria changing the direction of the flow. This increase in the flux to the South is not expected as the fresh water discharge together with the Coriolis effect, tends to turn right (this case to the North). This is due to the angle of the discharge, which points southwest, forcing the water to move to the southern integration box.

There is a substantial difference in the amounts of nutrients and phytoplankton flowing through the boxes of scenario 1 and scenario 2, meaning that the water quality near the mouth of the Ria is determined almost exclusively by the net export of nutrients and phytoplankton generated inside it. The influence of the submarine outfall is barely noticed, except for the northern box, as the discharge cell is very close to it. For the remaining fluxes the influence of this outfall is less than 6%, which suggest the influence of this outfall in the concentration of nitrate and phytoplankton near the domain borders will be very small. This influence will be analyzed further ahead in this chapter.

Regarding phytoplanckton fluxes to the North, a diferent trend can be seen when comparing scenario 1 (no discharges) and scenario 2 (Ria de Aveiro) for the February period, where the flux for both scenarios have the same direction. This can be explained by the net export of phytoplanckton from the estuary. Since it's concentration is higher than in the ocean, whenever the water flows North, it takes the higher concentration of Phyhtoplancton, which makes up for the change in the flow direction from scenario 1 to scenario 2. The same thing happens with nitrate flux, although the diference between scenarios is smaller and almost inverted when the discharge of the Ria is implemented.

March results (Table 3) compared with February results (Table 2) show a significant increase of all fluxes to the North and a slight increase of phytoplankton flux to the South influenced by the discharges of Ria de Aveiro and the submarine outfall. As for the effect of the discharge, during these two months the estuary's discharge flows either south or north depending on wind, local hydrodynamics and discharge angle. Nitrate fluxes are dominated by the estuary's discharge, which accounts for an increase of 260 and 150 ton to the South in February and March, respectively, and the same happens to the phytoplankton fluxes.

As for the submarine outfall, results show a slight increase in all fluxes as was expected, but its influence is less than 10% in the primary production and nitrate concentration, which means that either the nitrate concentration is high enough already for maximum phytoplankton growth or there is not enough time for the nitrate discharge to have a higher effect before leaving the integration box, at least for the times when the water flows North and West.

Where the time series are concerned, these show that near the domain border, at a distance of about 40 km, the influence of both Ria de Aveiro and submarine outfall in the nitrate and phytoplankton concentrations is notable, even if the concentrations are very low (see Figure 4 and Figure 5). Furthermore, the time series located in the West and in the South show a significantly smaller importance of the discharges in the water quality with maximum differences of about 10% for Ria de Aveiro and 1% for the submarine outfall. The only case where the concentrations are truly affected by the discharges is the time series located in the location of the discharge of the submarine outfall, in which the concentrations of nitrate and phytoplankton are always higher for the discharge scenarios.

Table 2. *Fluxes through the integration boxes considered, for the period 08/02/2011 – 08/03/2011.*

	Scenario	Center to South	Center to West	Center to North
Water flow 10^6 m^3 month^{-1}	1	-1448	791	641
	2	2332	-1487	-612
	3	2389	-1524	-630
Nitrate ton month^{-1}	1	-17	4	-12
	2	250	5	-0.6
	3	269	16	15
Phytoplankton ton month^{-1}	1	-100	64	149
	2	113	-124	87
	3	121	-122	107

Table 3. *Fluxes through the integration boxes considered, for the period 08/03/2011 – 08/04/2011.*

	Scenario	Center to South	Center to West	Center to North
Water flow 10^6 m^3 month^{-1}	1	-232	-1393	1632
	2	1233	-2682	1700
	3	1282	-2672	1643
Nitrate ton month^{-1}	1	-0.07	-2.36	0.6
	2	152	62	157
	3	156	67	172
Phytoplankton ton month^{-1}	1	-15	-165	221
	2	159	-246	449
	3	189	-215	480

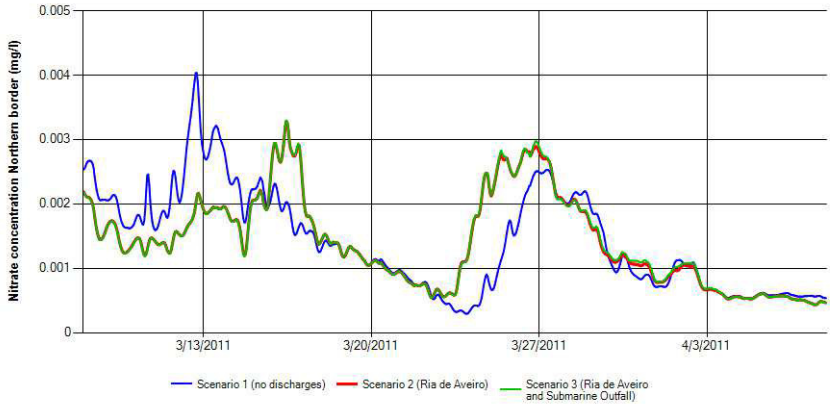

Figure 4. *Nitrate concentration in the Northern border of the domain.*

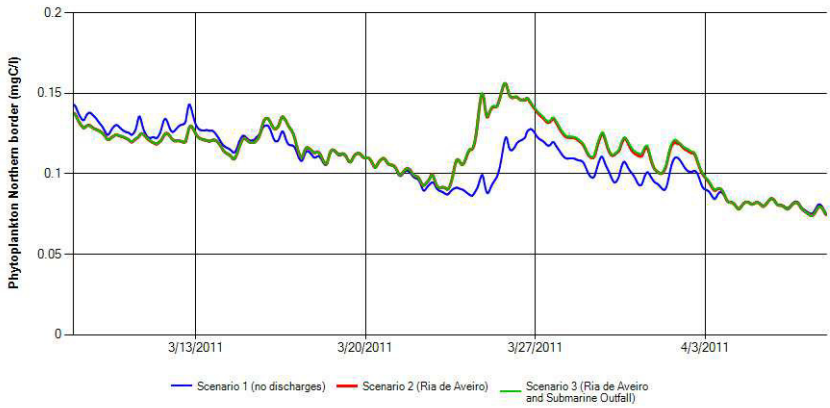

Figure 5. *Phytoplankton concentration in the Northern border of the domain.*

Figure 6 and Figure 7 also show tidal influence of Ria de Aveiro, with high concentrations in the low tide and low concentrations during the high tide. However the submarine outfall barely has any influence in the concentration of these water properties, even in its main area of influence, and when compared to that of Ria de Aveiro, its contribution is less than 0.5% for all borders considered, except for the area near its discharge, where the contribution reaches 1%. As for phytoplankton concentrations, the same trends are registered, with Ria de Aveiro playing the most important role near its mouth, and a low influence from the submarine outfall throughout the study area.

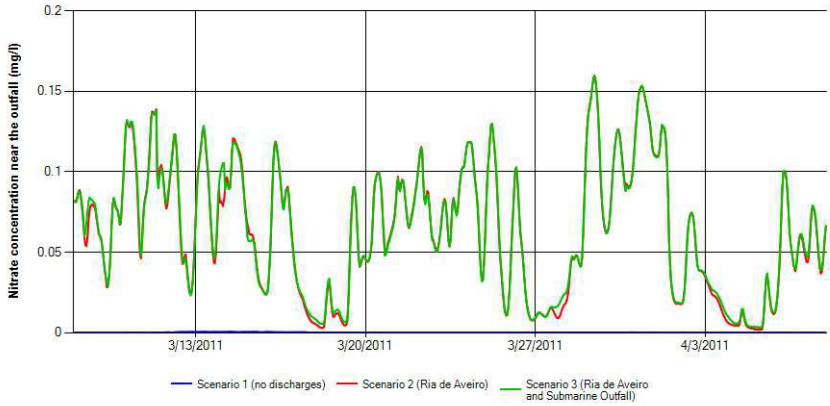

Figure 6. *Nitrate concentration in the surface cell of the location of the discharge of the submarine outfall.*

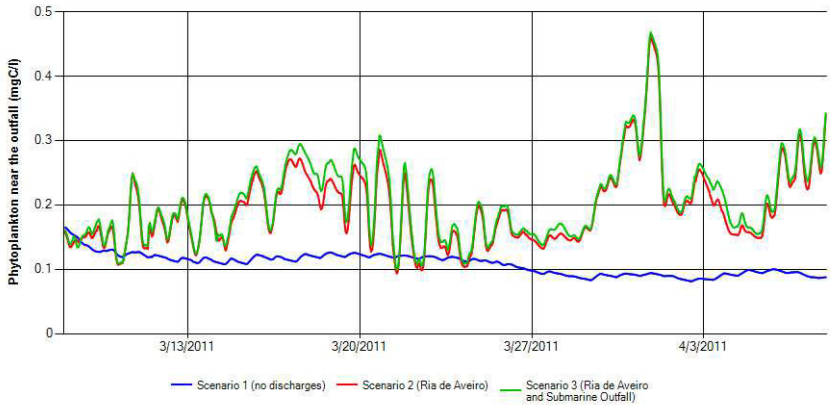

Figure 7. *Phytoplankton concentration in the surface cell of the location of the discharge of the submarine outfall.*

7 CONCLUSIONS

The main focus of this work was to study the contribution of the ocean, the Estuary of the Vouga river (or Ria de Aveiro), and of the S. Jacinto submarine outfall in the nutrient concentration (in this case only nitrate was presented) inside the study area and its effect on primary production. The MOHID 3-dimension ecological model proved its ability to represent hydrodynamic features such as the upwelling events, and nutrient and phytoplankton dynamics with accuracy, and it was able to show the influence of the submarine outfall, which, as results show, is less than 0.5%, when compared with the discharge of Ria de Aveiro, for all domain borders except for the area near its discharge). It was also concluded that the main hydrodynamic forcers close to land are the wind and the fresh water discharge (associated with the tide). It can also be concluded that the implementation of another level of treatment in the WWTP will have little impact on primary production and in nutrient concentration in the waters, as the dilution due to the ocean is very strong and capable of diminish its influence to only 1% near its discharge and almost undetected values at a distance of 40 km (Northern domain border). However, there is still work to be done in order to study the influence of this discharge in the water quality near Aveiro Coast, especially in terms of refractory organic matter. Another issue that should be addressed is the natural subterranean water discharge along the coast which was not considered but can also contribute to the nutrient dynamics near the coast where higher phytoplankton concentrations are found.

ACKNOWLEDGEMENTS

The author is thankful to Prof. Ramiro Neves (mechanics department, IST) for the guidance of this work, the teachings and discussions regarding models and modelling, and to Guillaume (Maretec, IST) and Francisco (Maretec, IST) for the help and patience through the construction and implementation of this model and for teaching me the basics of the MOHID Studio tool. Finally, the author is also thankful to all members of the Maretec team for their help discussing several topics of the MOHID working scheme.

This work was partially supported by the Portuguese Science Foundation through the research project DyEPlume (PTDC/MAR/107939/2008), co-funded by COMPETE/QREN/UE.

REFERENCES

1. Lopes, J. F., Moita, M. T., Cardoso, A. C., Rocha, A. C., and Ferreira, J. A. (2009). Modelling the temperature and the phytoplankton distributions at the Aveiro near coastal zone, Portugal. ecological modelling, 220, pp. 940-961.
2. Stephens, J. C., and Jiusto, S. (2010). Assessing innovation in emerging energy technologies: Socio-technical dynamics ofcarbon capture and storage(CCS) and enhanced geothermal systems (EGS) in the USA. Energy policy.
3. Peliz, Á., Rosa, T., Santos, A., Miguel, P., and Pissarra, J. (2002). Fronts, jets, and counter-f lows in the Western Iberian upwelling system. Journal of Marine Systems, 35, pp. 61-77.
4. Silva, J. F., Duck, R. W., Anderson, J. M., McManus, J., and Monk, J. G. (2001). Airborne Observations of Frontal Systems in the Inlet Channel of the Ria de Aveiro, Portugal. Phys.Chem. Earth (B), 26, pp. 713 – 719.
5. Moita, M. (2001). Estrutura, Variabilidade e Dinâmica do Fitoplâncton na Costa de Portugal Continental. PhD, Faculdade de Ciências da Universidade de Lisboa.
6. Metcalf and Eddy. (2003). Wastewater Engineering: Treatment and Reuse. McGraw-Hill.

USING LAGRANGIAN ELEMENTS TO SIMULATE ALONGSHORE TRANSPORT OF HARMFUL ALGAL BLOOMS

M. Mateus • A. Silva • H. de Pablo • M. T. Moita • T. Quental • L. Pinto

CHAPTER SYNOPSIS

Background
Harmful Algal Blooms (HABs) therefore poses serious restrictions to the sustainable development of coastal areas and raises serious challenges to their management. From a management perspective, a major concern regarding HABs is the ability to predict where a bloom is likely to initiate, to be transported from its last known location and for how long it will persist. The assessment of potential impacted areas is crucial when there is a serious risk of contamination of marine resources, posing a threat to human health.

Results
The work described in this chapter focus on the transport and dispersion of HAB (post-bloom detection), and represents a critical step towards the development of an alarm system of impending HAB formation. Simulations described here start with a possible location for bloom initiation and describe its transport determined by surface currents, and the extent and location of the bloom. Model predictions are compared with field data from selected HAB events along the Portuguese coast.

Conclusions
The model simulations contained in this chapter illustrate the capability of the model to predict the bloom transport and dispersion. Also, the results showed here help to interpret field data and to test hypothesis regarding the epicentre of the blooms and the possible pathways of its transport along the coast.

1 HARMFUL ALGAL BLOOMS AND THEIR IMPLICATIONS

The base of aquatic food chains is composed by around 4000 species of phytoplankton. Some of these species are considered to be harmful because they have a potential negative impact on human health through the production of a range of potent natural biotoxins. As an example, the presence of Diarrhetic Shellfish Poisoning (DSP) toxins from *Dinophysis* spp. or Paralytic Shellfish Poisoning (PSP) in the case of *Gymnodinium catenatum* leads to prolonged shellfish closures for periods that can last for several weeks in Portugal, Spain, France and Ireland [1, 2]. This also means that these episodes have a detrimental effect on the economy through their negative impact on fish or shellfish farming or other human use of ecosystem services.

Harmful Algal Blooms (HABs) therefore poses serious restrictions to the sustainable development of coastal areas and raises serious challenges to their management. It is difficult to forecast HAB initiation. Nevertheless, predicting and monitoring HABs is a fundamental step to develop proactive strategies to ameliorate their impact on human health and the economics of coastal communities. From a management perspective, a major concern regarding HABs is the ability to predict where a bloom is likely to initiate, to be transported from its last known location and for how long it will persist. The assessment of potentially impacted areas is crucial when there is a serious risk of contamination of marine resources, posing a threat to human health.

Current blooms locations, future bloom locations, and areas of impacts are critical components of a forecast system. The work described in this chapter focus on the transport and dispersion of HAB (post-bloom detection), and represents a critical step towards the development of an alarm system of impending HAB occurrences. Simulations described here start with a possible location for bloom initiation and describe its transport determined by surface currents, and the extent and location of the bloom. Model predictions are compared with field data from selected HAB events along the Portuguese coast.

2 KEY EVENTS AND OBSERVATIONS

The in-situ data are from the National Monitoring Program of HABs, held by the phytoplankton laboratory of IPMA - IPIMAR. Several nearshore stations along the Portuguese coast are weekly sampled throughout the year. A number of HAB events that occurred along the west and south coasts of Portugal have been selected for the model simulations based on 2 main criteria: (1) Availability of field data (raw data, processed data, published data, etc.) to allow a proper synoptic description of the bloom, and relevance of the blooms (magnitude, impact or other relevant aspects); (2) Availability of data for model forcing.

Despite the significant number of HAB episodes that could be used in the modelling exercises, the availability of data to force the regional model imposed restrictions on the time window. Simulations were made in hindcast mode of the PCOMS model [3], and given that the model runs since the beginning of 2009, all simulations correspond to events from 2009 onwards. Four HAB episodes in the Portuguese coast have been selected for the modelling simulations, two on the west coast and two on the south coast (Figure 1).

- A bloom of *Gymnodinium catenatum* that occurred in summer 2009 in the northwest coast;
- A bloom of *Dinophysis acuminata* that took place in the northwest coast during spring 2011;
- A bloom of *Ostreopsis ovata* that occurred in the south coast in late summer 2011;
- A bloom of *Pseudo-nitzschia* spp. that occurred in the south coast in spring 2012.

A summary of these events, along with the dates and probable location of their origin is presented in Table 1, and the main geographic location of the study areas is found in Figure 1.

2.1 *Gymnodinium catenatum* blooms

Inshore concentration on *G. catenatum* blooms depends on the cross shelf transport by upwelling and the transport velocity of the blooms seems to be lower than the driving currents. Bloom initiation and development apparently depends on a minimal concentration of cells ($> 10^3$ cells L^{-1}). Temporal fluctuations in *G. catenatum* concentration follow the upwelling-downwelling events.

Gymnodinium catenatum blooms were absent from the Portuguese coast for a decade (1996-2004) being the last major blooms recorded between 1985 and 1994, from August to November. In early September 2005, in Lisbon Bay, a bloom of this species initiated. There

was a progressive increase in the concentrations northward, reaching the Galician rias in November [4]. The northward shift of the population was related to the northward surface flow that develops at the end of the upwelling season [5]. In late November/early December, *G. catenatum* reached a maximum concentration (43×10^3 cells L^{-1}) on the Aveiro coast and lasted in northern Portuguese waters until January 2006.

The northward propagation of the bloom, based on densities of cells above 10^3 cells L^{-1} observed along time on the NW coast monitoring stations, was calculated to be ~ 0.06 m s^{-1}, about one order of magnitude lower than velocities (0.2 - 0.6 m s^{-1}) from a northward coastal current observed at the same time off the Galician rias and obtained from a lagrangian drifter (NOAA/Coast Watch) [6]. In subsequent years these events initiate elsewhere and expanded further south.

2.2 *Dinophysis acuminata* blooms

Dinophysis acuminata blooms are normally associated with buoyant plumes of lower salinity. A major bloom occurred in 2011 from mid-June to the end of July at the NW coast of Portugal, with an epicentre in Galicia (SP), and progressing towards south until Aveiro (PT). Maximum values observed at Espinho (PT) from 11 - 17 July.

2.3 *Ostreopsis ovata* blooms

Ostreopsis spp. is a subtropical epibenthic genus that bloomed at the south coast of Portugal (Algarve) for the first time in September 2011 [7]. The bloom was spotted in the shallow waters of D. Ana beach (Lagos coast) due to the presence of mucilaginous filaments at the surface. Cells normally proliferate forming a thin pellicle that covers the substrate and cell aggregates are normally released in the water column after events of increasing hydrodynamic regime (waves, currents). The bloom progressed towards W along the coast.

2.4 *Pseudo-nitzschia* spp. blooms

The ubiquitous pennate diatom genus *Pseudo-nitzschia* was associated with a major outbreak in the south coast of Portugal, in May 2012 with two possible origin scenarios (Lagos or Olhão coasts). The genus is composed of roughly 20 species [8], a number of which are responsible for the production of the neurotoxin, domoic acid (DA) and the associated Amnesic Shellfish Poisoning (ASP). These events give to the genus worldwide environmental, economic and human health importance. This particular event in 2012 persisted for 3 weeks and was responsible for shellfish closures for DA contamination during one week before cells decreased in the water.

On the Portuguese coast, blooms of *Pseudo-nitzschia* are recurrent events during spring-summer upwelling episodes, but only after 1995, ASP episodes were associated with the presence of the DA producer *Pseudo-nitzschia australis* [9]. A statistical model developed to connect the physical variables UI and Sea Surface Temperature (SST) with *Pseudo-nitzschia* concentration in Lisbon Bay [10], showed for the west coast an upwelling index limited to be less than 1000 $m^3\ s^{-1}\ km^{-1}$ (north winds <8 m s^{-1}) for bloom maintenance and development. Stronger upwelling events did not contribute to increase phytoplankton concentrations

since high turbulence conditions seem to promote the dispersion of cells. The model placed *Pseudo-nitzschia* in the second step of the phytoplankton succession, after 4 - 6 days of the intensification of the upwelling event.

3 MODELLING APPROACH

3.1 Model characteristics, implementation and validation

The model used in this operational platform for west Iberia is the MOHID model (see http://www.mendeley.com/profiles/mohid-water-modelling-system for a long list of references), which is an open-source geophysical regional circulation model anchored at MARETEC, a research group in Instituto Superior Técnico, Portugal. A full description of model characteristics, setup of the model implementation and validation is presented elsewhere [3] and will be avoided here.

3.2 Particle tracking model

The methodology followed in this study to model HAB dispersion and transport is similar to the methodology presented in [11]. The modelling approach requires the input of one or several polygons in the form of a series of points called Lagrangian Elements (LE) to be moved through time and space. The LE particles have passive transport and are moved around in two dimensions (x and y) according to local current fields pre-calculated by the hydrodynamic model. The LE is used in an offline coupling in which the hydrodynamic simulation output is first saved and then used (by reading in) to drive the particles kinetics. A major benefit of the offline linkage approach is the ability to utilize previously computed hydrodynamic solutions.

Surface currents from the hydrodynamic model are used to estimate the likely trajectory of the LE in two dimensions without any additional input from the wind. Biotic factors were not considered in the particle-tracking simulations.

3.3 Simulated scenarios

The modelled scenarios were selected based on available information, as described previously. Also, as already mentioned, the scenarios try to simulate the transport and extent of the HAB based on an origin that is assumed to be known, or define hypothetical locations as the bloom origin. Regardless of the origin (known or hypothetical), model predictions are used to test it.

Table 1 provides information on the origin of the bloom for the simulations, as well as the starting date for all tested scenarios. Simulations are arranged in a way to be grouped by species, and the results from the hindcast will be presented according to this arrangement. The location of each site along the Portuguese coast can be seen in Figure 1.

Scenarios GC–N1 and GC–N2 address the same bloom event and aim at identifying a possible origin for a *G. catenatum* bloom. For *D. acuminata* the same applies to scenarios DA–N1 and DA–N2 that simulate a bloom of this species with the same origin in the NW coast of Iberia, but with different starting dates. For the *Ostreopsis ovata* bloom only one scenario is presented (O–S1) corresponding to the geographic location and time when the bloom was first spotted in routine monitoring analysis of HABs. Finally, *Pseudo-nitzschia* spp. bloom in the south coast of Portugal presented two possible origins for the event, PN–S1 and PN–S2.

Table 1. *Modelled scenarios for HAB events hindcast runs.*

Year	Species	Scenario	Box # (Fig. 1)	Origin	Date
2009	*Gymnodinium catenatum*	GC – N1	2	Aguda/Porto	6 Sep2009
		GC – N2	2	Vagueira	6 Sep 2009
2011	*Dinophysis acuminata*	DA – N1	1	Galicia	29 Jun 2011
		DA – N2	1	Galicia	6 Jul 2011
	Ostreopsis ovata	O – S1	3	Praia D. Ana (Lagos)	20 Sep 2011
2012	*Pseudo-nitzschia* spp.	PN – S1	3	Lagos	23 May 2012
		PN – S2	3	Olhão	23 May 2012

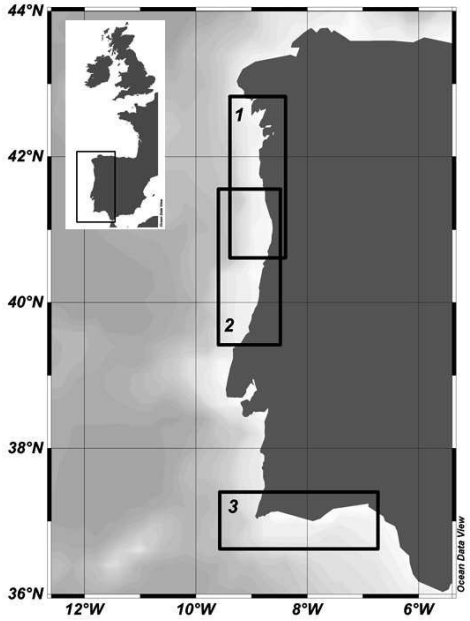

Figure 1. *Model domain of the MOHID-PCOMS model used in the hindcast simulations. Specific areas of modelled HAB transport episodes comprehend the Galician coast, Spain, and the north-western Portuguese coast (1), the NW Portuguese coast (2), and the Algarve on the south coast of Portugal (3).*

4 MODEL RESULTS

4.1 *Gymnodinium catenatum* bloom simulations

Two scenarios were simulated for the NW coast bloom (GC–N1 and GC–N2), corresponding to two distinct origins and initiation date. In the first scenario (GC–N1), the bloom is assumed to start in Aguda beach, NW coast (Figure 2, Table 1).

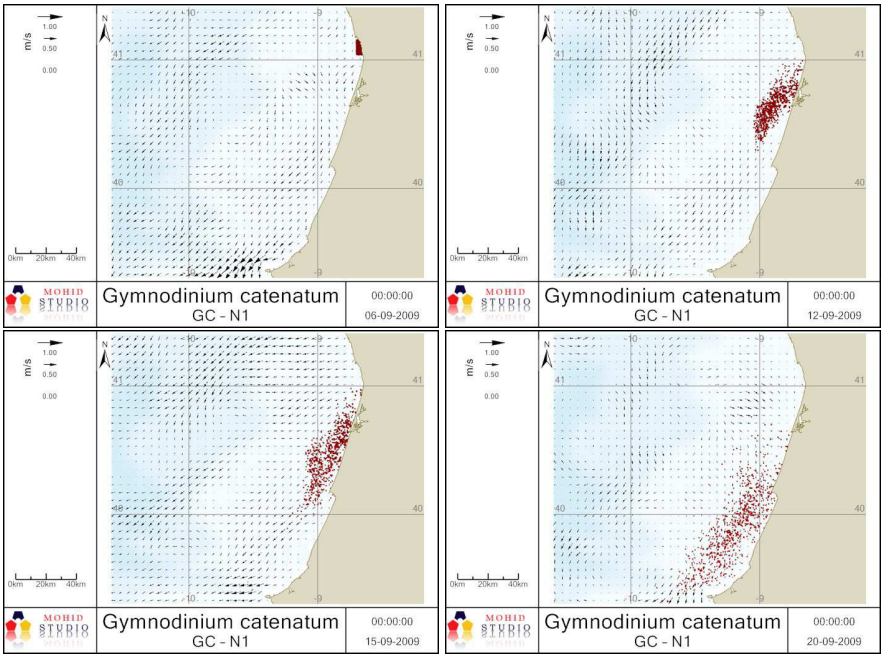

Figure 2. *Transport of the G. catenatum bloom with an origin in the Aguda area (scenario GC-N1).*

From the beginning of the simulation it is possible to see that the particles are transported south with the higher density of particles progressing off the coast. In situ data showed that the bloom seems to have started in Aguda (GC–N1) between 24-30 August (1500 cells L^{-1}). An increased in cell concentrations begin to be observed nearshore Aveiro between 31/08 and 06/09 to reach maxima of 54 - 63×10^3 cells L^{-1} one-two weeks later (14-20/09) as also seen in the model image of 19/09 (Figure 4). The presence of the species was still observed further south in the subsequent days, as visible through the small amount of particles in the Vagueira beach and South from there.

In this event the model was able to reproduce the timing of the bloom transport along the coast, after its start in the Aguda/Oporto area. The results supported the idea of an epicenter located in this area, from which the blooms was transported south.

Results for the scenario GC–N2 (Figure 3, Figure 4) didn't compared well with field data, since the hypothesis tested in this simulation could not explain the in situ values. As such, the origin of the bloom in this scenario was ruled out.

4.2 *Dinophysis acuminata* bloom simulations

Two scenarios were simulated for *D. acuminata* blooms in the northwestern coast (DA–N1 and DA–N2). Both simulations assume the same bloom origin (Galicia), but with different starting dates. These simulations intended to explain the 5000 cells L^{-1} that were observed in the monitoring station of Espinho (NW coast) from 11 to 17 July 2011.

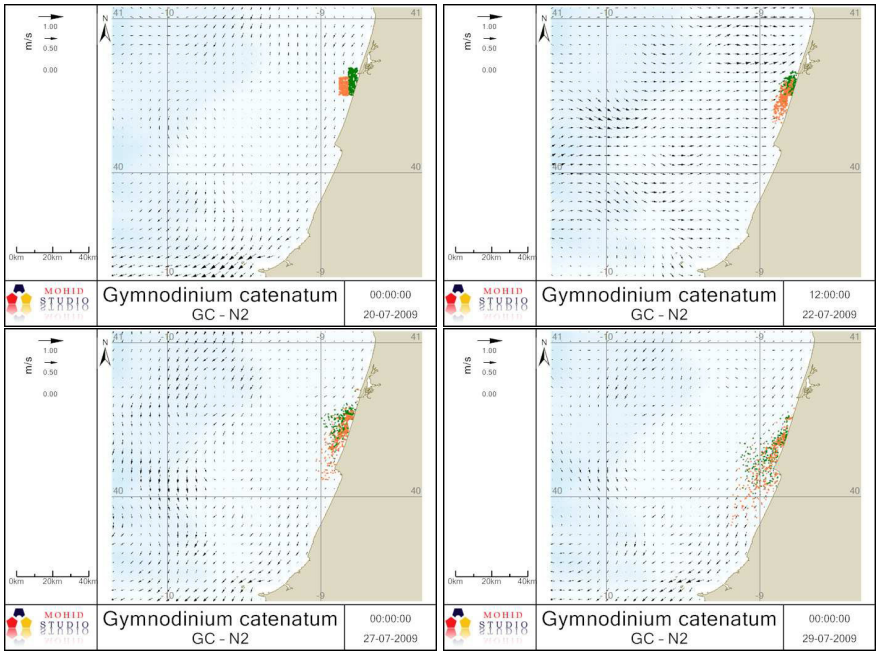

Figure 3. *Transport of the G. catenatum bloom with an origin in the Vagueira area (scenario GC-N2). Particles with distinct colors are used to differentiate the path of particles with different origins.*

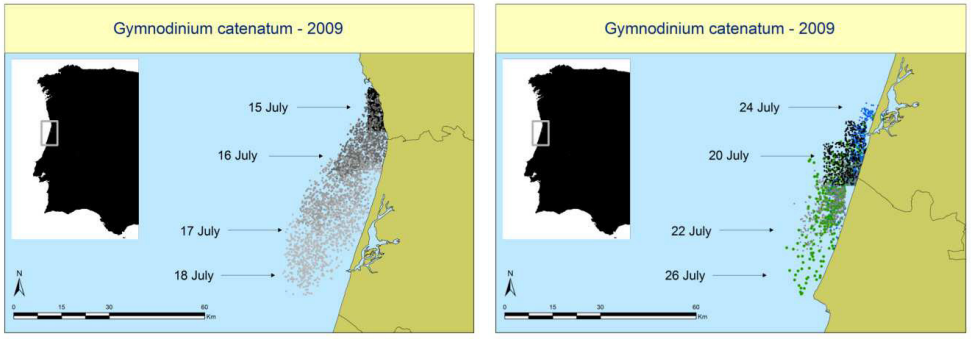

Figure 4. *Summary of model simulations (scenario GC-N1 and GC-N2) for the dispersion of a Gymnodinium catenatum bloom in 2009. Simulations differ in the timing and location of possible bloom formation.*

In both scenarios the bloom is transported southward from its origin, as a direct influence of surface currents induced by the northerly winds that predominate during this period of the year. There is, however, a significant difference between the scenarios, namely the position of the particles during the transport. As it is possible to see in Figure 5, the bloom initiated by the end of June has an initial transport to N for the first two days, and then it is transported south. The initial deflection towards N transports the bloom offshore an then south, in this scenario

only a small fraction of the particles actually reach the coast. The monitoring weekly sampling could not corroborate this scenario.

In the second scenario (DA–N2) the hydrodynamic conditions traps the bloom against the coast line where it stays throughout the subsequent transport southward (Figure 6). The particles are transported along the Portuguese NW coast and reach Aveiro area by 13 July, when 260 cells L^{-1} were observed in the water. Espinho is further south and the simulation show particles in this area around 15 July, what can be confirmed by the in-situ data. This scenario seems to explain the origin of the cells hypothesized above.

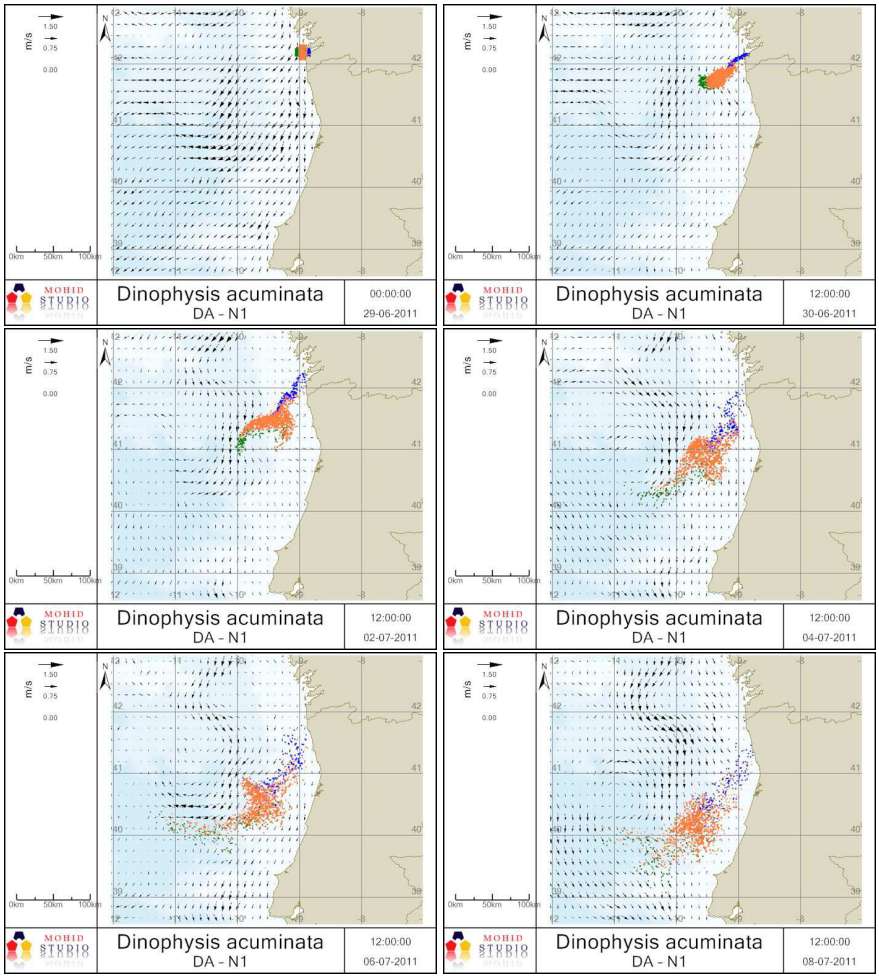

Figure 5. *Time series for the D. acuminata bloom with an origin in the Galician coast, Spain (scenario DA-N1).*

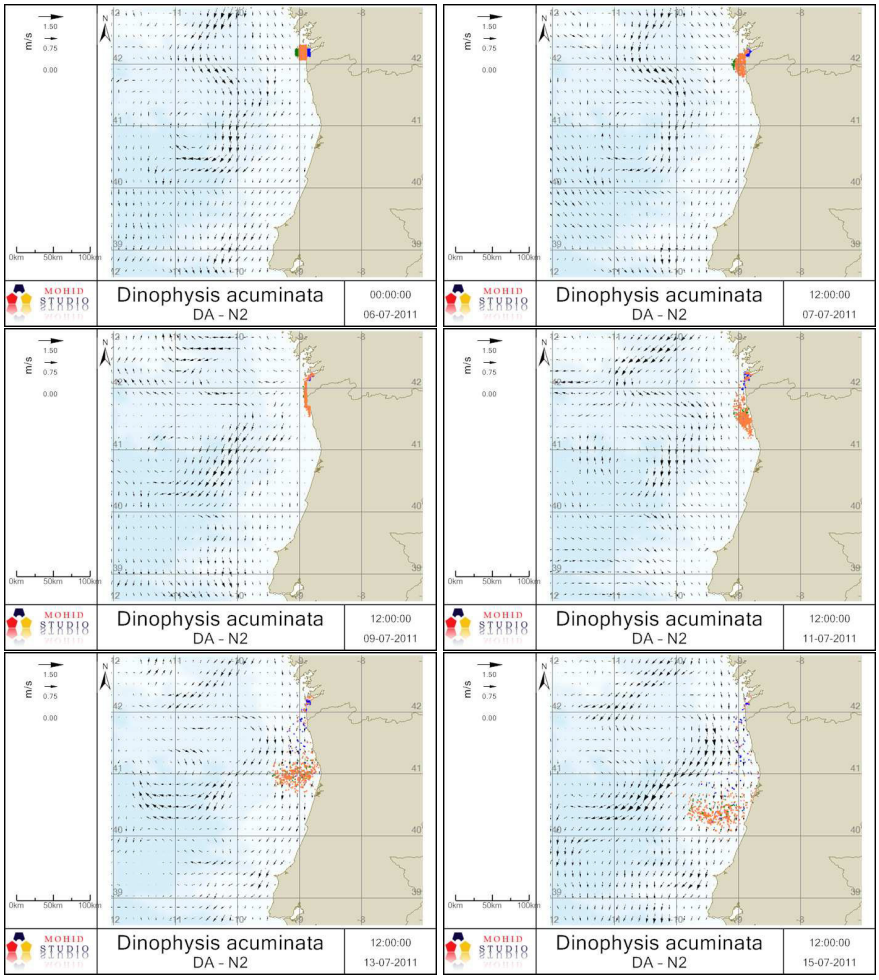

Figure 6. *Time series for the D. acuminata bloom with an origin in the Galician coast, Spain (scenario DA-N2).*

4.3 *Ostreopsis ovata* bloom simulations

The bloom was spotted for the first time in 20 of September 2011 at D. Ana beach (Lagos coast) due to the presence of mucilaginous filaments at the surface of the water. Thus, in the simulation is assumed that the origin of the bloom is the D. Ana beach (Figure 7; Figure 3, box 3). To understand the progress of the bloom, a period of 5 days of simulation, between 20 September (12.00 h) and 25 September 2011 (00.00 h), is performed (O-S1).

The analysis of the simulation results show that the bloom progress is strongly influenced by the surface currents in the area. During the period simulated the direction of the currents varied between W and SW with a maximum velocity of $\sim$1.5 m s^{-1}. During the two first days due to the relatively weak currents predominantly to W a dispersion of the bloom along the coast is observed. In two days, the bloom was transported around 10 Km W. On the third day

the currents change direction to SW promoting the dispersion of the bloom offshore and to W, and the same pattern is observed until September 24th. At the end of the period simulated the bloom was dispersed along the coast to W and off the coast to a distance of about 15 km (Figure 7). Additional details on this bloom can be found in [7].

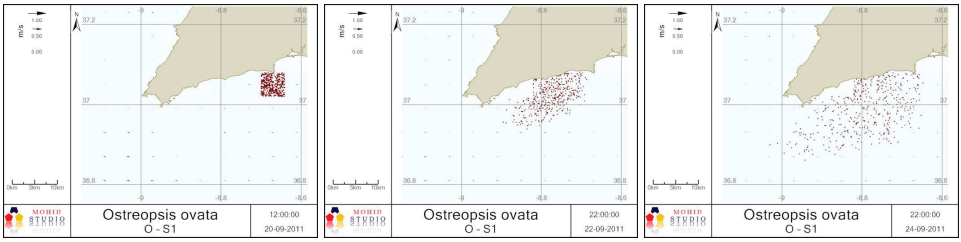

Figure 7. *Time series for the Ostreopsis ovata bloom event. Snapshots for the initial instant, t = 2 days and t = 5 days (scenario O-S1).*

4.4 *Pseudo-nitzschia* spp. bloom simulations

Two simulations were setup for the *Pseudo-nitzschia* bloom, both with the same starting date but with different origins. The hypothesis consists of 2 multi-specific blooms whose evolution in simultaneous produced different species peaking on the W and E sides of the Faro promontory. The model confirmed that the two populations did not overlap. The circulation pattern at the surface during the simulated period is dominated by an eastward flow. However, some inflections in the direction do occur in result to the shift in the wind direction. As observed in the results (Figure 8 and Figure 9), the different origins in the bloom led to a rather different scenario in the dispersion and in the potential impacted areas.

In the first scenario (PN–S1, Figure 8) the bloom disperses but stays confined to an area off Lagos (origin) between 23 and 27 May, reaching 17×10^3 cells L^{-1}. From 28 May onwards the blooms spreads and was transported to east along the coast, with a maximum concentration of 90×10^3 cells L^{-1} (30/05 in Armação de Pêra). After a 10-days period the bloom is widely spread along the southern coast and covering a large area both onshore and offshore.

The second scenario, PN–S2 shows a striking different transport and dispersion pattern of the particles, seen in Figure 9. As the simulation begins (in situ cells at 28/05/12, were 47×10^3 per liter), part of the cells remained in the area until 06/06/12, reaching 293×10^3 cells L^{-1} while according to the model, a growing number of particles are further transported away from the coast into open ocean by a jet consisting of deflection of the eastward current along because of the Ria Formosa promontory.

5 CONCLUDING REMARKS

Even a rudimentary forecast system can be useful and could be used as a baseline for future improvements [11, 12]. Once a feature or algal bloom has been identified in imagery or field data, it enables to track bloom position, thus compensating for missing imagery, and creating a nowcast and forecast for potential impacted areas. The model simulations contained in this chapter illustrate the capability of the model to predict the bloom transport and dispersion.

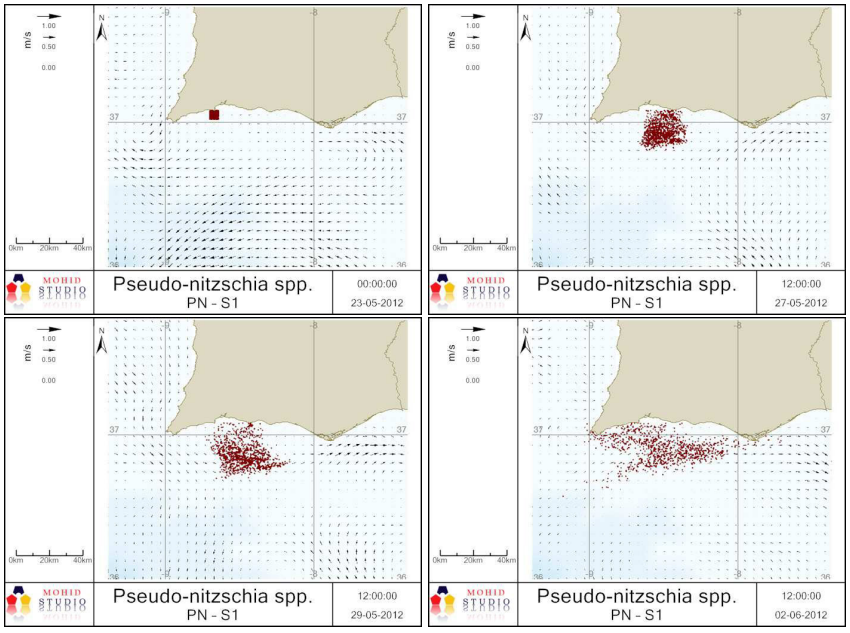

Figure 8. *Time series for the Pseudo-nitzschia spp. bloom with an origin in Lagos (scenario PN-S1).*

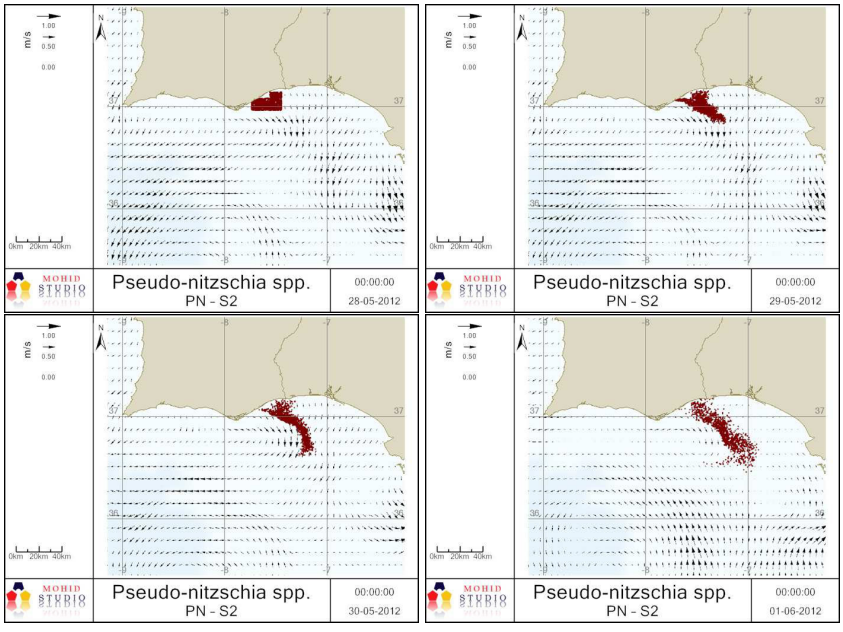

Figure 9. *Time series for Pseudo-nitzschia spp. bloom with an origin in Olhão (scenario PN-S2).*

Also, the results showed here help to interpret field data and to test hypothesis regarding the epicentre of the blooms and the possible pathways of its transport along the coast. While relaying only in physical transport simulations, the use of LE provides significant information on the fate of a specific bloom. In most cases, given the limitation of data, this modelling approach can offer the only way to track the dispersion pathways of a bloom after being spotted by in situ data. This might be the case of blooms occurring in thin-layers such as *Dinophysis* and *Pseudo-nitzschia* which are frequently associated with the pycnocline or nutricline [13, 14], thus impossible to track by remote sensing.

Model validation is a fundamental step in any modelling exercise and vital to determine model behaviour and to identify needed improvements. The skill assessment of the operational forecasts depends on the ability of the model to forecast conditions at an appropriate time and space resolution. As far as the work presented here goes, the only undertaken validation of the modelling forcing data was by comparing the skin temperature of the model with remote sensing data, and by a qualitative evaluation of the surface current fields. In this study there is a limitation imposed by the lack of field physical data and its coarse resolution near shore, not allowing further simulations of small scale features such as the presence of counter-currents or the patchy distribution of phytoplankton.

Although the present results can simulate major surface current patterns adequately, the 6 km resolution may impose serious limitations to simulate the dispersion and transport in the proximity of land. This limitation points to the need of having high-resolution subdomains nested in the actual solution, especially in areas where HAB have, historically, a relevant impact. However, after being tested with weekly HAB monitoring data, the model was able to simulate events with larger space scales helping to understand the dispersion processes in some HAB episodes that occurred in the Portuguese coast, and to test some hypothesis regarding their epicenter and transport (e.g., alongshore transport of *Dinophysis acuminata* at the Algarve coast in 2011). The model helped in real time decisions at smaller scales, when simulations were performed in a forecast mode to predict the impact areas during the first *Ostreopsis ovata* event in the south coast of Portugal (September 2011).

6 FUTURE DEVELOPMENTS OF THE MODEL

Current blooms locations, future bloom locations, and areas of impacts are critical components of a forecast system. The modelling approach presented in this study shows that models are essential tools to predict bloom transport and help in the identification of potentially impacted areas along the coast.

Validation and skill assessment are vital to forecasting, not only to determine model behaviour, but also to identify needed improvements. Similar studies point that systematic sampling is decisive for model validation, even when using qualitative descriptors [15].

The next steps in the modelling efforts towards a HAB forecast capability will be:

- Devise a validation scheme for the LE simulations;
- Assess the need for higher spatial resolution on some areas of the Portuguese coast, in particular neashore by incorporating small scale features in order to accurately simulate patchy type distributions and alongshore transport;

- Include ecological processes in the model simulations. Chlorophyll fields from remote sending data will then be used to identify transport and intensification of particular blooms, and to validate the model;
- Focus on a particular species and try to reproduce the main ecological features in an attempt to determine the conditions for bloom initiation and growth.

ACKNOWLEDGEMENTS

This work was developed in the research project ASIMUTH – Applied Simulations and Integrated Modelling for the Understanding of Toxic and Harmful Algal Blooms, supported by the EC FP7 Programme, Space Theme (Grant Agreement No. 261860). The first author of this work is supported by the Portuguese Science Foundation program Ciência2008. The second author of this work is supported by an FCT grant SFRH/BPD/63106/2009. We are thankful to all colleagues that have been contributing to the phytoplankton analysis of the National Monitoring Plan of HABs.

REFERENCES

1. Escalera, L., B. Reguera, Y. Pazos, A. Morono, and J.M. Cabanas, Are different species of Dinophysis selected by climatological conditions? African Journal of Marine Science, 2006. 28(2): p. 283-288.
2. Trainer, V.L., G.C. Pitcher, B. Reguera, and T.J. Smayda, The distribution and impacts of harmful algal bloom species in eastern boundary upwelling systems. Progress in Oceanography, 2010. 85(1-2): p. 33-52.
3. Mateus, M., G. Riflet, P. Chambel, L. Fernandes, R. Fernandes, M. Juliano, F. Campuzano, H. de Pablo, and R. Neves, An operational model for the West Iberian coast: products and services. Ocean Science, 2012. 8(4): p. 713-732.
4. Pitcher, G.C., F.G. Figueiras, B.M. Hickey, and M.T. Moita, The physical oceanography of upwelling systems and the development of harmful algal blooms. Progress in Oceanography, 2010. 85(1-2): p. 5-32.
5. Moita, M.T., S. Palma, P.B. Oliveira, T. Vidal, S. A., and G. Vilarinho, The return of Gymnodinium catenatum after 10 years: bloom initiation and transport off the Portuguese coast, in Poster nº PO.06-14 on XII International conference on HABs2006.
6. Pazos, Y., Á. Moroño, J. Triñanes, M. Doval, P. Montero, and M.G. Vilarinho, Early detection and intensive monitoring during an unusual toxic bloom of Gymnodinium catenatum advected into the Galician Rías (NW, Spain), in Painel nº PO.13-53, 12th International Conference on HABs2006: Copenhagen.
7. David, H., A. Laza-Martínez, E. Orive, A. Silva, M.T. Moita, M. Mateus, and H. de Pablo, First bloom of Ostreopsis cf. ovata in the continental Portuguese coast. Harmful Algae News, 2012. 45: p. 12-13.
8. Lundholm, N., N. Daugbjerg, and Ø. Moestrup, Phylogeny of the Bacillariaceae with emphasis on the genus Pseudo-nitzschia (Bacillariophyceae) based on partial LSU rDNA. European Journal of Phycology, 2002. 37(1): p. 115-134.
9. Vale, P. and M.A.M. Sampayo, Domoic acid in Portuguese shellfish and fish. Toxicon, 2001. 39(6): p. 893-904.
10. Palma, S., H. Mouriño, A. Silva, M.I. Barão, and M.T. Moita, Can Pseudo-nitzschia blooms be modeled by coastal upwelling in Lisbon Bay? Harmful Algae, 2010. 9(3): p. 294-303.
11. Wynne, T.T., R.P. Stumpf, M.C. Tomlinson, D.J. Schwab, G.Y. Watabayashi, and J.D. Christensen, Estimating cyanobacterial bloom transport by coupling remotely sensed imagery and a hydrodynamic model. Ecological Applications, 2011. 21(7): p. 2709-2721.
12. Velo-Suárez, L., B. Reguera, S. González-Gil, M. Lunven, P. Lazure, E. Nézan, and P. Gentien, Application of a 3D Lagrangian model to explain the decline of a Dinophysis acuminata bloom in the Bay of Biscay. Journal of Marine Systems, 2010. 83: p. 242-252.

13. Moita, M.T., L. Sobrinho-Goncalves, P.B. Oliveira, S. Palma, and M. Falcao, A bloom of Dinophysis acuta in a thin layer off north-west Portugal. African Journal of Marine Science, 2006. 28(2): p. 265-269.
14. Suárez, V., S. González-Gil, P. Gentien, M. Lunven, C. Bechemin, L. Fernand, R. Raine, and B. Reguera, Thin layers of Pseudo-nitzschia spp. and the fate of Dinophysis acuminata during an upwelling-downwelling cycle in a Galician Ría. Limnology and Oceanography, 2008. 53(5): p. 1816-1834.
15. Stumpf, R.P., M.C. Tomlinson, J.A. Calkins, B. Kirkpatrick, K. Fisher, K. Nierenberg, R. Currier, and T.T. Wynne, Skill assessment for an operational algal bloom forecast system. J Mar Syst, 2009. 76(1-2): p. 151-161.

MODELLING THE ENVIRONMENTAL AND PRODUCTIVE CARRYING CAPACITY OF A GREAT SCALE AQUACULTURE PARK IN THE MEDITERRANEAN COAST AND ITS IMPLICATIONS

A. I. Perán • F. J. Campuzano • T. Senabre • M. Mateus • J. M. Gutiérrez • A. Belmonte • V. Aliaga • R. Neves

CHAPTER SYNOPSIS

Background
Mohid Modelling System was used to assess the carrying capacity of a Marine Culture Park located on the coast of Murcia (SE Spain). This location includes seven facilities with a global production of near 7000 tons of finfish. To assess the Productive Carrying Capacity (PCC), three distinct scenarios of increasingly unfavourable hydrodynamic conditions were modelled using toxic ammonia levels and hypoxia risk as indicators. The Environmental Carrying Capacity (ECC) was evaluated under different production scenarios. In this case, the ECC was assessed by means of eutrophy levels in sediments and water column and the tolerance of benthic organisms to organic matter sedimentation.

Results
Ammonia concentrations would not reach toxic levels for the culture under the analysed distribution scheme. However, oxygen consumption due to fish breath could result in first symptoms of hypoxia stress in downstream located cages when coinciding with prolonged low hydrodynamic periods.
In any of the studied scenarios, modelled dissolved nutrient concentrations were found significantly different from local average values. Eulerian and lagrangian model results showed moderate benthic impact. The benthic effects were mainly due to uneaten feed.

Conclusions
The effect on culture and environment could be reduced by means of simple distance rules obtained from the production and environmental carrying capacity analysed in this work. An efficient feeding management that decrease the unconsumed feed would significantly improve the environmental compatibility, on the contrary mismanagement would produce very high impact on the bottom. The followed methodology in this work is highly adaptable to any area and cultured species.

1 INTRODUCTION

1.1 The San Pedro Marine Culture Park

Mariculture production in the Region of Murcia has grown since the mid 90's, with just over half a ton, up to the current 10,000 tons of fish placed on the market. Murcia has become in little more than 15 years in one of the leaders of the offshore aquaculture in Spain. This activity produced in 2008 revenues of more than 60 million Euros due to the degree of specialization achieved by companies through continuous improvement of facilities, equipment, technical training and research. Thus, marine finfish culture has become a strategic economic sector at regional level, with growing potential and able to generate a significant number of jobs.

In order to prevent socioeconomic and environmental conflicts local authorities delimited an aquaculture coastal area where facilities were grouped. Currently, this area named "Polígono de Cultivo Marinos" (the Spanish term for Marine Culture Park, hereafter referred as MCP) (Law 2/2007 on Marine Fisheries and Aquaculture of the Region of Murcia). The

MCP includes seven administrative concessions authorized to produce annually around 7000 tons of Atlantic bluefin tuna (*Thunnus thynnus*), gilthead seabream (*Sparus aurata*, hereafter referred as seabream), and European seabass (*Dicentrarchus labrax*, hereafter referred as seabass) among other species present in a testimonial number. The production is achieved by an estimated cultured biomass around 11,000 tons of fish, depending on species proportion, commercial size and conversion rates. The San Pedro MCP could be regarded as one of the biggest open sea facilities dedicated to caged fish production in the Mediterranean Sea.

In spite that every facility has a different owner; the MCP could be regarded as a single environmental and sanitary unit in management terms. To date, the facilities operation has not led to any environmental impact above the permissible levels as the environmental monitoring plans results has been showing since the beginning of the activity. Thus, according to the adaptive monitoring approach [1] adopted in Murcia [2] the production in the study area could be increased.

The San Pedro MCP is an interesting study case to test the ability of modern hydrodynamic and ecological models to deal with multipurpose and multisource discharges and evaluate resilient capacity at local and regional scales.

1.2 Numerical models as a tool for aquaculture management

Mathematical models were used on the last thirty years as an administrative tool for aquaculture management. Initial applications were simple dispersion models [3], without any regard to the systems' hydrodynamics, centred on the benthos impact by particulated materials accumulation. Lagrangian models, i.e. DEPOMOD [4], soon were considered as adequate tools for the particulated discharges study due to its high spatial resolution, but their incapacity to simulate neither the hydrodynamic fields nor the biology of the water column restricted them to very local scale applications and to scenarios where impact of soluble waste could be neglected. For these reasons, fully 3D hydrodynamic models as the Mohid Modelling System [5], able to simulate both the dissolved and particulated discharges and to represent heterogeneous hydrodynamic fields, were found suitable for this study purposes. The Mohid model included, in addition to the eulerian and lagrangian dispersion modules, several modules than could resolve sediment biochemistry, zooplankton communities (NPZD) models, pathogen dispersion from fish faeces as faecal coliforms, floating oils derived from feed pellets, etc.

1.3 Mariculture and its effects in the environment

Impacts of aquaculture activity are mainly related with the nature and quantity of wastes and oxygen consumption from the water column. Any generic input-output flow schema should comprise (Figure 1):

- Particulate Discharges: integrated by different fractions of decomposing faeces and uneaten feed. The smallest fraction is incorporated into the suspended particulate matter or detritus, which is also composed of faecal matter, waste substances, and the body remains of planktonic organisms. These particles are readily colonized by bacteria, protozoa and heterotrophs that actively remineralise organic matter releasing mainly ammonium, which is incorporated into the water column, while consuming oxygen for

the aerobic metabolism. In contrast, larger particulate matter settles in the substrate at a distance which is a function of its sedimentation speed, distance to the seabed and ambient currents. Once the solids have settled in the bottom, a small part could return to the water column in dissolved form, as a result of microbial activity and invertebrates feeding. These processes are simultaneous to the cages discharge.

- The dissolved discharge: composed mainly of ammonium excreted by fish and from remineralised organic matter. Ammonia is excreted as un-ionised form (NH_3), and depending of pH, salinity and temperature in seawater, it could be ionised forming NH_4^+. Microbial and invertebrate metabolism releases nitrogen as ammonium (NH_4), although the amount of ammonia entering the water column through remineralisation is much less than which enters directly in dissolved form by excretion and fish feed. A side effect of the particulate fraction is increasing turbidity and therefore the inadequacy of photo-synthetically active fraction of light available in the water column. Lethal concentration for 50% of the population (96h-LC_{50}) in marine caged fish has been estimated in 40 mg l^{-1} for seabass [6]. The un-ionised ammonia is 300 to 400 times more toxic than ionised form [7]. Independently of ammonia toxicity, the final effect of both types of discharges, particulate and dissolved, would be an increase in the dissolved nitrogen availability. There is a clear relationship between nutrient enrichment and water quality deterioration. Eutrophication takes place when nutrient discharge rate exceeds the processing capacity or elimination from the system and exceeding nutrients stimulate excessive biological production. Once ammonia is oxidized to nitrate is directly assimilated by phytoplankton and stimulates the development of planktonic communities, including mesoplankton, provided there is no limitation by phosphorus and silica. An increase in plankton biomass entails even greater risk of increasing populations of certain toxic algae which extreme event are red tides. Within this scheme, changes on nutrient concentration could be regarded as an undesirable water quality disturbance [8] which could significantly alter the planktonic production, increasing the risk of eutrophication or red tides events.
- Oxygen consumption: In addition to the nutrient supply, oxygen concentrations could be regarded as an indicator of aquaculture impact. Settled organic matter remineralisation imply a series of associated processes including oxygen consumption that could lead to hypoxia and anoxia events, and the rise of the red-ox potential discontinuity, that could lead to sulphide production, with the consequent impoverishment of the benthic macrofauna diversity, richness and biomass following the spatial and temporal gradients according to the Pearson and Rosenberg model [9]. Particulated matter deposited on the sediment should be considered as an undesirable disturbance when the sedimentary oxygen demand increases significantly, which could imply a benthic simplification at the community level. Thousands of tons of fish breathing in a constrained net-pen could produce a marked reduction in the water column dissolved oxygen concentration. Moderated water column hypoxia would limit growth rates and high levels would conduce to brachicardia and extreme levels to death [10].

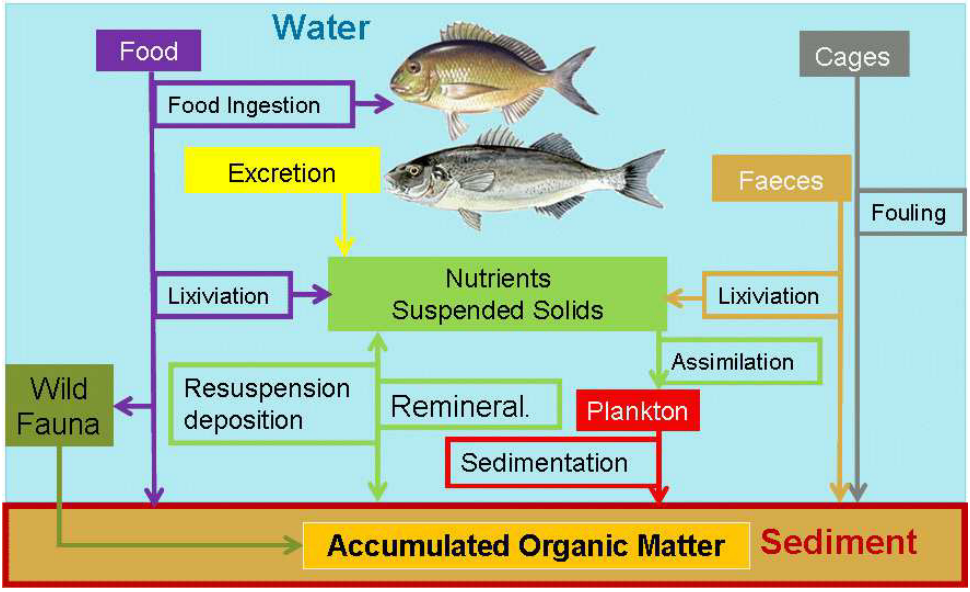

Figure 1. *Conceptual model for the aquaculture nutrient including the actors (filled boxes) and their associated processes (empty boxes). In this study, all the processes were modelled except the wild fauna (in dark green) and the cages (in grey) processes.*

In general, aquaculture facilities impacts produce small-scale disturbances, which isolated could be considered ecologically not significant. In offshore aquaculture, only minor impacts on nutrients concentrations and plankton communities were documented, especially in areas where, as in this case, the currents pattern promotes a high renewal rate of water masses [11]. In cases where some degree of confinement was added, such as aquaculture in fjords, bays and lakes, water quality could be altered by the aquaculture activity. In any case, the result of these small impacts should be monitored and should be regarded as undesirable on any aquaculture management context. Most of these studies refer to production scales much reduced than those analyzed in the present work [11], which exceeds 28,000 tons.

1.4 Objectives

The main objectives of this study include the evaluation of the Production Carrying Capacity (PCC) and the Ecological Carrying Capacity (ECC) as defined by the New Zealand National Institute of Water and Atmospheric Research (NIWA) [12] with the aid of numerical modelling tools.

Regardless of the methodological approach, in order to address the carrying capacity of an aquaculture development area, a number of issues should be taken into consideration: factors that could determine the environment productivity, the amount of food/waste that would be consumed / produced, the environment reaction to the waste discharge and the allowed change [8].

2 THE STUDY AREA

2.1 Localization

The aquaculture study area is located 6 km off the coast of the Autonomous Community of Murcia, in the municipality of San Pedro on the southeast coast of the Iberian Peninsula (Figure 2). The stretch of the Murcia coast from the north end to Cape Palos, with predominant exposure to the East, is characterized by a wide continental shelf of very gentle slope, up to 35 km from the coastline to reach 200 m depth. The aquaculture facilities are located 35 m over the seabed. The adjacent stretch of coast correspond to the San Pedro salt marshes natural reserve where the coast keeps the dunes belt and typical coastal vegetation thought most of neighbouring coastal area is occupied by large residential resorts.

2.2 Hydrodynamics

The study area is located in the transitional zone between the waters moving south from the Alghero-Provençal basin and the waters of the Alboran Sea influenced by the entering waters from the Atlantic Ocean. On the surface, the Mediterranean Atlantic Water (MAW), loaded with nutrients and low salinity, after entering through the Gibraltar Strait and circulating in two cyclonic eddies, is directed towards the inner Mediterranean Sea. Eventually, a third cyclonic gyre may occur in western Algerian waters leading the MAW to the study area. These waters could be responsible of planktonic blooms, contributing significantly to the production in the area, though this relation has been poorly studied. The influence of these cyclonic eddies is significant since the composition analyzed phytoplankton is apparently similar to the Alboran Sea [13].

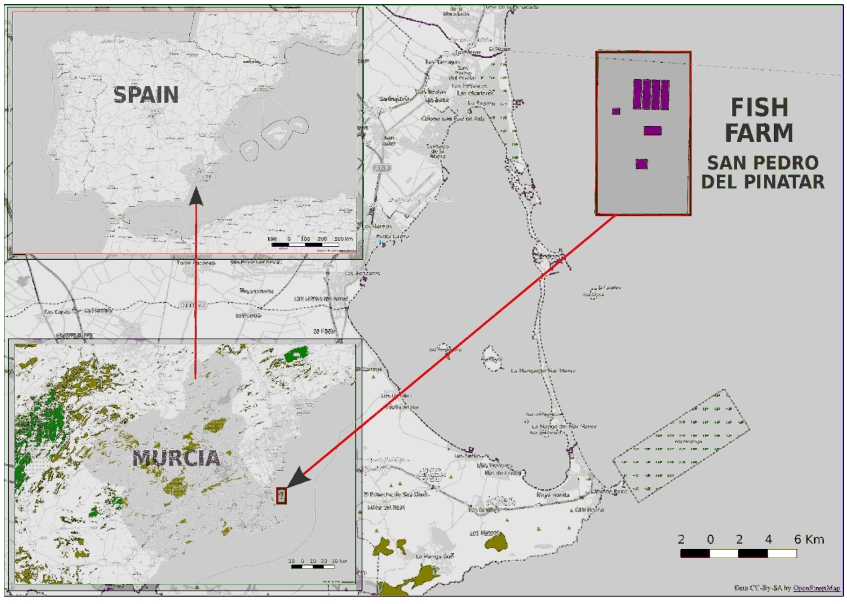

Figure 2. *Map of the SE Spanish coast where the Marine Culture Park is located.*

2.3 Water quality

The data used to characterize the regional waters come from the project MEDATLAS DS3 [14] limited to 200 m for nutrients. Nitrogen concentrations range from 0.5 mmol m^{-3} at the surface to 8.3 mmol m^{-3} in depth, with minimal seasonal deviation. The same variation occurs to phosphorus concentrations ranging from 0.3 mmol m^{-3} at the surface to 0.83 mmol m^{-3} in depth. At the local scale, data were obtained from TAXON coastal campaigns (2007-2009), in this case limited to the first 50 m depths.

The non-refractory dissolved organic matter (nrDOM) above the thermocline represents between 25-35% of dissolved organic carbon (DOC), 30-35% of the dissolved organic nitrogen (DON) and 60-80% of the dissolved organic phosphorus (DOP). The relationships between each of the elements is variable in the Mediterranean Sea, generally nrDOM concentrations are lower than refractory dissolved organic matter (reDOM), except for C:N (nrDOC:nrDON 10–19, nrDOC:nrDOP 160–530 and nrDON:nrDOP 15–38). The DOM stoichiometry in the Mediterranean Sea suggests that heterotrophic activity could probably be the dominating process in this oligotrophic sea.

2.4 Sediment quality

The seabed at the MCP is predominantly sandy, with average percentages of sand up to 74 % and a range that varies from 36 to 89% of total sand. The finer materials (silts and clays) are also quite variable, ranging between 7.7 and 57.6%, the average value for the area of 16%. The average content of organic matter is 0.7%, with a range of values in the study area ranges between 0.35% and 1.84% dry weight. These values correspond to submerged areas with some external inputs.

2.5 Trophic status

In general, the Mediterranean waters are nutrient limited, and therefore present low biological productivity, comparable to that of the Sargasso Sea and the oceanic central gyres. The oligotrophy increases from east to west with local increases based on higher nutrients supply. Medatlas data showed that nitrogen concentrations range from 0.5 mmol m-3 at the surface to 8.3 mmol m^{-3} in depth, with reduced seasonal variations. Phosphorus concentrations present a similar pattern, ranging from 0.3 mmol m-3 at surface to 0.83 mmol m^{-3} in depth [14].

Eastern Iberia coastal waters correspond to coastal subtypes characterised by the existence of a spring phytoplanktonic bloom where the planktonic biomass could double, while offshore waters generally do not present this bloom [15]. When comparing local data these waters could be regarded as productive, reaching values of 1 mg Chla m^{-3} in bloom conditions, while average Mediterranean waters do not exceed 0.28 mg Chla m^{-3}.

Trophic structure is dominated by heterotrophs over autrotrophs in terms of biomass and respiration [16]. In particular, the bacterial carbon demand might exceed the primary production. Micro and mesozooplankton exhibit the ability to feed directly from the detritus, preventing its nutrients to end up in the phytoplankton compartment and producing massive blooms [17]. This ”top down” control seems to lead to a high resilience to eutrophication [18]. Thus, the autotrophic community would not be limited by nutrients availability, but by POM demand.

3 MATERIAL AND METHODS

3.1 Mohid description

The MOHID Water is an open source numerical model included in MOHID Water Modelling System [5] developed since 1985 Instituto Superior Técnico (IST), Portugal. The core of the model is a fully 3D hydrodynamic model coupled to different modules comprising water quality, atmosphere processes, discharges, oil dispersion, mixing zone model for point source discharges, and catchment area. MOHID is programmed in ANSI FORTRAN 95 using an object orientated philosophy able to simulate eulerian and lagrangian processes. Lagrangian transport model manages the evolution of water parcels and have been used to simulate different processes as near field outfall dispersion, oil dispersion and during this work the aquaculture production processes were increased to its code.

In this work, the MOHID WaterQuality module was parameterised to the specific characteristics of the Mediterranean ecology and the aquaculture activities. Particularly, a coupled application of the WaterQuality module, a nutrient-phytoplankton-zooplankton-detritus (NPZD) module, was coupled to the hydrodynamic module to simulate nitrogen, phosphorus and oxygen cycles both in the water column and the bottom sediments. This module has a phytoplankton compartment expressed in mg C l^{-1} and nutrients and organic matter compartments also expressed in mg l^{-1} of nitrogen or phosphorus. Five particulate organic nitrogen and phosphorus pools (PON_{1-5} and POP_{1-5} respectively) with independent sinking rates (Table 1) were implemented to simulate the particulated organic discharge from the fish cages. The main features of this NPZD model were:

- Independent sinking rate for each pool defined in the FreeVerticalMovement module input file;
- Conversion of PON_x to ammonium and reDON , and POP_x to phosphate and reDOP, using the same mineralization rate and PON and POP partitioning coefficients defined in the WaterQuality module input file;
- Sedimentation and resuspension of the POM pools, with bottom mineralization (PON_x conversion to NH_4, and POP_x conversion to PO_4);
- Oxygen consumption by POM mineralization;
- Zooplankton ingestion of PON_1 and POP_1.

Table 1. *Characteristics of the simulated POM pools (origin, sinking rate and volume).*

Particle	Type	Sedimentation Velocity (m/s)	% Volume
PON_1 & POP_1	Detritus	0.00905	21.2
PON_2 & POP_2	Faeces	0.0246	18.6
PON_3 & POP_3	Faeces	0.0356	32.9
PON_4 & POP_4	Faeces	0.0463	22.1
PON_5 & POP_5	Not Consumed Feed	0.15	5.2

3.2 Aquaculture waste production model

A ”production unit” was defined to deal with multiples configurations of sea cages and incremental production scenarios. This unit was based in a standard sea cage with 25 m diameter and 20 m deep, which is the most common used cage for the seabream and seabass culture. An annual production of 100 tons by net-pen (50% of seabream and 50% seabass) was estimated. All amounts here presented are related to this unit and replicated later to construct individual scenarios. Good management practices were assumed and uneaten feed was estimated as the 3% of the total feed delivered.

A simple mass balance equation between food and excretory products was used to estimate global waste inputs [3]. A detailed characterization of different wastes forms (PON_{1-5} and POP_{1-5}, ammonia and lixiviated products), temporal evolution and influence of temperature was attained by means of bioenergetic model for seabream and seabass [19]. Daily estimated waste and oxygen consumption was distributed at hourly scale according to Calderer [10]. One entire cycle, until commercial size was attained, for seabream and seabass production was modelled (Figure 3). The simulated discharge corresponded to the daily release cycle for a production unit with 100 tons of caged biomass at the end of the production cycle.

3.3 Production Carrying Capacity (PCC)

Ammonia and oxygen concentrations were selected as indicators of the PCC. The analysis of allowable limits of these variables should provide simple regulations for the aquaculture facilities design, in terms of culture density and minimum distances between cages rows.

Analysis was conducted under an hypothetical hydrodynamic scenario of a uniform 40 meter bathymetry composed with 111×29 cells of 25×25 m wide, and three sigma vertical layers (20 m, 16 m and 0.4 m). The model was fed by a uniform North-South constant current. Three scenarios with progressively worsening current conditions were defined: calm currents: 0.04 $\mathrm{m\,s^{-1}}$; average currents: 0.3 $\mathrm{m\,s^{-1}}$ and extreme currents: 1 $\mathrm{m\,s^{-1}}$. All scenarios included 60 production units aligned north-south disposed in three sets of ten pairs of cages with a separation between cages of 25 m and between rows of 50 m.

The environmental physicochemical parameters used to feed the model were: temperature, salinity, oxygen, nitrate, phosphate and silicate, whose climatological profiles were imposed at the mesh boundaries from NOAA World Ocean Atlas 2005 data [20].

3.4 Environmental Carrying Capacity (ECC)

The ECC was evaluated in terms of the risk of eutrophication and the allowable benthos degradation. Nutrient concentrations in the water column, organic matter discharge rate and organic matter percentage in the sediment were the selected indicators. The organic matter discharge rate integrated the five types of particles simulated and was converted to organic matter concentration per unit area and day. The organic matter percentage in the sediment includes besides particulates from the marine culture, the natural organic matter from the water quality module, therefore it should be regarded as the organic matter concentration often used as an indicator in monitoring plans.

An independent hydrodynamic model of PCC scenarios was constructed. In this case a two nested domains were necessary to obtain accurate local hydrodynamics (Figure 4). Level 1, or regional level, included a regular domain covering the entire Region of Murcia with a horizontal resolution of 886 m formed by 130 cells wide by 80 cells. This was a 2D simulation and its vertical dimension was discretised with a single sigma layer of variable size forced by winds and tides. Finally level 2, or San Pedro level, was composed of 73 cells wide by 73 cells wide with a horizontal resolution of 246 m defining a simulation domain 18 km^2. This domain was 3 Dimensional whose vertical dimension was discretised by a set of 10 sigma layers.

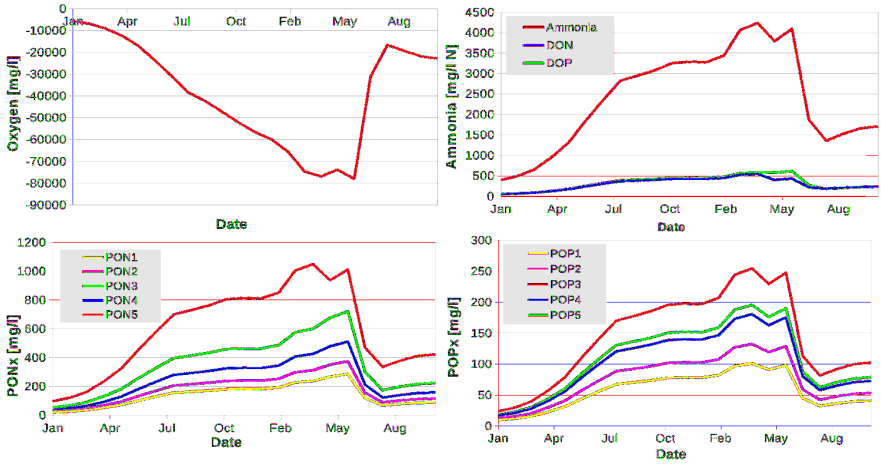

Figure 3. *Complete cycle of oxygen consumption (top left), dissolved discharges (top right), organic nitrogen particles (bottom left) and organic phosphorus particles (bottom right) for a hypothetical cage with mixed seabream and seabass culture used as input to simulate the different considered load scenarios.*

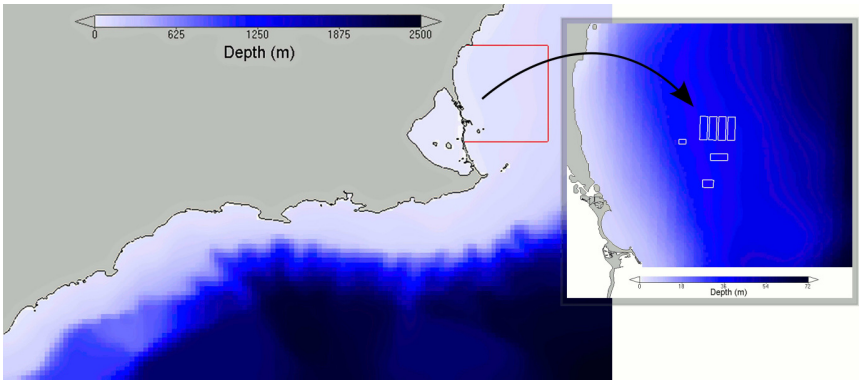

Figure 4. *Bathymetry employed for the 2D hydrodynamic domain covering the coast of the Autonomous Community of Murcia with a horizontal resolution of 886 m (Left). The red polygon corresponds to the 3D San Pedro nested domain with a horizontal resoluiton of 246 m (right). The white polygons represent the location of the aquaculture facilities in the MCP.*

For creating the model gridded bathymetries, a high-resolution digital terrain model from the ESPACE project of the Spanish Institute of Oceanography (IEO) [21] was used. Hydrodynamics were forced by local wind data from the nearby San Javier airport and by the reduced local tides, imposed in the Level 1 domain with tidal components obtained from the global tide model FES2004 [22]. At the San Pedro level the model was coupled with the water quality module where the environmental physicochemical parameters used to feed the model were the same as in the channel model described in the above section.

This realistic San Pedro hydrodynamic level was coupled with a lagrangian dispersion model. Several dispersion scenarios based on different configurations of number and spatial distribution of the production units were analysed:

1. Caged fish biomass of 11100 Tm (Figure 5a): integrated a total of 111 production units irregularly spaced and distributed in seven groups, obtaining an estimated annual production around 4,700 tons.
2. Caged fish biomass of 14000 Tm (Figure 5b): 140 production units arranged in regular distribution of 7 rows of 10 pairs of cages, accounting for an estimated annual production of 5,850 metric tons.
3. Caged fish biomass of 28000 Tm (Figure 5c): Maintaining technical and environmental efficiency of the second alternative but doubling the number of production units.

Both, eulerian and lagrangian approaches, were followed. The eulerian approach was employed to obtain the water quality properties concentrations on the water column and in the benthos. The lagrangian approach was useful to estimate accurately the cages footprint, as lagrangian particles are not restricted by the horizontal resolution of the model.

4 RESULTS AND DISCUSSION

4.1 Modelling results from the PCC

Results from PCC scenarios reveal and addition effect of ammonia levels between successive net-pens (Figure 6). Ammonia maximum modelled concentrations, after the addition effect of the 60 production units, was 0,091 mg l^{-1} on calm conditions, 0.036 mg l^{-1} for average currents and 0.021 mg l^{-1} for extreme currents. These ammonia levels were below the interval of 0.2 to 2 mg l^{-1} that has deleterious effects on fish [7]. Although this range of values could sensibility vary depending on fish size and balance between its ionized and unionized form (NH_3) [6]. These results would indicate that the limiting concentrations could be achieved in water tanks, where the water renewal is low, but in open water conditions the nitrogen discharges would not limit the production, as the hydrodynamic conditions and red-ox process would modify the toxic forms into harmless forms.

Same addition effect was observed for oxygen depletion, although in this case some values dropped within the limit considered (Figure 6). Critical concentrations for culture growth (5.5 mg l^{-1}) [10] were reached nearly after the half of the second row of cages under calm conditions. More intense currents would imply higher renewal rates in the water column which in addition would lead to reduced decreases of dissolved oxygen partial pressure.

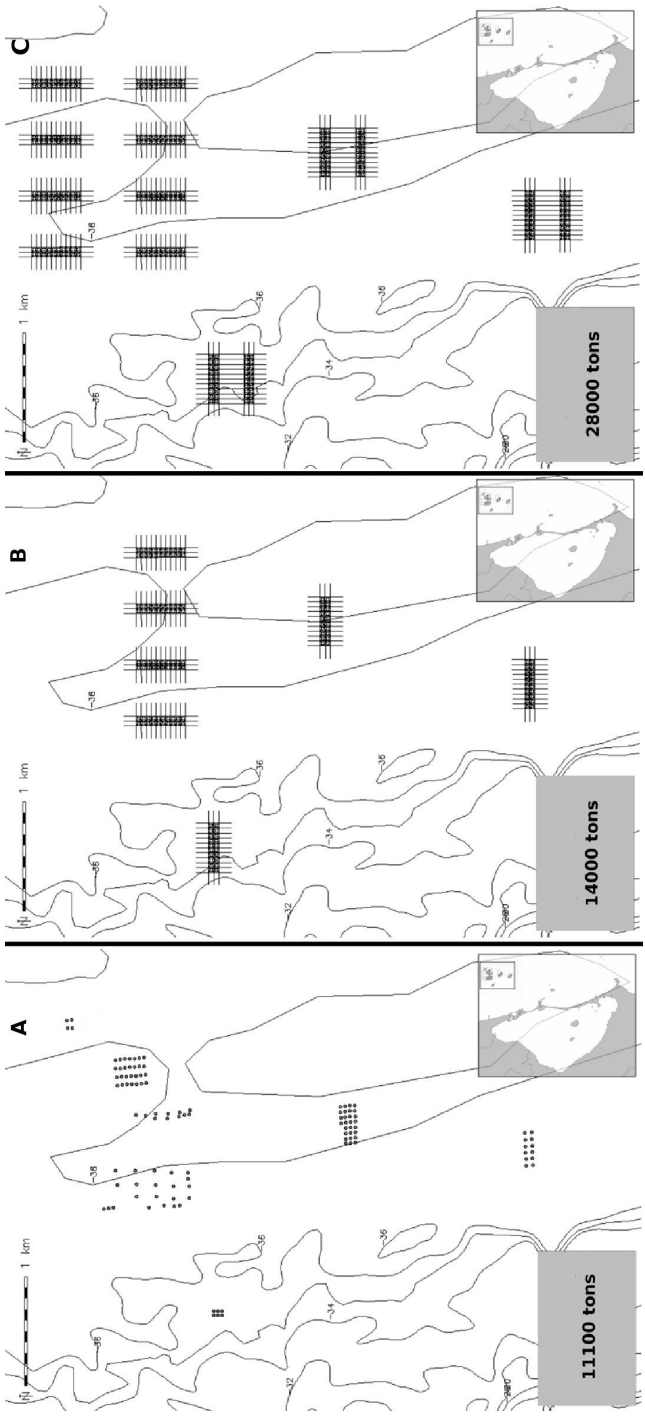

Figure 5. *Maps of the analysed alternatives for the San Pedro del Pinatar MCP environmental carrying capacity study: alternative description map: scenario I (a), scenario II (b), scenario III (c).*

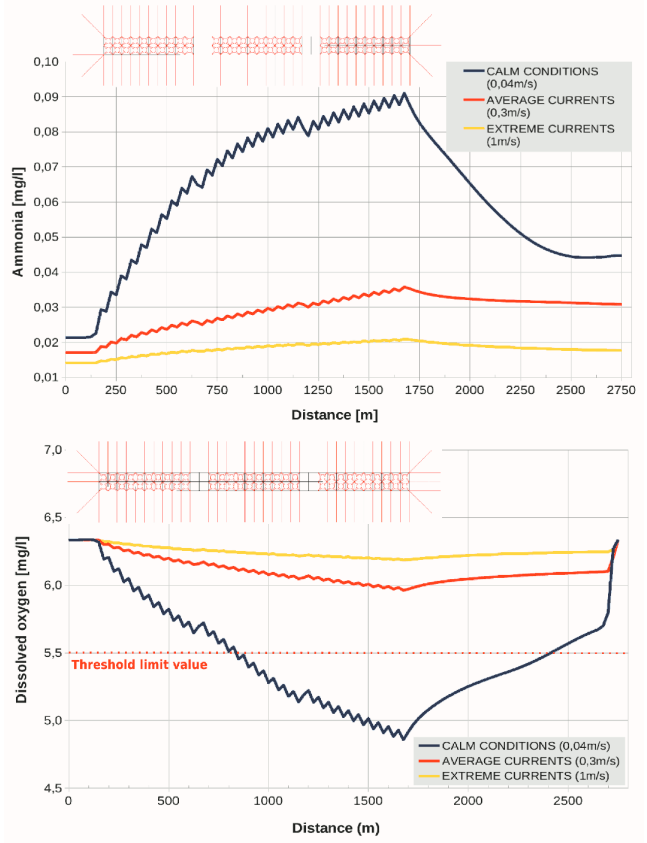

Figure 6. *Ammonia and oxygen modelled concentrations in the production carrying capacity study. The distance is measured from the beginning of the domain; the distribution of the cages is depicted on top of each figure. The threshold limit value for ammonia is out of the range of modelling results. The threshold limit value for oxygen concentration of 5.5* mg l^{-1} *is shown in the figure.*

From the results showed in figure 6, it could be estimated that the maximum number of cages that could be placed on the same row would be up to 24 cages; as from the twelfth pair of cages situations of stress might occur to the cultured fish. This curve could be used to obtain the minimum distance between installations, particularly in the case of two rows of 20 cages (ten pairs of cages) of 100 ton (Figure 6), a separation of 550 m would be necessary to ensure no negative effects due to possible hypoxia situations.

4.2 Results from the Environmental Carrying Capacity

Footprints from eulerian and lagrangian models were in agreement. Results from lagrangian approach simulations for the three different scenarios showed that footprint did not exceeded 475 meters from the facilities in the maximum amplitude axis (NW-SE) (Figure 7). Maximum rates of POM were obtained immediately below the cages (3,500 mg m^{-2} d^{-1}), being able to distinguish the individual cage footprints.

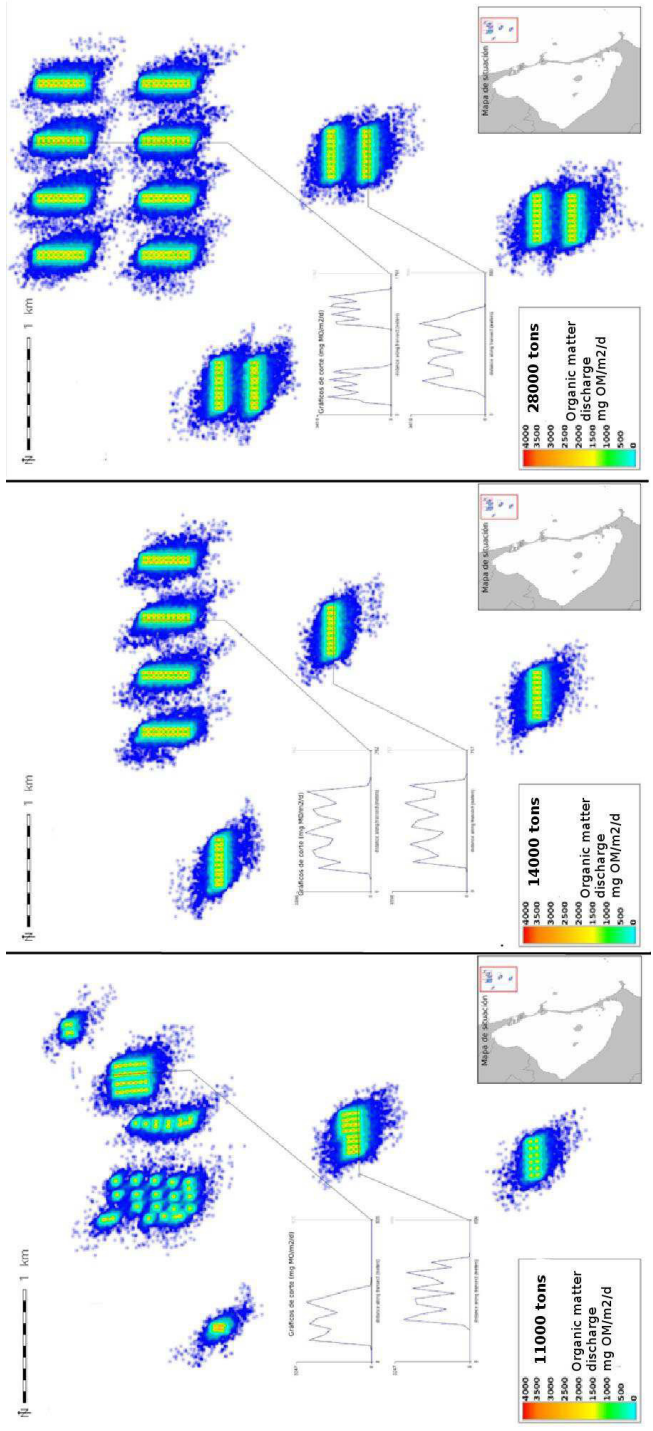

Figure 7. *Organic matter sedimentation rates obtained for the simulated alternatives (I, II and III).*

From the cages, sedimentation rates reduced rapidly, approximately 40 times in 50 m. It could be noted that facilities with low cage separation were less efficient in dispersing the discharges. Sedimentation rates around 1500 mg C m^{-2} d^{-1} would produce benthic community deterioration in mesocosm experiments [23,24]. Field experiments in East Mediterranean facilities [25] needed rates >4,100 mg C m^{-2} d^{-1} for altered conditions. Our modelling results reached rates between 100 and 1,000 mg C m^{-2} d^{-1}, corresponding to certain enrichment.

Results from the eulerian approach provided organic matter percentage values in sediment (Figure 8). The highest organic matter concentration in sediment was found in the ECC scenario of 28,000 tons (2.2%), surprisingly followed by the lower production case (11,100 tons) (2.1%); the 14,000 tons scenario has 1.7% of organic matter in sediments. These results could be explained because the alternatives caging higher biomass (alternative 2 and 3) spread their discharge over larger areas achieving lower sediment organic matter concentrations than the first alternative. These values would correspond to submerged areas with external inputs, slightly higher than maximum natural values in the study area. None of the simulated alternatives reaches values over the environmental quality standards (<2% out of the AZE; <4% within the AZE) established by the Region of Murcia administration [2].

5 CONCLUSIONS

Under the above assumptions and according to the MOHID model results, the discharges would not produce any significant change out of the MCP. Inside the MCP, the footprint could achieve early to moderate early stages of contamination according to the Pearson-Rosenberg model [9]. It was also observed that footprint was almost entirely due to the uneaten feed. Therefore, an efficient feeding management would reduce the unconsumed feed and would significantly improve the environmental compatibility. On the contrary mismanagement would produce a severe impact on the bottom sediments and benthic communities.

The definition of allowable change in an ECC study could be regarded as the most problematic issue due to the limited ability to predict the ecological and economic effects of environmental changes. The recovery assessment approach determines what is an acceptable impact or an undesirable perturbation *sensu* Tett et al. [8]. The recovery period of an area affected by organic matter enrichment depends on the temporal and spatial scale of hypoxia or anoxia. The longer the period of hypoxia the larger the amount of organic matter in the affected area that should be oxidized before macrofauna recolonisation could begin [26].

From the modelling results, aligning more than 12 production units should not be a recommended practice, as low oxygen levels could appear in the water column that might result in fish stress. When considering groups of 10 production units, the minimum distance between groups to overcome potential hypoxia would be of 550 m. Moreover, this distance is greater than footprint radio and would also avoid a synergic effect between facilities on the benthos.

Finally, the Mohid model adaptations that combined a NPZD model with the ability of zooplankton to consume directly organic matter were able to simulate the eutrophication resilience of the Mediterranean Sea waters. In addition, the implementation of the different organic matter pools related to the aquaculture production with lagrangian tracers resulted in a complete tool that would aid managers in terms of aquaculture production and coastal management.

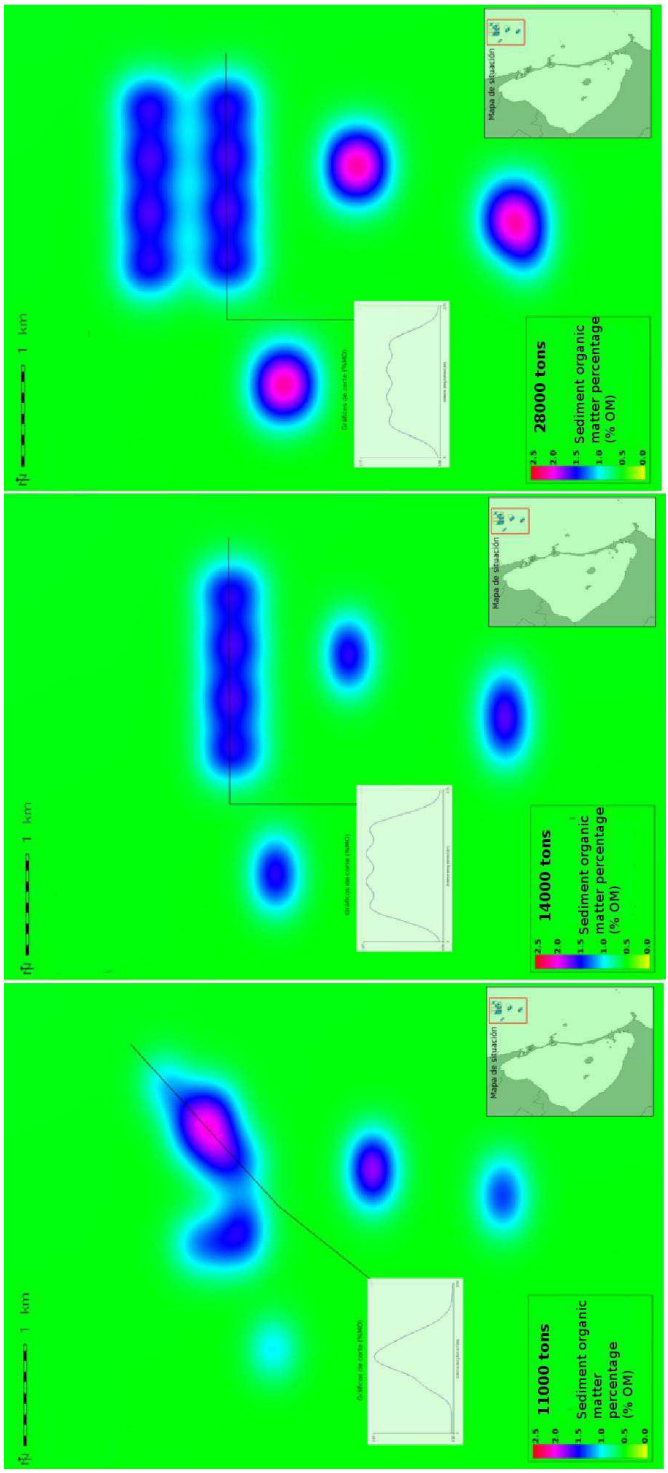

Figure 8. *TOrganic matter content in sediments for the simulated alternatives (I, II and III).*

ACKNOWLEDGEMENTS

The authors wanted to acknowledge the support to the Fisheries and Aquaculture Service of the Autonomous Community of the Region of Murcia.

REFERENCES

1. IUCN, 2009. Guide for the Sustainable Development of Mediterranean Aquaculture 2. Aquaculture site selection and site management, IUCN, Gland, Switzerland and Malaga, Spain. 303 pp.
2. TAXON, 2007. Protocolo para la Realización de los Planes de Vigilancia Ambiental de las Instalaciones de Acuicultura Marina en la Región de Murcia. Servicio de Pesca y Acuicultura. Comunidad Autónoma de la Región de Murcia. 148 pp.
3. Gowen, R.J., Bradbury, N.B., Brown, J.R., 1989. The use of simple models in assessing two of the interactions between fish farming and marine environment. R. Billard, N., de Pauw, Aquaculture - a Technology in progress, European Aquaculture Society, Bredene Belgium, 1071-1080
4. Cromey, C.J., Nickell, T.D., Black, K.D., 2002. DEPOMOD—modelling the deposition and biological effects of waste solids from marine cage farms, Aquaculture, 214(1–4): 211-239.
5. Braunschweig, F., Martins, F., Leitão, P., Neves, R., 2003. A methodology to estimate renewal time scales in estuaries: the Tagus Estuary case. Ocean Dynamics, 53: 137–145.
6. Person-Le Ruyet, J., Chartois, H., Quemener, L., 1995. Comparative acute ammonia toxicity in marine fish and plasma ammonia response. Aquaculture, 136 (1-2): 181-194.
7. Lemarié, G., Dosdat, A., Covès, D., Dutto, G., Gasset, E., Person-Le Ruyet, J., 2004. Effect of chronic ammonia exposure on growth of European seabass (Dicentrarchus labrax) juveniles. Aquaculture, 229(1-4): 479-491.
8. Tett, P., Read, P., Fernandes, T., Huxham, M., Gilpin, L., Wilkinson, M., Kennington, K., Malcolm, S., Mills, D., Gowen, R., Service, M., 2004. Understanding of undesirable disturbance in the context of eutrophication, and development of UK assessment methodology for coastal and marine waters. Stage 1 project report: what is undesirable disturbance? Report for DEFRA March 2004.
9. Pearson, T., Rosenberg, R., 1978. Macrobenthic succession in relation to organic enrichment and pollution of the marine environment. Oceanography and Marine Biology Annual Review, 16: 229-311.
10. Calderer, A. 2001., Influencia de la temperatura y salinidad sobre el crecimiento y consumo de oxígeno de dorada (Sparus aurata L.). PhD Thesis. Universidad de Barcelona.
11. Beveridge, M.C.M., 2004. Cage aquaculture. Malcolm C. M. Beveridge (Ed). Blackwell Publishing Ltd. 368 pp.
12. NIWA, 2000. An overview of factors affecting the carrying capacity of coastal embayments for mussel culture. NIWA Client Report: CHC00/69.
13. Bouza, N., Aboal, M., 2008. Checklist of phytoplankton on the South coast of Murcia (SE Spain, SW Mediterranean Sea). V. Evangelista, L. Barsanti, A.M. Frassanito, V. Passarelli, P. Gualtieri, Algal Toxins: nature, occurrence, effect and detection. The NATO Science for Peace and Security Programme, 179 -196.
14. MEDAR Group, 2002. MEDATLAS/2002 database. Mediterranean and Black Sea database of temperature salinity and bio-chemical parameters. Climatological Atlas. IFREMER Edition (4 Cdroms).
15. D'Ortenzio, F., D'Alcala, M.R., 2009. On the trophic regimes of the Mediterranean Sea: a satellite analysis. Biogeosciences, 6(2): 139-148.
16. Duarte, C.M., Agustí, S., 1998. The CO2 balance of unproductive aquatic ecosystem. Science, 281: 234-236.
17. Duarte, C.M., Agustí, S., Agawin, N.S.R., 2000b. Response of a Mediterranean phytoplankton community to increased nutrient inputs: a mesocosm experiment. Marine Ecology Progress Series, 195: 61–70.
18. Agustí, S., Duarte, C.M., Canfield, D.E., 1992. Self-regulation, bottom-up, and top-down control of phytoplankton communities: a reply to the comment by Kamenir. Limnology and Oceanography, 37: 683–687.

19. Lupatsch, I., 2004. Gilthead Seabream. Aqua Feeds: Formulation & Beyond, 1(1): 16-18.
20. Garcia, H.E., Locarnini, R.A., Boyer, T.P., Antonov, J.I., 2006. World Ocean Atlas 2005, Volume 4: Nutrients (phosphate, nitrate, silicate). S. Levitus, Washington D.C. (EEUU), U.S. Government Printing Office.
21. Sanz, J.L., Tello, O., Hermida, N., Fernández-Salas, I.M., González-Serrano, J.L., 2004. Características del estudio sistemático de la plataforma continental y talud superior españoles (proyecto ESPACE). Revista GEO-TEMAS, 6(2): 261-264.
22. Lyard, F., Lefevre, F., Letellier, T., Francis, O., 2006. Modelling the global ocean tides: modern insights from FES2004. Ocean Dynamics, 56: 394-415.
23. Frithsen, J.B., Oviatt, C.A., Keller, A.A., 1987. A comparison of ecosystem and single-species tests of sewage effluent toxicity: a mesocosm experiment data report. MERL Series, report No. 7. The University of Rhode Island, Kingston, Rhode Island, USA.
24. Kelly, J.R., Nixon, S.W. 1984. Experimental studies of the effect of organic deposition on the metabolism of a coastal marine bottom community. Marine Ecology Progress Series, 17: 157-169
25. Eleftheriou, A., Moore, D.C., Basford, D.J., Robertson, M.R., 1982. Underwater experiments on the effects of sewage sludge on a marine ecosystem. Netherlands Journal of Sea Research, 16: 465-473.
26. Díaz, R.J., Rosenberg, R., 1995. Marine benthic hypoxia: a review of its ecological effects and behavioural responses of benthic macrofauna. Oceanography Marine Biology Annual Review, 33: 245-303.